A geochemical and geothermometric study of the Nahlin ophiolite, northwestern British Columbia

by

Siobhan S. G. McGoldrick
Bachelor of Science (Hons.), Dalhousie University, 2014

A Thesis Submitted in Partial Fulfillment
of the Requirements for the Degree of

MASTER OF SCIENCE

in the School of Earth and Ocean Sciences

University of Victoria

Supervisory Committee

A geochemical and geothermometric study of the Nahlin ophiolite, northwestern British Columbia

by

Siobhan S. G. McGoldrick
Bachelor of Science (Hons.), Dalhousie University, 2014

Supervisory Committee

Dr. Dante Canil, School of Earth and Ocean Sciences
Supervisor

Dr. Laurence Coogan, School of Earth and Ocean Sciences
Departmental Member

Dr. Kristin Morell, School of Earth and Ocean Sciences
Departmental Member

Abstract

The Nahlin ophiolite represents one of the largest (~80 km long) and best-preserved ophiolites in the Cordillera of British Columbia and Yukon, Canada, yet it has been understudied compared to other ophiolites worldwide. Bedrock mapping at 1:20,000 scale in the Menatatuline Range area shows that the ophiolite is structurally disrupted with mantle bodies divisible into two massifs: Hardluck and Menatatuline. Studies of 30 samples show that both massifs consist of spinel harzburgites and minor lherzolites that have been strongly depleted by melt extraction (<2 wt % Al_2O_3 and ~45 wt % MgO). Clinopyroxene REE abundances determined by LA-ICP-MS illustrate different extents of depletion between the two massifs, with Yb_N varying from 2.3 – 5.0 and 1.7 – 2.2 in the Hardluck and Menatatuline massifs, respectively. Inversion modelling of the clinopyroxene REE abundances yields ~10 – 16% melting in the Hardluck massif and ~16 – 20% melting in the Menatatuline massif, with melt compositions that are compositionally similar to the gabbros and basalts proximal to the mantle rocks. All these extrusive and intrusive rocks in the ophiolite have an arc-signature, implying that the Nahlin ophiolite formed in a supra-subduction zone (SSZ) environment.

The Nahlin peridotites document a two-stage evolution: depletion of a locally heterogeneous mantle source by hydrous fractional melting, followed by refertilization of the refractory harzburgite in the mantle wedge evidenced by LREE enrichment in clinopyroxene and whole-rock chemistry. This two-stage evolution is also recorded by the thermal history of the harzburgites. The REE-in-two-pyroxene thermometry has been reset following cryptic and modal metasomatism and relatively slow cooling, whereas major element two pyroxene geothermometry records temperatures varying from near solidus (~1290 °C) to ~800 °C, with the highest temperatures recorded in samples from the Menatatuline massif. The refractory nature of the Menatatuline harzburgites in combination with the arc-influenced volcanic geochemistry provides overwhelming evidence for a SSZ origin. Peridotite from the Hardluck massif displays characteristics of both abyssal and SSZ peridotites. These geochemical and geothermometric constraints can be reconciled by evolution of the Hardluck and Menatatuline massifs as two separate segments along a backarc ridge system, later juxtaposed by dextral strike-slip faulting. Alternatively, the Nahlin ophiolite may represent proto-forearc seafloor spreading associated with subduction initiation akin to the proposed origins of the Izu-Bonin-Mariana arc (Stern et al.

2012; Maffione et al. 2015). In any case, the geochemical data for peridotites and magmatic rocks herein require that the SSZ-type Nahlin ophiolite reside in the upper plate at an intraoceanic convergent margin. This interpretation has strong implications for models of northern Cordilleran tectonics, where the Cache Creek terrane is typically shown as a subducting ocean basin during Cordilleran orogenesis.

Table of Contents

Supervisory Committee ii

Abstract iii

Table of Contents v

List of Tables vii

List of Tables (Appendix) viii

List of Figures ix

Acknowledgments xvii

Dedication xviii

Method of presentation 1

Chapter 1. Introduction 2

1.1 Ophiolites: keys to understanding the oceanic lithosphere 2

1.2 Cordilleran ophiolites and the Cache Creek conundrum 3

1.3 Thesis objectives 6

1.4 Methodological approach 8

Chapter 2. Geochemistry of volcanic and plutonic rocks from the Nahlin ophiolite with implications for a Permo-Triassic arc in the Cache Creek terrane, northwestern British Columbia 9

2.1 Abstract 9

2.2 Introduction 10

2.3 Regional Geology 12

2.4 Geology of the Menatatuline Range area 14

2.5 Geochemistry 20

2.6 Discussion 25

2.7 Conclusions 39

Chapter 3. A tale of two massifs: geochemical and geothermometric constraints on the history of the harzburgite in the Nahlin ophiolite, British Columbia, Canada 41

3.1 Abstract 41

3.2 Introduction 42

3.3 Regional Geology 45

3.4 Petrography 50

3.5 Methods 52

3.6 Results 54

3.7 Discussion 71

3.8 Conclusions 88

Chapter 4. Conclusions 90

4.1 Conclusions from the crust 90

4.2 Conclusions from the mantle 90

4.3 Regional tectonic implications 91

4.4 Suggestions for future study 92

References 95

Appendix 111

List of Tables

Table 2-1: Summary of new and existing geochronological data..................................... 14

Table 3-1: Peridotite sample locations and coordinates. 51

Table 3-2: Calculated modal mineralogy.. 63

Table 3-3: Geothermometry results 67

List of Tables (Appendix)

Table A 1: Sample locations……………………………………………………..151

Table A 2: Volcanic and plutonic whole-rock chemistry…………………………..152

Table A 3: Petrography notes……………………………………………………… 153

Table A 4: Peridotite whole-rock chemistry from the Menatatuline massif………..154

Table A 5: Peridotite whole-rock chemistry from the Hardluck massif…………… 155

Table A 6: Representative olivine major element chemistry……………………….. 156

Table A 7: Representative spinel major element chemistry………………………... 157

Table A 8: Representative orthopyroxene major element chemistry ……………… 158

Table A 9: Representative orthopyroxene trace element chemistry…...................... 159

Table A 10: Representative clinopyroxene major element chemistry………………160

Table A 11: Representative clinopyroxene trace element chemistry………………. 161

Table A 12: Accuracy of LA-ICP-MS over period of study………………………. 162

Table A 13: Detection limits of LA-ICP-MS over period of study………………... 163

List of Figures

Figure 1.1: (Top) North polar projection showing the global distribution of Phanerozoic orogenic belts and examples of different ophiolite types, including sites of modern ophiolite formation (e.g., the Izu-Bonin-Mariana (IBM) and Tonga-Kermadec arc-trench rollback systems). (Bottom) Examples of different Phanerozoic ophiolite types and their distribution through geologic time. Supra-subduction zone ophiolites (red stars) include: 1-Zambales (Philippines), 3-Troodos (Cyprus), Kizildag (Turkey), and Semail (Oman), 4-Xigaze (Tibet), 6-Mirdita (Albania) and Pindos (Greece), 9-Magnitogorsk (southern Urals, Russia), 11-Solund-Stavfjord (southwestern Norway), 13-Bay of Islands (Canada), 15-Lachlan (southeastern Australia and Tasmania). Volcanic arc type ophiolites (light green triangles) include: 1-Itogon (Philippines), 4-Smartville and Josephine (California), 5-D'Aguilar (eastern Australia), and 7-Magnitogorsk (Russia). Modified after Dilek and Furnes (2014). 4

Figure 1.2: (A) Terranes of the northern Cordillera (modified after Nelson and Colpron 2011). Star denotes approximate location of study area. (B and C) Current tectonic framework for the evolution and accretion of the Cache Creek terrane onto ancestral North America. (B) Schematic reconstruction of Early Jurassic terrane configurations showing the closure of the Cache Creek "ocean" in map view (modified after Nelson and Colpron 2007). Red line denotes where the relationships shown in schematic cross-section (C) will be found after the Cache Creek "ocean" has closed. (C) Schematic cross-sectional model of Cache Creek terrane accretion ~173 Ma by Mihalynuk et al. (1994) whereby the Cache Creek "ocean" is subducted beneath both the Stikinia and Quesnellia arc terranes, analogous to the modern Molucca Sea region.................................. 6

Figure 1.3: Map of British Columbia highlighting the Cache Creek terrane and exposures of ultramafic rocks based on compiled British Columbia Geological Survey data (Mihalynuk et al. 1996). White dashed box approximates the location of the Menatatuline Range study area located ~ 100 km southeast of Atlin, BC. Black polygons within this box represent the mantle section of the Nahlin ophiolite.. 7

Figure 2.1**:** Lower inset map shows terranes of northern British Columbia and Yukon highlighting the Cache Creek terrane (CC; yellow) and location of the Menatatuline Range study area (red star). Main panel shows the regional geology of the northern Cache Creek terrane in Yukon and British Columbia. The Menatatuline Range study area is outlined in red dashed lines. Other localities referenced in text include: Nakina transect (NK, black dashed box), Hall Lake (HL), "Moho Saddle" (MS), Mount Nimbus (MN), French Range (FR), and the Kutcho assemblage (KT). Diamond symbols refer to locations of geochronological data described in Table 2-1. Inset map modified after Nelson and Colpron (2011). Main panel map modified after Zagorevski et al. (2015). 11

Figure 2.2: Bedrock geology of the Menatatuline Range area, from Peridotite Peak to Nahlin Mountain, based on 2015 – 2016 mapping and compiled British Columbia Geological Survey data (Mihalynuk et al. 1996). Sample locations symbolized by lithology and chemical affinity as discussed in text. Dikes are shown schematically. Names of geological features referenced in text are in italic font (e.g. Nahlin fault). Informal place names are indicated by quotation marks (e.g.,

"Tseta Creek area"). Background topographic raster image from Natural Resources Canada (1990a, 1990b). 12

Figure 2.3: Ultramafic rocks of the Nahlin ophiolite. (A) Primary tectonic fabric (S_1), and pyroxenite dike transposed into S_1, in harzburgite tectonite truncated by a replacive dunite pod near Peridotite Peak. (B) Tight, near isoclinal folding of a pyroxenite dike in harzburgite tectonite on Peridotite Peak. 16

Figure 2.4: Intrusive rocks of the Nahlin ophiolite in the Menatatuline Range area. (A) Boudinaged altered ultramafic cumulate (pale) with scalloped margins surrounded by harzburgite (dun brown), near the southern side of the Hardluck massif. (B) Varitextured gabbro intrusion near the southern side of the Hardluck massif, in the Menatatuline Range area. Grain size within the gabbroic intrusions varies from fine grained (top of sample shown) to pegmatitic (bottom portion of sample shown). (C) Straight margins (white dashed lines) of a gabbroic dike intruding harzburgite at Nahlin Mountain. (D) Boudinaged gabbroic dikes protrude along the slopes of Nahlin Mountain among recessively weathering serpentinite scree. 18

Figure 2.5: Mafic volcanic rocks previously grouped as part of the Nakina Formation, in northwestern British Columbia. (A) Locally fragmental texture in pervasively hematized volcaniclastic rocks. (B) Photomicrograph of an ultramafic crystal tuff with orthopyroxene crystal fragments, and serpentine pseudomorphs after rounded olivine fragments in PPL, and (C) in XPL. (D) Photomicrograph of a mafic tuff with lapilli in PPL, and (E) in XPL. 20

Figure 2.6: Menatatuline Range area lithogeochemical data for immobile trace elements plotted on rock classification diagrams after Pearce (1996) for (A) volcanic rocks, and (B) plutonic rocks. (A) Two samples plot as alkali basalts (blue circles; Group C volcanic rocks), whereas the Group A and B volcanic rocks are subalkaline and basaltic in composition (green triangles, Group A; red triangles, Group B). (B) Group A intrusive rocks of the Nahlin ophiolite, including gabbro pods (red circles) and gabbroic to diabasic dikes and sills (blue squares), share compositional similarities with the Group A subalkaline volcanic rocks in (A). Reference composition for normal mid-ocean ridge basalt (N-MORB), enriched mid-ocean ridge basalt (E-MORB), and ocean island basalt (OIB) shown in grey symbols for comparison (Sun and McDonough 1989). Data from igneous rocks of the Nakina transect shown for comparison (black crosses; English et al. 2010). 22

Figure 2.7: Discrimination of magma series by trace element data following the method of Ross and Bédard (2009). Group B and C volcanic rocks plot as transitional and calc-alkaline, respectively. Group A volcanic rocks are predominantly tholeiitic. Volcanic rocks from the southern Cache Creek terrane shown for comparison with northern Cache Creek data (black "x" symbols; Tardy et al. 2001, Lapierre et al. 2003). All other symbols as for Figure 2.6. 23

Figure 2.8: Lithogeochemical data for samples from the northern Cache Creek terrane plotted in Nb/Yb – Th/Yb space to discriminate between depleted and enriched sources, and potential enrichment mechanisms. Reference compositions for N-MORB, E-MORB, and OIB are shown for comparison (grey symbols; Sun and McDonough 1989). Samples derived from an enriched source plot near the OIB reference point with high Th/Yb and Nb/Yb ratios. The Group A

plutonic and volcanic rocks plot near the N-MORB reference value, but show evidence of subduction-related enrichment. Group B and C volcanic rocks plot near reference values for E-MORB and OIB, respectively, indicating derivation from a more enriched source. Data from the Nakina Transect (English et al. 2010), and from volcanic rocks in the southern Cache Creek terrane in central BC (Tardy et al. 2001; Lapierre et al. 2003) are shown for comparison. Samples from the southern Cache Creek plot along the source enrichment trend, and appear to lack any subduction enrichment. Modified after Pearce (1982), and English et al. (2010).......... 24

Figure 2.9: Rare-earth element (REE) multi-element concentrations relative to chondrite (Sun and McDonough 1989) for the Menatatuline Range area intrusive and extrusive igneous rocks. (A) Group A volcanic and volcaniclastic rocks (green triangles) compared to the range of compositions of island arc tholeiites (IAT) and backarc basin basalts (BABB) in the Nakina transect, and to mafic volcanic rocks from the Kutcho assemblage (white triangles, Childe and Thompson 1997). (B) Group B (red triangles) and Group C (blue circles) volcanic rocks from the Menatatuline Range area, compared to the range of compositions of E-MORB and OIB volcanic rocks in the Nakina transect. (C) Group A plutonic rocks, including dikes ± sills (blue squares) and gabbro pods (red circles). Data from Nakina transect gabbros shown by the grey shaded region. (D) Group A ultramafic and gabbroic cumulates from the Nahlin ophiolite. All data for the Nakina transect (shaded regions) from English et al. (2010).. 26

Figure 2.10: Rare-earth element (REE) multi-element concentrations relative to N-MORB (Sun and McDonough 1989) for the Menatatuline Range area intrusive and extrusive igneous rocks. Symbols and shaded regions as for Figure 2.9. All data for the Nakina transect from English et al. (2010).. 27

Figure 2.11: Schematic stratigraphic columns for the upper plate, lower plate, and overlap assemblages of the northern Cache Creek terrane based on new and existing geochronological data. Age constraints for lower plate sedimentary rocks after Monger (1975, 1977), Cordey et al. (1991), and Mihalynuk et al. (2003, 2004b). Age constraints for the overlap assemblage sedimentary rocks after Cordey et al. (1991), and Mihalynuk et al. (2003, 2004b), and for the upper plate (ophiolite) assemblage after Gordey et al. (1998), Devine (2002), Mihalynuk et al. (2004b), and Zagorevski et al. (2016a)... 28

Figure 2.12: (A) Group A volcanic rock compositions from the Nahlin ophiolite (grey triangles; this study) and correlative Nakina transect BABB and IAT compositions (light and dark grey shaded areas; English et al. 2010) compared to melt model results relative to chondrite. Dot-dashed black line indicates the bulk-rock starting composition, and coloured dashed lines reflect segregated melt compositions after 1 - 20% non-modal fractional partial melting of a DMM source in the spinel stability field. (B) Bulk-rock REE concentrations for peridotite samples from nearby Peridotite Peak, “Moho Saddle”, and Peridotite Peak East (grey circles; Babechuk et al 2010) compared to modeled residue compositions after depletion by 1 – 20% non-modal fractional partial melting of a DMM source in the spinel stability field. All model parameters for (A) and (B) follow those of Warren (2016). Starting DMM bulk-rock composition after Workman and Hart (2005), partition coefficients calculated for a mantle of DMM composition at a potential temperature of 1300 °C (Sun and Liang 2014; Warren 2016). Melting follows the

reaction of Wasylenki et al. (2003) for DMM1 composition at 1.0 GPa: 0.56 Opx + 0.72 Cpx + 0.04 Sp = 0.34 Ol + 1.0 Melt. 32

Figure 2.13: Potential configurations of the lower plate OIB-carbonate assemblage and the Nahlin ophiolite during the formation of the Nahlin ophiolite as a result of subduction initiation (A, B and C; modified after Maffione et al. 2015), or during spreading in a backarc setting (D) and in a southern Havre Trough-like setting (E). (A) Progressive development of a new subduction zone parallel a paleo-spreading centre or other pre-existing plane of weakness in the oceanic crust. In response to far-field ridge-perpendicular compression, deformation is localized along a pre-existing detachment fault and an underthrust develops. (B) The underthrust propagates laterally, nucleating a new subduction zone. Fluids are released from the subducting plate. (C) Extension on the overriding plate triggers renewed magmatism along the paleo-spreading centre, thereby forming new SSZ-type crust. The SSZ-type crust is preserved in what may later become the forearc region of a mature arc, and therefore has high potential to be preserved as a SSZ-type ophiolite. (D) Plate configuration for development of the Nahlin ophiolite along a backarc spreading centre. Combination of decompression (dry) and flux melting reconciles the BABB-like chemistry of the Group A volcanic rocks. (E) Formation of the Nahlin ophiolite in a southern Havre Trough-like setting, where cross-arc chains of constructive volcanic centres are separated by zone of tectonically accommodated extension erupting BABB along basinal rifts (Wysoczanski et al. 2010). Along-strike variations in volcanic chemistry, from volcanic arc basalts (e.g., Kutcho arc assemblage) to BABB (e.g., Group A arc tholeiites), may explain the lack of preserved arc in the immediate vicinity of the Nahlin ophiolite. 36

Figure 2.14: Rare-earth element (REE) multi-element N-MORB normalized plots for the Group A volcanic and volcaniclastic rocks of the Nahlin ophiolite (green triangles) compared to the range of compositions reported for forearc basalts (FAB) in the Bonin arc (orange shaded region; Ishizuka et al. 2011) and in the Mariana arc (yellow shaded region; Reagan et al. 2010; Reagan et al. 2013), and to the global average for backarc basin basalt (BABB, dark grey squares; Gale et al. 2013). 40

Figure 3.1: Map of British Columbia highlighting the Cache Creek terrane and exposures of ultramafic rocks based on compiled British Columbia Geological Survey data (Mihalynuk et al. 1996). White dashed box approximates the location of the Menatatuline Range study area (Figure 3.2) located ~ 100 km southeast of Atlin, BC. 44

Figure 3.2: Bedrock geology of the Menatatuline Range area, from Peridotite Peak to Nahlin Mountain, based on 2015 – 2016 mapping and compiled British Columbia Geological Survey data (Mihalynuk et al. 1996). Peridotite samples symbolized by location. Dikes are shown schematically. Lines A-B and C-D denote lines of cross sections (Figure 3.3). Names of geological features referenced in text are in italic font (e.g. Nahlin fault). Informal place names are indicated by quotation marks (e.g., “Moho Saddle”). Background topographic raster image from Natural Resources Canada (1990a, 1990b). For lithological legend see Figure 3.3. 45

Figure 3.3: Schematic cross-sections through the Nahlin ophiolite in the Menatatuline Range area (line A-B) and at Peridotite Peak (line C-D), with 2x vertical exaggeration. See Figure 3.4

for field photographs of some interpreted structures, particularly D_1 faults and late strike slip faults (‘Silver Salmon fault’)... 47

Figure 3.4: Peridotites and field relations within the Nahlin ophiolite. (A) Primary tectonic fabric (S1) in harzburgite (harz.) tectonite crosscut by pyroxenite dikes (pxite), on Peridotite Peak East. (B) Tight, near isoclinal folding of a pyroxenite dike in harzburgite tectonite on Peridotite Peak. (C) Subhorizontal contact between relatively fresh harzburgite tectonite and serpentinite extensively intruded by a gabbroic dike-and-sill complex (Gab.), looking WNW from Peridotite Peak East. (D) True “Cache Creek terrane” suture (D_1) exposed near Mt. Nimbus. Ophiolite harzburgite and gabbro thrust over Tethyan fauna-bearing Mississippian limestone (Carb.) intercalated with OIB-type lavas. (E) Harzburgite in the Menatatuline massif thrust over basaltic supracrustal rocks (Bas.) of the Nahlin ophiolite. Northeast-vergent D_1 thrust is extensively serpentinized. (F) Steeply-dipping ‘Silver Salmon fault’ transposes harzburgite of the Hardluck massif against siliciclastic rocks of the Kedahda Formation north of Peridotite Peak................ 49

Figure 3.5: Photomicrographs of peridotites from the Nahlin ophiolite. (A) Kink-banded orthopyroxene porphyroclasts in spinel harzburgite in sample DC0339. Irregular boundaries and embayments of olivine (Ol emb) into orthopyroxene suggest partial orthopyroxene dissolution during melt-rock interactions in the lithosphere. Some olivine divided into smaller sub-grains by mesh texture of serpentine veinlets. (B) Exsolution lamellae and irregular grain boundaries of orthopyroxene porphyroclasts in notably fresh spinel harzburgite sample DC0319. (C) Fine grained anhedral spinel in a well-equilibrated spinel harzburgite, as shown by ~120 ° grain boundaries between olivine and orthopyroxene in sample DC0318. 50

Figure 3.6: Whole-rock major and trace element data for the peridotites in the Nahlin ophiolite. Plots show variations of MgO against major oxides (A) Al_2O_3, (B), CaO, and trace elements (C) Sc, (D) Ni, (E) V, and (F) Yb. All major elements in oxide wt % and all trace elements in ppm. 56

Figure 3.7: Whole-rock chondrite-normalized REE profiles for peridotites in the Nahlin ophiolite, as measured by ActLabs (A) and Laurentian University (B). Chondrite normalization values after Sun and McDonough (1989). (A) Data from this study show flat to “U-shaped” REE patterns in peridotite from the Menatatuline massif. (B) Data reported in Babechuk et al. (2010) show distinct LREE-depleted patterns in peridotite from “Moho Saddle”, Peridotite Peak, and Peridotite Peak East (Hardluck massif). Symbology as for Figure 3.6. 57

Figure 3.8: Variations in spinel, clinopyroxene (A), and orthopyroxene (B) Cr# throughout the Nahlin ophiolite. Error bars are one standard deviation based on average Cr# calculated from 2 – 10 analyses in a given sample. Grey dashed lines represent degree of spinel facies partial melting (F) as calculated by spinel Cr# (Warren 2016). Symbology as for Figure 3.6............................ 59

Figure 3.9: Chondrite-normalized pyroxene REE profiles compared to modeled clinopyroxene compositions (A) and to compiled REE data from other ophiolites worldwide (B and D). Measured REE concentrations in clinopyroxene (A) and orthopyroxene (C) for the Hardluck (green lines) and Menatatuline (grey lines) massifs. Dashed black lines in (A) reflect residual clinopyroxene compositions following 10, 15, and 20% spinel facies non-modal fractional partial

melting. Source clinopyroxene composition shown by solid black line. All model parameters follow those of Warren (2016) and are described in the main text of this thesis. The range of REE concentrations measured in clinopyroxene (B) and orthopyroxene (D) in this study compared to pyroxene compositions reported in other ophiolites (thin black lines; Dygert and Liang 2015, and sources therein). Chondritic REE abundances after Sun and McDonough (1989). 61

Figure 3.10: Modeled residual clinopyroxene Ti and Dy concentrations during anhydrous and hydrous partial melting. Anhydrous melting models of a DMM-source (Warren 2016) and a MORB-source (Bizimis et al. 2000). Model for hydrous melting of a MORB-source after Bizimis et al. (2000). In anhydrous models, clinopyroxene is consumed by ~23% melting, whereas it persists in the residue up to 29% melting in the hydrous melting model. Fields for clinopyroxene in abyssal (Johnson et al. 1990; Johnson and Dick 1992) and SSZ (Bizimis et al. 2000, and references therein) peridotites shown by the green and grey shaded areas, respectively. Clinopyroxene from the Menatatuline massif plots inside the SSZ peridotite field, whereas peridotites from the Hardluck massif fall largely within the abyssal peridotite field and require lower degrees of partial melting to reproduce clinopyroxene Ti and Dy concentrations. Symbology as for Figure 3.6. 62

Figure 3.11: Correlations between whole-rock Al_2O_3 and (A) the degree of peridotite partial melting (F) estimated by spinel Cr# (see text for methodology), (B) modal clinopyroxene, and (C) modal olivine. Correlations show that the most refractory samples contain the lowest bulk-rock concentrations of Al_2O_3, the lowest proportions of clinopyroxene and the highest proportions of olivine. Symbology as for Figure 3.6. 64

Figure 3.12: Histogram of two pyroxene thermometry results for grain cores in the Hardluck massif (green), Menatatuline massif (red) and compiled to supra-subduction zone (SSZ) ophiolites worldwide (white). The Menatatuline massif appears to be uncommonly hot compared to other SSZ ophiolites. Histograms showing data from this study are constructed from average core closure temperature recorded in each sample within a given massif. Compiled T Ca-in-Opx data for other SSZ ophiolites from Pomonis et al. (2006), Choi et al. (2008), Batanova et al. (2011), Pirard et al. (2013), and Stewart et al. (2016). 66

Figure 3.13: Histograms of two pyroxene thermometry results from grain cores in the Nahlin ophiolite, compared to mid-ocean ridge (MOR) and supra-subduction zone (SSZ) ophiolites worldwide. (A) Distribution of core T_{BKN} (diagonal lines) and T_{REE} (solid colour) results from the Menatatuline massif. Menatatuline massif samples display temperature distributions unlike those calculated for any other MOR or SSZ-type ophiolite: T_{BKN} temperatures are unusually hot, and some T_{REE} results are anomalously cool. (B) Hardluck massif T_{BKN} and T_{REE} results are similar to compiled SSZ ophiolites. (C) Compiled thermometry results from MOR and (D) SSZ ophiolites. Histograms showing data from this study are constructed from average closure temperature recorded in each sample within a given massif. Results of T_{BKN} and T_{REE} thermometers for MOR and SSZ ophiolites (panels C and D) from Dygert and Liang (2015) and sources therein. 70

Figure 3.14: Plot of oxygen fugacity against spinel Cr# (rim) recorded in the peridotites from the Nahlin ophiolite. Oxygen fugacity, expressed as the deviation from the QFM buffer in log units ($\Delta \log f O_2$ QFM), calculated following the method of Ballhaus et al. (1990) using major element data measured in grain rims. Green, grey, and blue shaded areas show the approximate fields for abyssal and forearc peridotites, and Mariana forearc harzburgites (Parkinson and Pearce 1998). Arrows show the expected trend in increasing Cr# and fO_2 as mantle peridotite interacts with SSZ-type magmas (Arai 1994; Gaetani and Grove 1998; Parkinson and Pearce 1998). All data points symbolized as for Figure 3.6. 71

Figure 3.15: (A) Spatial variations in closure temperature within the Hardluck massif recorded by the orthopyroxene - spinel thermometry (Liermann and Ganguly 2003, 2007). Distance along the x-axis is measured in km from a reference point located ~1 km NNW of Hardluck Peaks. Symbols represent the average temperature calculated for a given sample. Error bars represent one standard deviation. (B) Schematic spreading centre showing interpreted stratigraphy within the Hardluck massif based on spatial trend of thermometry results. Samples from Peridotite Peak and Peridotite Peak East are less depleted (Figure 3.8) and record lower temperatures, indicative of slower cooling at a deeper level within the residual mantle column. Diagram modified after Langmuir et al. (1992). Symbology as for Figure 3.6. 78

Figure 3.16: Chemical evidence for secondary processes in the Nahlin peridotites. (A) Chondrite-normalized Yb in clinopyroxene against whole-rock Yb shows a trend among samples from the Hardluck massif. In contrast, there is little to no variation in clinopyroxene Yb with whole-rock Yb in samples from the Menatatuline massif. Data from the Hardluck massif were acquired at Laurentian University whereas data from the Menatatuline massif were acquired at ActLabs. (B) Olivine Mg# (Mg/(Mg + Fe)) against calculated modal olivine (volume %) showing the lack of correlation in the Nahlin peridotite data compared to expected trends for residues of simple partial melting in experimental data (1 - Baker and Stolper 1994) and abyssal peridotite data (2 - Baker and Beckett 1999). Symbology as for Figure 3.6. 80

Figure 3.17: Evidence of metasomatism in peridotites from the Menatatuline massif shown by outlying data points indicating enrichment of Sr in clinopyroxene in some samples recording relatively cool T_{REE}. Enriched Sr in clinopyroxene indicates that secondary processes have altered clinopyroxene chemistry in some samples. The results of this metasomatism are the outlying anomalously cool temperatures recorded within the Menatatuline massif. Dashed lines indicate the minimum and maximum detection limits for Sr on the LA-ICP-MS over several sessions. 83

Figure 3.18: Chondrite-normalized REE profiles for the lower crustal and supracrustal igneous rocks of the Nahlin ophiolite. (A) Group A volcanic rocks (grey triangles; McGoldrick et al. 2017) and correlative Nakina transect BABB (light grey shaded area) and IAT (dark grey shaded area) volcanic rocks (English et al. 2010) compared to modeled melt compositions. (B) Gabbro and gabbroic dikes of the Nahlin ophiolite (McGoldrick et al. 2017) relative to modeled melt compositions. Solid black lines indicates the bulk-rock starting composition, and coloured dashed lines reflect segregated melt compositions after 5 - 20% non-modal fractional partial melting of a DMM source in the spinel stability field, as described in the text. Melt modeling parameters as for Figure 3.9. Based on REE profiles, the Group A plutonic and volcanic rocks

represent segregated melts following <5 to ~20% partial melting. Chondritic REE abundances after Sun and McDonough (1989).. 88

Figure A 1: Variations in core and/or rim closure temperatures with increasing grain size for several geothermometers. 111

Figure A 2: Electron microprobe analysis locations... 113

Figure A 3: Laser ablation ICP-MS analysis locations... 134

Acknowledgments

I would like to express my sincere gratitude to my supervisor Dante Canil for his encouragement, detailed feedback, open door policy and willingness to have me partake in two summers of field work during this project. Secondly, thank you to Alex Zagorevski at the Geological Survey of Canada, without whom this project would not have been possible. Alex is also thanked for his guidance and collaboration on field reports and subsequent papers, and for giving me the freedom to plan and execute my own field mapping. I would like to thank my committee members for their thoughtful questions and input that helped shape this thesis: Laurence Coogan, Kristin Morell, Derek Thorkelson, and Dante Canil. Additional thanks to Simon Carroll, Anne-Sophie Corriveau, Sebastian Bichlmaier, Chris Lawley, and Mitch Mihalynuk for assistance, collaboration, and great debates in the field. Thanks to Norm Graham and Paula Vera at Discovery Helicopters for safe transport to and from Atlin, BC. Thanks also to Edith Czech and Mati Raudsepp (UBC) for their assistance on the EMP, and Jody Spence (UVic) for his assistance on the LA-ICP-MS. I would also like to express my thanks to the faculty and lab instructors in the School of Earth and Ocean Sciences for their guidance and support in the various teaching assistant roles I filled during my time at UVic: David Nelles, Duncan Johannessen, Casey Brant, Kathy Gillis, Laurence Coogan, and Dante Canil. Thanks to the cohort of graduate students for their friendship and support, and for the lively lunch and coffee time discussions. Special thanks to fellow petrology lab graduate students Rameses D'Souza and Rebecca Lynch. Thanks to Val Jackson, Luke Ootes, Rebecca Jamieson, Martin Gibling, and to my uncle Richard Brown for their mentorship, support, and encouragement to pursue graduate studies. Finally, thank you to my mother Beverly, and to my partner Jeff for their tireless encouragement and faith in me.

This project was supported by the Geological Survey of Canada's Geomapping for Energy and Minerals program (GEM2) (GSC contribution # 20150308), Research Affiliate Program Bursary (S. McGoldrick), Natural Sciences and Engineering Research Council of Canada (NSERC) and Geoscience BC scholarships (S. McGoldrick), and NSERC Discovery grant (D. Canil).

Dedication

For my mother, Beverly Gail.
The strongest and most self-less person I know.

Method of presentation

This thesis is presented as two self-contained papers (Chapters 2 and 3), each contributing to the common goals of reconstructing the tectonic setting, magmatic and thermal history of the Nahlin ophiolite. This method of presentation is intended to facilitate the publication of research presented herein. Consequently, this format does introduce redundancies. Chapters 1 and 4 are introductory and conclusion chapters, respectively. These chapters describe how the self-contained manuscripts form a collective and coherent thesis by outlining the aims of the current study and suggestions for further research. I am the primary author of all the manuscripts presented herein (Chapters 2 and 3), and each is co-authored by my supervisor, Dante Canil, and by Alex Zagorevski (Geological Survey of Canada). At the time of thesis submission, Chapter 2 has been accepted for publication in the Canadian Journal of Earth Sciences. Chapter 3 is currently being revised for submission to Contributions to Mineralogy and Petrology with the goal of submitting in fall 2017.

Chapter 1. Introduction

1.1 Ophiolites: keys to understanding the oceanic lithosphere

Ophiolites constitute one of the most valuable means of studying the oceanic lithosphere. They represent the only window into past oceanic crust and uppermost mantle, as there is no oceanic lithosphere over ~170 Ma preserved in modern oceans. The study of ophiolites has offered insight into mantle chemistry, lithospheric structure of ancient ocean basins, and the interplay of magmatic and tectonic processes at spreading centres. Ophiolites are also vital to reconstructing the tectonic evolution of orogenic belts (Figure 1.1), where they commonly mark sutures along which ancient ocean basins have been consumed. As a result of orogenesis, ophiolites are typically highly altered and faulted, making it difficult to reconstruct pre-obduction stratigraphy (Stern et al. 2012). This is particularly true of Cordilleran ophiolites, many of which have been dismembered during their emplacement and subsequent continental growth along the western margin of ancestral North America (e.g., Ash 1994; Beccaluva et al. 2004; Shervais et al. 2004). The dissection of ophiolites during orogenesis therefore increases the level of complexity compared to studies of modern spreading ridges. Furthermore, unlike investigations of modern seafloor spreading and abyssal peridotites, studies of ophiolites are often complicated by the confusion surrounding paleo tectonic setting (e.g., in the Troodos ophiolite; Miyashiro 1973; Varga and Moores 1985; Batanova and Sobolev 2000; Moores et al. 2000). Historically, ophiolites were considered the product of seafloor spreading at mid-ocean ridges (Anonymous 1972) but this was called into question with the recognition of island arc magmatism associated with ophiolites (Miyashiro 1973). Presently, many ophiolites are considered to have subduction-related origins, such as formation in volcanic arc or supra-subduction zone settings (Figure 1.1; Dilek and Furnes 2014).

Pivotal studies of ophiolites in Oman (e.g., Coleman 1981; Pearce et al. 1981; Kelemen et al. 1995, 1997a), Cyprus (e.g., Miyashiro 1973; Varga and Moores 1985; Batanova and Sobolev 2000; Dilek and Furnes 2009), and the Coast Ranges of California (e.g., Shervais and Kimbrough 1985; Kelemen and Dick 1995; Shervais et al. 2004; Choi et al. 2008a, b) have produced major advancements in the understanding of mantle melting, melt production, melt movement at spreading centers, hydrothermalism, and the formation and cooling of oceanic mantle lithosphere. Despite this, there remain many ophiolites of similar size and exposure in other collisional margins that have been understudied. This is particularly true in the Canadian Cordillera, where exposures of ophiolites are typically in remote areas.

1.2 Cordilleran ophiolites and the Cache Creek conundrum

Upper Paleozoic to Lower Mesozoic ophiolites exposed throughout British Columbia and Yukon (Figure 1.1) play a crucial role in Cordilleran orogenesis, because they are commonly interpreted to mark remnants of closed ocean basins (e.g., Tempelman-Kluit 1979; Ash and Arksey 1990; Struik et al. 2001). In the Cordillera, as with ophiolites elsewhere, interpretations of tectonic setting typically rely solely on the geochemical signatures of the volcanic section of the ophiolite (e.g., Miyashiro 1973; Alabaster et al. 1982; Ishikawa et al. 2002; Dilek et al. 2008). In British Columbia and Yukon this has led to conflicting views on the role of “oceanic” terranes, particularly the Cache Creek terrane, in tectonic models of the Cordilleran orogen (Figure 1.2) (Tardy et al. 2001; Lapierre et al. 2003; English et al. 2010).

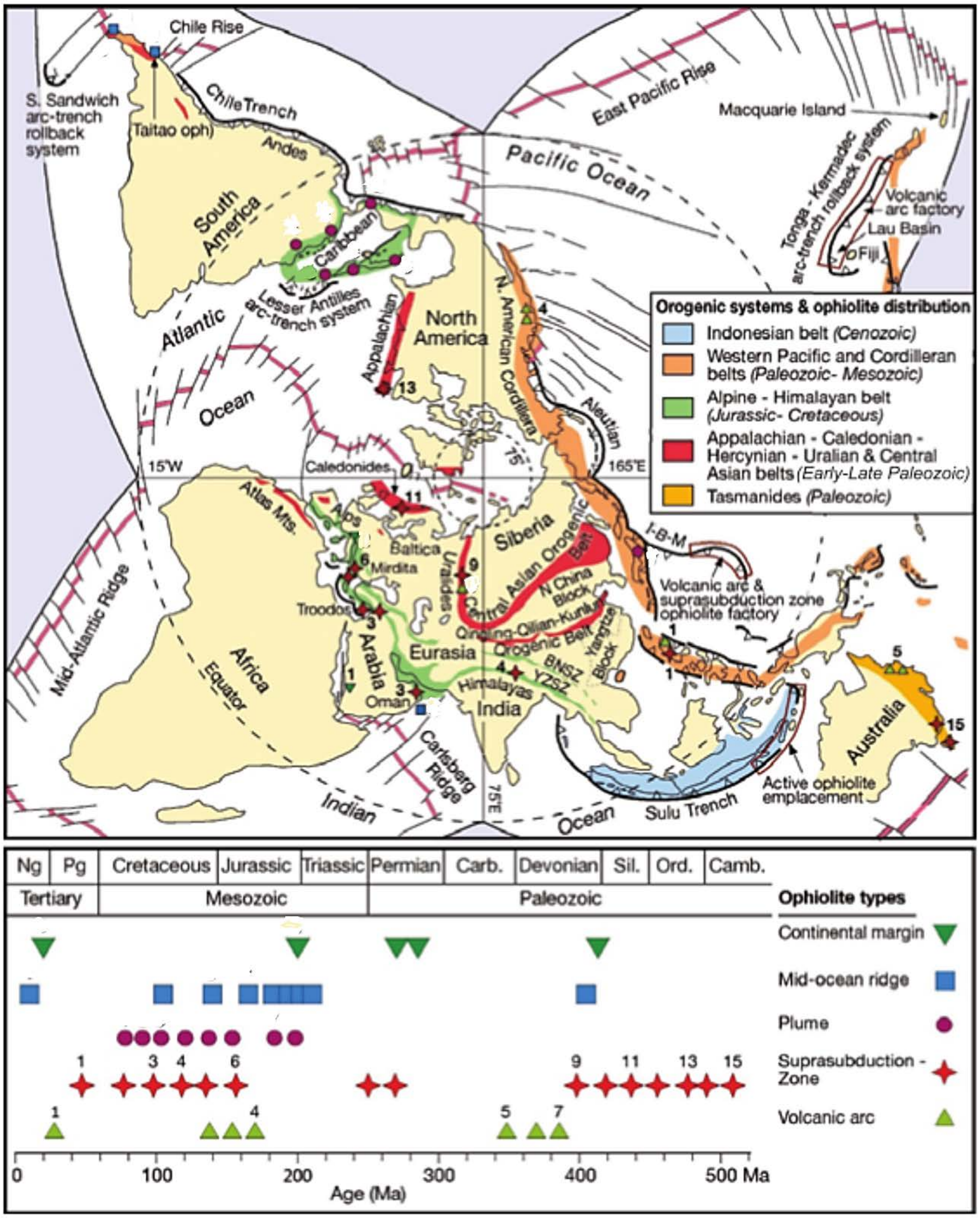

Figure 1.1: (Top) North polar projection showing the global distribution of Phanerozoic orogenic belts and examples of different ophiolite types, including sites of modern ophiolite formation (e.g., the Izu-Bonin-Mariana (IBM) and Tonga-Kermadec arc-trench rollback systems). (Bottom) Examples of different Phanerozoic ophiolite types and their distribution through geologic time. Supra-subduction zone ophiolites (red stars) include: 1-Zambales (Philippines), 3-Troodos (Cyprus), Kizildag (Turkey), and Semail (Oman), 4-Xigaze (Tibet), 6-Mirdita (Albania) and Pindos (Greece), 9-Magnitogorsk (southern Urals, Russia), 11-Solund-Stavfjord (southwestern Norway), 13-Bay of Islands (Canada), 15-Lachlan (southeastern Australia

and Tasmania). Volcanic arc type ophiolites (light green triangles) include: 1-Itogon (Philippines), 4-Smartville and Josephine (California), 5-D'Aguilar (eastern Australia), and 7-Magnitogorsk (Russia). Modified after Dilek and Furnes (2014).

The Cache Creek terrane has long been an enigma in Cordilleran geology: how can a so-called "exotic terrane" bearing Tethyan fauna (Monger and Ross 1971; Orchard et al. 2001) be entrapped between two arc terranes characterised by North American fauna? Models have invoked various processes to solve this puzzle, including proposed growth of a ribbon continent outboard of Laurentia (Johnston and Borel 2007) and oroclinal closure of an ocean basin between two arcs (Figure 1.2; Mihalynuk et al. 1994). Yet in many of these models, the Cache Creek terrane represents the downgoing plate. Considering the role of ophiolites at this collisional margin, this begs the question, why has so much mantle peridotite been preserved from the subducting oceanic lithosphere? Given the prevalence of supra-subduction zone and volcanic arc-related ophiolites worldwide (Figure 1.1), does this lower plate configuration seem favourable for ophiolite preservation in the Cache Creek terrane?

Such questions have never been approached by studying the lithospheric mantle preserved in several large ophiolites in the northern Cache Creek terrane. This study aims to fill this gap in knowledge by presenting complementary petrological studies of crustal and mantle sections of the Nahlin ophiolite (Figure 1.3) that provide crucial clues to its evolution and role in regional tectonics. Peridotite whole-rock and mineral chemical data can address questions about the setting and extent of melting in the mantle section of the ophiolite, and the relationship between the mantle peridotite and overlying basaltic crust; questions that have hitherto been largely ignored in discussions of the Canadian Cordilleran ophiolites.

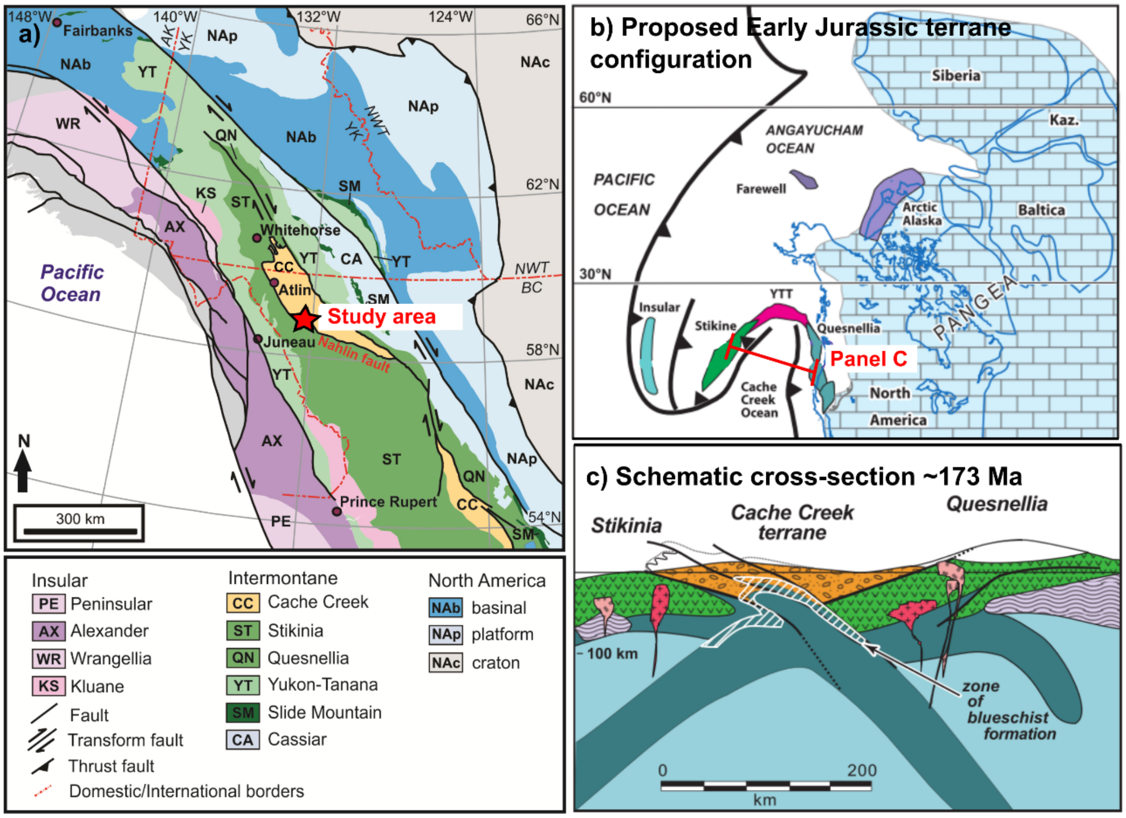

Figure 1.2: (A) Terranes of the northern Cordillera (modified after Nelson and Colpron 2011). Star denotes approximate location of study area. (B and C) Current tectonic framework for the evolution and accretion of the Cache Creek terrane onto ancestral North America. (B) Schematic reconstruction of Early Jurassic terrane configurations showing the closure of the Cache Creek "ocean" in map view (modified after Nelson and Colpron 2007). Red line denotes where the relationships shown in schematic cross-section (C) will be found after the Cache Creek "ocean" has closed. (C) Schematic cross-sectional model of Cache Creek terrane accretion ~173 Ma by Mihalynuk et al. (1994) whereby the Cache Creek "ocean" is subducted beneath both the Stikinia and Quesnellia arc terranes, analogous to the modern Molucca Sea region.

1.3 Thesis objectives

The objectives of this study are to:

1) examine the petrogenetic relationships between mantle, lower crustal and supracrustal rocks of the Nahlin ophiolite,
2) define the tectonic setting represented by the crustal igneous rocks of the Nahlin ophiolite,

3) constrain the tectonic setting and the magmatic and thermal history of peridotites in the Nahlin ophiolite,
4) determine whether the two peridotite massifs that comprise the mantle section of the Nahlin ophiolite originated at the same spreading centre as a contiguous mantle section, and
5) discuss the significance of these conclusions on the distribution of terranes during amalgamation of the northern Canadian Cordillera.

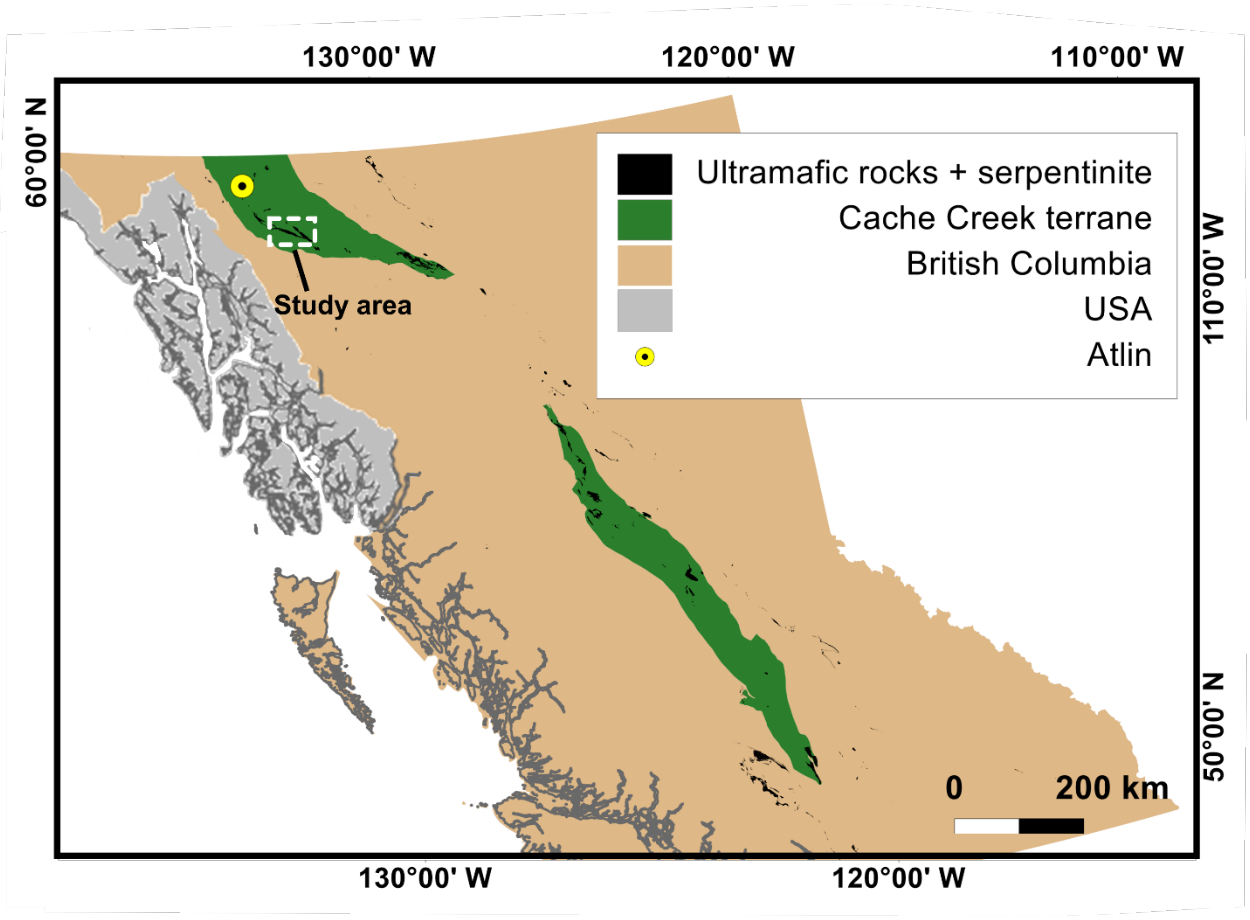

Figure 1.3: Map of British Columbia highlighting the Cache Creek terrane and exposures of ultramafic rocks based on compiled British Columbia Geological Survey data (Mihalynuk et al. 1996). White dashed box approximates the location of the Menatatuline Range study area located ~ 100 km southeast of Atlin, BC. Black polygons within this box represent the mantle section of the Nahlin ophiolite.

1.4 Methodological approach

This is a field-based study stemming from bedrock mapping and sampling conducted over six days in July 2015 and five days in July 2016 in the Menatatuline Range study area (Figure 1.3). Access to the field area was by helicopter from Atlin, BC. A list of sample locations is provided in Table A 1. Using the volcanic and plutonic rocks collected during bedrock mapping, an investigation of petrography and geochemistry was undertaken to place the Nahlin ophiolite in the broader context of the northern Cache Creek terrane. Whole-rock geochemical data from these samples were augmented by data from the Nakina transect, an along-strike section mapped by the British Columbia Geological Survey in 2001-2003 (English et al. 2002, 2010; Mihalynuk et al. 2003).

Peridotite samples from the Nahlin ophiolite were examined to further constrain its interpreted tectonic setting. Spinel harzburgite samples were collected from the Menatatuline massif during 2015-2016 mapping, and were processed and analysed for whole-rock chemistry at ActLabs Ltd. Peridotite samples from the Hardluck massif were collected by Dante Canil in 2002 and 2003. Whole-rock geochemical data from the peridotites of the Menatatuline massif were augmented by existing whole-rock data from the Hardluck massif, originally reported by Canil et al. (2006) and Babechuk et al. (2010). Major and trace element mineral chemical data for this study were acquired by electron microprobe at the University of British Columbia and laser ablation ICP-MS at the University of Victoria, respectively.

Chapter 2. Geochemistry of volcanic and plutonic rocks from the Nahlin ophiolite with implications for a Permo-Triassic arc in the Cache Creek terrane, northwestern British Columbia

2.1 Abstract

The origin of the Nahlin ophiolite in the northern Cache Creek terrane, and its role in Cordilleran orogenesis, has long remained controversial. In the Menatatuline Range area in northwestern British Columbia, the Nahlin ophiolite comprises spinel harzburgite tectonite with minor lherzolite, lower crustal gabbro and plagioclase-bearing olivine websterite cumulates, gabbro dikes intruding mantle harzburgite, and basaltic volcanic and volcaniclastic rocks. New lithogeochemical data from the Menatatuline Range area confirm that plutonic and volcanic rocks of the ophiolite are tholeiitic and arc-related, whereas only a minor component of volcanic rocks are alkaline intraplate basalts. Tholeiitic basalts of the Nahlin ophiolite represent the products of up to 20% partial melting, and peridotite from the ophiolite mantle section may represent the residue complement of this spinel facies fractional melting. Correlative tholeiitic volcanic sections can be found elsewhere in the northern Cache Creek terrane, and may be linked to a regionally extensive (~200 km) intraoceanic Permo-Triassic arc. The arc tholeiite geochemistry of the lower and supracrustal rocks, and the highly depleted nature of the mantle residues, imply that the Nahlin ophiolite formed in a supra-subduction zone (SSZ) environment. The Nahlin ophiolite therefore occupied the upper plate during intraoceanic collision prior to emplacement of the Cache Creek terrane onto ancestral North America. The volumetrically minor OIB-type volcanic rocks in the northern Cache Creek terrane are associated with carbonate successions bearing Tethyan fauna and likely represent fragments of oceanic plateaux

and their carbonate atolls “sliced off” of the subducting plate. These sequences are unrelated to the Nahlin ophiolitic arc system.

2.2 Introduction

Ophiolites are ubiquitous features of Phanerozoic orogens where they represent fragments of oceanic lithosphere preserved along suture zones. Upper Paleozoic–Lower Mesozoic ophiolites exposed throughout the Canadian Cordillera are commonly interpreted to mark remnants of closed ocean basins (e.g., Tempelman-Kluit 1979; Ash and Arksey 1990; Struik et al. 2001). However, despite their importance to tectonic models of the Cordillera, few detailed studies of the ophiolitic rocks have been carried out in northern British Columbia and Yukon (Terry 1977; Ash and Arksey 1990; Ash 1994; Canil et al. 2006). The Cache Creek terrane in northwestern British Columbia preserves aerially extensive ophiolite mantle and crustal sections well suited to detailed petrological and geochemical studies. Herein we build on work by English et al. (2010) in the northern Cache Creek terrane, which identified two distinct petrogenetic components in this region: abundant subalkaline plutonic and volcanic rocks with arc signatures, and minor alkaline within-plate volcanic rocks, an association also noted in central British Columbia (Tardy et al. 2001; Lapierre et al. 2003). The close spatial association of volcanic rocks originating in two different plate settings has implications for the emplacement of the Nahlin ophiolite, closure of the Cache Creek ocean basin, and models of terrane accretion during continental growth in the Cordillera.

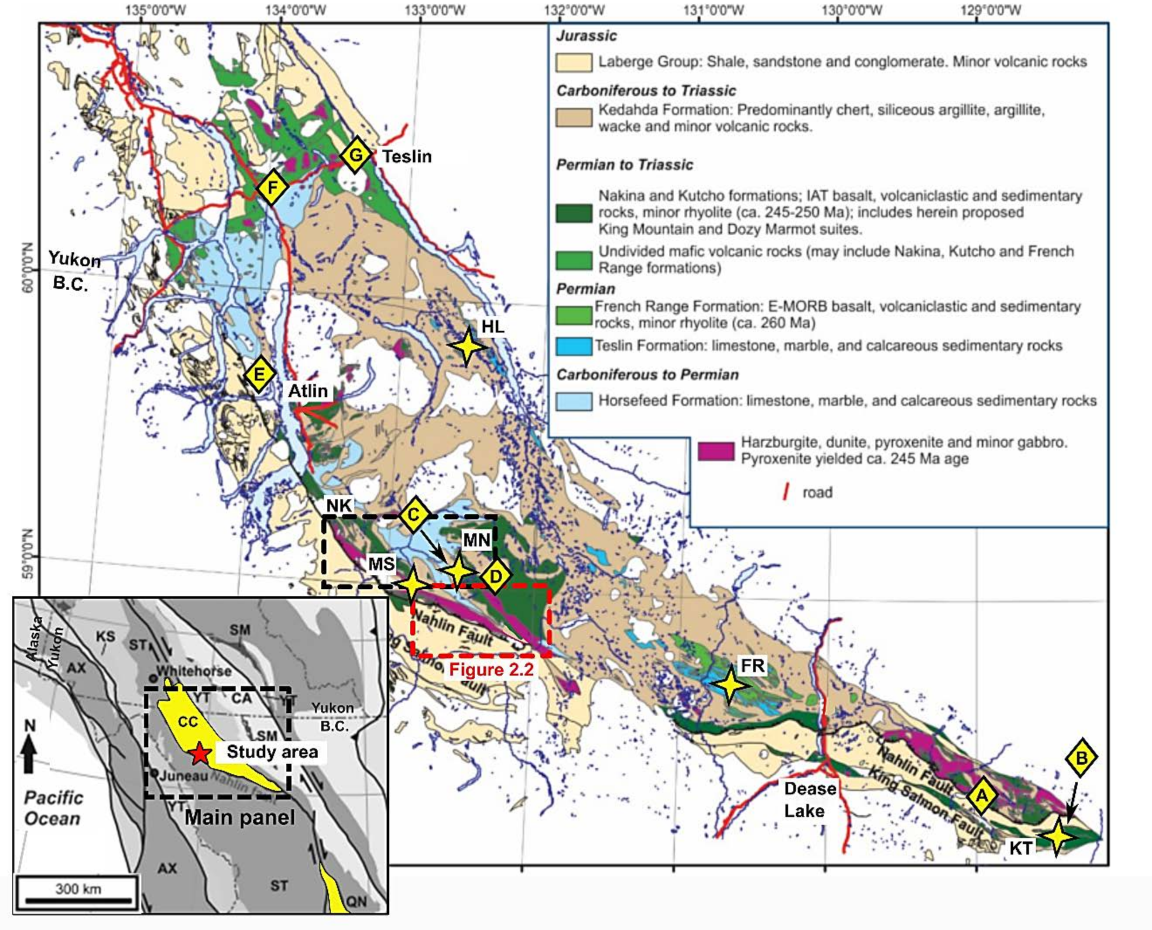

Figure 2.1: Lower inset map shows terranes of northern British Columbia and Yukon highlighting the Cache Creek terrane (CC; yellow) and location of the Menatatuline Range study area (red star). Main panel shows the regional geology of the northern Cache Creek terrane in Yukon and British Columbia. The Menatatuline Range study area is outlined in red dashed lines. Other localities referenced in text include: Nakina transect (NK, black dashed box), Hall Lake (HL), "Moho Saddle" (MS), Mount Nimbus (MN), French Range (FR), and the Kutcho assemblage (KT). Diamond symbols refer to locations of geochronological data described in Table 2-1. Inset map modified after Nelson and Colpron (2011). Main panel map modified after Zagorevski et al. (2015).

In this contribution, I investigate the geological relationships and petrochemistry of the Nahlin ophiolite and adjacent rocks in the Menatatuline Range area of northern British Columbia. The Nahlin ophiolite is the largest, best-preserved and well exposed ophiolite in the Cache Creek terrane (Figure 2.1), however, due to its remoteness it has not been investigated in detail since Terry (1977). I present new field and lithogeochemical data constraining the relationships between mantle, lower crustal and supracrustal rocks in the Nahlin ophiolite, and the spatial connection to accreted alkaline basalt and carbonate platform sequence. I also discuss the significance of these data on the distribution of terranes during amalgamation of the northern Canadian Cordillera.

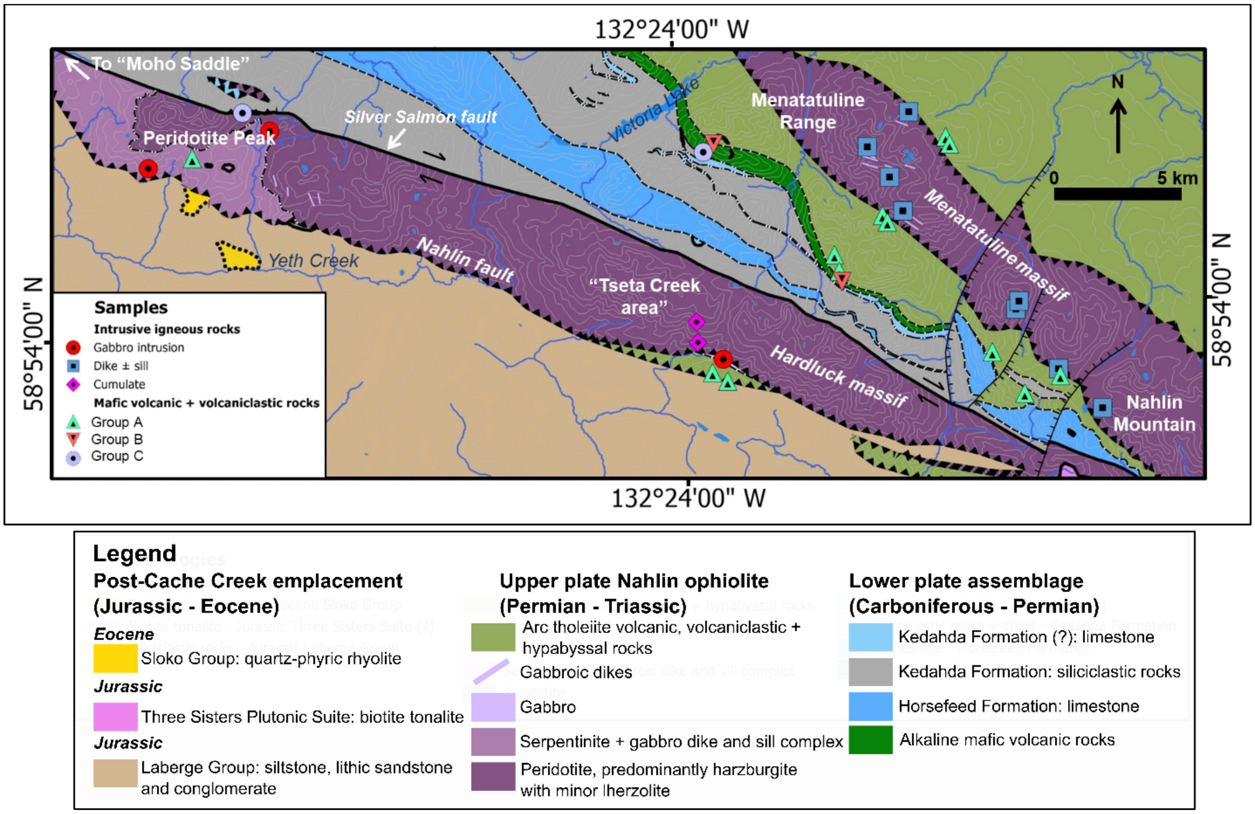

Figure 2.2: Bedrock geology of the Menatatuline Range area, from Peridotite Peak to Nahlin Mountain, based on 2015 – 2016 mapping and compiled British Columbia Geological Survey data (Mihalynuk et al. 1996). Sample locations symbolized by lithology and chemical affinity as discussed in text. Dikes are shown schematically. Names of geological features referenced in text are in italic font (e.g. Nahlin fault). Informal place names are indicated by quotation marks (e.g., "Tseta Creek area"). Background topographic raster image from Natural Resources Canada (1990a, 1990b).

2.3 Regional Geology

The Mississippian to Lower Jurassic Cache Creek terrane is discontinuously exposed through British Columbia and southern Yukon and is bound by the peri-Laurentian Yukon-Tanana, Quesnellia and Stikinia terranes. Carboniferous to Permian carbonate rocks of the Cache Creek terrane contain Tethyan fauna that is distinctly different from fauna found in adjacent Stikinia and Quesnellia, indicating that parts of the Cache Creek terrane are exotic with respect to Laurentia and adjacent terranes (Monger and Ross 1971; Orchard et al. 2001). The Cache Creek and adjacent terranes were amalgamated with North America and stitched together by crosscutting plutons by the Middle Jurassic at the latest (Gabrielse 1991; Mihalynuk et al. 1992, 1998). The presence of contrasting faunal assemblages between the accreted terranes has strongly influenced the tectonic models for the northern Cordillera (e.g., Mihalynuk et al. 1994; Johnston and Borel 2007). Despite the proposal of several models, the tectono-stratigraphy and tectonic setting of the Cache Creek terrane remain poorly understood, and some authors have treated the whole or parts of the Cache Creek terrane as a subduction zone melange or an accretionary complex (e.g., Mihalynuk et al. 1994, 2004b; Mihalynuk 1999; English and Johnston 2005; English et al. 2010).

The northern Cache Creek terrane near Atlin, BC has been the focus of several studies that vary from regional to thematic in scope (e.g., Aitken 1959; Souther 1971; Monger 1975; Terry 1977; Bloodgood and Bellefontaine 1990; Ash 1994; Mihalynuk et al. 1994). Conflicting interpretations based on these studies suggest that the Cache Creek terrane in this region comprises several distinct and possibly unrelated components including: an ophiolite and/or rifted arc (e.g., Childe and Thompson 1997; English et al. 2010; Bickerton et al. 2012; Schiarizza 2012), seamounts and/or oceanic plateaux (e.g., English et al. 2010), and a subduction-related accretionary complex (Monger 1975; Terry 1977; Ash 1994; Mihalynuk et al. 1998; English and Johnston 2005). Hence, in this work I refer to the Cache Creek terrane as a composite terrane consisting of at least two potentially unrelated domains.

Direct age constraints on the formation of the ophiolites in the northern Cache Creek terrane have historically been scarce, but recent geochronological data indicate some regional age variation of ophiolitic magmatism (Figure 2.1; Table 2-1). Near Dease Lake, tholeiitic to boninitic ophiolitic rocks in the King Mountain area yield ca. 255 to 250 Ma zircon and titanite U-Pb crystallization and hornblende Ar-Ar cooling ages (Zagorevski et al. 2016a). In southwest Yukon near Jakes Corner, zircon grains from a varitextured gabbro that stitches the mantle and crustal section of an ophiolite yielded a ca. 245 Ma U-Pb crystallization age (Zagorevski et al. 2016a) similar to a trondhjemite dike that cuts peridotites in the Teslin area (245.4 ± 0.8 Ma U-Pb zircon; Gordey et al. 1998). Northwest of the study area, quartz diorite in the plutonic section of the ophiolite at Mount Nimbus yielded 255 ± 2.8 Ma (Devine 2002). North of the study area, intrusion of the Tseta Creek tonalite into hypabyssal microgabbro of the ophiolitic crust is constrained to 261.4 ± 0.3 Ma (U-Pb zircon crystallization age; Mihalynuk et al. 2003). Mount Nimbus and Tseta Creek intrusive rocks thus constrain the age of the ophiolitic crustal section north of and along strike of the Menatatuline massif (see following) to be ca. 255 to 261.4 Ma.

Table 2-1: Summary of new and existing geochronological data constraining the timing of magmatism related to Permo-Triassic arc activity, including evolution of the Nahlin ophiolite, in the northern Cache Creek terrane (Childe and Thompson 1997; Gordey et al. 1998; Mihalynuk 1999; Devine 2002; Mihalynuk et al. 2003; English et al. 2010; Schiarizza 2012; Zagorevski 2016; Zagorevski et al. 2017).

Map	Location	Lithologies	Affinity	Method	Age (Ma)	Reference*
A	King Mountain (BC)	harzburgite, gabbro, dikes	IAT, BON	U-Pb zrn, ttn; Ar-Ar hbl	ca. 250-255	1, 2
B	Kutcho (BC)	bimodal volcanic rocks	IAT	U-Pb zrn	ca. 242-251.71	3, 4
C	Mount Nimbus (BC)	quartz diorite intruding into harzburgite	IAT	U-Pb zrn	255±2.8	5, 6, 2
D	Tseta Creek (BC)	diorite in mafic volcanic and intrusive rock	IAT	U-Pb zrn	261.4±0.3	6, 7
E	Graham Creek (BC)	basalt, diabase, harzburgite and chert	BABB	Radiolaria	Middle Triassic	8, 9
F	Jakes Corner (YK)	gabbro stitching harzburgite and basalt	IAT	U-Pb zrn	ca. 245	1, 2
G	Teslin (YK)	trondhjemite in ophiolite	IAT	U-Pb zrn	245.4±0.8	1, 2, 10

*[1]Zagorevski et al. (2016a), [2]Zagorevski (2016), [3]Schiarizza (2012), [4]Childe and Thompson (1997), [5]Devine (2002), [6]English et al. (2010), [7]Mihalynuk et al. (2003), [8]Mihalynuk et al. (1999); [9]Zagorevski et al. (2017) [10]Gordey et al. (1998)

2.4 Geology of the Menatatuline Range area

In the Menatatuline Range area, the Cache Creek terrane comprises remnants of oceanic lithospheric mantle, mafic intrusions, mafic volcanic rocks, and sedimentary rocks (e.g., carbonate, chert and siliciclastic). The mantle and the mafic intrusive and extrusive rocks together make up the Nahlin ophiolite, which was first recognized by Aitken (1959). A summary of the geology of the ophiolite is presented below. Detailed descriptions of all the lithological units within the Menatatuline Range area are presented elsewhere (Zagorevski et al. 2015, 2016a; McGoldrick et al. 2016).

Ultramafic rocks in the Nahlin ophiolite

The best exposures of ultramafic rocks occur in a discontinuous belt from Atlin to Nahlin Mountain about 150 km southeast (Figure 2.1). For convenience I herein subdivide the Nahlin ophiolite into the Hardluck, and Menatatuline massifs. The Menatatuline massif trends northwest from Nahlin Mountain to the Menatatuline Range (Aitken 1959, Terry 1977) whereas the Hardluck massif is more west-northwest trending (Figure 2.2; Mihalynuk et al. 2004b). Ultramafic rocks in both the Hardluck and Menatatuline massifs comprise variably serpentinized harzburgite with pyroxenite dikes, and replacive dunite pods (McGoldrick et al. 2016). Massive and layered harzburgite is the dominant lithology and varies between ~45-65% olivine, ~25-40% orthopyroxene, 3-8% clinopyroxene, and <5% spinel. Layering defined by modal and textural variation of pyroxene is variably developed in both massifs. Lherzolite rarely occurs in the Hardluck massif, where it is characterized by emerald-green clinopyroxene (<15%) (Mihalynuk et al. 2004b). A primary mantle tectonite fabric (S_1) defined by orthopyroxene elongation is variably developed in both massifs, and varies from parallel to oblique to modal layering.

Orthopyroxenite dikes (5–10 cm wide) are variably abundant. In both massifs, pyroxenite dikes are variably layer-discordant or concordant with respect to the harzburgite layering (Figure 2.3a). Dikes are locally deformed into meter-scale folds (Figure 2.3b) and rarely cut folded harzburgite-pyroxenite layering. Discrete dunite pods comprise as much as 20% of the Menatatuline and Hardluck massifs. The size of individual pods is variable, ranging from submetre scale up to 100 m across. Dunite bodies have sharp contacts against harzburgite, are locally folded and locally crosscut pyroxenite, indicating that there are several generations of replacive dunite and pyroxenite dikes. Dunite likely represents melt channels formed as a result of melt-rock interaction with the host harzburgite (Kelemen and Dick 1995).

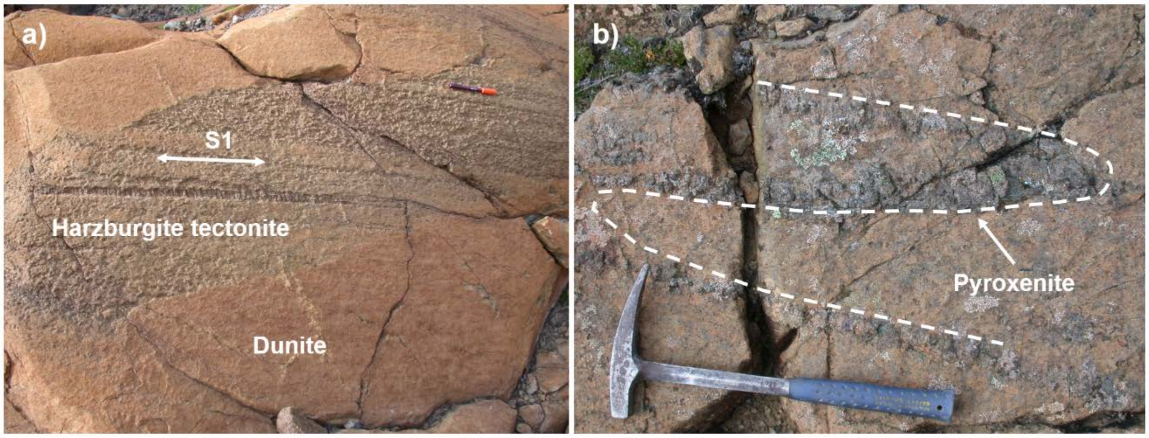

Figure 2.3: Ultramafic rocks of the Nahlin ophiolite. (A) Primary tectonic fabric (S_1), and pyroxenite dike transposed into S_1, in harzburgite tectonite truncated by a replacive dunite pod near Peridotite Peak. (B) Tight, near isoclinal folding of a pyroxenite dike in harzburgite tectonite on Peridotite Peak.

Lower crustal cumulates

Lower crustal mafic-ultramafic cumulates are rare in the northern Cache Creek terrane and have been documented only in select localities (Terry 1977; Gabrielse 1998; Mihalynuk et al. 2004b; Zagorevski et al. 2016b). Minor lower crustal cumulates have been documented in the Hardluck massif north of the study area (“Moho Saddle”, Figure 2.1; Mihalynuk et al. 2004b). Pods of pyroxenitic to gabbroic cumulates intrude variably serpentinized harzburgite on the southern margin of the Hardluck massif in the Tseta Creek area (Figure 2.2). Some pods have highly irregular “scalloped” margins against the host harzburgite suggesting high temperature, ductile deformation within the lithosphere (Figure 2.4a). Cumulates include varitextured plagioclase-bearing olivine websterite and gabbronorite, that vary in grain size from fine grained to pegmatitic over meters. Granoblastic textures and primary mineralogy are variably overprinted by amphibole, chlorite, serpentine, sericite and/or prehnite.

Gabbroic rocks

Gabbroic rocks intrude the mantle tectonite along the southern margin of the Hardluck massif, and crosscut harzburgite tectonite throughout the Menatatuline massif. In the Hardluck massif, gabbroic dikes and pods with locally distinctive chilled margins commonly intrude serpentinite, most notably north of the Nahlin fault near Peridotite Peak. Gabbro (plagioclase-pyroxene ± amphibole) is strongly varitextured and ranges from fine grained to pegmatitic (Figure 2.4b). Foliated amphibolite- and trondhjemite-rich zones are locally present. Gabbro becomes less abundant toward the north, where it typically forms thin dikes ± sills and reticulated dike and vein swarms within variably serpentinized peridotite. It is unclear whether these gabbroic intrusions exclusively represent dikes, sills, or a combination of both, as their original orientation within the mantle is ambiguous. Locally, exposures of gabbro comprise boudinaged rodingite pods completely enveloped within fresh peridotite.

West- to north-trending and variably-dipping gabbroic and locally diabasic dikes ± sills ranging in width from <2 to 20 m occur as a swarm crosscutting the Menatatuline massif. Some are undeformed (Figure 2.4c), whereas others are boudinaged and suggest high-temperature deformation within the lithosphere or asthenosphere (Figure 2.4d). Dike cores typically comprise fine to medium grained equigranular plagioclase (40–50%) and pyroxene (1–3 mm). Many of these dikes display subophitic to intergranular textures, and are variably plagioclase ± clinopyroxene ± orthopyroxene-phyric (<5%, 2-4 mm phenocrysts). Some dikes have chilled margins against the host harzburgite. Primary mafic mineralogy, including sparse igneous amphibole, is variably altered to lower greenschist facies assemblages of chlorite + epidote ± actinolite ± sericite.

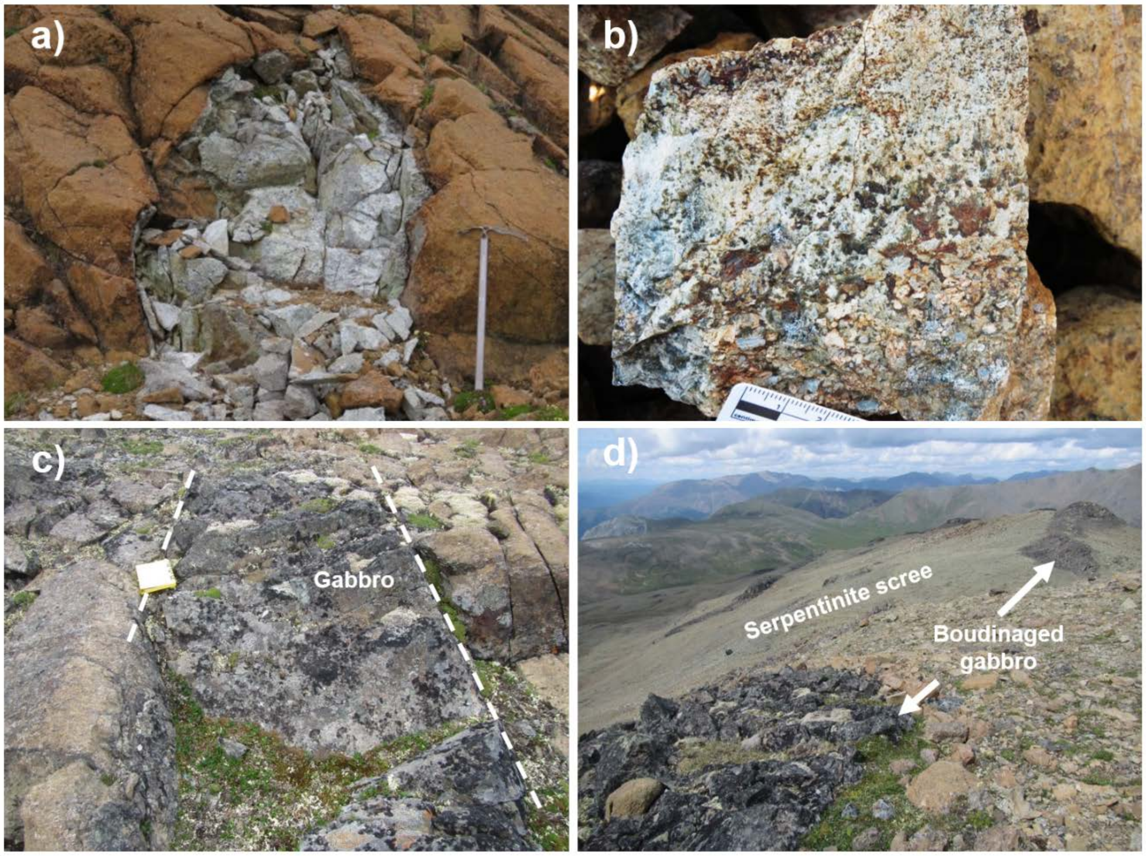

Figure 2.4: Intrusive rocks of the Nahlin ophiolite in the Menatatuline Range area. (A) Boudinaged altered ultramafic cumulate (pale) with scalloped margins surrounded by harzburgite (dun brown), near the southern side of the Hardluck massif. (B) Varitextured gabbro intrusion near the southern side of the Hardluck massif, in the Menatatuline Range area. Grain size within the gabbroic intrusions varies from fine grained (top of sample shown) to pegmatitic (bottom portion of sample shown). (C) Straight margins (white dashed lines) of a gabbroic dike intruding harzburgite at Nahlin Mountain. (D) Boudinaged gabbroic dikes protrude along the slopes of Nahlin Mountain among recessively weathering serpentinite scree.

Volcanic and volcaniclastic rocks

Volcanic and volcaniclastic rocks are aerially extensive in the northern Cache Creek terrane. Some of these were previously mapped as the Nakina Formation (Monger 1977; Mihalynuk et al. 1996, 2002; English et al. 2002), although this stratigraphic name was originally defined only for Mississippian – Permian volcanic rocks associated with carbonate successions (Monger 1975). Here I avoid this nomenclature to prevent further confusion.

Brecciated, massive and rare pillowed flows, with locally pervasive chlorite ± hematite alteration are exposed northeast of the Menatatuline massif, and between the Menatatuline and Hardluck massifs (Figure 2.2). Younging directions and contact relationships within these sequences could not be determined. The mafic volcanic rocks are plagioclase, clinopyroxene, and orthopyroxene porphyritic. Some plagioclase phenocrysts display sieve textures and growth zoning. Flows are locally highly vesicular, with calcite ± chlorite-filled amygdules. Primary mafic minerals are variably altered to chlorite ± actinolite (clinopyroxene), and to chlorite + calcite ± epidote ± sericite (plagioclase).

The volcaniclastic rocks comprise mafic crystal and lapilli tuffs that are fine grained, locally vesicular and flow banded. Lapilli and crystal fragments are rounded to subangular, and rarely elongate or shard-like (Figure 2.5). Crystal fragments comprise plagioclase ± orthopyroxene ± clinopyroxene, and one sample contains serpentine pseudomorphs of equant olivine phenocrysts. Lapilli fragments in the pervasively chloritized ± hematized groundmass preserve volcanic textures, such as intergranular and pseudotrachytic groundmass textures, to varying degrees.

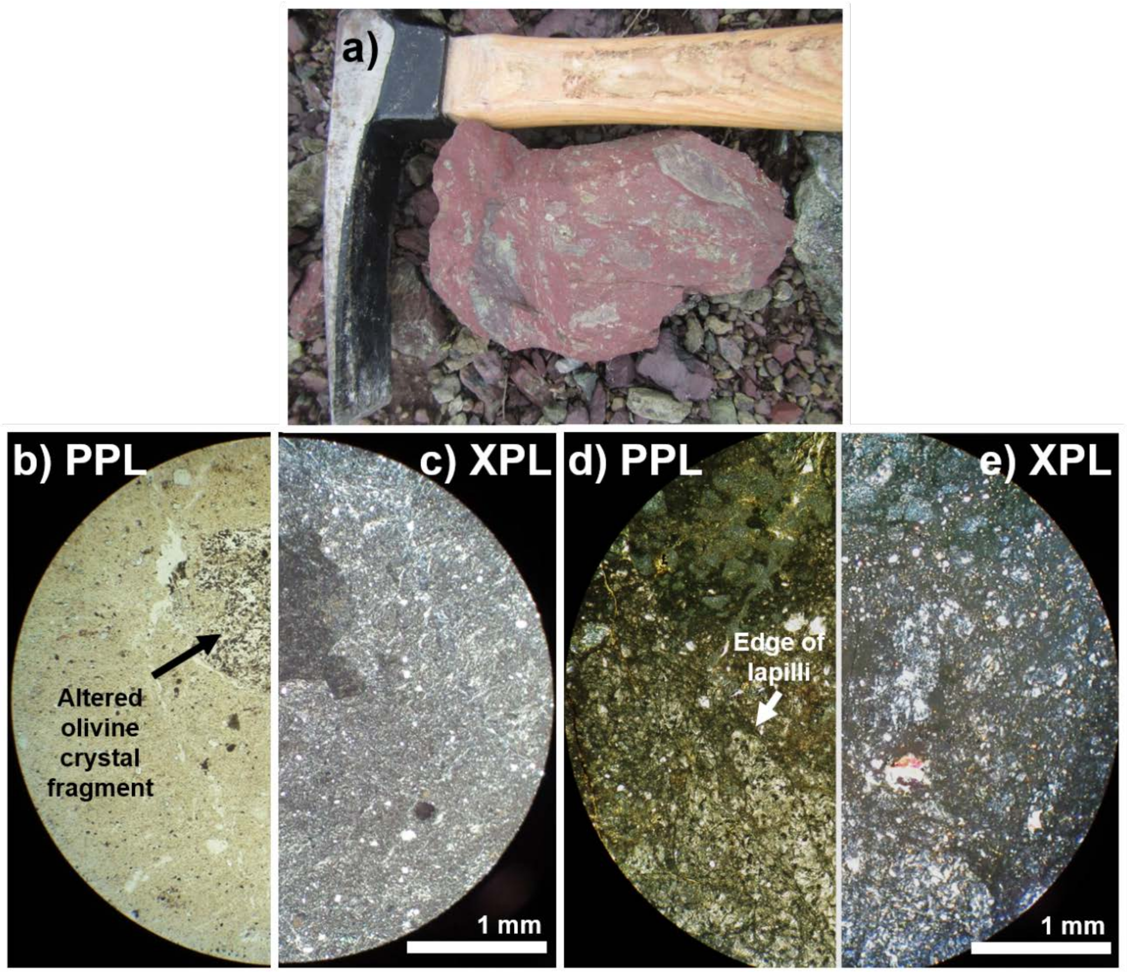

Figure 2.5: Mafic volcanic rocks previously grouped as part of the Nakina Formation, in northwestern British Columbia. (A) Locally fragmental texture in pervasively hematized volcaniclastic rocks. (B) Photomicrograph of an ultramafic crystal tuff with orthopyroxene crystal fragments, and serpentine pseudomorphs after rounded olivine fragments in PPL, and (C) in XPL. (D) Photomicrograph of a mafic tuff with lapilli in PPL, and (E) in XPL.

2.5 Geochemistry

Methods

Representative samples of all the lithologies described above were selected for lithogeochemical analysis to constrain the petrogenesis of the igneous rocks in the Nahlin ophiolite. The new major, minor, and trace element data presented herein are from 28 samples of lower and supracrustal rocks; data from the harzburgite tectonite will be presented elsewhere

(Chapter 3). Samples were cut into slabs with a rock saw at the University of Victoria, and were crushed and processed for bulk rock geochemistry at Activation Laboratories in Ancaster, Ontario (Table A 2). Major oxides were measured by lithium metaborate/tetraborate fusion and ICP-OES, whereas minor and trace elements were determined by ICP-MS. The suite of standards analysed along with the Menatatuline Range area samples reproduce reported concentrations of major elements to within 9%, large-ion lithophile elements (LILE) to within 13%, high-field strength elements (HFSE) to within 9%, and rare-earth elements (REE) to within 7% (Table A 2).

All the samples have experienced greenschist facies metamorphism, which can result in mobility of some elements. The HFSE, such as Ti, Zr, Hf, Nb, and Ta, and the REE have been shown to be relatively immobile during hydrothermal alteration and up to greenschist facies metamorphism (MacLean 1990; Jenner 1996; Pearce 1996). These trace elements are therefore employed herein to subdivide igneous rocks and elucidate their tectonic setting. The Menatatuline Range area samples can be subdivided into groups A, B, and C on the basis of chemical affinity.

Group A volcanic and plutonic rocks

Basalts and gabbroic dikes

The vast majority of the Menatatuline Range area intrusive, volcanic, and volcaniclastic samples are subalkaline and basaltic (Figure 2.6). Many of the samples are similar to the reference normal mid-ocean ridge basalt (N-MORB) composition (grey triangle, Figure 2.6), and trace element data indicate that these rocks are predominantly tholeiitic (Figure 2.7). Ratios of Nb/Yb indicate that the Group A volcanic and plutonic samples from the Nahlin ophiolite plot near reference values for N-MORB (Figure 2.8), suggesting derivation from a depleted source. However, many also show variable enrichment of Th/Nb over N-MORB, and plot along the subduction enrichment trend. Multi-element REE plots show that the Group A volcanic and plutonic rocks have similar flat to slightly LREE-depleted trace element profiles at roughly 10 to 30x chondritic abundance (Figure 2.9). These samples display a consistent negative Th-Nb-La anomaly on N-MORB normalized trace element plots (Figure 2.10).

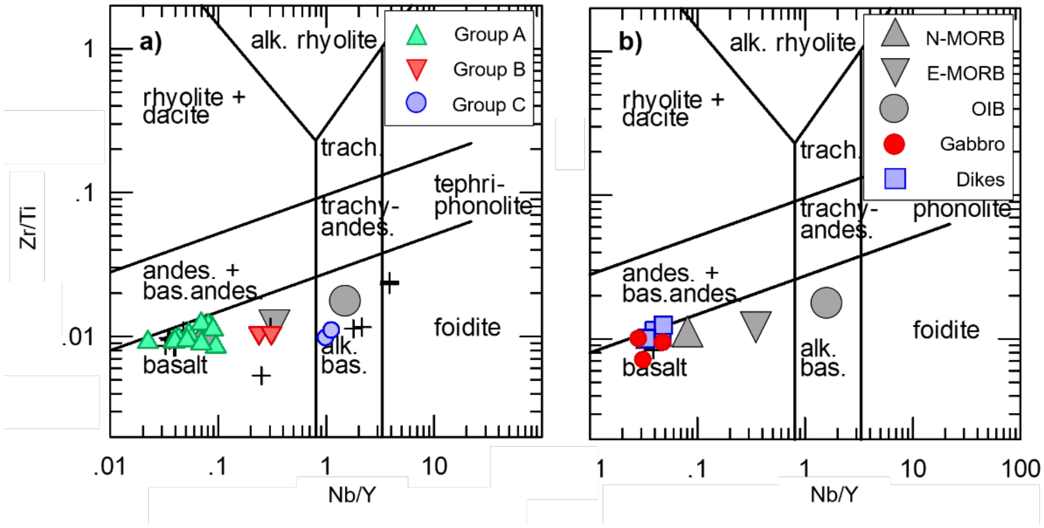

Figure 2.6: Menatatuline Range area lithogeochemical data for immobile trace elements plotted on rock classification diagrams after Pearce (1996) for (A) volcanic rocks, and (B) plutonic rocks. (A) Two samples plot as alkali basalts (blue circles; Group C volcanic rocks), whereas the Group A and B volcanic rocks are subalkaline and basaltic in composition (green triangles, Group A; red triangles, Group B). (B) Group A intrusive rocks of the Nahlin ophiolite, including gabbro pods (red circles) and gabbroic to diabasic dikes and sills (blue squares), share compositional similarities with the Group A subalkaline volcanic rocks in (A). Reference composition for normal mid-ocean ridge basalt (N-MORB), enriched mid-ocean ridge basalt (E-MORB), and ocean island basalt (OIB) shown in grey symbols for comparison (Sun and McDonough 1989). Data from igneous rocks of the Nakina transect shown for comparison (black crosses; English et al. 2010).

Ultramafic to mafic cumulates

Some of the diagrams employed above to characterize the volcanic and plutonic rocks are inappropriate for cumulates (Langmuir 1989; Bédard 1994; Pearce 1996). Multi-element plots, however, can still be useful in the petrogenetic interpretation of these non-liquidus compositions (Bédard 1994). The plagioclase-bearing olivine websterite and gabbronorite cumulates have slightly positive REE slopes nearly an order of magnitude more depleted than the other Group A intrusive rocks of the Nahlin ophiolite (Figure 2.9). The plagioclase-bearing olivine websterite has a pronounced negative Eu anomaly, whereas the gabbroic cumulates show slight positive Eu anomalies, reflecting variable fractionation and accumulation of plagioclase. All the cumulate samples are enriched in Th ± Nb relative to the REE, but lack the negative Nb ± Ti anomalies characteristic of other Group A plutonic rocks (Figure 2.10).

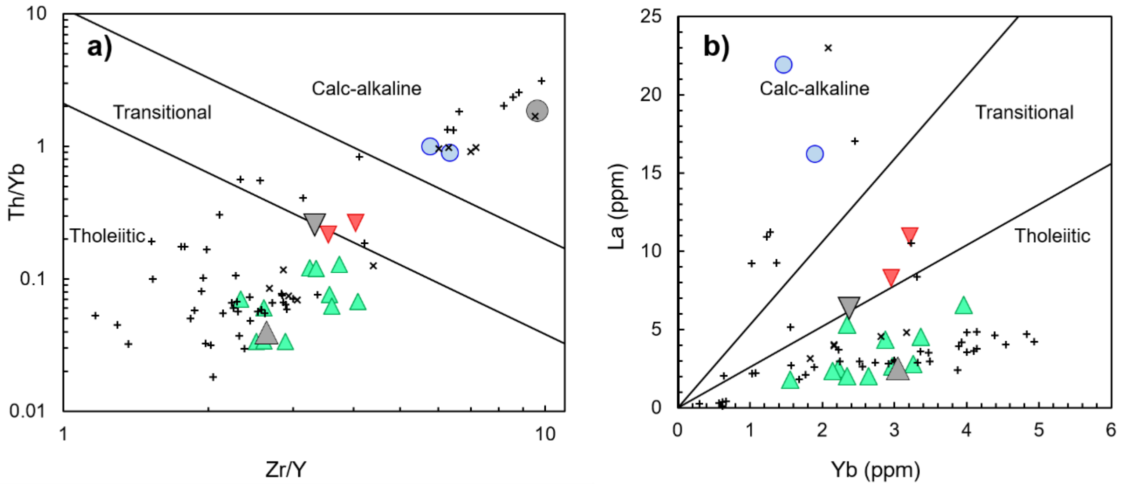

Figure 2.7: Discrimination of magma series by trace element data following the method of Ross and Bédard (2009). Group B and C volcanic rocks plot as transitional and calc-alkaline, respectively. Group A volcanic rocks are predominantly tholeiitic. Volcanic rocks from the southern Cache Creek terrane shown for comparison with northern Cache Creek data (black “x” symbols; Tardy et al. 2001, Lapierre et al. 2003). All other symbols as for Figure 2.6.

Group B volcanic rocks

Two mafic volcanic samples define a narrow unit of distinctly more enriched volcanic rocks in the Menatatuline Range area (Figure 2.2). These are subalkaline basalts with higher Nb/Y ratios than the Group A volcanic rocks associated with the Nahlin ophiolite and close to the reference value for enriched mid-ocean ridge basalt (E-MORB) (Figure 2.6; Sun and McDonough 1989). Trace element data indicate that these volcanic rocks are tholeiitic to transitional (Figure 2.7). Other trace element ratios indicate that these samples have E-MORB-like chemistry, and plot along the source enrichment trend between reference compositions for N-MORB (depleted source) and OIB (enriched source) (Figure 2.8). The E-MORB-like volcanic rocks lack the subduction enrichment of Th/Nb recorded in the Group A volcanic rocks (Figure 2.8). Multi-element diagrams highlight the enrichment of LREE over HREE, and lack of Th-Nb-La and Ti anomalies in these samples (Figure 2.9 and 2.10).

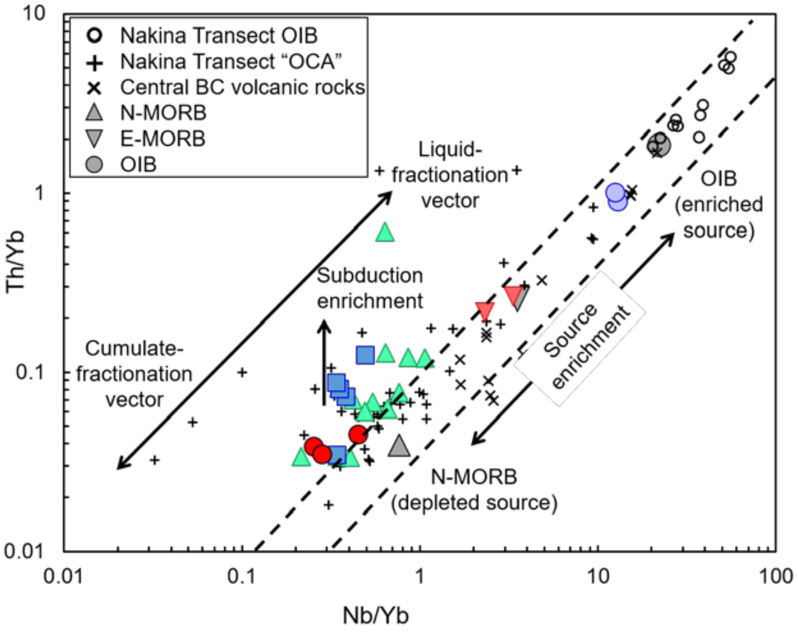

Figure 2.8: Lithogeochemical data for samples from the northern Cache Creek terrane plotted in Nb/Yb – Th/Yb space to discriminate between depleted and enriched sources, and potential enrichment mechanisms. Reference compositions for N-MORB, E-MORB, and OIB are shown for comparison (grey symbols; Sun and McDonough 1989). Samples derived from an enriched source plot near the OIB reference point with high Th/Yb and Nb/Yb ratios. The Group A plutonic and volcanic rocks plot near the N-MORB reference value, but show evidence of subduction-related enrichment. Group B and C volcanic rocks plot near reference values for E-MORB and OIB, respectively, indicating derivation from a more enriched source. Data from the Nakina Transect (English et al. 2010), and from volcanic rocks in the southern Cache Creek terrane in central BC (Tardy et al. 2001; Lapierre et al. 2003) are shown for comparison. Samples from the southern Cache Creek plot along the source enrichment trend, and appear to lack any subduction enrichment. Modified after Pearce (1982), and English et al. (2010).

Group C volcanic rocks

Although grouped initially with the ophiolitic volcanic rocks based on field observations, samples of vesicular olivine ± plagioclase ± orthopyroxene porphyritic basalts are petrographically and geochemically distinct from the Group A volcanic rocks. These porphyritic basalts contain sparse subhedral to euhedral 1-4 mm plagioclase phenocrysts which are variably altered to sericite + calcite, sparse serpentine pseudomorphs after subhedral to euhedral 0.5 to 1 mm olivine phenocrysts, and up to 30% calcite-filled amygdules that are typically 1 mm in diameter. These two mafic volcanic rocks plot in the alkali basalt field (Figure 2.6), and plot along a source enrichment trend near the reference composition for ocean island basalt (OIB; Sun and McDonough 1989), with no evidence for subduction enrichment (Figure 2.8). These alkali basalts have extended trace element profiles similar to OIB (Sun and McDonough 1989), with significant enrichment in LREE over HREE, and a lack of Th-Nb-La and Ti anomalies (Figure 2.9 and 2.10).

2.6 Discussion

Tectono-stratigraphy and structure of the Nahlin ophiolite

The Nahlin ophiolite lacks some classic Penrose-style ophiolite components (Anonymous 1972), such as coherent sections of gabbro and sheeted dykes, and although some primary contact relations may be obscured by faulting, it is still possible to constrain the tectono-stratigraphy of the ophiolite (Figure 2.11). Summarized briefly here, a full description of the interpreted tectono-stratigraphy is provided by Zagorevski et al. (2015, 2016a).

The mantle harzburgite massifs at the base of the Nahlin ophiolite are locally crosscut by multiple generations of gabbroic dikes, some of which are essentially unstrained (Figure 2.4c) whereas others have been boudinaged within the mantle (Figure 2.4d). Lower crustal cumulates and sheeted dike complexes are volumetrically minor in the northern Cache Creek terrane, and are discontinuous, absent or were not recognized in past studies of the Nahlin ophiolite in the Menatatuline Range area. Locally, gabbroic dike-and-sill complexes extensively intrude the mantle rocks, which have been pervasively serpentinized. These melt conduits presumably fed volcanic flows at the surface, which are represented by the aerially-extensive Group A tholeiitic basalt and related mafic volcaniclastic rocks in the Menatatuline Range area (in part formerly mapped as Nakina Formation). Some of these massive mafic rocks have previously been mapped as volcanic flows, even where they lack any extrusive textures (Gabrielse 1998; Mihalynuk 1999; Mihalynuk et al. 2003). Locally, some of these outcrops are now recognized as hypabyssal dike-and-sill and sill-sediment complexes (Zagorevski et al. 2016a).

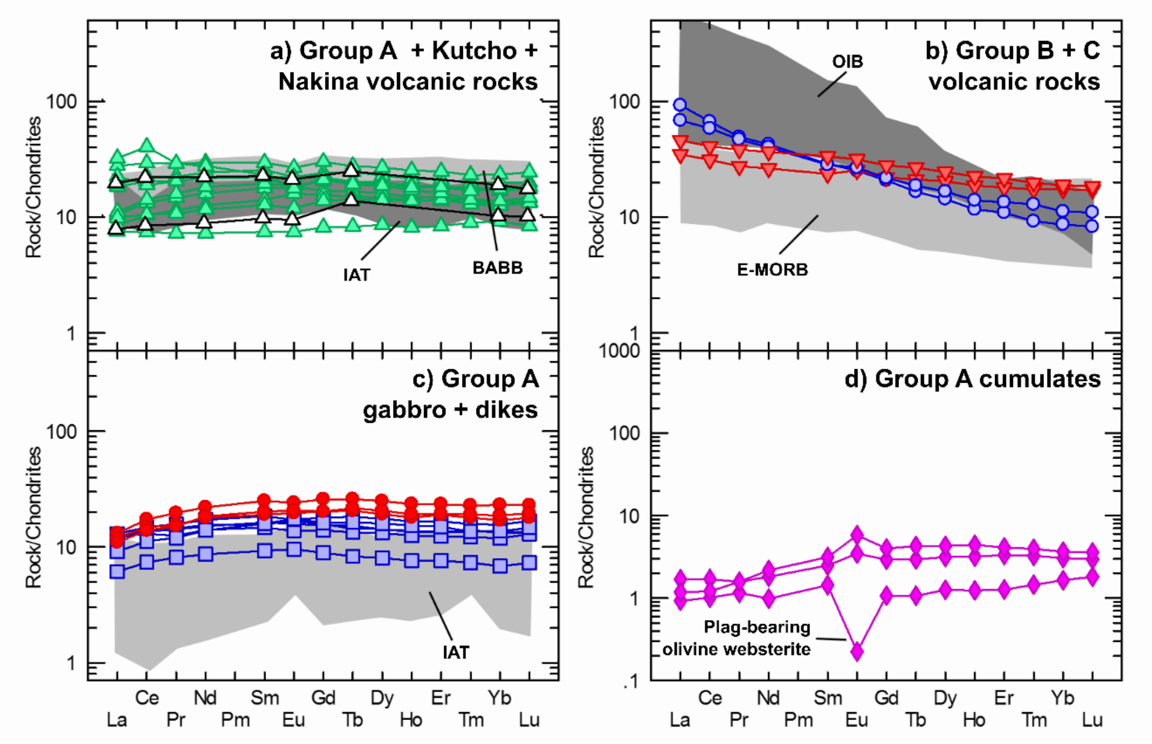

Figure 2.9: Rare-earth element (REE) multi-element concentrations relative to chondrite (Sun and McDonough 1989) for the Menatatuline Range area intrusive and extrusive igneous rocks. (A) Group A volcanic and volcaniclastic rocks (green triangles) compared to the range of compositions of island arc tholeiites (IAT) and backarc basin basalts (BABB) in the Nakina transect, and to mafic volcanic rocks from the Kutcho assemblage (white triangles, Childe and Thompson 1997). (B) Group B (red triangles) and Group C (blue circles) volcanic rocks from the Menatatuline Range area, compared to the range of compositions of E-MORB and OIB volcanic rocks in the Nakina transect. (C) Group A plutonic rocks, including dikes ± sills (blue squares) and gabbro pods (red circles). Data from Nakina transect gabbros shown by the grey shaded region. (D) Group A ultramafic and gabbroic cumulates from the Nahlin ophiolite. All data for the Nakina transect (shaded regions) from English et al. (2010).

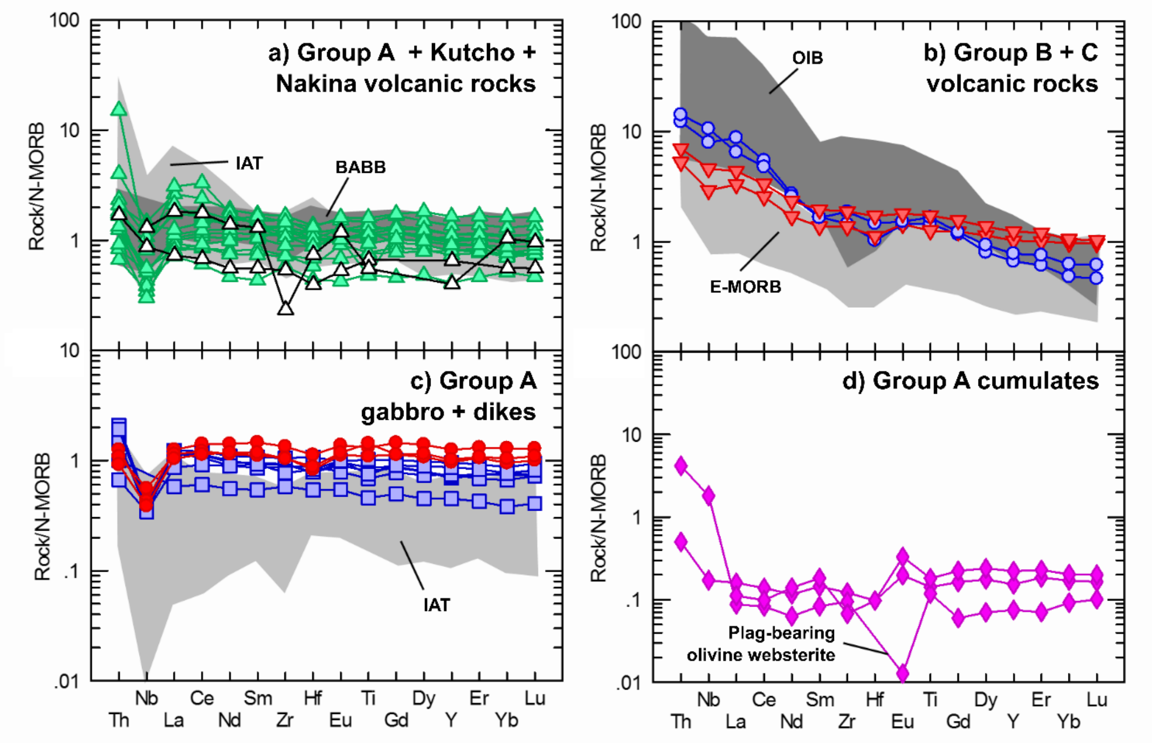

Figure 2.10: Rare-earth element (REE) multi-element concentrations relative to N-MORB (Sun and McDonough 1989) for the Menatatuline Range area intrusive and extrusive igneous rocks. Symbols and shaded regions as for Figure 2.9. All data for the Nakina transect from English et al. (2010).

Although it is possible to reconstruct tectono-stratigraphy in the Nahlin ophiolite, constraining the stratigraphic way-up is not everywhere straightforward. A section through the uppermost mantle and into the lowermost crust is exposed in the “Moho Saddle” (Figure 2.2) to the northwest of Peridotite Peak, and indicates that the ophiolite youngs towards the south (Mihalynuk et al. 2004b). The presence of rare pyroxenitic and gabbroic cumulates exclusively on the southern side of the Hardluck massif supports this interpretation. Elsewhere in the Nahlin ophiolite, however, the harzburgite massifs are fault-bound, leaving little evidence as to the way-up in stratigraphy. These fault-bound sections of mantle commonly juxtapose harzburgite tectonite against supracrustal rocks, such as basalt or chert. A possible interpretation for this juxtaposition and the locally missing lower crustal section is that the Nahlin ophiolite represents an intraoceanic core complex (Zagorevski et al. 2015). Similar to other fossil oceanic core complexes recognized in the rock record (e.g., Ohara et al. 2003; Maffione et al. 2013; Lagabrielle et al. 2015), the spinel-facies harzburgite tectonite may have been exhumed along a low angle normal fault to shallow depths (plagioclase stability zone), where it acted as a rigid body during the intrusion of later gabbroic dikes.

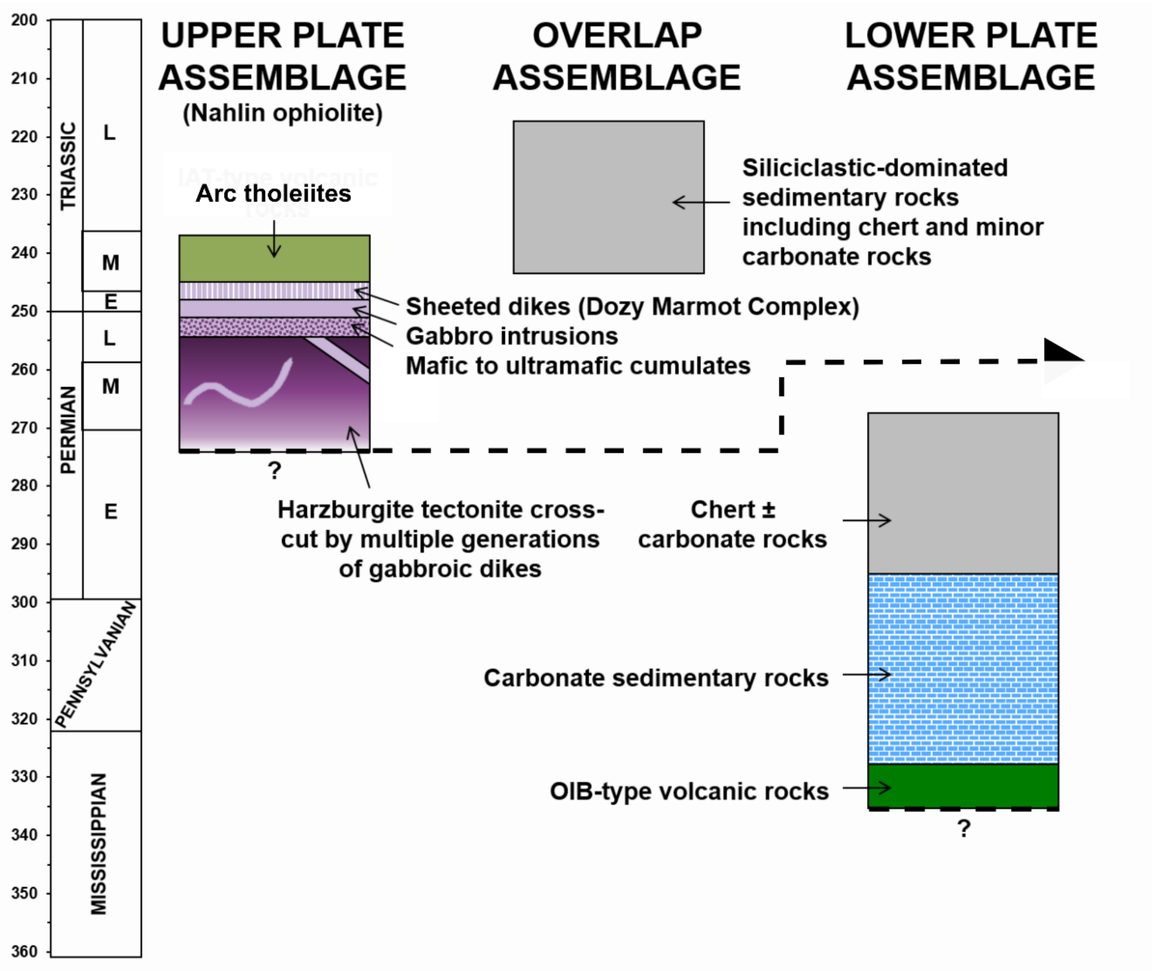

Figure 2.11: Schematic stratigraphic columns for the upper plate, lower plate, and overlap assemblages of the northern Cache Creek terrane based on new and existing geochronological data. Age constraints for lower plate sedimentary rocks after Monger (1975, 1977), Cordey et al. (1991), and Mihalynuk et al. (2003, 2004b). Age constraints for the overlap assemblage sedimentary rocks after Cordey et al. (1991), and Mihalynuk et al. (2003, 2004b), and for the upper plate (ophiolite) assemblage after Gordey et al. (1998), Devine (2002), Mihalynuk et al. (2004b), and Zagorevski et al. (2016a).

Tectonic setting of the Nahlin ophiolite

The reconstructed tectono-stratigraphy of the Nahlin ophiolite based on recent field work in the northern Cache Creek terrane can be corroborated using lithogeochemical data. The Group A gabbroic dikes that crosscut the mantle sections of the Nahlin ophiolite have tholeiitic arc-related chemistry, and REE profiles identical to those of spatially associated Group A basalt and mafic volcaniclastic rocks (Figure 2.9 and 2.10). The flat to low positive slope of these REE profiles relative to chondrite, and the low Nb/Yb ratios, indicate derivation from a LREE-depleted mantle source that experienced earlier melt extraction (Jenner 1996; Pearce 1996). The Group A intrusive and extrusive rocks are enriched in Th/Yb over typical N-MORB values (Figure 2.8), suggesting that subduction-related fluids played a role in the genesis of the ophiolitic crust. All of the Group A plutonic and volcanic rocks display a negative Th-Nb-La anomaly (Figure 2.10) and enrichment of LILE over HFSE. These characteristics are generally considered a “subduction zone signature” similar to that of island arc tholeiites (IAT) or backarc basin basalts (BABB), and are linked to relative contributions of these elements from the subducting slab to the source of the arc magmas (Pearce and Norry 1979; Saunders et al. 1988; Pearce and Peate 1995; Jenner 1996; Pearce 1996). The remarkably consistent chemistry, subduction-related enrichment, and the crosscutting relationships linking the gabbroic rocks to the mantle suggest that the Hardluck and Menatatuline massifs represent a supra-subduction zone (SSZ) ophiolite. This type of ophiolite is characterized by the structure of oceanic crust with the geochemistry of an island arc, suggesting derivation by seafloor spreading above an intraoceanic subduction zone (Miyashiro 1973; Pearce et al. 1984).

Rare earth element profiles of the Group A extrusive igneous rocks in the Nahlin ophiolite can be compared to melt compositions produced by fractional melting of peridotite, to constrain the degree of melting required to generate the Nahlin ophiolitic crust.

Melting models employed in this study follow the methodology of Warren (2016), in which a depleted MORB mantle (DMM) source (Workman and Hart 2005) undergoes non-modal fractional melting in the spinel stability field according to the melting reaction 0.56 Opx + 0.72 Cpx + 0.04 Sp = 0.34 Ol + 1.0 Melt (Wasylenki et al. 2003). Depleted MORB mantle is a hypothetical composition calculated for the depleted upper mantle using the average isotopic composition of MORB (Salters and Stracke 2004; Workman and Hart 2005), and was assumed for this model as per convention in recent studies of mantle melting (Bezard et al. 2015; Marchesi et al. 2016; Warren 2016). Partition coefficients for the REE are after Sun and Liang (2014) and Warren (2016), and are calculated assuming a mantle of DMM composition at a potential temperature of 1300 °C. The range of REE profiles of the Group A basaltic rocks of the Nahlin ophiolite is reproduced by modeled segregated melts following 2 to 20% non-modal fractional melting (Figure 2.12). This suggests that some of the volcanic rocks represent erupted products of low degrees of partial melting, whereas others result from combined segregated melts of up to 20% melting. Considering the range of MgO values for these volcanic rocks (~3 to 20 wt %; Table A 2), it is likely that most do not represent primary or primitive melts (Niu and Batiza 1991; Kinzler and Grove 1992b). Therefore it is also likely that the range of REE compositions shows a minor increase in abundances due to crystal fractionation of early olivine. In this way the concentrations of REE are higher than in their original primitive parental melts, implying that our melt estimates are minima.

The mantle melting model (see previous) also provides the residual mantle composition, which can be compared to peridotites from the Nahlin ophiolite. Whole-rock REE data from peridotite samples near “Moho Saddle”, Peridotite Peak, and Peridotite Peak East (Babechuk et al. 2010) require 10 to 20% partial melting to reproduce measured HREE concentrations (Figure 2.12). Light REE enrichment of the Nahlin peridotites is not predicted by the modeled residue compositions. This enrichment may be related to “cryptic” mantle metasomatism or refertilization that is observed in many abyssal and ophiolitic peridotites (e.g., Bizimis et al. 2000; Warren and Shimizu 2010; Uysal et al. 2016). The range of melt depletion recorded in the peridotites (10 – 20 %) overlaps with the melt estimates necessary to generate the Group A arc tholeiites of the Nahlin ophiolite (2 – 20 % minimum). This relationship suggests that the Group A intrusive and extrusive igneous rocks in the Menatatuline Range area are plausibly the products of the harzburgites in the Nahlin ophiolite with which they are spatially associated. Alternatively, the arc tholeiite magmatism in the Nahlin ophiolite may have been built on mantle that had experienced previous arc magmatism. Geochronological constraints on the timing of volcanism are needed to discriminate between these hypotheses. Regardless, the mantle harzburgites of the Nahlin ophiolite are thus not related to the Group B (E-MORB) and C (OIB) volcanic sequences.

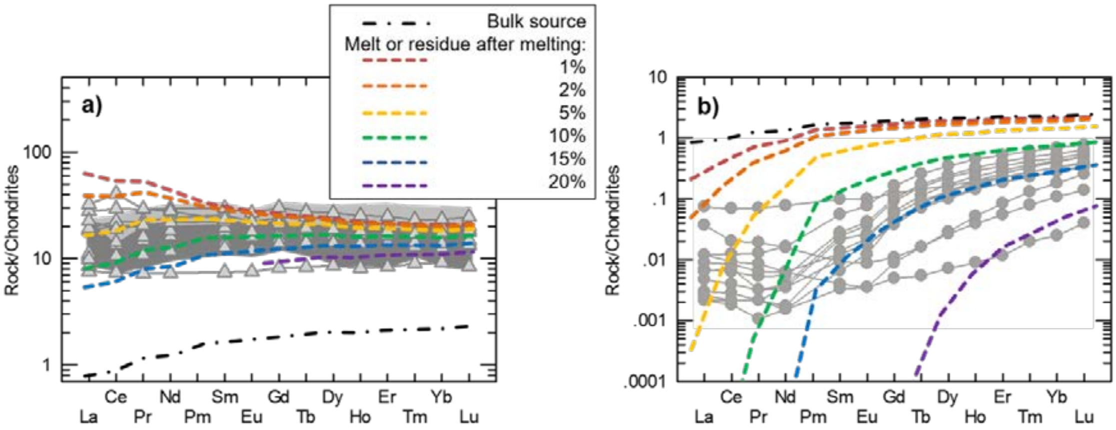

Figure 2.12: (A) Group A volcanic rock compositions from the Nahlin ophiolite (grey triangles; this study) and correlative Nakina transect BABB and IAT compositions (light and dark grey shaded areas; English et al. 2010) compared to melt model results relative to chondrite. Dot-dashed black line indicates the bulk-rock starting composition, and coloured dashed lines reflect segregated melt compositions after 1 - 20% non-modal fractional partial melting of a DMM source in the spinel stability field. (B) Bulk-rock REE concentrations for peridotite samples from nearby Peridotite Peak, “Moho Saddle”, and Peridotite Peak East (grey circles; Babechuk et al 2010) compared to modeled residue compositions after depletion by 1 – 20% non-modal fractional partial melting of a DMM source in the spinel stability field. All model parameters for (A) and (B) follow those of Warren (2016). Starting DMM bulk-rock composition after Workman and Hart (2005), partition coefficients calculated for a mantle of DMM composition at a potential temperature of 1300 °C (Sun and Liang 2014; Warren 2016). Melting follows the reaction of Wasylenki et al. (2003) for DMM1 composition at 1.0 GPa: 0.56 Opx + 0.72 Cpx + 0.04 Sp = 0.34 Ol + 1.0 Melt.

Connection to other Cache Creek assemblages

Tholeiitic plutonic and volcanic rocks of the Nahlin ophiolite (Group A) display a predominantly volcanic arc-backarc geochemical signature. A similar arc-backarc setting has been inferred along-strike in the Nakina area (English et al. 2010), and in the Kutcho assemblage (Childe and Thompson 1997; Mihalynuk and Cordey 1997) (Figure 2.1). The Nakina area “oceanic crustal assemblage” (English et al. (2010) comprises Middle to Late Permian intrusive and extrusive igneous rocks of variable affinity (e.g., IAT, BABB, calc-alkaline) that formed from a depleted N-MORB-like source in an arc or backarc setting (Devine 2002; English et al. 2010). As these rock are physically continuous with and chemically similar to the Group A rocks in the Menatatuline Range area, they form part of the same arc-backarc system as the Nahlin ophiolite (Figure 2.9 and 2.10). The Early to Middle Triassic Kutcho arc exposed near Dease Lake (Figure 2.1) was previously correlated with the Nakina area (English and Johnston 2005; English et al. 2010). The Kutcho assemblage is characterized by bimodal tholeiitic volcanic and volcaniclastic rocks that formed in a juvenile, intraoceanic arc ca. 254-242 Ma (Barrett et al. 1996; Childe and Thompson 1997; Barrett and MacLean 1999; Schiarizza 2012).

The Kutcho assemblage and Nahlin ophiolitic rocks likely represent different segments of the same, extensional Late Permian to Middle Triassic arc-backarc system, similar to modern

Izu-Bonin-Mariana (Reagan et al. 2010, 2013; Ishizuka et al. 2011) or Tonga-Tofua-Kermadec (Smith and Price 2006) arcs. In such analogues, the Nahlin ophiolite could represent more advanced stages of rifting, similar to the Lau and Parece-Vela basins, whereas the Kutcho assemblage either represents an incipient rift or highly extended arc (e.g., southern termination of west Mariana Trough or parts of the of the Lau basin). Similarly, the Kutcho assemblage and Nahlin ophiolitic rocks may represent along strike variations in magmatic versus tectonic-accommodated extension in the backarc region, and in the nature of the slab derived components added to the mantle wedge as described in the southern Havre Trough (Wysoczanski et al. 2010; Todd et al. 2011). This configuration reflects anomalous thermal regimes in the mantle wedge ("hot fingers", Tamura et al. 2002; Todd et al. 2011) which result in cross-arc chains of constructive volcanic centres separated by basinal 'rift regimes' in which BABB are erupted (Wysoczanski et al. 2010). Application of such a setting to the northern Cache Creek terrane may explain the apparent lack of a mature Permo-Triassic arc spatially associated with the Nahlin ophiolite (Figure 2.13).

Alternatively, the Nahlin ophiolite may have formed in a proto-forearc setting associated with subduction initiation. Similar to the proposed origin of the Izu-Bonin-Mariana arc, nucleation of a new intraoceanic subduction zone may have been accompanied by seafloor spreading in what would become the forearc region (Figure 2.13; Stern et al. 2012; Maffione et al. 2015). A progressive change in volcanic chemistry from initial forearc spreading to development of a mature arc is invoked from the evolution of tholeiitic MORB-like volcanic rocks (forearc basalts) at the base to volcanic arc-like basalts including boninites at the top of the volcanic sequence in the forearc (Reagan et al. 2010, 2013; Ishizuka et al. 2011; Stern et al. 2012). If present, this chemostratigraphy is not currently recognized in the Nahlin ophiolite, likely due to structural dismemberment. It has, however, been recognized in other SSZ ophiolites including the Mirdita and Pindos ophiolites in Albania and Greece (Saccani and Photiades 2004; Dilek et al. 2008; Whattam and Stern 2011). A subduction initiation origin may also account for the lack of a preserved arc associated with the Nahlin ophiolite, as a newly nucleated convergent margin may be short-lived and need not develop a mature arc (Whattam and Stern 2011).

The OIB and E-MORB problem

The two E-MORB-type Group B volcanic rocks in the Menatatuline Range area define a thin belt along the contact of the Group A volcanic rocks and the Kedahda Formation (Figure 2.2). These volcanic rocks require an enriched non-arc source indicating that these rocks cannot be directly related to the Group A arc tholeiites. Enriched MORB-like basalts have been described to the north in the Nakina area, where they were grouped with volcanic rocks of IAT and BABB affinities within the “oceanic crustal assemblage” (English et al. 2010). However, the lack of relative age constraints makes this interpretation ambiguous. The volumetrically minor E-MORB magmatism could represent continued spreading in the backarc environment and tapping of a more enriched mantle source or it may reflect a heterogeneous mantle source that includes both depleted and enriched components (e.g., Pomonis et al. 2006; Dilek and Furnes 2009; Gale et al. 2013; Wilson et al. 2013). Alternatively, the E-MORB-type Group B volcanic rocks may be unrelated to the ophiolite. The complete lack of any subduction zone signature, and the proximity of these basalts to a fault imbricated package of siliciclastic, chert and carbonate rocks, may indicate that the E-MORB-type samples are related to the Tethyan carbonate successions.

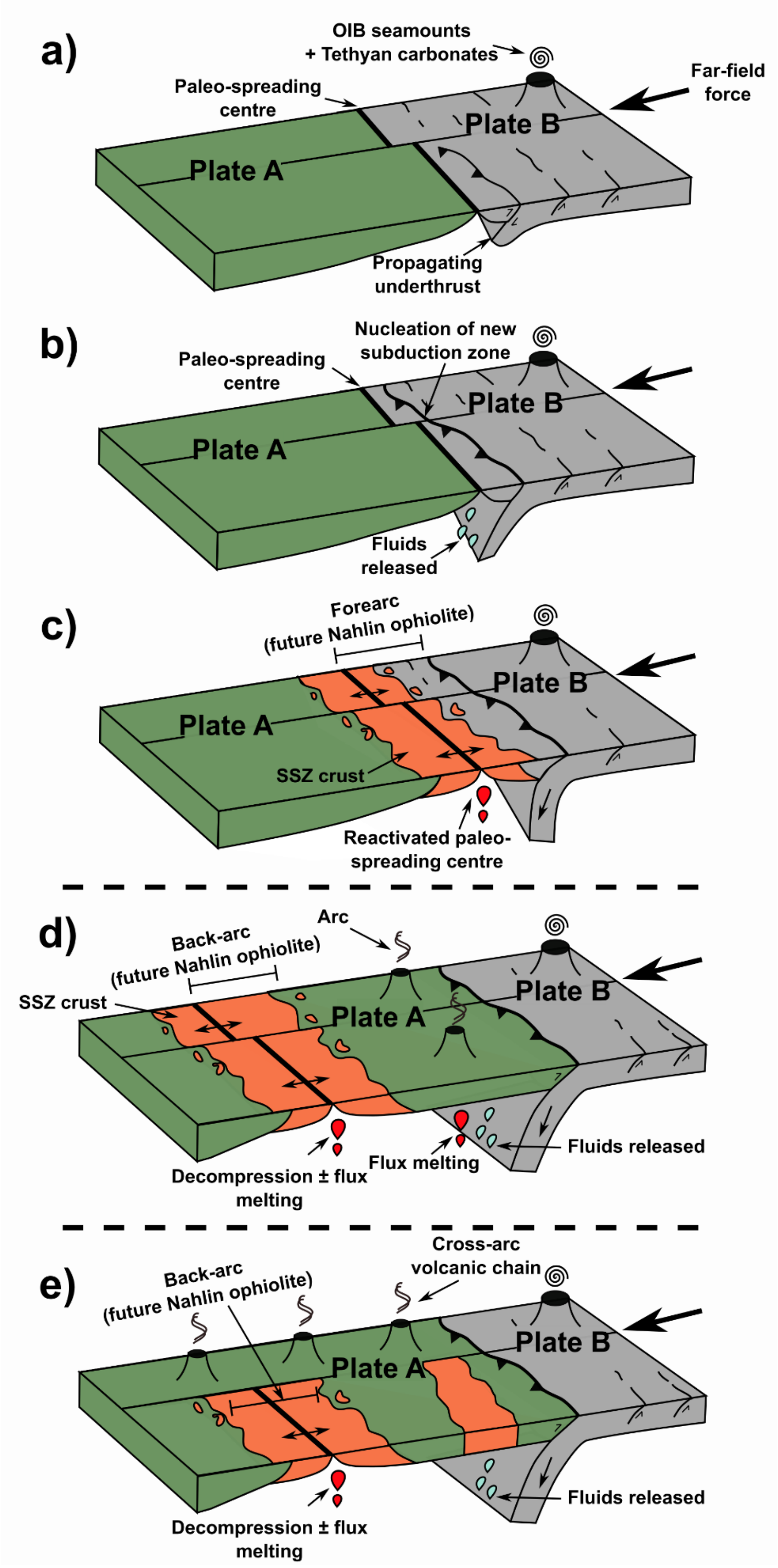
a)
OIB seamounts
+ Tethyan carbonates
Paleo-spreading
centre
Far-field
force
Plate B
Plate A
Propagating
underthrust
b)
Nucleation of new
subduction zone
Paleo-spreading
centre
Plate B
Plate A
Fluids
released
c)
Forearc
(future Nahlin ophiolite)
Plate B
Plate A
SSZ crust
Reactivated paleo-
spreading centre
d)
Arc
Back-arc
(future Nahlin ophiolite)
SSZ crust
Plate B
Plate A
Fluids released
Flux melting
Decompression ± flux
melting
e)
Cross-arc
volcanic chain
Back-arc
(future Nahlin ophiolite)
Plate B
Plate A
Fluids released
Decompression ± flux
melting

Figure 2.13: Potential configurations of the lower plate OIB-carbonate assemblage and the Nahlin ophiolite during the formation of the Nahlin ophiolite as a result of subduction initiation (A, B and C; modified after Maffione et al. 2015), or during spreading in a backarc setting (D) and in a southern Havre Trough-like setting (E). (A) Progressive development of a new subduction zone parallel a paleo-spreading centre or other pre-existing plane of weakness in the oceanic crust. In response to far-field ridge-perpendicular compression, deformation is localized along a pre-existing detachment fault and an underthrust develops. (B) The underthrust propagates laterally, nucleating a new subduction zone. Fluids are released from the subducting plate. (C) Extension on the overriding plate triggers renewed magmatism along the paleo-spreading centre, thereby forming new SSZ-type crust. The SSZ-type crust is preserved in what may later become the forearc region of a mature arc, and therefore has high potential to be preserved as a SSZ-type ophiolite. (D) Plate configuration for development of the Nahlin ophiolite along a backarc spreading centre. Combination of decompression (dry) and flux melting reconciles the BABB-like chemistry of the Group A volcanic rocks. (E) Formation of the Nahlin ophiolite in a southern Havre Trough-like setting, where cross-arc chains of constructive volcanic centres are separated by zone of tectonically accommodated extension erupting BABB along basinal rifts (Wysoczanski et al. 2010). Along-strike variations in volcanic chemistry, from volcanic arc basalts (e.g., Kutcho arc assemblage) to BABB (e.g., Group A arc tholeiites), may explain the lack of preserved arc in the immediate vicinity of the Nahlin ophiolite.

Non-arc magmatism is well-documented elsewhere in the northern Cache Creek terrane. For example, the Teslin Formation limestone with its Permian Tethyan fauna is stratigraphically intercalated with French Range Formation E-MORB-type basalt and related felsic volcanic rocks which yielded a ca. 263 Ma U-Pb zircon crystallization age (Monger 1975; Mihalynuk and Cordey 1997; English et al. 2010). Permian Teslin Formation limestone in the Hall Lake area is also intercalated with OIB (Monger 1975; Mihalynuk and Cordey 1997). Carboniferous OIB and related rhyolite is also known to occur within the Horsefeed Formation limestone (Devine 2002; Merran 2002).

Reconciling the relationship between the E-MORB, OIB, and arc ophiolitic rocks in the Cache Creek terrane is crucial to reconstructing tectonic models for the northern Cordillera. The intraplate volcanic rocks and their associated carbonate platforms have been proposed to represent fragments of oceanic plateaux or seamounts (Monger 1975; English et al. 2010). Some of these volcanic-carbonate successions are demonstrably exotic with respect to Laurentia (Monger and Ross 1971; Orchard et al. 2001). These successions were likely scraped off the downgoing plate and accreted to the Late Permian to Early Triassic arc which is, in part, represented by the Nahlin ophiolite (c.f. English et al. 2010). Incorporation of the E-MORB-OIB-carbonate platform sequences in to the subduction channel is supported by local preservation of blueschist-facies metamorphism in the French Range Formation (Mihalynuk et al. 1998).

Significance to Cordilleran tectonic models

Field and lithogeochemical data indicate that mantle, lower crustal and supracrustal rocks of the Nahlin ophiolite formed within, or proximal to, a Permo-Triassic arc system. The geochemical characteristics of volcanic rocks in the Nahlin ophiolite are similar to basalts sampled from the forearc basement of the Izu-Bonin-Mariana arc (Reagan et al. 2010, 2013; Ishizuka et al. 2011), and to the global average composition of BABB (Gale et al. 2013) (Figure 2.14). Volcanic rocks of the northern Cache Creek terrane, including those spatially associated with ophiolites, were previously grouped with the intraplate volcanic rocks, and Tethyan carbonate successions, as part of the subducting slab of the Cache Creek ocean basin (e.g., Ash, 1994; Monger 1975, 1977; Mihalynuk et al. 1992, 1994, 1999, 2004a; Nelson and Colpron 2007). The preservation potential of large tracts of ophiolitic rocks that form part of the subducting plate is very poor, as the subducting ophiolitic crust lacks the buoyancy and volume to cause orogenesis (Cloos 1993). Furthermore, the accreted ophiolites are typically small and lack lower crust and mantle sections (Kimura and Ludden 1995; Zagorevski et al. 2009; Zagorevski and van Staal 2011). In contrast, the herein proposed arc-marginal setting of the Nahlin ophiolite has a greater preservation potential and is consistent with the preservation of an extensive mantle section, which is characteristic of obducted ophiolites (Zagorevski and van Staal 2011). The Nahlin ophiolite thus represents the upper plate at an intraoceanic convergent margin (Figure 2.13). The structurally-imbricated Mississippian to Permian limestone, alkaline volcanic rocks and chert, including those that are characterized by Tethyan fauna, must represent part of the subducting ocean basin. This is supported by preservation of blueschist in French Range (Figure 2.1; Mihalynuk et al. 1998).

The upper and lower plate domains (Figure 2.11) represent fundamentally different associations of rocks, and therefore meet the definition of two separate “terranes”: fault-bound areas possessing unique tectonic assemblages that differ from those of adjacent terranes (Gabrielse et al. 1991). Therefore, in addition to the currently mapped terrane-bounding fault, the Nahlin fault (Figure 2.1; English and Johnston 2005), there exists another suture within the Cache Creek terrane, between the upper and lower plate assemblages. Contrary to current terrane boundaries, this suture cannot be neatly drawn as an orogen near-parallel fault, but its approximate equivalents can be observed in outcrop. At Mount Nimbus (Figure 2.1), for example, ophiolitic rocks are thrust over Mississippian carbonate successions bearing OIB-type volcanic rocks (Zagorevski et al. 2016a).

The regional map patterns in the northern Cache Creek terrane are complicated by overprinting deformation episodes including poorly exposed obduction structures, Jurassic E-W trending folds and thrust faults, and northwest trending Cretaceous strike-slip faults (Mihalynuk et al. 2003, 2004b, Zagorevski et al. 2015, 2016a). The ophiolitic rocks are generally exposed to the southwest of the so-called Cache Creek Complex (the subduction accretionary complex including OIB-carbonate successions, English et al. 2010). This distribution suggests that the ophiolitic rocks were obducted along northeast-vergent structures over a southwest dipping intraoceanic subduction zone (cf. English et al 2010).

The proposed separation of the Cache Creek terrane into arc and seamount terranes has significant implications for the interpretation of Cordilleran “oceanic” terranes, including the southern Cache Creek terrane, where grouping of overriding and subducting plates into a single terrane resulted in significant confusion. For example, detailed studies of the Cache Creek terrane near Fort St. James suggested a ridge-centered or near-ridge oceanic island plateau environment for the formation of the Cache Creek terrane (Tardy et al. 2001; Lapierre et al. 2003). This was largely based on the presence of OIB, E-MORB and N-MORB-like basalts. Some of Cache Creek MORB-like samples presented in Lapierre et al. (2003; Type 1 N-MORB) actually show significant negative Nb anomalies relative to MORB basalt indicating that these samples are likely island arc tholeiites and are not related to alkaline lavas. Their association with gabbroic and harzburgitic rocks suggest that, together with the mantle harzburgite, the arc tholeiites are correlative to the Nahlin ophiolite, consistent with their inferred age (ca. 257 Ma; Struik et al. 2001). These rocks also lie adjacent to the Sitlika Assemblage (Childe and Schiarizza 1997), a correlative of the Kutcho arc assemblage. Following the herein proposed tectono-stratigraphic relationships for the northern Cache Creek terrane, the alkaline and E-MORB volcanic rocks and associated carbonates in Fort St. James area form part of the lower, partly subducted plate onto which Trembleur ophiolitic rocks and Kutcho - Sitlika arc rocks were obducted.

2.7 Conclusions

Intrusive and extrusive igneous rocks of the Nahlin ophiolite (Group A) in the northern Cache Creek terrane are dominantly tholeiitic and of arc-affinity. The basaltic rocks represent the products of up to 20% partial melting, and are the melt complement to similar levels of melting recorded by harzburgite residues in the mantle section of the ophiolite. The Group A volcanic rocks, considered to represent the supracrustal section of the Nahlin ophiolite, are likely correlative to the nearby subalkaline volcanic rocks in the Nakina transect and Kutcho assemblage, and may be linked to a regionally extensive Permo-Triassic intraoceanic arc-backarc system. During the amalgamation of the Cache Creek terrane, the Nahlin ophiolite occupied the upper plate thereby facilitating the preservation of extensive fragments of oceanic lithospheric mantle. The volumetrically minor Group B (E-MORB) and C (OIB) volcanic rocks associated with Tethyan fauna-bearing carbonate successions represent fragments of oceanic plateaux and their carbonate atolls sliced off of the subducting plate and incorporated into a subduction accretionary complex. These sequences are older than and petrogenetically unrelated to the Nahlin ophiolite. This configuration challenges some accepted models for the Cache Creek terrane, and calls for the recognition of additional terrane-bounding faults or suture zones within the Cache Creek terrane. A re-evaluation of the northern Cache Creek terrane in this light is paramount to a better understanding of the assembly and displacement of terranes in the northern Cordillera.

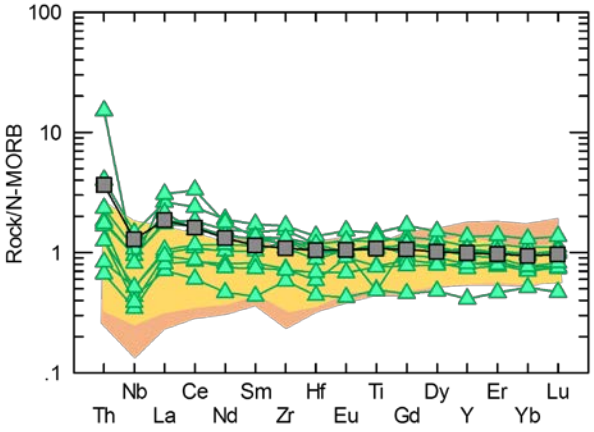

Figure 2.14: Rare-earth element (REE) multi-element N-MORB normalized plots for the Group A volcanic and volcaniclastic rocks of the Nahlin ophiolite (green triangles) compared to the range of compositions reported for forearc basalts (FAB) in the Bonin arc (orange shaded region; Ishizuka et al. 2011) and in the Mariana arc (yellow shaded region; Reagan et al. 2010; Reagan et al. 2013), and to the global average for backarc basin basalt (BABB, dark grey squares; Gale et al. 2013).

Chapter 3. A tale of two massifs: geochemical and geothermometric constraints on the history of the harzburgite in the Nahlin ophiolite, British Columbia, Canada

3.1 Abstract

The Nahlin ophiolite represents one of the largest and best-preserved ophiolites in the Cordillera of British Columbia and Yukon, Canada. Bedrock mapping in the Menatatuline Range area shows that the ophiolite is structurally disrupted with exposures of mantle rocks divisible into two massifs: Hardluck and Menatatuline. Both massifs consist of spinel harzburgite and minor lherzolite that have compositions consistent with significant depletion by melt extraction (<2 wt % whole-rock Al_2O_3, ~45 wt % whole-rock MgO, and clinopyroxene Yb_N 2-5). Inversion modelling of the clinopyroxene REE abundances yields ~10 – 20% melting, with melt compositions that are compositionally similar to the tholeiitic gabbros and basalts in the crustal section of the ophiolite. Modelling of Ti and Dy in clinopyroxene shows that peridotites from the Menatatuline massif are compositionally similar to supra-subduction zone (SSZ) peridotites, and suggests that they represent residues of hydrous melting.

The Nahlin peridotites document a two-stage evolution: depletion of a locally heterogeneous mantle source by hydrous fractional melting, followed by refertilization of the refractory harzburgite in the mantle wedge. Evidence for this includes strongly zoned Ca in orthopyroxene, and local enrichment of LREE in whole-rock and clinopyroxene chemistry. This two-stage evolution is also recorded by the thermal history of the harzburgites, whereby some thermometric systems may have been reset following cryptic and modal metasomatism and relatively slow cooling. The refractory nature of the Menatatuline harzburgites in combination with the arc-related volcanic geochemistry provides overwhelming evidence for a SSZ origin.

Peridotite from the Hardluck massif displays characteristics of both abyssal and SSZ peridotites. These geochemical and geothermometric constraints can be reconciled by evolution of the Hardluck and Menatatuline massifs as two separate segments along a backarc or proto-forearc ridge system, later juxtaposed by dextral strike-slip faulting.

3.2 Introduction

Ophiolites provide a window into the oceanic lithosphere, and studies of key ophiolites worldwide (e.g., Troodos, Varga and Moores 1985; Batanova and Sobolev 2000; Oman, Coleman 1981; Kelemen et al. 1995, 1997b) have greatly enhanced our understanding of the interplay of tectonic and magmatic processes at spreading centres. In the Cordillera (Figure 3.1), as with ophiolites elsewhere, interpretations of tectonic setting typically rely solely on the geochemical signatures of the volcanic section of the ophiolite (e.g., Miyashiro 1973, Alabaster et al. 1982, Ishikawa et al. 2002, Dilek et al. 2008). Compared to volcanic geochemistry alone, the magmatic and thermal history of mantle lithosphere provides crucial clues to the evolution of an ophiolite and its role in regional tectonics. Whole-rock and mineral chemical data can address questions about the setting and extent of melting in the mantle section of the ophiolite, and the relationship between the mantle peridotite and overlying basaltic crust.

The Cordilleran orogen in British Columbia and Yukon, Canada, hosts several large ophiolites (Figure 3.1). Many of these ophiolites are within the Cache Creek terrane, a terrane which represents a crucial component in many models of Cordilleran accretionary tectonics. Key hypotheses of oroclinal bending and entrapment of the Cache Creek “ocean basin” in these models hinge on the role of relatively dense subducting oceanic crust and thick subduction-stalling oceanic plateaux (Mihalynuk et al. 1994; English and Johnston 2005; Johnston and Borel 2007; Nelson and Colpron 2007). Many of these models suggest that the Cache Creek terrane represents the downgoing plate, subducted beneath adjacent arc terranes (Stikinia and Quesnellia; Figure 1.2). The ophiolite sequences of the northern Cache Creek terrane play a crucial role in challenging these models. Preservation of ophiolites with significant mantle lithosphere from subducting plates is highly unlikely (Cloos 1993; Kimura and Ludden 1995; Zagorevski et al. 2009; Zagorevski and van Staal 2011), and would be geodynamically unfavourable in some of the existing models (e.g., Ash 1994; Mihalynuk et al. 1994; Johnston and Borel 2007; Nelson and Colpron 2007). Conducting a detailed study of a Cache Creek terrane ophiolite may therefore shed light on the nature of the Cache Creek “ocean basin”, and its closure. Particularly, unravelling the thermal history of one of these ophiolites may elucidate the relative roles of lithospheric and post-obduction cooling, as well as the likelihood of peridotite preservation based on buoyancy. Thus in this work I present new geochemical and geothermometric data from peridotites in the Nahlin ophiolite - one of the largest and best-preserved ophiolites in the Canadian Cordillera (Figure 3.1 andFigure 3.2). Due to its remote location, it has never been investigated in detail. The new data presented herein constrain the supra-subduction zone (SSZ) setting and the magmatic and thermal history of peridotites in the Nahlin ophiolite, with implications for the emplacement of the ophiolite, closure of ocean basins during orogenesis and continental growth in the Cordillera.

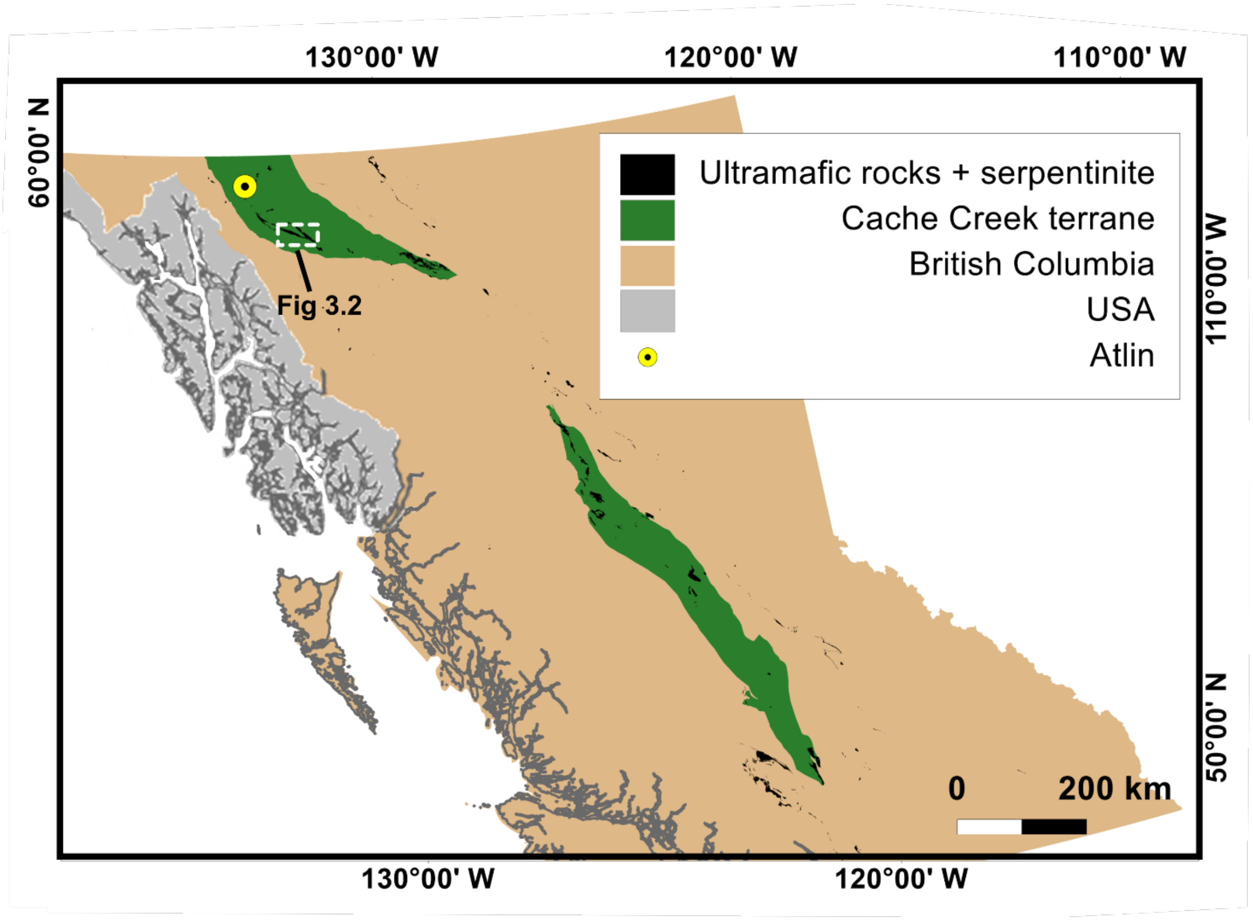

Figure 3.1: Map of British Columbia highlighting the Cache Creek terrane and exposures of ultramafic rocks based on compiled British Columbia Geological Survey data (Mihalynuk et al. 1996). White dashed box approximates the location of the Menatatuline Range study area (Figure 3.2) located ~ 100 km southeast of Atlin, BC.

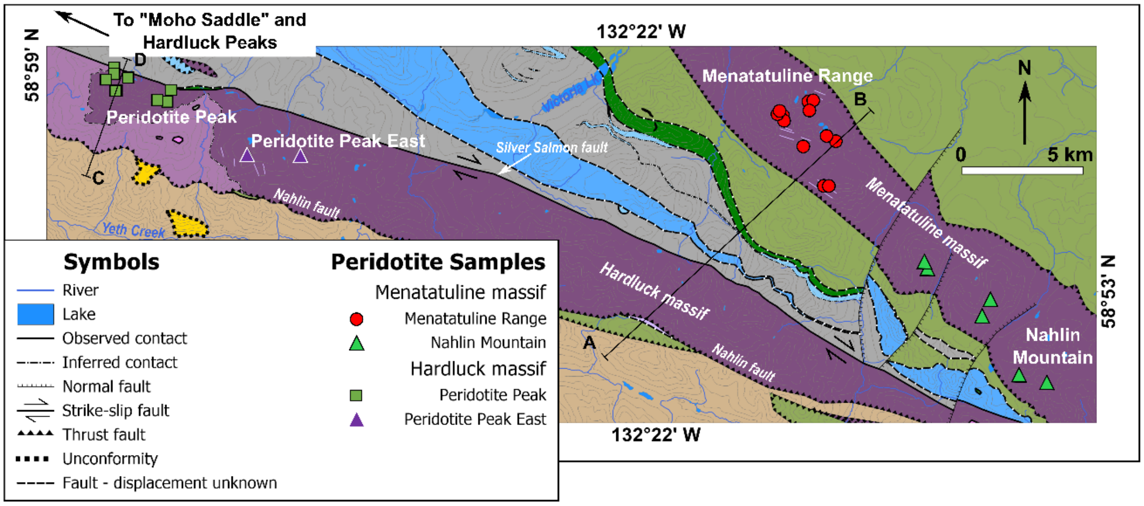

Figure 3.2: Bedrock geology of the Menatatuline Range area, from Peridotite Peak to Nahlin Mountain, based on 2015 – 2016 mapping and compiled British Columbia Geological Survey data (Mihalynuk et al. 1996). Peridotite samples symbolized by location. Dikes are shown schematically. Lines A-B and C-D denote lines of cross sections (Figure 3.3). Names of geological features referenced in text are in italic font (e.g. Nahlin fault). Informal place names are indicated by quotation marks (e.g., "Moho Saddle"). Background topographic raster image from Natural Resources Canada (1990a, 1990b). For lithological legend see Figure 3.3.

3.3 Regional Geology

The Nahlin ophiolite is part of the Mississippian to Lower Jurassic Cache Creek terrane in British Columbia and Yukon. The Cache Creek and adjacent Stikinia and Quesnellia terranes were accreted to North America and stitched together by crosscutting plutons by the Middle Jurassic (Gabrielse 1991; Mihalynuk et al. 1992, 1998). The terrane comprises contrasting assemblages of exotic Carboniferous to Permian carbonate sequences built on intraplate volcanic rocks (Cordey et al. 1991; Orchard et al. 2001), and Permo-Triassic volcanic arc successions (Mihalynuk et al. 2004b; English et al. 2010; Zagorevski et al. 2016a, 2017). The tectonic setting of the Cache Creek terrane remains ambiguous, with some authors treating the whole or its parts as a subduction zone melange or an accretionary complex (Mihalynuk et al. 1994, 1999, 2004b, English and Johnston 2005, English et al. 2010, and others).

In the Menatatuline Range area in northwest British Columbia (white box in Figure 3.1; Figure 3.2), the Cache Creek terrane comprises remnants of oceanic lithospheric mantle, mafic intrusions, mafic volcanic rocks, and sedimentary rocks (carbonate, chert and siliciclastic). The mantle and mafic intrusive and extrusive rocks together make up the Nahlin ophiolite, which was first recognized by Aitken (1959). Plutonic and volcanic rocks of the ophiolite are tholeiitic and arc-related (English et al. 2002, 2010; McGoldrick et al. 2017). Only a minor component of volcanic rocks in northern Cache Creek terrane are alkaline intraplate basalts representing fragments of the subducting plate scraped off at an intraoceanic convergent margin (English et al. 2002, 2010; McGoldrick et al. 2017). Correlative tholeiitic volcanic sections can be found elsewhere in the Cache Creek terrane (Barrett et al. 1996; Childe and Schiarizza 1997; Childe and Thompson 1997; Mihalynuk and Cordey 1997), and may be linked to a regionally extensive intraoceanic Permo-Triassic arc-backarc system. The timing of magmatism in ophiolites of the northern Cache Creek terrane varies along its strike from ~245 to 261 Ma (see Table 2-1). Zircon crystallization ages from quartz diorite (Devine 2002) and tonalite (Mihalynuk et al. 2003) constrain the age of the crustal section of the Nahlin ophiolite north of and along strike of the Menatatuline Range study area to be ca. 255 to 261.4 Ma.

Nahlin ophiolite

The Nahlin ophiolite locally lacks some classic Penrose-style ophiolite components (Anonymous 1972), such as coherent sections of gabbro and sheeted dykes, and although some primary contact relations may be obscured by faulting (Figure 3.3), it is still possible to reconstruct the stratigraphy of the ophiolite (Zagorevski et al. 2015, 2016a). A discussion of the lower and supracrustal igneous rocks from the Nahlin ophiolite is presented elsewhere (Chapter 2; McGoldrick et al. 2017).

Extensive tracts of mantle harzburgite are exposed along the southwestern margin of the Cache Creek terrane, along a southeast trending discontinuous belt stretching ~150 km from Atlin, BC to Nahlin Mountain. The two most aerially extensive and continuous massifs (Menatatuline and Hardluck) together form the mantle component of the Nahlin ophiolite (Figure 3.2), and were previously mapped by Aitken (1959) and Terry (1977). The Menatatuline massif trends northwest and underlies Nahlin Mountain and the Menatatuline Range, whereas the Hardluck massif underlies a series of west-northwest-trending peaks from east to west - Peridotite Peak East, Peridotite Peak, “Moho Saddle”, and Hardluck Peaks.

Ultramafic rocks of both massifs comprise variably serpentinized massive and layered harzburgite with pyroxenite dikes, and replacive dunite pods (McGoldrick et al. 2016). The dominant lithology, harzburgite, consists of ~45-65% olivine, ~25-40% orthopyroxene, lesser clinopyroxene (3-8%), and rare spinel (<5%). Locally at Peridotite Peak, however, layers of lherzolite contain up to 15% clinopyroxene (Mihalynuk et al. 2004b). In both massifs harzburgite tectonite locally preserves a primary mantle tectonic fabric (S_1) defined by orthopyroxene elongation and variably developed pyroxene-defined layering (Figure 3.4a). Thin (5-10 cm) pyroxenite dikes, and discrete replacive dunite channels are variably layer-discordant or concordant with respect to this layering, and are locally deformed into meter-scale folds (Figure 3.4a and b).

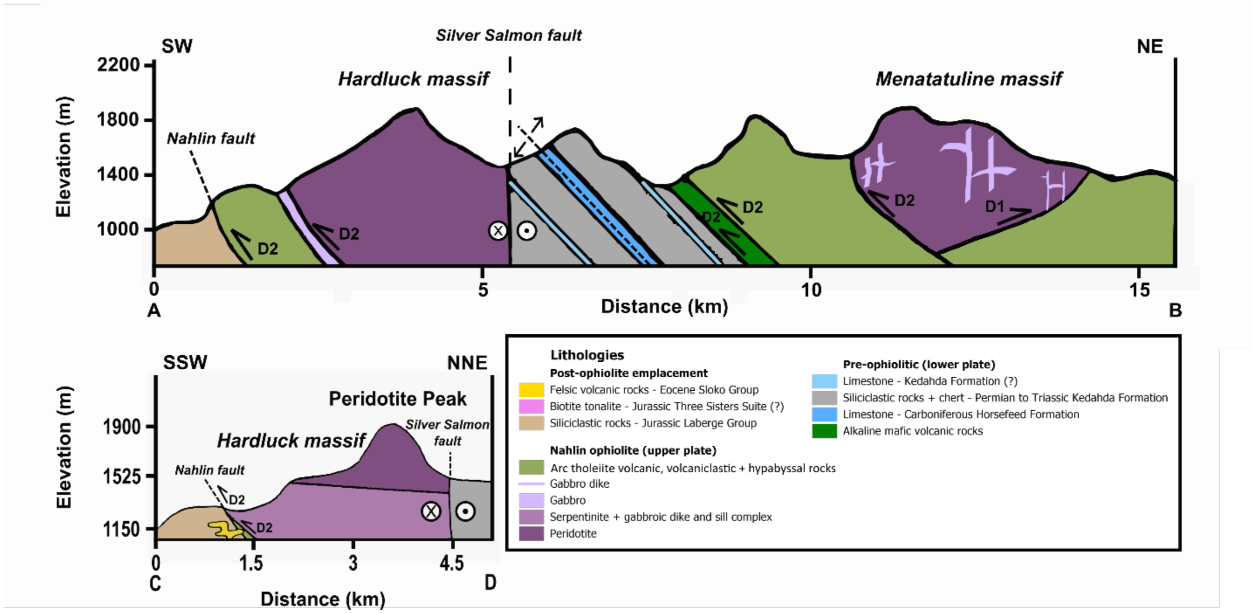

Figure 3.3: Schematic cross-sections through the Nahlin ophiolite in the Menatatuline Range area (line A-B) and at Peridotite Peak (line C-D), with 2x vertical exaggeration. See Figure 3.4 for field photographs of some interpreted structures, particularly D_1 faults and late strike slip faults ('Silver Salmon fault').

Lower crustal cumulates and sheeted dike complexes are volumetrically minor in the Nahlin ophiolite in the Menatatuline Range area. The harzburgite tectonite is locally crosscut by multiple generations of gabbroic dikes of arc tholeiite affinity, some of which are essentially unstrained, whereas others have been boudinaged. In some areas, gabbroic dike-and-sill complexes extensively intrude highly serpentinized mantle harzburgite (Figure 3.3 and 3.4c). These melt conduits presumably fed the arc tholeiites and related mafic volcaniclastic rocks in the Menatatuline Range area.

Structural relationships between the Nahlin ophiolite and adjacent non-ophiolite assemblages are complicated by poorly exposed obduction structures, Jurassic-aged E-W trending folds and thrust faults, and northwest trending Cretaceous strike-slip faults (Mihalynuk et al. 2003, 2004b, Zagorevski et al. 2015, 2016a). With the exception of the mantle-crust transition exposed to the northwest of the field area ("Moho Saddle", Figure 3.2, Mihalynuk et al. 2003), the harzburgite massifs of the Nahlin ophiolite are fault-bound, leaving little evidence as to the way-up in stratigraphy. These fault-bound sections of mantle juxtapose harzburgite tectonite against basalt or chert (Figure 3.3). Some of these are interpreted as earlier thrust faults denoted as D_1 herein, placing the Nahlin ophiolite over Carboniferous limestone intercalated with OIB lavas (Figure 3.4d). Northeast-vergent D_1 thrust faults also place harzburgite tectonite over supracrustal rocks of the ophiolite (peridotite over basalt, Figure 3.4e). Elsewhere, later southwest-vergent thrust faults denoted as D_2 herein re-imbricate the ophiolite (upper plate) and OIB-carbonate (lower plate) assemblages, resulting in local "young-over-old" relationships across D_2 faults. The sharp contact along the northern side of the Hardluck massif (Figure 3.3 and 3.4f) represents a steeply dipping northwest trending fault (Figure 3.2), which juxtaposes the Hardluck massif against the siliciclastic and carbonate sedimentary rocks of the predominantly Middle Triassic-aged Kedahda Formation (Monger 1975; Cordey et al. 1991; Mihalynuk et al. 2003).

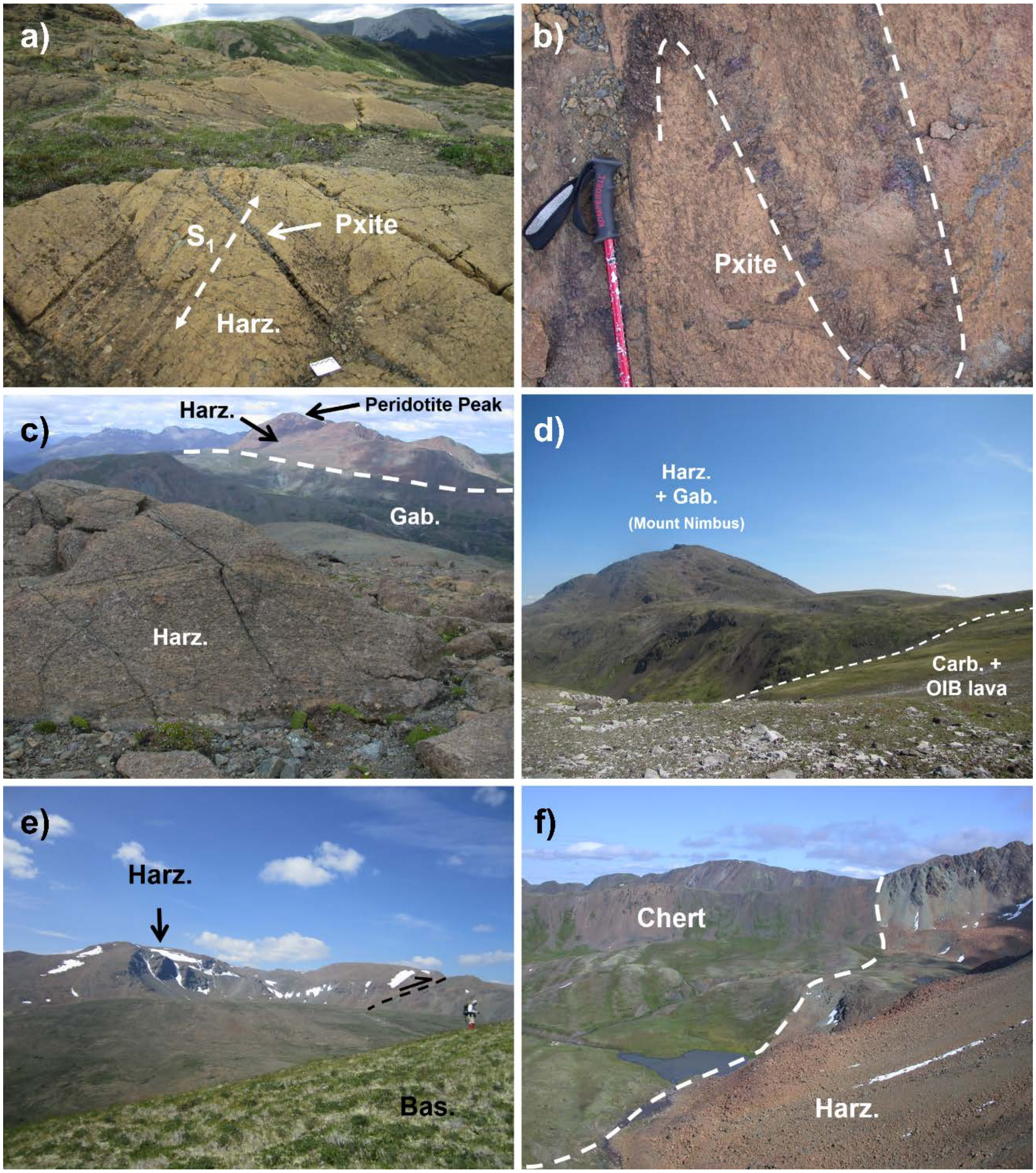

Figure 3.4: Peridotites and field relations within the Nahlin ophiolite. (A) Primary tectonic fabric (S1) in harzburgite (harz.) tectonite crosscut by pyroxenite dikes (pxite), on Peridotite Peak East. (B) Tight, near isoclinal folding of a pyroxenite dike in harzburgite tectonite on Peridotite Peak. (C) Subhorizontal contact between relatively fresh harzburgite tectonite and serpentinite extensively intruded by a gabbroic dike-and-sill complex (Gab.), looking WNW from Peridotite Peak East. (D) True “Cache Creek terrane” suture (D_1) exposed near Mt. Nimbus. Ophiolite harzburgite and gabbro thrust over Tethyan fauna-bearing Mississippian limestone (Carb.) intercalated with OIB-type lavas. (E) Harzburgite in the Menatatuline massif thrust over basaltic supracrustal rocks (Bas.) of the Nahlin ophiolite. Northeast-vergent D_1 thrust is extensively serpentinized. (F) Steeply-dipping ‘Silver Salmon fault’ transposes harzburgite of the Hardluck massif against siliciclastic rocks of the Kedahda Formation north of Peridotite Peak.

3.4 Petrography

A list of peridotite samples collected for this study is summarized in Table 3-1. Mantle rocks from throughout the Nahlin ophiolite are predominantly spinel harzburgite and minor lherzolite with protogranular to porphyroclastic textures (Table A 3) (Mercier and Nicolas 1975; Nicolas 1989). Orthopyroxene porphyroclasts (2 - 6 mm in diameter) are anhedral with irregular grain boundaries and some display kink banding (Figure 3.5a). Clinopyroxene is anhedral and finer grained than orthopyroxene (0.5 - 3 mm). Both pyroxenes display thin (5 - 25 µm) exsolution lamellae (Figure 3.5b). Olivine (2 - 6 mm diameter) displays highly irregular to well-equilibrated grain boundary textures (Figure 3.5c). Spinel (0.2 - 2 mm) displays a variety of morphologies, including anhedral “holly leaf” and subhedral to euhedral equant. The degree of serpentinization varies from nearly zero to ~40% both within and between massifs. Serpentine minerals fill fractures in olivine grains, and in rare cases alter orthopyroxene. Clinopyroxene, orthopyroxene, and spinel are unaffected by serpentinization, however some spinel grains display ferrochromite ± magnetite alteration along grain boundaries.

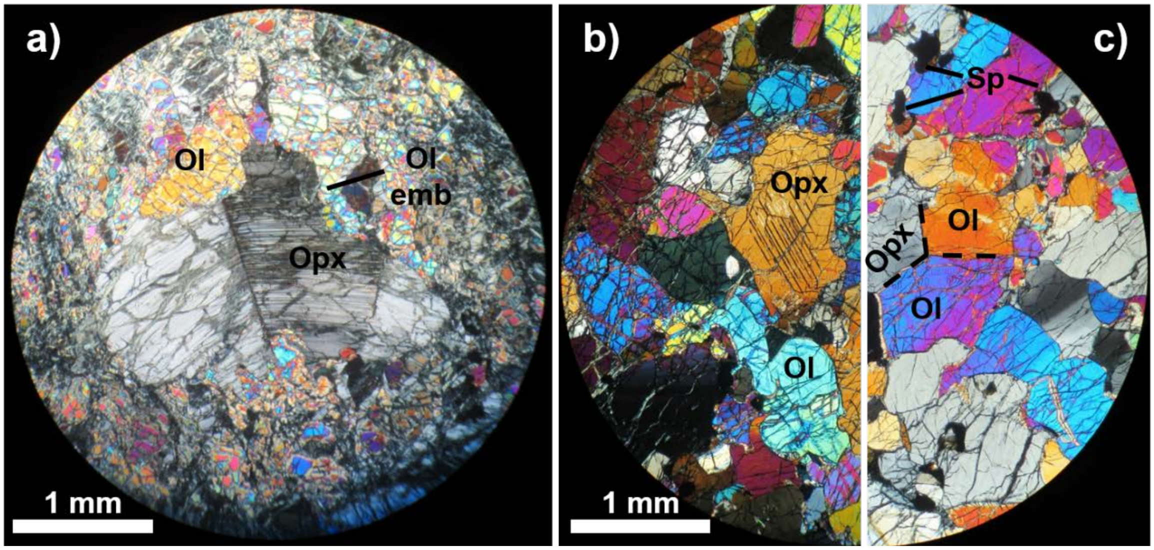

Figure 3.5: Photomicrographs of peridotites from the Nahlin ophiolite. (A) Kink-banded orthopyroxene porphyroclasts in spinel harzburgite in sample DC0339. Irregular boundaries and embayments of olivine

(Ol emb) into orthopyroxene suggest partial orthopyroxene dissolution during melt-rock interactions in the lithosphere. Some olivine divided into smaller sub-grains by mesh texture of serpentine veinlets. (B) Exsolution lamellae and irregular grain boundaries of orthopyroxene porphyroclasts in notably fresh spinel harzburgite sample DC0319. (C) Fine grained anhedral spinel in a well-equilibrated spinel harzburgite, as shown by ~120 ° grain boundaries between olivine and orthopyroxene in sample DC0318.

Table 3-1: Peridotite sample locations and coordinates.

Sample	Location[1]	Rock class	Lithology[2]	Station code[3]	Station[4]	Latitude (°N)	Longitude (°W)
15SM023A	Menat	Ultramafic	Harz	15SM	23	58.951	132.232
15SM023B	Menat	Ultramafic	Harz	15SM	23	58.951	132.232
15SM038	Menat	Ultramafic	Harz	15SM	38	58.953	132.238
15SM045	Menat	Ultramafic	Harz	15SM	45	58.962	132.250
15SM055B	Menat	Ultramafic	Harz	15SM	55	58.949	132.255
15SM056	Menat	Ultramafic	Harz	15SM	56	58.966	132.250
15SM057	Menat	Ultramafic	Harz	15SM	57	58.966	132.248
16SM190	Menat	Ultramafic	Harz	16SM	190	58.962	132.272
16SM192	Menat	Ultramafic	Harz	16SM	192	58.961	132.273
16SM193	Menat	Ultramafic	Harz	16SM	193	58.960	132.269
16SM160	Nahlin	Ultramafic	Harz	16SM	160	58.904	132.171
16SM162	Nahlin	Ultramafic	Harz	16SM	162	58.901	132.169
16SM181	Nahlin	Ultramafic	Harz	16SM	181	58.860	132.106
16SM184	Nahlin	Ultramafic	Harz	16SM	184	58.857	132.086
16SM187	Nahlin	Ultramafic	Harz	16SM	187	58.883	132.131
16SM188	Nahlin	Ultramafic	Harz	16SM	188	58.889	132.125
DC0205	Hardlk	Ultramafic	Harz	DC02	205	59.044	132.956
DC0206	Hardlk	Ultramafic	Harz	DC02	206	59.045	132.956
DC0303	Moho	Ultramafic	Harz	DC03	303	59.029	132.877
DC0304	Moho	Ultramafic	Harz	DC03	304	59.029	132.877
DC0310	Per Pk	Ultramafic	Lherz	DC03	310	58.979	132.752
DC0312	Per Pk	Ultramafic	Lherz	DC03	312	58.980	132.753
DC0313	Per Pk	Ultramafic	Lherz	DC03	313	58.980	132.753
DC0318	Per Pk	Ultramafic	Lherz	DC03	318	58.988	132.753
DC0322	Per Pk	Ultramafic	Harz	DC03	322	58.975	132.716
DC0327	Per Pk	Ultramafic	Lherz	DC03	327	58.984	132.744
DC0334	Per Pk	Ultramafic	Lherz	DC03	334	58.985	132.754
DC0336	Per Pk E	Ultramafic	Harz	DC03	336	58.953	132.619
DC0345	Per Pk E	Ultramafic	Harz	DC03	345	58.954	132.659

1 - Hardlk, North of Hardluck Peaks; Menat, Menatatuline Range; Moho, "Moho Saddle"; Nahlin, Nahlin Mountain; Per Pk, Peridotite Peak; Per Pk E, Peridotite Peak East.

2 - Harz, harzburgite; Lherz, lherzolite.

3 - Station code refers to the senior mapping geologist and year (i.e., Zagorevski mapping in 2015 denoted as "ZE15", D. Canil mapping in 2003 denoted as "DC03").

4 - Station number refers to mapping geologist and station (i.e., S. McGoldrick's second station denoted as "SM02").

3.5 Methods

Lithogeochemistry

The major, minor, and trace element data presented herein are from 19 samples of spinel harzburgite from Menatatuline Range and Nahlin Mountain (Table A 4). Samples were slabbed for lithogeochemistry and petrographic thick section, and were crushed and processed at Activation Laboratories in Ancaster, Ontario (Table A 4). Major oxides were measured by lithium metaborate/tetraborate fusion and inductively coupled plasma optical emission spectrometry (ICP-OES), whereas minor and trace elements were determined by inductively coupled plasma mass spectrometry (ICP-MS). The suite of standards analysed along with the Menatatuline Range area samples reproduce reported concentrations of major elements to within 6%, large-ion lithophile elements (LILE) to within 13%, high-field strength elements (HFSE) to within 9%, and rare-earth elements (REE) to within 7% (Table A 4). These data are augmented by existing whole-rock data from 11 spinel harzburgites and lherzolites from the Hardluck massif (Table A 5) reported by Canil et al. (2006) and Babechuk et al. (2010). Two of these samples from Peridotite Peak and Peridotite Peak East originally analysed in Babechuk et al. (2010) were re-analysed in this study to compare inter-laboratory data quality (Table A 5).

Mineral chemistry

Least altered samples were selected for further analysis based on volatile concentrations (low LOI wt %) and petrography. Some samples were cut and mounted with epoxy in 1” plastic pucks in preparation for analysis, whereas others were analysed in polished thick section (~200 µm).

Electron microprobe (EMP)

Major element concentrations of olivine, spinel, clinopyroxene, and orthopyroxene were measured on a fully-automated Cameca SX-50 electron microprobe at the University of British Columbia operating on wavelength dispersion mode using an acceleration voltage of 15 kV, a 40 nA beam current and ~ 5 µm beam diameter. Grain boundaries, fractures, and exsolution lamellae were avoided during beam placement. Counting time for all elements was 20 s on the peak and 10 s on each background, except for Ca, Al, and Cr in olivine, for which a peak counting time of 60 s and background counting times of 30 s were used. Data were reduced using the 'PAP' $\phi(\rho Z)$ method (Pouchou and Pichoir 1985), and are reported averages and one standard deviation of ~3 to 15 mineral analyses from a given sample (Tables A 6, A 7, A 8, and A 10). Typically, two to six grains of each mineral were analysed per sample, with two to three points in both the grain rim and core. Ferric and ferrous iron concentrations in spinel were calculated assuming perfect stoichiometry (Droop 1987).

Laser ablation ICP-MS

Mineral minor and trace element compositions were acquired by laser ablation inductively-coupled plasma mass spectrometry (LA-ICP-MS) at the University of Victoria, on a Thermo X-Series II (X7) quadrupole ICP-MS equipped with a New Wave UP-213 laser using He carrier gas. A series of MPI-DING glasses (ML-3B, GOR-128, GOR-132, and KL-2G) were run as internal standards at the beginning and end of each session, as well as following every 10-15 analyses throughout the day. The BCR-2 glass was run as an external standard along with the MPI-DING glasses at the same frequency (Table A 12). Analyses were conducted along laser raster lines varying from ~80 – 160 µm in length traversed in four passes of the laser, at a scanning rate of 15 µm/s. Laser beam size varied from 40 – 100 µm, with the majority of data collected using a 80-100 μm beam size. Grain boundaries and inclusions were avoided during line placement to minimize contamination from ablation into adjacent phases or alteration. Total counting times varied with line length, but were typically ~60 – 100 s on the peak and 20 s on the background. Data were reduced using the Thermo PlasmaLab software (Wills et al. 2007), and are reported as averages and one standard deviation of ~3 to 12 mineral analyses from a given sample (Table A 9 and A 11). In general, two to three analyses were acquired per grain, and one to six grains of a given mineral were analysed per sample. This was particularly dependent upon the number of clinopyroxene grains of appropriate size present in a given thick section or puck. The detection limit for each analyte was calculated as three times the standard deviation of all background analyses on that analyte during a given session. Variations in detection limits on the LA-ICP-MS over the course of this study are presented in Table A 13.

3.6 Results

Peridotite lithogeochemistry

The data in Table A 4 for the Menatatuline massif are supplemented by published whole-rock data for the Hardluck massif (Figure 3.2; Peridotite Peak East, Peridotite Peak, “Moho Saddle”, and Hardluck Peaks) (Canil et al. 2006; Babechuk et al. 2010). Spinel harzburgite from both the Hardluck and Menatatuline massifs is highly refractory, commonly containing less than 2 wt % Al_2O_3 and ~45 wt % MgO (Tables A 4 and A 5). Concentrations in Al_2O_3, CaO, Sc, V, and Yb decrease and Ni increases with increasing MgO, as expected for residues of mantle partial melting (Figure 3.6).

Some whole-rock trace element data, particularly the REE, show discrepancies between data from ActLabs (this study) and Laurentian University (Babechuk et al. 2010). Rare earth element data acquired at ActLabs show flat to slightly “U-shaped” chondrite-normalized profiles (Figure 3.7), whereas data from Babechuk et al. (2010) show LREE depletion relative to HREE. To test this apparent difference in LREE depletion, powders of two samples from the Babechuk study were re-analysed at ActLabs along with some samples from this study. The resulting data show that the LREE to MREE measured at ActLabs are near detection limits in some samples or appear to be enriched by ~1 order of magnitude in others, relative to concentrations reported in Babechuk et al. (2010). The ActLabs results can, however, reproduce the HREE (Dy to Lu) to within ~2 to 22% of concentrations measured in the Babechuk study (Table A 5). I thus have confidence in comparing the whole-rock HREE concentrations between massifs for samples analysed at different laboratories. Samples from the Hardluck massif generally have similar to 2x higher concentrations of HREE relative to peridotite samples from Menatatuline massif (Figure 3.7). As shown in appendix Table A 5, some minor and trace elements (e.g., MnO, Na_2O, TiO_2, Ga, Zr, and Ba) are significantly more enriched in the ActLabs analyses compared to the low-level measurements of Babechuk et al. (2010). This implies that the ActLabs data for these elements in samples from the Menatatuline massif (Table A 4) cannot be fairly compared with those from the Hardluck massif (Table A 5) presented by Babechuk et al. (2010).

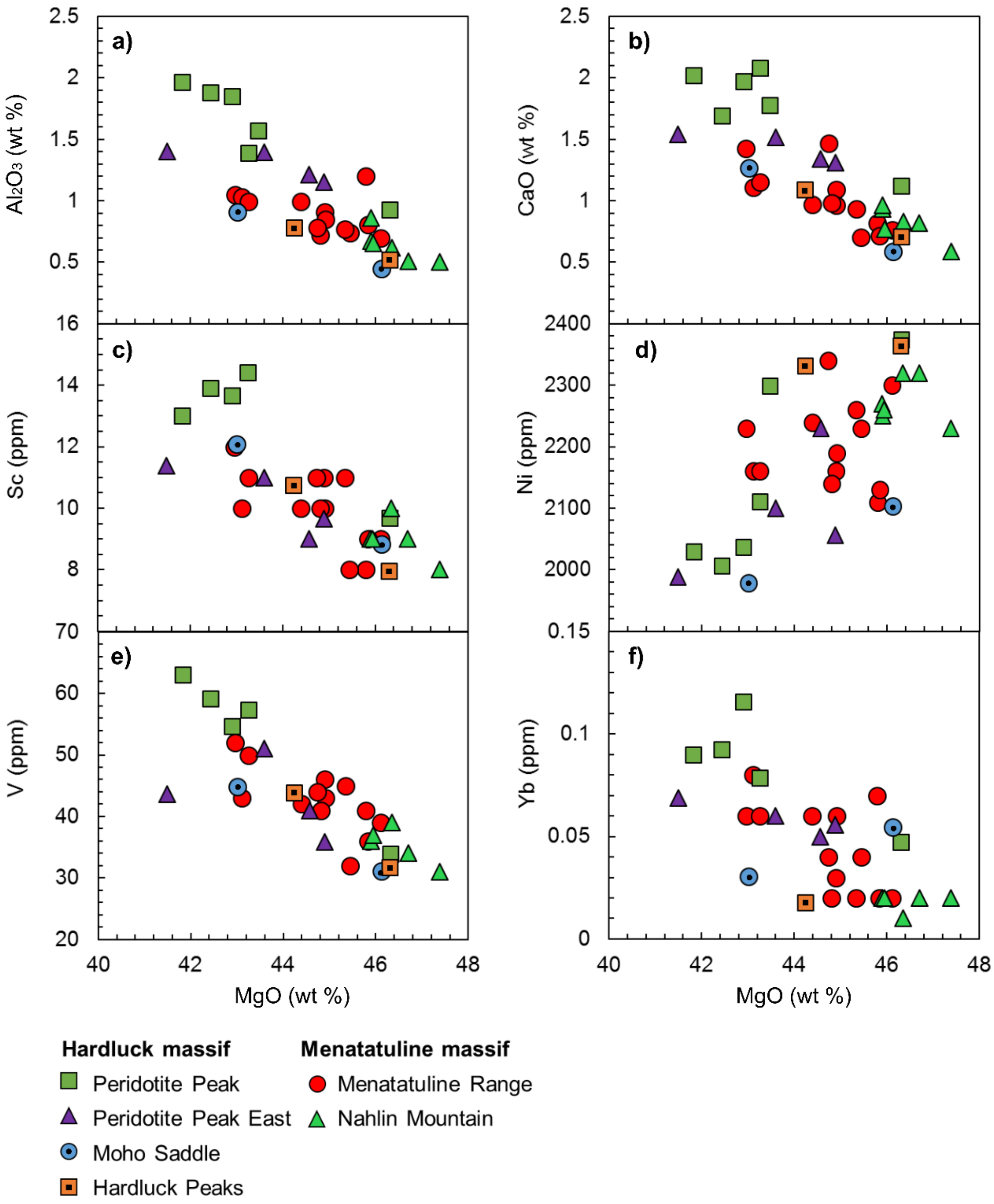

Figure 3.6: Whole-rock major and trace element data for the peridotites in the Nahlin ophiolite. Plots show variations of MgO against major oxides (A) Al_2O_3, (B), CaO, and trace elements (C) Sc, (D) Ni, (E) V, and (F) Yb. All major elements in oxide wt % and all trace elements in ppm.

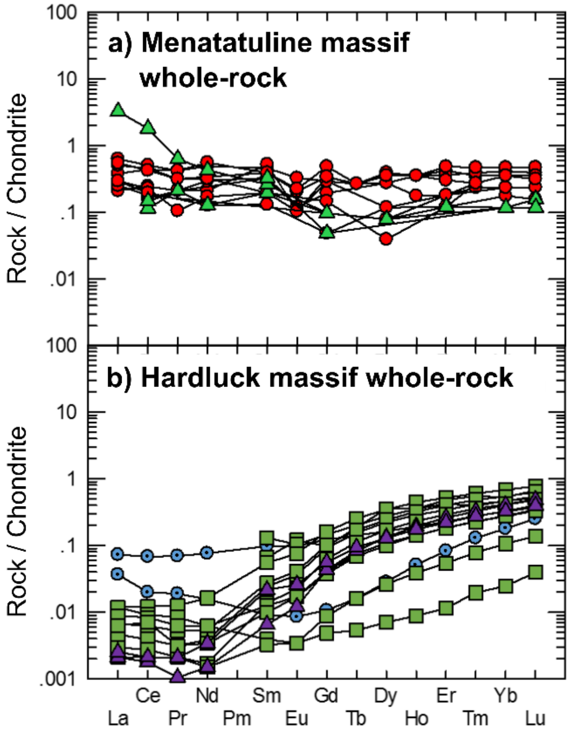

Figure 3.7: Whole-rock chondrite-normalized REE profiles for peridotites in the Nahlin ophiolite, as measured by ActLabs (A) and Laurentian University (B). Chondrite normalization values after Sun and McDonough (1989). (A) Data from this study show flat to "U-shaped" REE patterns in peridotite from the Menatatuline massif. (B) Data reported in Babechuk et al. (2010) show distinct LREE-depleted patterns in peridotite from "Moho Saddle", Peridotite Peak, and Peridotite Peak East (Hardluck massif). Symbology as for Figure 3.6.

Peridotite mineral chemistry

Olivine

Olivine cores range in composition from $Fo_{90.7}$ to $Fo_{92.0}$ within the Menatatuline massif, and from $Fo_{90.4}$ to $Fo_{91.5}$ within the Hardluck massif (Table A 6). In both massifs, olivine rims tend to have slightly higher Fo than olivine cores. Olivine forsterite content increases with spinel Cr# (Cr/(Cr + Al) atomic ratio) along the olivine-spinel mantle array (Arai 1994). Differences in olivine chemistry between the two massifs are most apparent in Cr, Ni, and Ca concentrations. Olivine cores from the Menatatuline massif contain up to 1300 ppm Cr, ~2500 - 3700 ppm Ni, and up to 800 ppm Ca. Rim compositions show lower Cr and Ca rims than cores. In the Hardluck massif, olivine core compositions yield up to 400 ppm Cr, ~4100 ppm Ni, and ~400 ppm Ca. Some olivine rim compositions from the Hardluck massif are significantly enriched in Cr (up to ~2000 ppm) relative to core compositions. Olivine from Peridotite Peak and Peridotite Peak East contains the lowest Ca concentrations among any samples analysed from the Nahlin ophiolite, and some peridotites from these peaks have slightly higher concentrations of Ca in olivine rims than in cores.

Spinel

Spinel from throughout the Nahlin ophiolite show slightly higher Mg# (Mg/(Mg + Fe^{2+}) atomic ratio) and lower Cr# and Y Cr (Cr/(Al + Cr + Fe^{3+})) in grain rims than in grain cores (Table A 7). Spinel from both massifs tend to have low concentrations of Ti in both cores and rims (generally <300 ppm). Ferric iron concentrations (expressed as Y Fe^{3+} and calculated as Fe^{3+}/(Al + Cr + Fe^{3+})) are also low (~0.02 to 0.05), and are generally distributed equally between the grain core and rim. Spinel from the Menatatuline massif has higher Cr# than spinel from the Hardluck massif, but the latter shows greater variation in spinel Cr# (cores ~20 to 65, rims ~16 to 65) than in the Menatatuline massif (cores Cr# ~45 to 59, rims ~44 to 56). In general, spinel from Peridotite Peak and Peridotite Peak East within the Hardluck massif are the least refractory, displaying the lowest average Cr# values. Throughout the Nahlin ophiolite, increases in spinel Cr# are accompanied by coupled increases in ortho- and clinopyroxene Cr numbers (Figure 3.8).

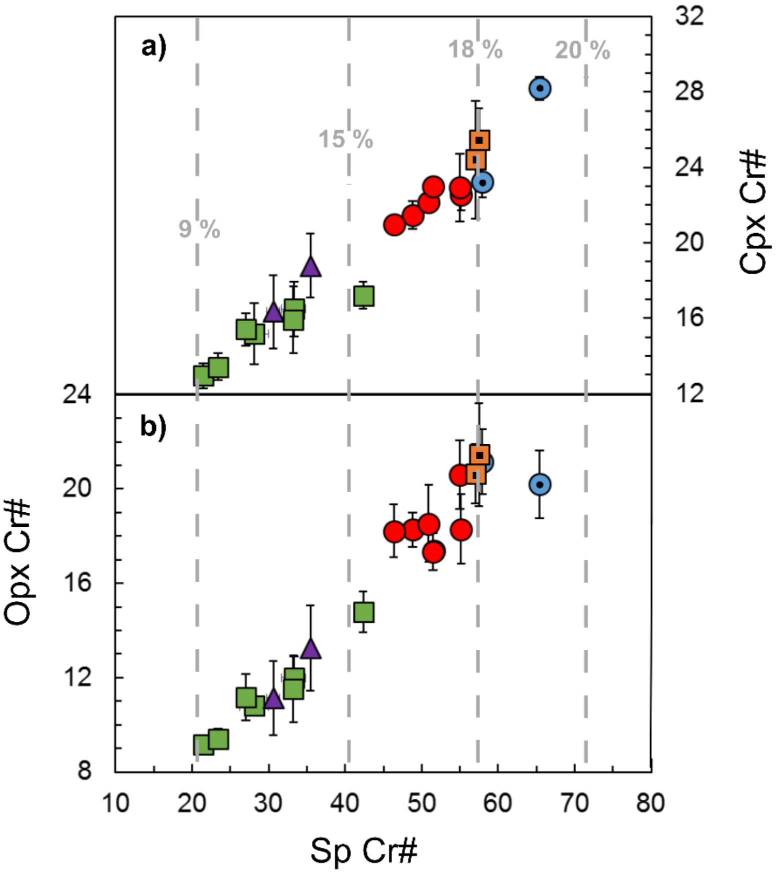

Figure 3.8: Variations in spinel, clinopyroxene (A), and orthopyroxene (B) Cr# throughout the Nahlin ophiolite. Error bars are one standard deviation based on average Cr# calculated from 2 – 10 analyses in a given sample. Grey dashed lines represent degree of spinel facies partial melting (F) as calculated by spinel Cr# (Warren 2016). Symbology as for Figure 3.6.

Orthopyroxene

Orthopyroxene Mg# (~ 90 to 91) and Al_2O_3 (~2-3 wt %) yield similar values for core and rim analyses in samples from both the Menatatuline and Hardluck massifs (Table A 8). In both massifs, orthopyroxene has higher CaO in the core than in the rim. Orthopyroxene from the Menatatuline massif have relatively high Ca concentrations (up to 3 wt % CaO), as do orthopyroxene from Hardluck Peaks and “Moho Saddle” in the Hardluck massif (up to 3 - 4 wt %). Peridotite Peak and Peridotite Peak East stand out among samples from the Hardluck massif for orthopyroxene cores with high Al concentrations (up to 3.5 wt %), and notably low Ca (0.6 to 0.9 wt %) and Cr# (9 to 14).

Differences in orthopyroxene chemistry between the Menatatuline and Hardluck massifs are most apparent in the trace element data (Table A 9). Hardluck massif samples contain orthopyroxene with higher Ti, Y, and REE concentrations than samples from the Menatatuline massif. The LREE and some MREE (La, Ce, Pr, Nd, Sm, and Eu) in orthopyroxene from both massifs are typically below detection limits (Figure 3.9c), whereas the HREE are in similar concentrations to those measured in whole-rock analyses (Figure 3.7). The HREE in orthopyroxene from the Menatatuline massif are up to one order of magnitude more depleted than those from the Hardluck massif. Rare earth element concentrations in orthopyroxene from both massifs are generally more depleted than orthopyroxene reported in other ophiolites (Figure 3.9d).

Clinopyroxene

Clinopyroxene chemistry best highlights the differences between the Menatatuline and Hardluck massifs with the former having lower Mg# and CaO content, and higher Cr# and Al_2O_3 content (Table A 10). Clinopyroxene from both massifs are generally weakly zoned, if at all. All clinopyroxene has similar or slightly higher Mg# and CaO (wt %), and similar to slightly lower Cr# and Al_2O_3 (wt %) in grain rims than in grain cores.

Similar to orthopyroxene, clinopyroxene from the Hardluck massif contains higher concentrations of Ti, Y and REE than samples from the Menatatuline massif (Table A 11). Most LREE and some MREE (La, Ce, Pr, Nd ± Sm) are below detection limits in clinopyroxene from the Hardluck massif, whereas clinopyroxene from the Menatatuline massif show enriched LREE (including La) that are above detection limits in some samples (Figure 3.9a). Clinopyroxene from the Menatatuline massif are more depleted than those from the Hardluck massif, and some samples from the former show elevated LREE similar to whole-rock data (Figure 3.7). As for orthopyroxene, REE concentrations in clinopyroxene from both massifs tend to be lower than in other ophiolites (Figure 3.9b). The coupled depletion of Ti and Dy, in particular, further highlights the more refractory nature of the peridotites from the Menatatuline massif (Figure 3.10).

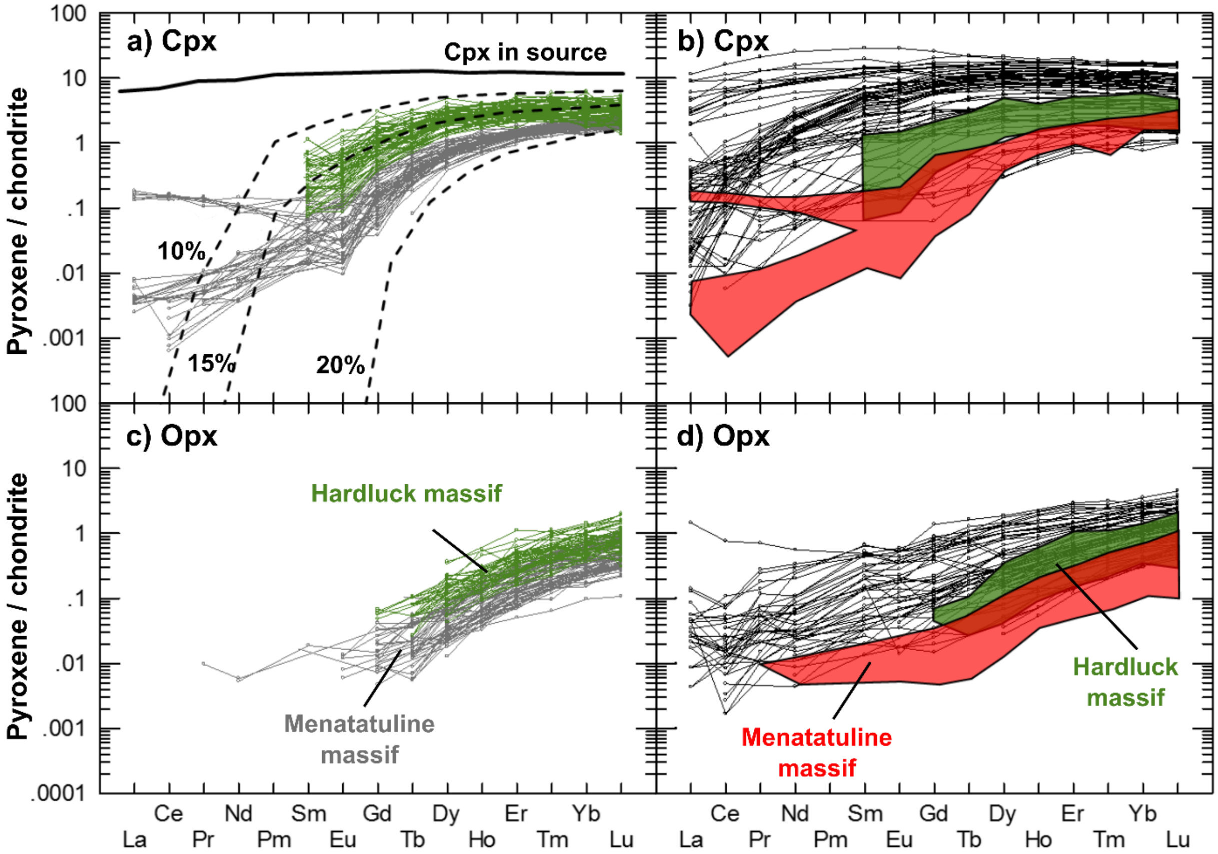

Figure 3.9: Chondrite-normalized pyroxene REE profiles compared to modeled clinopyroxene compositions (A) and to compiled REE data from other ophiolites worldwide (B and D). Measured REE concentrations in clinopyroxene (A) and orthopyroxene (C) for the Hardluck (green lines) and Menatatuline (grey lines) massifs. Dashed black lines in (A) reflect residual clinopyroxene compositions following 10, 15, and 20% spinel facies non-modal fractional partial melting. Source clinopyroxene composition shown by solid black line. All model parameters follow those of Warren (2016) and are described in the main text of this thesis. The range of REE concentrations measured in clinopyroxene (B) and orthopyroxene (D) in this study compared to pyroxene compositions reported in other ophiolites (thin black lines; Dygert and Liang 2015, and sources therein). Chondritic REE abundances after Sun and McDonough (1989).

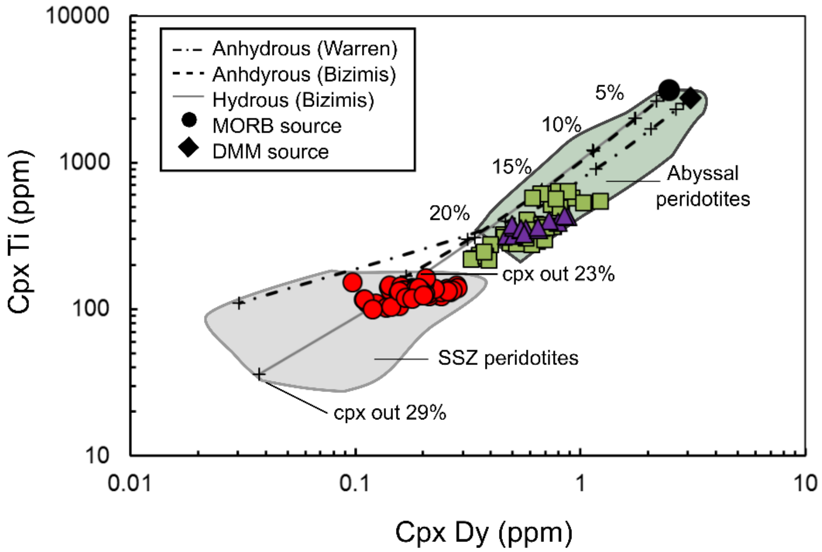

Figure 3.10: Modeled residual clinopyroxene Ti and Dy concentrations during anhydrous and hydrous partial melting. Anhydrous melting models of a DMM-source (Warren 2016) and a MORB-source (Bizimis et al. 2000). Model for hydrous melting of a MORB-source after Bizimis et al. (2000). In anhydrous models, clinopyroxene is consumed by ~23% melting, whereas it persists in the residue up to 29% melting in the hydrous melting model. Fields for clinopyroxene in abyssal (Johnson et al. 1990; Johnson and Dick 1992) and SSZ (Bizimis et al. 2000, and references therein) peridotites shown by the green and grey shaded areas, respectively. Clinopyroxene from the Menatatuline massif plots inside the SSZ peridotite field, whereas peridotites from the Hardluck massif fall largely within the abyssal peridotite field and require lower degrees of partial melting to reproduce clinopyroxene Ti and Dy concentrations. Symbology as for Figure 3.6.

Modal mineralogy

Modal mineralogy was calculated by mass balance, for 16 peridotite samples for which appropriate whole-rock and four phase mineral data had been acquired, using an algorithm for least-squares fitting of major element whole-rock and mineral chemical data (Albarede and Provost 1977). Calculated modes (Table 3-2) correlate with indicators of degree of melt depletion, such as whole-rock Al_2O_3 (Figure 3.11). There are moderate to strong correlations between modal olivine and whole-rock MgO and NiO, as well as between modal clinopyroxene and whole-rock REE concentrations.

Geothermometry

Closure temperatures for the peridotites of the Nahlin ophiolite are established using several geothermometers. Temperatures reported in Table 3-3 are the average and one standard deviation of ~2-10 calculated temperatures for mineral cores and rims using pairs of adjacent grains in each sample. Variations in pressure have only small effects on resulting temperatures (typically <0.2 to ~0.5 °C/GPa), and pressure is assumed to be 1 GPa. It should be noted that there are no consistent trends of closure temperature recorded in grain cores or rims by any of the geothermometers applied herein with increasing grain size (Figure A 1).

Table 3-2: Calculated modal mineralogy.

		Calculated modes			
Sample	Location	Opx	Cpx	Ol	Sp
DC0303	Moho Saddle	35	2	62	1
DC0304	Moho Saddle	16	1	80	2
DC0310	Peridotite Peak	19	8	71	2
DC0312	Peridotite Peak	22	8	68	2
DC0313	Peridotite Peak	29	6	64	1
DC0322	Peridotite Peak	5	5	89	2
DC0327	Peridotite Peak	22	7	70	1
DC0336	Peridotite Peak East	30	5	61	2
DC0345	Peridotite Peak East	15	5	79	2
15SM23B	Menatatuline	30	3	65	1
15SM38	Menatatuline	18	3	76	2
15SM45	Menatatuline	31	4	63	2
15SM55B	Menatatuline	20	2	75	2
15SM56	Menatatuline	19	5	73	1
15SM57	Menatatuline	30	2	66	1

Olivine – spinel geothermometry

The range of calculated closure temperatures varies with the calibrations of Fe-Mg exchange between olivine and spinel applied: the Ballhaus et al. (1991) calibration (T_{Ball}) yields core closure temperatures as low as ~630 °C for the Nahlin peridotites, the Jianping et al. (1995) version ($T_{Jianping}$) yields core closure temperatures in the range of ~820 – 960 °C, and the Fabries

(1979) method (T_{Fab}) produces core closure temperatures between those two (Table 3-3). Only the Jianping et al. (1995) calibration gives results that approach those from two pyroxene thermometry. In all calibrations, grain cores tend to preserve closure temperatures that are up to ~60 °C higher than in grain rims.

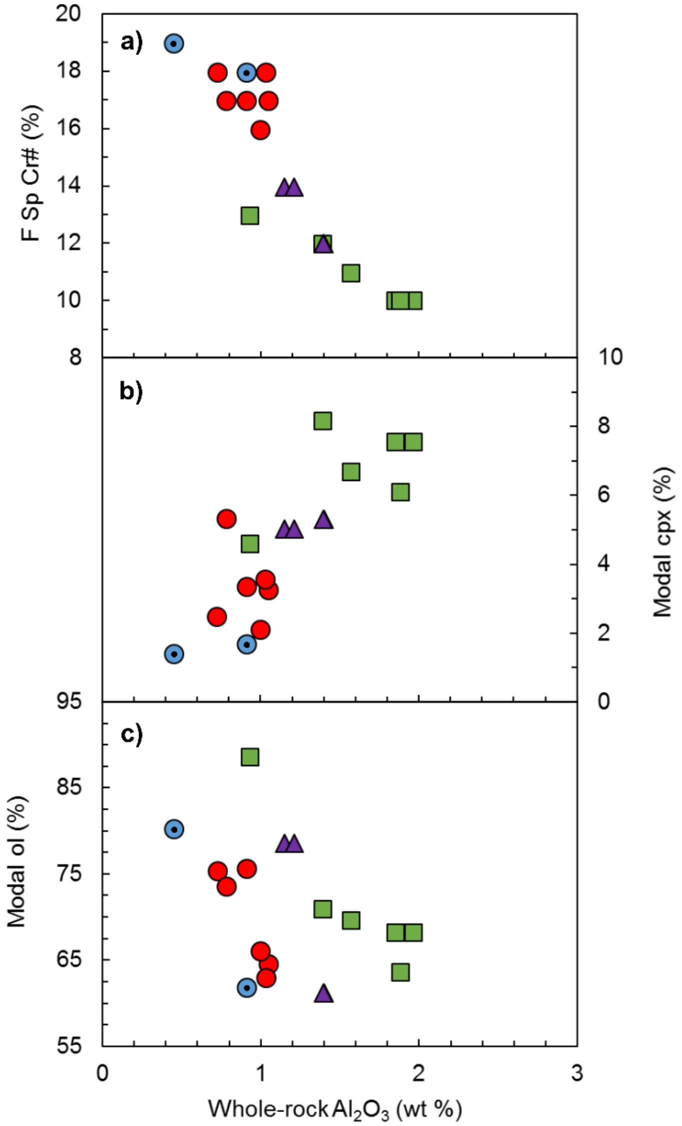

Figure 3.11: Correlations between whole-rock Al_2O_3 and (A) the degree of peridotite partial melting (F) estimated by spinel Cr# (see text for methodology), (B) modal clinopyroxene, and (C) modal olivine. Correlations show that the most refractory samples contain the lowest bulk-rock concentrations of Al_2O_3, the lowest proportions of clinopyroxene and the highest proportions of olivine. Symbology as for Figure 3.6.

Orthopyroxene – spinel geothermometry

The exchange of Fe^{2+} and Mg between orthopyroxene and spinel can be utilized in a geothermometer ($T_{Opx\text{-}Sp}$; Liermann and Ganguly 2003, 2007). Nahlin peridotites preserve core $T_{Opx\text{-}Sp}$ between 680 – 930 °C, similar to the range of closure temperatures calculated using the T_{Fab} olivine – spinel thermometer (Table 3-3). Samples from Peridotite Peak and Peridotite Peak East generally record higher temperatures in grain rims than cores, whereas elsewhere in the Hardluck massif samples tend to preserve higher temperature cores than rims. In the Menatatuline massif, the results are split: some samples preserve higher temperature cores and others hotter rims. Average closure temperatures recorded in grain cores in the Menatatuline and Hardluck massifs are 830 ± 42 °C and 800 ± 69 °C, respectively.

Two pyroxene geothermometry

The Brey and Köhler (1990) calibration of clinopyroxene – orthopyroxene cation exchange thermometers T_{BKN} and $T_{Ca\text{-}in\text{-}Opx}$ was selected for this study as it is applicable over a wide range of temperatures and mineral compositions. As with the olivine – spinel thermometry, pyroxene grains tend to preserve higher T_{BKN} and $T_{Ca\text{-}in\text{-}Opx}$ cores than rims by up to 170 °C in some cases (Table 3-3). Results from $T_{Ca\text{-}in\text{-}Opx}$ are generally higher in both grain cores and rims than T_{BKN} in a given sample (Figure 3.12 and 3.13). The Menatatuline massif has significantly hotter core and rim T_{BKN} and $T_{Ca\text{-}in\text{-}Opx}$ than the Hardluck massif. Core closure temperatures in the Hardluck massif range from 730 – 960 °C (T_{BKN}) and from 840 – 1250 °C ($T_{Ca\text{-}in\text{-}Opx}$), whereas the Menatatuline massif samples record core closure temperatures varying from 870 – 1190 °C and 960 – 1290 °C for T_{BKN} and $T_{Ca\text{-}in\text{-}Opx}$, respectively. Within the Hardluck massif, samples from “Moho Saddle” and near Hardluck Peaks yield notably high $T_{Ca\text{-}in\text{-}Opx}$ compared to samples along strike near Peridotite Peak (core average 1210 ± 102 °C vs 950 ± 57 °C).

The REE-in-two-pyroxene thermometer by Liang et al. (2013) is applied to the peridotites to compare with the thermal history provided by major element thermometry. This thermometer examines the temperature dependence of the partition of the REE and Y between coexisting pyroxenes fitted by a least-squares inversion. As REE and Y data were only acquired in grain cores, all the T_{REE} results in this study represent core closure temperatures. Results of the T_{REE} thermometer differ from those of the major element-based geothermometers applied in this study in that harzburgite from the Menatatuline massif preserves core closure temperatures between 850 – 1200 °C (Figure 3.13), similar to those of the Hardluck massif (860 – 1090 °C). The highest temperatures in the Nahlin ophiolite are preserved in samples from the Menatatuline massif, in agreement with the results of the two pyroxene thermometers of Brey and Köhler (1990).

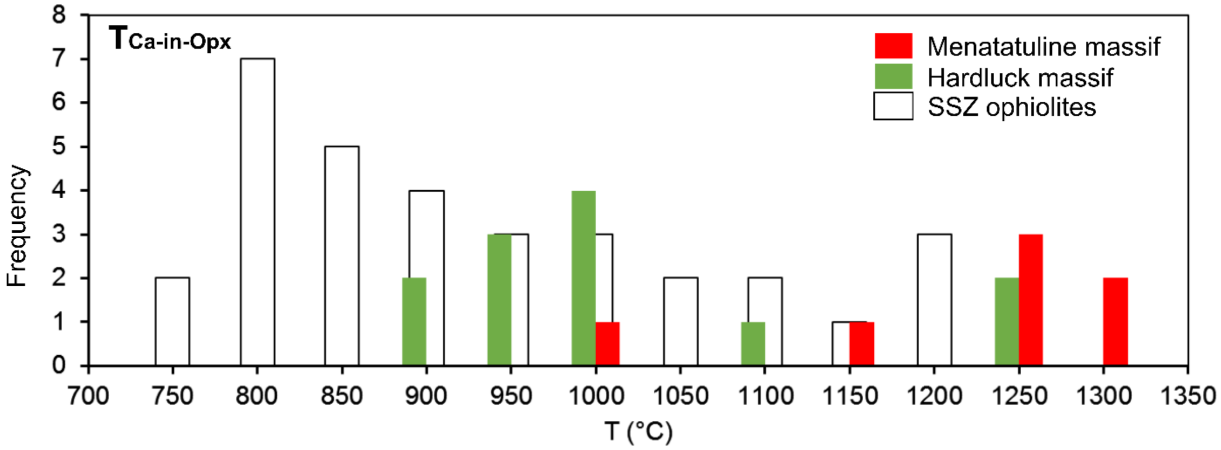

Figure 3.12: Histogram of two pyroxene thermometry results for grain cores in the Hardluck massif (green), Menatatuline massif (red) and compiled to supra-subduction zone (SSZ) ophiolites worldwide (white). The Menatatuline massif appears to be uncommonly hot compared to other SSZ ophiolites. Histograms showing data from this study are constructed from average core closure temperature recorded in each sample within a given massif. Compiled T Ca-in-Opx data for other SSZ ophiolites from Pomonis et al. (2006), Choi et al. (2008), Batanova et al. (2011), Pirard et al. (2013), and Stewart et al. (2016).

Table 3-3: Geothermometry results for peridotites from the Nahlin ophiolite (σ = one standard deviation, n.d. indicates no data). All results in °C.

Sample	Location		T_{Ball}	σ	T_{Fab}	σ	$T_{Jianping}$	σ	$T_{Opx\ -\ Sp}$	σ
DC0205	Hardluck Peaks	core	742	14	832	14	943	16	860	10
		rim	678	20	772	20	871	24	805	27
DC0206	Hardluck Peaks	core	711	16	801	15	910	18	846	11
		rim	662	26	752	27	850	33	815	23
DC0303	Moho Saddle	core	752	11	838	10	956	11	899	10
		rim	725	16	810	14	922	18	896	14
DC0304	Moho Saddle	core	722	3	811	2	906	5	813	18
		rim	702	5	792	5	879	3	805	7
DC0310	Peridotite Peak	core	648	5	750	7	837	8	n.d.	n.d.
		rim	n.d.	n.d.	n.d.	n.d.	n.d.	n.d.	n.d.	n.d.
DC0312	Peridotite Peak	core	646	n.d.	745	n.d.	841	n.d.	n.d.	n.d.
		rim	634	n.d.	732	n.d.	825	n.d.	n.d.	n.d.
DC0313	Peridotite Peak	core	656	5	760	5	860	4	738	18
		rim	638	38	734	42	833	55	788	31
DC0318	Peridotite Peak	core	681	n.d.	784	n.d.	883	n.d.	734	13
		rim	656	n.d.	754	n.d.	844	n.d.	755	22
DC0322	Peridotite Peak	core	687	n.d.	787	n.d.	891	n.d.	737	28
		rim	648	n.d.	745	n.d.	841	n.d.	763	40
DC0327	Peridotite Peak	core	645	10	748	11	849	12	737	10
		rim	625	20	720	21	818	29	760	18
DC0334	Peridotite Peak	core	683	21	780	18	879	23	793	27
		rim	661	28	756	30	854	40	781	28
DC0336	Peridotite Peak East	core	647	11	748	12	842	12	755	24
		rim	629	6	725	7	814	8	745	4
DC0345	Peridotite Peak East	core	627	9	724	10	817	12	712	15
		rim	633	5	730	5	823	6	729	11
15SM23A	Menatatuline	core	n.d.	n.d.	n.d.	n.d.	n.d.	n.d.	n.d.	n.d.
		rim	n.d.	n.d.	n.d.	n.d.	n.d.	n.d.	n.d.	n.d.
15SM23B	Menatatuline	core	753	29	845	26	959	32	892	45
		rim	768	41	855	39	970	48	910	48
15SM34-2	Menatatuline	core	718	15	811	12	916	18	n.d.	n.d.
		rim	733	7	823	6	932	8	n.d.	n.d.
15SM38	Menatatuline	core	699	46	791	44	896	53	777	2
		rim	700	27	790	24	895	30	721	10
15SM45	Menatatuline	core	721	28	811	27	907	34	839	21
		rim	675	16	762	16	849	21	829	19
15SM55B	Menatatuline	core	722	35	811	31	922	38	838	45
		rim	682	53	773	50	870	67	864	21
15SM56	Menatatuline	core	743	14	835	12	942	15	838	3
		rim	695	10	785	9	881	11	812	10
15SM57	Menatatuline	core	725	9	820	9	932	11	849	5
		rim	718	17	813	18	921	20	853	2

Table 3-3 (continued): Geothermometry results for peridotites from the Nahlin ophiolite (σ = one standard deviation, n.d. indicates no data). All results in °C.

Sample	Location		T_{BKN}	σ	$T_{Ca\ in\ Opx}$	σ	T_{REE}	σ
DC0205	Hardluck Peaks	core	811	78	1229	15	n.d.	n.d.
		rim	n.d.	n.d.	n.d.	n.d.	n.d.	n.d.
DC0206	Hardluck Peaks	core	n.d.	n.d.	n.d.	n.d.	n.d.	n.d.
		rim	n.d.	n.d.	n.d.	n.d.	n.d.	n.d.
DC0303	Moho Saddle	core	960	61	1249	109	n.d.	n.d.
		rim	n.d.	n.d.	n.d.	n.d.	n.d.	n.d.
DC0304	Moho Saddle	core	902	14	1053	8	n.d.	n.d.
		rim	823	4	1028	2	n.d.	n.d.
DC0310	Peridotite Peak	core	827	29	935	24	933	36
		rim	804	38	819	36	n.d.	n.d.
DC0312	Peridotite Peak	core	823	1	985	21	942	48
		rim	805	1	899	9	n.d.	n.d.
DC0313	Peridotite Peak	core	845	25	987	13	1063	11
		rim	834	70	832	10	n.d.	n.d.
DC0318	Peridotite Peak	core	923	0	893	0	1005	23
		rim	754	0	917	0	n.d.	n.d.
DC0322	Peridotite Peak	core	935	0	968	0	1094	66
		rim	790	0	934	0	n.d.	n.d.
DC0327	Peridotite Peak	core	807	40	986	51	1036	13
		rim	781	50	895	58	n.d.	n.d.
DC0334	Peridotite Peak	core	798	36	944	31	931	29
		rim	757	19	909	45	n.d.	n.d.
DC0336	Peridotite Peak East	core	727	92	894	62	1080	32
		rim	752	27	834	21	n.d.	n.d.
DC0345	Peridotite Peak East	core	820	51	911	43	857	32
		rim	804	88	878	20	n.d.	n.d.
15SM23A	Menatatuline	core	1187	15	1287	51	847	34
		rim	1089	7	1325	17	n.d.	n.d.
15SM23B	Menatatuline	core	1117	43	1270	43	871	40
		rim	1070	31	1155	22	n.d.	n.d.
15SM34-2	Menatatuline	core	n.d.	n.d.	n.d.	n.d.	n.d.	n.d.
		rim	n.d.	n.d.	n.d.	n.d.	n.d.	n.d.
15SM38	Menatatuline	core	1114	69	1243	48	1202	77
		rim	999	19	1126	59	n.d.	n.d.
15SM45	Menatatuline	core	872	67	956	56	931	47
		rim	845	36	968	40	n.d.	n.d.
15SM55B	Menatatuline	core	935	68	1229	73	943	40
		rim	1012	42	1231	66	n.d.	n.d.
15SM56	Menatatuline	core	1023	51	1115	83	1029	19
		rim	955	48	1024	48	n.d.	n.d.
15SM57	Menatatuline	core	1050	23	1249	59	1144	71
		rim	1059	7	1175	48	n.d.	n.d.

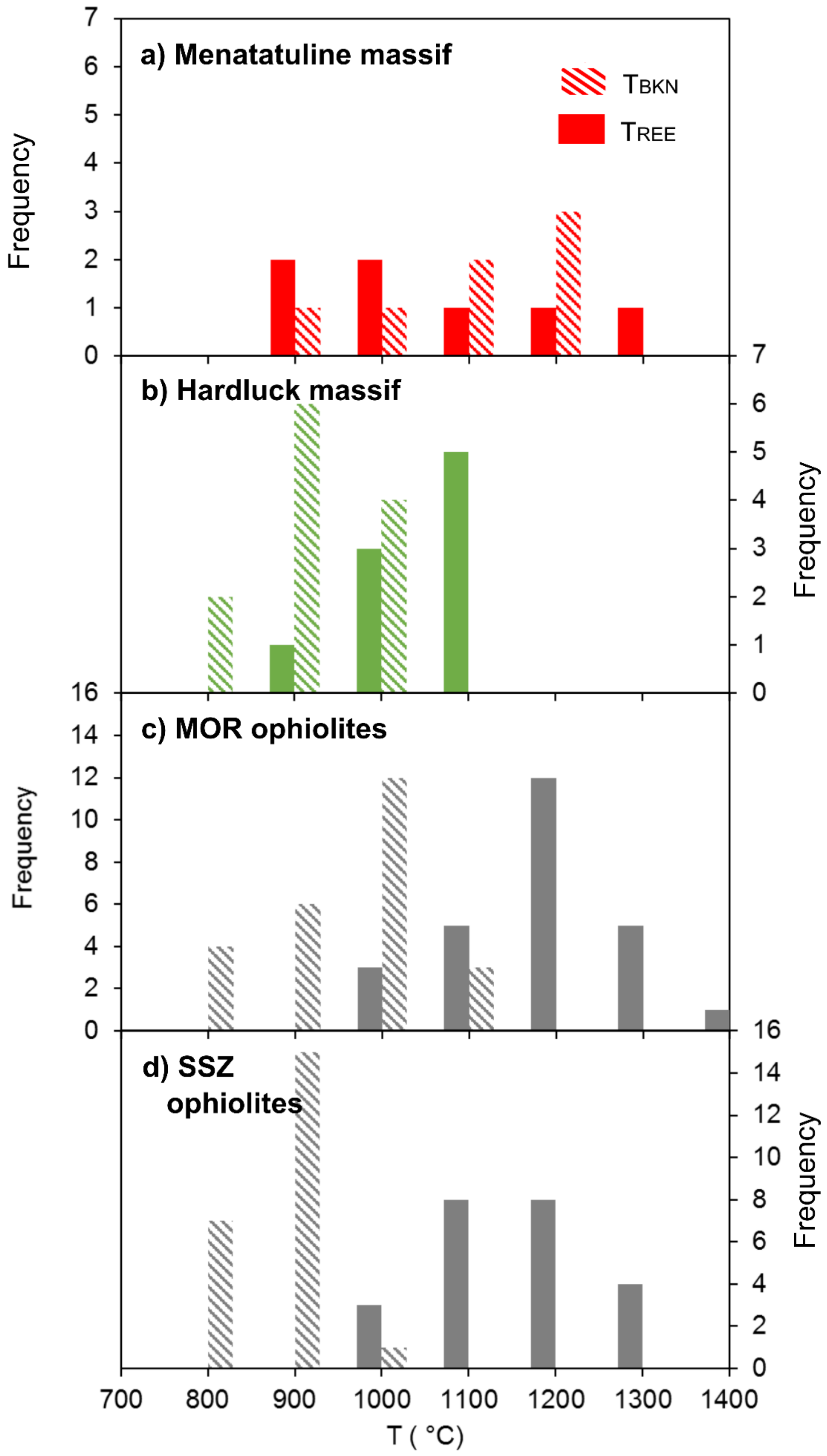
a) Menatatuline massif
TBKN
TREE
b) Hardluck massif
c) MOR ophiolites
d) SSZ ophiolites
Frequency
0
1
2
3
4
5
6
7
0
2
4
6
8
10
12
14
16
700
800
900
1000
1100
1200
1300
1400
T (°C)

Figure 3.13: Histograms of two pyroxene thermometry results from grain cores in the Nahlin ophiolite, compared to mid-ocean ridge (MOR) and supra-subduction zone (SSZ) ophiolites worldwide. (A) Distribution of core T_{BKN} (diagonal lines) and T_{REE} (solid colour) results from the Menatatuline massif. Menatatuline massif samples display temperature distributions unlike those calculated for any other MOR or SSZ-type ophiolite: T_{BKN} temperatures are unusually hot, and some T_{REE} results are anomalously cool. (B) Hardluck massif T_{BKN} and T_{REE} results are similar to compiled SSZ ophiolites. (C) Compiled thermometry results from MOR and (D) SSZ ophiolites. Histograms showing data from this study are constructed from average closure temperature recorded in each sample within a given massif. Results of T_{BKN} and T_{REE} thermometers for MOR and SSZ ophiolites (panels C and D) from Dygert and Liang (2015) and sources therein.

Redox conditions in the Nahlin peridotite

Oxygen fugacity (fO_2) is calculated following the method of Ballhaus et al. (1990), and results are presented in terms of deviation from the fayalite – quartz – magnetite (QFM) buffer in log units. To constrain subsolidus changes in fO_2, the oxygen fugacity is calculated using mineral chemical data and T_{Ball} temperatures from both grain cores and rims. All the peridotites from the Nahlin ophiolite record fO_2 within one log unit of the QFM buffer (Figure 3.14), similar to the range of fO_2 recorded in some abyssal and forearc peridotites (Ballhaus 1993; Parkinson and Pearce 1998). Based primarily on variations in spinel Cr# rather than fO_2, peridotite from the Menatatuline massif and samples from “Moho Saddle” and Hardluck Peaks plot largely within fields for Mariana forearc harzburgites and other forearc peridotites (Figure 3.14). Samples from Peridotite Peak and Peridotite Peak East are less refractory than samples from elsewhere in the Nahlin ophiolite. Some plot within the abyssal peridotite field, whereas others are displaced to higher fO_2 values for a given spinel Cr#.

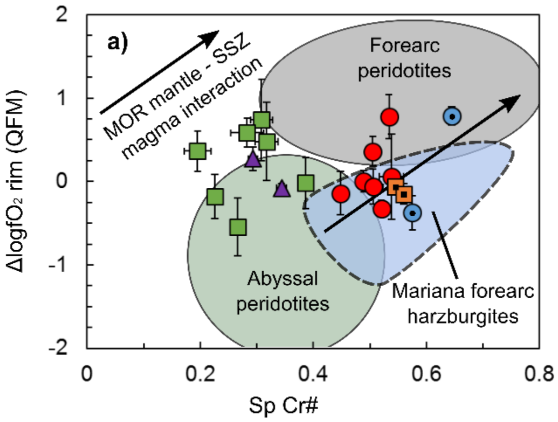

Figure 3.14: Plot of oxygen fugacity against spinel Cr# (rim) recorded in the peridotites from the Nahlin ophiolite. Oxygen fugacity, expressed as the deviation from the QFM buffer in log units ($\Delta \log f O_2$ QFM), calculated following the method of Ballhaus et al. (1990) using major element data measured in grain rims. Green, grey, and blue shaded areas show the approximate fields for abyssal and forearc peridotites, and Mariana forearc harzburgites (Parkinson and Pearce 1998). Arrows show the expected trend in increasing Cr# and $f O_2$ as mantle peridotite interacts with SSZ-type magmas (Arai 1994; Gaetani and Grove 1998; Parkinson and Pearce 1998). All data points symbolized as for Figure 3.6.

3.7 Discussion

Extent of melt depletion

The low abundances of incompatible elements in ophiolite peridotites predominantly reflect depletion by partial melting (Dick et al. 1984; Johnson et al. 1990; Niu 1997; Niu and Hékinian 1997). Rare earth element concentrations in relict clinopyroxene are known to record the degree of melt depletion (F) in oceanic lithospheric mantle (Johnson et al. 1990; Johnson and Dick 1992). To examine the degree of melting in the Nahlin peridotites, I used the melting model of Warren (2016). In this model, a source of depleted MORB mantle (DMM) composition (Workman and Hart 2005) undergoes non-modal fractional melting in the spinel stability field according to the melting reaction 0.56 Opx + 0.72 Cpx + 0.04 Sp = 0.34 Ol + 1.0 Melt (Wasylenki et al. 2003). Melt-mineral REE partition coefficients are after Sun and Liang (2014) and Warren (2016), and are calculated assuming a mantle of DMM composition at a potential temperature of 1300 °C. Unlike some studies of mantle melting, the use of a LREE-depleted lherzolite (e.g., Johnson et al. 1990) or one of several estimates of primitive upper mantle (PUM) (Hart and Zindler 1986; McDonough and Sun 1995; Lyubetskaya and Korenaga 2007) as a source composition herein was deemed to be too enriched, and was eschewed in favour of a more depleted source. A DMM source, considered to be more representative of the depleted upper mantle, is used in this study for ease of comparison with more recent studies (Salters and Stracke 2004; Workman and Hart 2005; Bezard et al. 2015; Marchesi et al. 2016; Warren 2016). The highly incompatible LREE are more susceptible to enrichment by secondary processes (see discussion on metasomatism to follow), and in many samples are below detection limits in clinopyroxene (Figure 3.9). Consequently, only the MREE to HREE in clinopyroxene are used in this study to constrain the degree of melt depletion.

The MREE to HREE contents in clinopyroxene from the Menatatuline massif can be reproduced by 16 to 20% fractional melting (Figure 3.9), whereas those in the Hardluck massif indicate a lower degree of melting (F = 10 to 16%). These estimates are ~3 – 5% lower for both massifs than the degree of melting estimated by Ti and Dy in clinopyroxene (Figure 3.10). In the latter, Ti and Dy concentrations in Nahlin peridotites are compared to models for anhydrous (Bizimis et al. 2000; Warren 2016) and hydrous (Bizimis et al. 2000) melting of a MORB (Bizimis et al. 2000) and DMM (Warren 2016) source in the spinel stability field. Clinopyroxene in the Menatatuline massif are best approximated by the hydrous melting model of Bizimis et al. (2000), whereas the model of Warren (2016) overestimates Ti concentrations. Titanium and Dy concentrations in clinopyroxene from the Hardluck massif are reasonably reproduced by anhydrous and hydrous models of both authors.

Models of partial melting using REE concentrations in clinopyroxene indicate that the peridotites are best reproduced by 10 to 20% spinel facies non-modal fractional melting.

Peridotite in the Menatatuline massif is more refractory than peridotite from the Hardluck massif, as shown by more depleted clinopyroxene REE profiles (Figure 3.9). These REE concentrations measured do not necessarily reflect pyroxene composition at the time of melting. During subsolidus re-equilibration, REE are redistributed and preferentially partitioned into clinopyroxene (Sun and Liang 2014). Measured HREE concentrations in clinopyroxene re-equilibrated at low temperatures (e.g., 800 °C) may be up to 3 times higher than at solidus temperatures (~1300 °C, Sun and Liang 2014). Bearing this in mind, melt estimates based on clinopyroxene REE data presented herein are minima.

Nonetheless, the refractory nature of the peridotite whole-rock and mineral chemistry agree with the estimated degree of melt depletion in the Nahlin ophiolite. Low whole-rock Al_2O_3 (<2 wt %) and high MgO (~ 45 wt %) imply that the Nahlin peridotites have been strongly depleted by melt extraction. Furthermore, correlations between modal mineralogy and melt fraction in the Nahlin peridotites match those predicted by melting equations (e.g., Dick et al. 1984; Kinzler and Grove 1992a; Baker and Stolper 1994): modal clinopyroxene decreases as it is consumed during partial melting. The coupled increases in pyroxene and spinel Cr numbers (Figure 3.8) are further evidence of the melt depleted nature of the mantle peridotite preserved in both massifs.

Spinel chemistry can be used to corroborate partial melting estimates from clinopyroxene REE modeling, using an empirical relationship between spinel Cr# and F calibrated by Hellebrand et al. (2001) and revised by Warren (2016). Like trace elements in clinopyroxene, spinel Cr# is susceptible to modification by melt-rock interaction. Evidence of this metasomatism in other mantle peridotites, typically near dunite channels, includes a wide range of spinel Cr# on scales where such dramatic differences in degree of depletion are unrealistic

(Suhr et al. 2003; Morgan et al. 2008). Spinel chemistry within the Nahlin ophiolite, however, is consistent among several analyses in a given sample. Furthermore, samples within a relatively large geographic area define a consistent range of spinel Cr#: 21 – 35 (Peridotite Peak and Peridotite Peak East), 46 – 55 (Menatatuline massif), and 57 – 65 ("Moho Saddle" and Hardluck Peaks). Hence, these compositions are interpreted as representative and relatively unaffected by secondary processes.

The empirical equation of Hellebrand et al. (2001), modified by Warren (2016), is used to calculate the degree of melting (F) using measured spinel Cr# in the peridotites. Harzburgites from the Menatatuline massif record 16 to 18% melting (Figure 3.8). Within the Hardluck massif, Peridotite Peak and Peridotite Peak East record lower degrees of melting (9 to 15%), whereas samples from "Moho Saddle" and Hardluck Peaks have significantly more refractory compositions indicating 18 to 19% melting. These estimates for the Menatatuline massif and for samples from Peridotite Peak and Peridotite Peak East agree with estimates from clinopyroxene REE modeling (Figure 3.9).

The agreement between different methods of estimating F suggests that the spinel harzburgites of the Nahlin ophiolite preserve a signature of mantle depletion by partial melting. This signature has, nevertheless, been locally modified by subsequent melt-rock interaction. This is evident from the enrichment of LREE in whole-rock chemistry (Figure 3.7) and in clinopyroxene from the Menatatuline massif compared to modeled clinopyroxene compositions in residues of 10 – 20% melting (Figure 3.9), and will be further discussed below. Consequently, samples with higher concentrations of all the REE, such as those from Peridotite Peak, may reflect lower degrees of melting, or high degrees of melting overprinted by refertilization. Peridotite samples with low REE concentrations, on the other hand, may be the result of high degrees of melting and/or melting of a more depleted source than modeled herein. Additionally, differences in REE abundance between massifs in the Nahlin ophiolite, and hence differences in estimated degree of melting, may reflect pre-existing compositional heterogeneities.

Thermal history of the Nahlin ophiolite

By every geothermometer applied in this study, grain cores in the Nahlin peridotite generally preserve higher temperatures than grain rims. This pattern is consistent with cooling from a minimum initial temperature near the solidus during melt depletion (>1200 °C), to lower temperatures in the lithosphere. Olivine-spinel thermometers tend to record the lowest temperature history, as Fe-Mg diffusion between these phases is relatively rapid (Fabries 1979), whereas cation exchange involved in two-pyroxene thermometry proceeds more slowly and will record higher temperatures, depending on cooling rate (Ozawa 1983; Cherniak and Dimanov 2010). Nonetheless, because each geothermometer has a typical range of closure temperatures, I can compare results of several geothermometers to reconstruct the high temperature history of the Nahlin ophiolite. As the lowest temperatures recorded in this study (~600 °C) would only be found in lithospheric mantle located far off-axis of an active spreading centre (Forsyth 1977; Cuffaro and Miglio 2012), this cooling is likely not limited to conductive cooling of the lithosphere but also includes obduction related heat loss. Discrimination between these mechanisms of cooling, and determining the timing of obduction relative to the thermal history discussed herein is beyond the scope of this study.

The Menatatuline massif records higher temperatures than samples from the Hardluck massif by all major element thermometers in this study, and significantly higher T_{BKN} and $T_{Ca\text{-}in\text{-}Opx}$ than reported for any other ophiolite (Figure 3.13). Although the T_{REE} results in ophiolites and abyssal peridotites are typically hundreds of degrees above closure temperatures of T_{BKN} and $T_{Ca\text{-}in\text{-}Opx}$ and near mantle solidus temperatures (Dygert and Liang 2015; Marchesi et al. 2016), the Nahlin peridotite yields some unusually cool temperatures. For example, in the Menatatuline massif, T_{REE} are typically within error of T_{BKN} (Figure 3.13).

Peridotite melting experiments at ~1 GPa suggest that melting temperatures of 1240 to 1300 °C are required for depletion by 10 – 20% anhydrous melting in mantle residues such as observed in the Hardluck and Menatatuline massifs (Baker and Stolper 1994; Robinson et al. 1998; Wasylenki et al. 2003). If so, the T_{BKN} values in the Hardluck massif show it has cooled more than 300 °C below the lowest estimate of the dry peridotite solidus. In contrast, some samples from the Menatatuline massif record T_{BKN} within 125 °C of the solidus, whereas others have cooled by over 350 °C. Some samples collected within 20 m of one another in the Menatatuline massif display variations of more than 100 °C. Both $T_{Ca\text{-}in\text{-}Opx}$ and T_{REE} show a similar distribution: the Hardluck massif has cooled substantially from the solidus, and the Menatatuline massif displays significant variations in temperature within a relatively small area (~12 km^2).

Variations in closure temperature of any geothermometer can commonly be related to variable grain size and/or cooling rate (Dodson 1973). Although the peridotites in both massifs preserve a range in grain sizes, closure temperatures do not appear to vary with grain size in any regular or predictable manner (Figure A 1). Chemical zonation implied by variations between core and rim major element compositions and resulting generally hotter core than rim closure temperatures are consistent with a cooling history. However, as no major or trace element grain rim-to-rim profiles where measured in this study, I cannot confidently quantify cooling rate or its effect on chemical zoning.

In other studies, variable cooling rates within the lithosphere have been proposed to explain spatially-variable closure temperatures recorded by peridotites. In the Oman ophiolite, for example, significant inter-sample variability in closure temperatures has been explained by the insulation effect of variable depth beneath the Moho (Hanghøj et al. 2010). Shallower peridotite near the Moho in that study is interpreted to have cooled more rapidly, resulting in the preservation of higher closure temperatures (Hanghøj et al. 2010). Other factors proposed to locally accelerate the cooling rate of mantle peridotite include hydrothermal circulation, lack of overlying crust, for example by peridotite unroofed in an oceanic core complex, and faulting (Hanghøj et al. 2010; Dygert and Liang 2015).

Within the Hardluck massif, there is a consistent spatial trend amongst major element thermometers (T_{Ball}, T_{BKN}, $T_{Ca\text{-}in\text{-}Opx}$, and $T_{Opx\text{-}Sp}$) of increasing core closure temperature to the northwest (Figure 3.15). If higher closure temperatures indicate more rapid cooling, then it follows that peridotite to the west near “Moho Saddle” and Hardluck Peaks represents the uppermost mantle, at the top of the melting column where cooling rates are theoretically most rapid (Hanghøj et al. 2010). Indeed, samples in the study collected at “Moho Saddle” are within 500 m of the crust-mantle transition observed in outcrop (Mihalynuk et al. 2004b). Along strike to the southeast in the Hardluck massif, Peridotite Peak and Peridotite Peak East could therefore represent deeper lithospheric mantle that cooled more slowly. These hypotheses assume a constant cooling rate, and account for obduction-related cooling.

In the Menatatuline massif, by contrast, there appears to be no consistent correlation of cooling rate or closure temperature of any thermometer with proximity to known faults, contacts with supracrustal rocks, dikes, or elevation. Therefore, the range in closure temperatures that may indicate large variations in cooling rate for Menatatuline massif samples in such a small area appear geologically unrealistic. Furthermore, there are no systematic correlations of grain size and closure temperature by any of the geothermometers applied to the Menatatuline massif samples. Hence, the apparent variation in closure temperature within the Menatatuline massif may be an artifact of secondary processes (i.e., metasomatism).

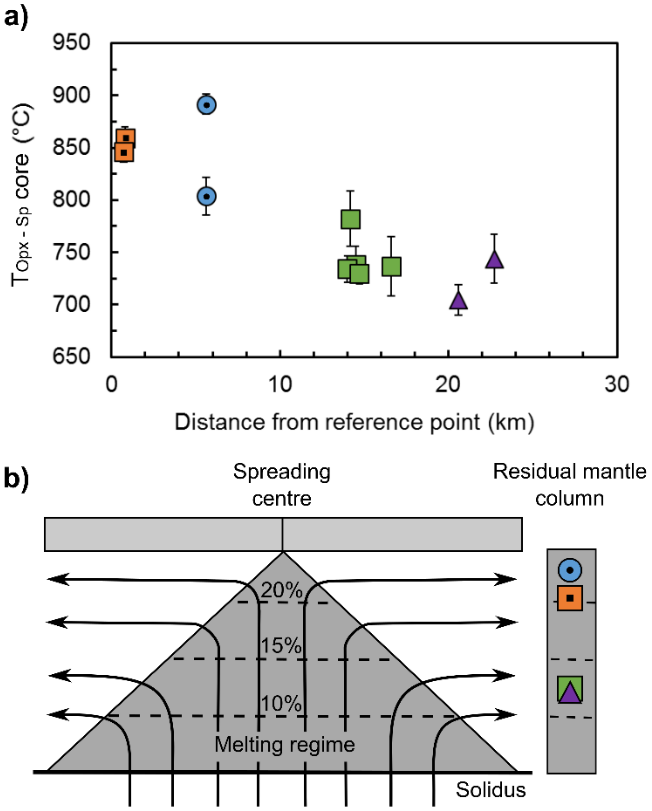

Figure 3.15: (A) Spatial variations in closure temperature within the Hardluck massif recorded by the orthopyroxene - spinel thermometry (Liermann and Ganguly 2003, 2007). Distance along the x-axis is measured in km from a reference point located ~1 km NNW of Hardluck Peaks. Symbols represent the average temperature calculated for a given sample. Error bars represent one standard deviation. (B) Schematic spreading centre showing interpreted stratigraphy within the Hardluck massif based on spatial trend of thermometry results. Samples from Peridotite Peak and Peridotite Peak East are less depleted (Figure 3.8) and record lower temperatures, indicative of slower cooling at a deeper level within the residual mantle column. Diagram modified after Langmuir et al. (1992). Symbology as for Figure 3.6.

Melt-peridotite interaction and metasomatism

The covariation of whole-rock Al_2O_3, CaO, and many trace elements with increasing MgO indicates a range in degree of depletion both within and between massifs of the Nahlin ophiolite (Figure 3.6). Despite this, there is little variability in clinopyroxene trace element chemistry (particularly HREE) within each massif. Comparing HREE abundances in whole-rock and clinopyroxene in terms of Yb_N (chondrite normalized Yb) highlights the consistency between samples in the Menatatuline massif, in particular (Figure 3.16). There appears to be a decoupling of mineral and whole-rock chemistry, as there is virtually no change in clinopyroxene Yb_N (~2) over a range of whole-rock Yb_N. (~0.1 – 0.5). As the whole-rock Yb data were acquired at two different laboratories, this may be an artifact of inter-laboratory data quality, however all the measured Yb in the Menatatuline samples are at least twice the reported detection limit. The consistent abundance of Yb_N and the enrichment in LREE over predictions of melting models (Figure 3.9) in clinopyroxene from some samples in the Menatatuline massif may reflect local equilibrium with infiltrating melt (Liang et al. 2013). Alternatively, perhaps some of these clinopyroxenes have experienced subsolidus re-equilibration, which would result in significant increases in clinopyroxene HREE, at the expense of orthopyroxene, without altering bulk-rock HREE abundances (Sun and Liang 2014).

In residues of simple progressive depletion by partial melting, indicators of depletion such as REE abundances should be consistent between whole-rock and mineral chemistry (Rampone et al. 2004). Moreover, in mantle residues with a history of simple partial melting, olivine Mg# and modal abundance are expected to be positively correlated (Baker and Stolper 1994; Baker and Beckett 1999). Peridotites in the Nahlin ophiolite, however, display very little change in olivine composition even with increasing proportions of olivine (Figure 3.16). The geochemistry and modal mineralogy of some peridotites in the Nahlin ophiolite therefore cannot be reconciled by partial melting alone, but require post-melting modification by secondary processes.

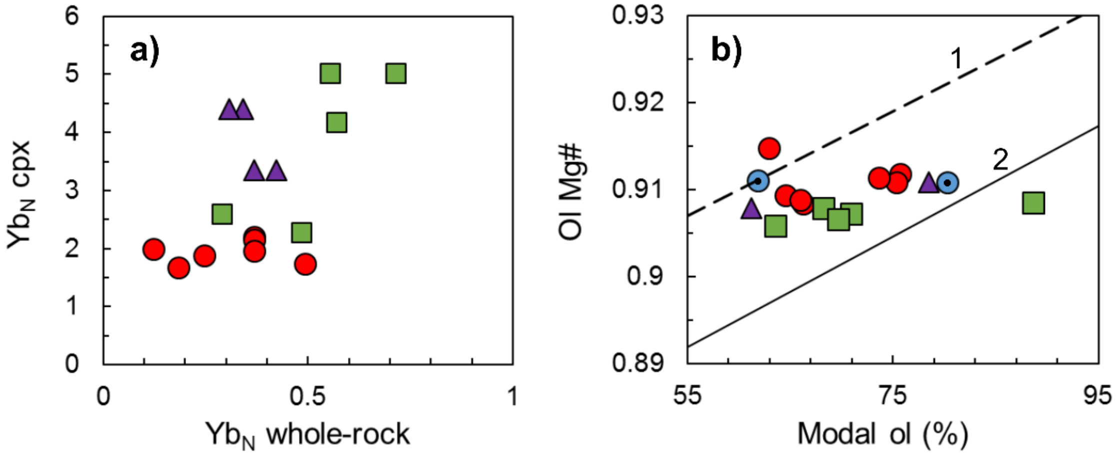

Figure 3.16: Chemical evidence for secondary processes in the Nahlin peridotites. (A) Chondrite-normalized Yb in clinopyroxene against whole-rock Yb shows a trend among samples from the Hardluck massif. In contrast, there is little to no variation in clinopyroxene Yb with whole-rock Yb in samples from the Menatatuline massif. Data from the Hardluck massif were acquired at Laurentian University (Babechuk et al. 2010) whereas data from the Menatatuline massif were acquired at ActLabs. (B) Olivine Mg# (Mg/(Mg + Fe)) against calculated modal olivine (volume %) showing the lack of correlation in the Nahlin peridotite data compared to expected trends for residues of simple partial melting in experimental data (1 - Baker and Stolper 1994) and abyssal peridotite data (2 - Baker and Beckett 1999). Symbology as for Figure 3.6.

The precipitation of secondary pyroxene during melt-rock interaction is commonly invoked in oceanic mantle lithosphere (Seyler et al. 2007; Warren and Shimizu 2010). Refertilization of depleted harzburgite by reactive porous flow of an infiltrating olivine-saturated basaltic melt dissolving pyroxene and precipitating olivine has been well documented in mantle peridotite elsewhere (Kelemen et al. 1992, 1997a; Niu 1997; Barth et al. 2003; Seyler et al. 2007; Warren and Shimizu 2010; Dygert et al. 2016). The migrating melt, modified by pyroxene dissolution, may later cool along grain boundaries within the metasomatized harzburgite, and crystallize secondary clino- and orthopyroxene ± olivine (Kelemen et al. 1992; Dygert et al. 2016). Field evidence for the possibility of such melt-rock interactions in the Nahlin ophiolite include replacive dunite channels, and gabbro dikes and sills in the harzburgite tectonite. Texturally, the secondary clino- and orthopyroxene in peridotites from the Nahlin ophiolite cannot be distinguished from primary pyroxene by petrography. Some evidence of pyroxene dissolution, however, can be seen in thin section, as shown by lobate grain boundaries and embayments of olivine into pyroxene (Parkinson and Pearce 1998; Seyler et al. 2007) (Figure 3.5).

Chemically, the secondary clino- and orthopyroxene can be identified by relative enrichments of Sr, Sc ± Zr. Trace element abundances in clino- and orthopyroxene can vary on kilometer to decameter scales, reflecting how crystals precipitated from and interacted with migrating melts at different times and scales in an changing open system (Kelemen et al. 1992). These variations in pyroxene chemistry likely give rise to the inter-sample variability in closure temperature observed in T_{REE} recorded in the peridotites – particularly those from the Menatatuline massif (Table 3-3). Every effort was made to identify and exclude pyroxene analyses with evidence for secondary or metasomatic processes from thermometric calculations. Nonetheless, some cryptic and/or modal metasomatism could only be identified by scrutinizing thermometric and chemical data post-temperature calculations. For instance, where unusually cool T_{REE} were calculated in clinopyroxene enriched in Sr (Figure 3.17).

Anomalously cool T_{REE} (~900 °C) calculated from metasomatized clinopyroxene ± orthopyroxene in some Menatatuline and Hardluck massif samples are contrary to expected T_{REE} results for samples affected by significant melt-rock interaction. Secondary clinopyroxene in equilibrium with the migrating melt rather than with the residual orthopyroxene during melt-rock interactions should result in anomalously high calculated T_{REE} (>1350 °C) (Liang et al. 2013; Dygert and Liang 2015). The abnormally low T_{REE} of some peridotites in the Nahlin ophiolite may thus be the result of slower cooling, whereby coexisting, melt-metasomatized clino- and orthopyroxene had sufficient time to re-equilibrate. Consequently, samples from the Nahlin ophiolite that preserve relatively hot temperatures (>1000 °C) by both major and rare earth element thermometry may record an earlier, post-melting but pre-metasomatism cooling at a relatively faster rate. It should be noted, however, that with the data presented herein the timing of this metasomatic overprint relative to the high temperature history described by the geothermometry is unclear.

A more conservative interpretation is that metasomatism has in some way compromised the REE-in-two-pyroxene thermometry in the Nahlin peridotites, and that T_{REE} results should be treated accordingly. The strong zonation of Ca in orthopyroxene, which is not reflected in the REE data as these were acquired only for grain cores, may also effect results of this thermometer. Concentrations of some major elements, including Ca, are used to calculate the coefficients in pyroxene-melt partitioning models that in turn are used to determine orthopyroxene-clinopyroxene partition coefficients for the REE (Liang et al. 2013). Meaning, strong variations in Ca within orthopyroxene in particular may have significant impact on calculated T_{REE}. Alternatively, the variability in T_{REE} temperatures may be the product of poor quality orthopyroxene REE data (Liang et al. 2013; Dygert and Liang 2015). The highly incompatible REE, particularly the LREE to MREE, are frequently near or below detection in orthopyroxene from the strongly depleted peridotites of the Nahlin ophiolite (Figure 3.9), which may result in large uncertainties in calculated T_{REE} (Liang et al. 2013; Dygert and Liang 2015). Compared to pyroxene REE data from other ophiolites compiled by Dygert and Liang (2015), REE data from the Menatatuline massif are notably depleted and “noisy”. Considering the significant limits imposed by chemical zonation and analytical capabilities, interpretations involving the results of the REE-in-two-pyroxene thermometer generated in this study should be restricted.

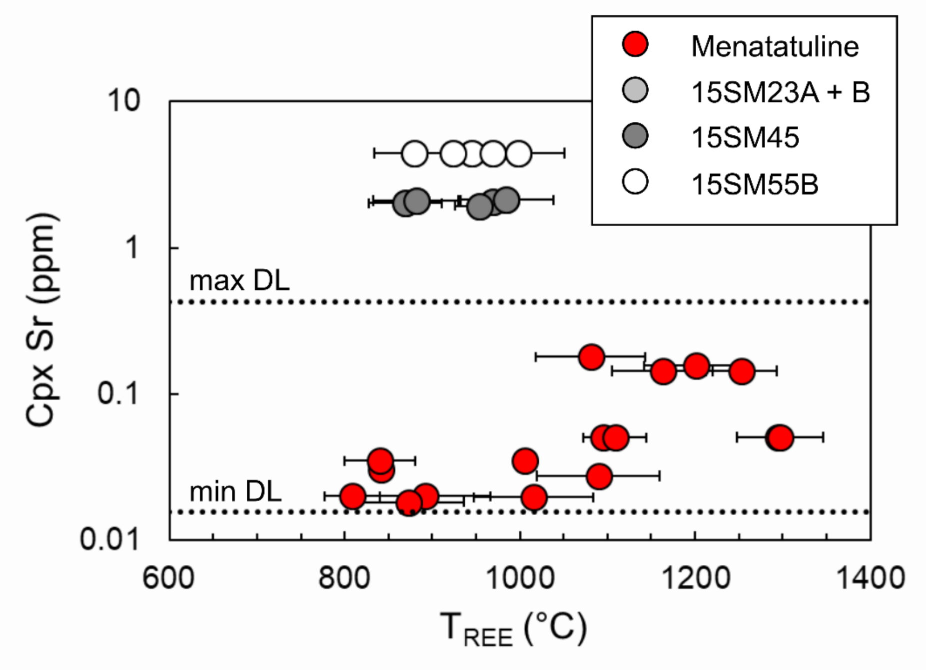

Figure 3.17: Evidence of metasomatism in peridotites from the Menatatuline massif shown by outlying data points indicating enrichment of Sr in clinopyroxene in some samples recording relatively cool T_{REE}. Enriched Sr in clinopyroxene indicates that secondary processes have altered clinopyroxene chemistry in some samples. The results of this metasomatism are the outlying anomalously cool temperatures recorded within the Menatatuline massif. Dashed lines indicate the minimum and maximum detection limits for Sr on the LA-ICP-MS over several sessions.

Tectonic setting of the Nahlin ophiolite

Geochemical studies of the mafic plutonic and volcanic sections of the Nahlin ophiolite indicate that it formed in an arc-marginal setting during the late Permian (English and Johnston 2005; English et al. 2010; Zagorevski 2016; Zagorevski et al. 2016a; McGoldrick et al. 2017). This interpretation is supported by peridotite mineral chemistry, as well as thermometry and results of partial melting models.

Chemical indicators of depletion in mantle residues, such as spinel Cr# (Figure 3.8) and clinopyroxene trace element concentrations (Figure 3.10), highlight differences between the two massifs of the Nahlin ophiolite. Peridotites from the Menatatuline massif plot within the field for SSZ peridotites based on clinopyroxene Ti and Dy concentrations. These mantle residues are relatively depleted, with high spinel Cr# and low trace element concentrations – characteristics typical of SSZ peridotites (Arai 1994; Bizimis et al. 2000). Samples from Peridotite Peak and Peridotite Peak East are notably less depleted than samples from elsewhere in the Hardluck massif, and consistently plot within the abyssal peridotite field.

The degree of partial melting, and more importantly the type of melting, provide further constraint on the tectonic setting of the Nahlin ophiolite. Two different estimates (Figure 3.8 and 3.9) suggest that the Menatatuline massif has been depleted by greater extents of partial melting than the Hardluck massif. Similarly, modeled variations in clinopyroxene Ti and Dy concentrations (Figure 3.10) indicate that the Menatatuline massif is more refractory in nature (Menatatuline F = 23 – 26%; Hardluck, F = 15 – 20%). Clinopyroxene compositions in peridotites from the Hardluck massif can be reproduced by both anhydrous and hydrous melting models. Peridotites from the Menatatuline massif, however, are best modeled by hydrous melting. This implies that the Hardluck massif may have undergone melting under dry or wet conditions, and that the Menatatuline likely experienced hydrous melting in a supra-subduction zone setting.

The formation of peridotites in the Nahlin ophiolite may therefore have involved a combination of decompression and flux melting in either a backarc or proto-forearc environment. Origin in a backarc setting reconciles the local presence of water during melting, and the arc-marginal chemistry of the volcanic and plutonic rocks of the ophiolite. Backarc origins for SSZ-type ophiolites were originally proposed in the 1970s to resolve structural requirements for seafloor spreading and geochemical constraints on subduction input (Miyashiro 1973; Dewey 1976). The lack of a mature volcanic arc spatially associated with the Nahlin ophiolite, however, complicates this interpretation. The volcanic arc may simply not have been preserved during emplacement of the Nahlin ophiolite. Alternatively, as discussed in Chapter 2, the backarc origin of the Nahlin ophiolite may have occurred in a setting similar to the southern Havre Trough. In this model, constructive volcanic arcs are developed synchronously along strike of backarc rift regimes, and the future ophiolite need not have an arc preserved between the backarc ophiolite and accretionary prism (Figure 2.13e; Wysoczanski et al. 2010).

The highly refractory nature of the peridotites in the Menatatuline massif, as well as the arc tholeiite (including forearc basalt-like) compositions of the volcanic and plutonic rocks in the Menatatuline massif (Chapter 2), are also reminiscent of forearc regions (Parkinson and Pearce 1998). According to studies in the Izu-Bonin-Mariana arc, forearc basalts were initially the products of decompression melting of a relatively fertile MORB-like mantle that was progressively depleted and metasomatized as subduction initiation proceeded, eventually forming a harzburgitic residue (Parkinson and Pearce 1998; Morishita et al. 2011; Whattam and Stern 2011). Progressive melting of this refractory residue in the proto-forearc produced volcanic arc basalts and island arc tholeiites that overlie the initial forearc basalts (Reagan et al. 2010, 2013; Ishizuka et al. 2011; Morishita et al. 2011). Although this chemostratigraphy has not been recognized in the volcanic section of the Nahlin ophiolite, the arc tholeiite – harzburgite association does not discount the possibility of formation in the proto-forearc region during subduction initiation.

Fingerprinting the Hardluck massif is more complicated, as it displays characteristics of both SSZ and abyssal (or MOR) ophiolites. These apparently contradictory characteristics can be reconciled by evolution at a backarc ridge. Peridotites from backarc basins tend to be compositionally similar to abyssal peridotites (Ohara et al. 2002, 2003; Choi et al. 2008b), yet can be modified by interaction with subduction-related melts. The compositional and thermometric traits of the Hardluck massif likely reflect a combination of chemical heterogeneities in the mantle lithosphere, low degrees of melting in a backarc setting or high degrees of melting followed by refertilization by infiltrating melts, and interaction with SSZ magmas ± fluids during residence in the mantle wedge. Despite impacts of metasomatism, the peridotites of the Nahlin ophiolite retain their chemical signatures as residues of partial melting in an arc-marginal setting.

A contiguous mantle section?

Historically, the Hardluck and Menatatuline massifs were interpreted as a single, contiguous exposure of mantle peridotite (Aitken 1959; Terry 1977). Recent mapping, however, has revealed that the two massifs are juxtaposed by the Silver Salmon fault, a dextral strike slip fault with potential for regional-scale displacement (Zagorevski et al. 2016a). Following the examination of the magmatic and thermal history of the Nahlin ophiolite presented herein, I conclude that the two massifs do not represent a contiguous mantle section. The Hardluck and Menatatuline massifs likely originated at the same backarc, or proto-forearc, spreading centre, based on the mutual influence of a subduction zone component. The two massifs represent different sections of this arc-marginal ridge system, along which the extent of mantle melting, influence of subduction-derived fluids on partial melting, and degree of metasomatism were spatially variable. Variations in degree of depletion and apparent tectonic affinity on similar scales have also been documented in peridotite massifs in the Coast Range ophiolite (Choi et al. 2008b), SW Turkey (Uysal et al. 2012, 2016), and Albania (Dilek et al. 2008). The Menatatuline massif represents the refractory, high temperature uppermost portion of the melting column, as do peridotites from the Hardluck Peaks and “Moho Saddle”. Peridotite Peak and Peridotite Peak East represent a more fertile, and likely deeper, lithospheric section, that cooled at a relatively slower rate. Spatial trends in geothermometry results and spinel Cr# estimates of degree of melting within the Hardluck massif support this interpreted stratigraphy (Figure 3.15).

Genetic relationship to northern Cache Creek volcanic rocks

The petrogenesis of the arc tholeiites and tholeiitic plutonic rocks in the northern Cache Creek terrane is constrained by field relations and geochemical modeling. Field observations link the arc-marginal dikes that crosscut the mantle peridotite to volcanic flows of nearly identical chemistry, suggesting that the mantle, lower crustal gabbro, and supracrustal volcanic sequences represent a Permo-Triassic SSZ ophiolite package. To support this interpretation, measured bulk-rock REE profiles for crustal igneous rocks are compared to modeled compositions of segregated melts to constrain the degree of melting required to generate the crustal section of the Nahlin ophiolite. The spinel facies non-modal fractional melting of a DMM source is modeled following the method of Warren (2016) described above (see Extent of melt depletion). Based on melt modeling (Figure 3.18) the arc tholeiites and gabbroic rocks of the Nahlin ophiolite could be derived by segregated melts following <5 to 20% melting of a DMM source. The range of melt depletion recorded in the peridotites (10 – 20%) overlaps with the melt estimates necessary to generate the basaltic rocks of the Nahlin ophiolite. This indicates that the intrusive and extrusive igneous rocks are plausibly the melt complement to the residual peridotite in the Nahlin ophiolite with which they are spatially associated. Alternatively, the crustal section of the Nahlin ophiolite was built on mantle that had experienced previous arc magmatism. Geochronological constraints on the timing of volcanism are needed to discriminate between these hypotheses.

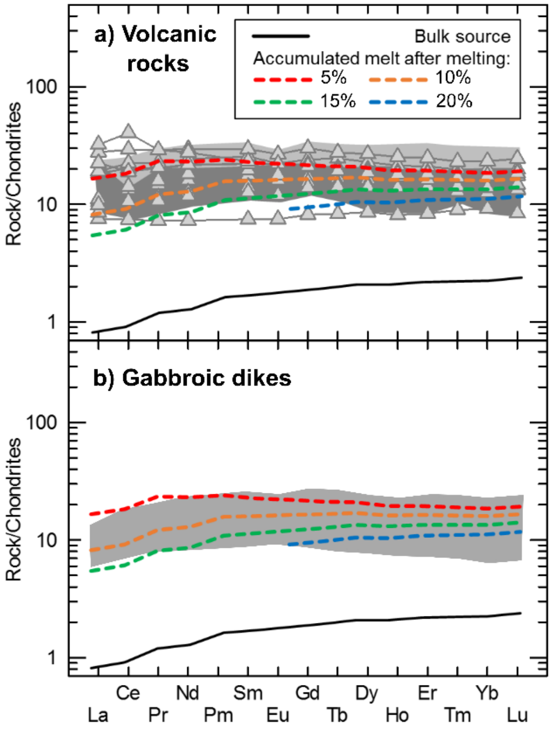

Figure 3.18: Chondrite-normalized REE profiles for the lower crustal and supracrustal igneous rocks of the Nahlin ophiolite. (A) Group A volcanic rocks (grey triangles; McGoldrick et al. 2017) and correlative Nakina transect BABB (light grey shaded area) and IAT (dark grey shaded area) volcanic rocks (English et al. 2010) compared to modeled melt compositions. (B) Gabbro and gabbroic dikes of the Nahlin ophiolite (McGoldrick et al. 2017) relative to modeled melt compositions. Solid black lines indicates the bulk-rock starting composition, and coloured dashed lines reflect segregated melt compositions after 5 - 20% non-modal fractional partial melting of a DMM source in the spinel stability field, as described in the text. Melt modeling parameters as for Figure 3.9. Based on REE profiles, the Group A plutonic and volcanic rocks represent segregated melts following <5 to ~20% partial melting. Chondritic REE abundances after Sun and McDonough (1989).

3.8 Conclusions

The mantle section of the Nahlin ophiolite consists of two massifs dominated by spinel harzburgite tectonites, with minor lherzolites. Both the Hardluck and Menatatuline massifs preserve chemical signatures of mantle residues, depleted by spinel facies partial melting. Both massifs have a two-stage evolution consisting of: depletion of a locally heterogeneous mantle source by non-modal fractional melting, followed by metasomatism in the mantle wedge by migrating basaltic melts and/or subduction related fluids. This two-stage evolution is defined not only by the magmatic history, but also by the thermal history of the peridotites. Initial cooling of the residual mantle tectonite following melt extraction was relatively rapid, particularly near the top of the melt column. This cooling records a decrease in temperature from a minimum initial temperature near the peridotite solidus to ~1000 °C. Subsequent melt-rock interaction between the peridotite and arc magmas resulted in kilometer to decameter scale cryptic and modal metasomatism. Relatively slow cooling following this post-melt extraction metasomatism locally “reset” the REE-in-two-pyroxene thermometry, resulting in scattered and notably cool T_{REE} compared to other SSZ ophiolites. The refractory nature of the Nahlin peridotites, and evidence of melt-rock interaction, suggest that the Nahlin ophiolite formed in a SSZ setting. Based on the interpreted setting of the crustal section of the ophiolite, the peridotites are interpreted to have formed in a backarc or proto-forearc setting as a residue of decompression melting, locally in the presence of water. Melting of the Nahlin peridotite generated the tholeiitic gabbroic dikes and mafic volcanic rocks spatially associated with the ophiolite in the northern Cache Creek terrane. The Hardluck and Menatatuline massifs originated as separate segments along this arc-marginal ridge system, and were later brought into structural juxtaposition post-Cache Creek emplacement along the Silver Salmon fault. Establishing the arc-marginal setting of and petrogenetic links between the mantle and crustal sections of the Nahlin ophiolite demands the re-evaluation of some accepted models of terrane accretion in the northern Canadian Cordillera.

Chapter 4. Conclusions

4.1 Conclusions from the crust

Crustal igneous rocks of the Nahlin ophiolite in the northern Cache Creek terrane are dominantly subalkaline and of arc-affinity. The Group A basaltic rocks represent the products of up to 20% partial melting, and are correlative to nearby tholeiitic volcanic rocks in the Nakina transect and Kutcho assemblage. Together, these volcanic rocks may be linked to a regionally extensive Permo-Triassic intraoceanic arc-backarc system. During the amalgamation of the Cache Creek terrane, this arc may have resided in the upper plate thereby facilitating the preservation of the extensive mantle massifs in the Nahlin ophiolite. Alternatively, the Nahlin ophiolite may represent a fossil spreading centre in a proto-forearc region, where the Group A arc tholeiites are the products of initial magmatism associated with nucleation of a new subduction zone. The volumetrically minor Group C (OIB-type) volcanic rocks in the northern Cache Creek terrane are likely older than and petrogenetically unrelated to the Nahlin ophiolite. These intraplate lavas are associated with carbonate successions bearing Tethyan fauna and represent fragments of oceanic plateaux and their carbonate atolls on the downgoing plate incorporated into a subduction accretionary complex.

4.2 Conclusions from the mantle

The mantle section of the Nahlin ophiolite consists of two massifs, Hardluck and Menatatuline, dominated by spinel harzburgite tectonites. Both massifs represent mantle residues depleted by spinel facies partial melting, and require a (minimum) two-stage evolution consisting of: depletion of a locally heterogeneous mantle source by non-modal fractional melting, followed by metasomatism in the mantle wedge by migrating melts. This two-stage evolution is defined not only by the magmatic history, but also by the thermal history. Initial cooling of the residual mantle tectonite from above the peridotite solidus to ~1000 °C was relatively rapid, particularly near the top of the melt column. Subsequent melt-rock interaction between the peridotite and arc magmas resulted in kilometer to decameter scale cryptic and modal metasomatism, which appears to have affected closure temperatures of the REE-in-two-pyroxene thermometer.

Based on the similarity of the Group A volcanic rocks to IAT, BABB and FAB, and on the refractory character of the peridotite, the mantle section of the Nahlin ophiolite is interpreted to have formed as a residue of partial melting in a proto-forearc or backarc setting, locally in the presence of water. Shallow (spinel facies) fractional melting of peridotite in the Nahlin ophiolite generated the tholeiitic Group A plutonic and volcanic rocks spatially associated with the ophiolite in the northern Cache Creek terrane. Differences in extent of depletion and thermal history between the two massifs imply that the Hardluck and Menatatuline massifs originated as separate segments along the spreading ridge. The Menatatuline massif represents the highly refractory, generally high temperature uppermost mantle lithosphere, whereas the Hardluck massif represents a transect from a similar lithospheric level proximal to the Moho to near the base of the residual mantle melting column. The two segments were later brought into structural juxtaposition along the Silver Salmon fault following the emplacement of the Cache Creek onto ancestral North America.

4.3 Regional tectonic implications

The petrogenetic links between the mantle peridotite, lower crustal intrusions, and supracrustal volcanic rocks of the Nahlin ophiolite and the geochemical evidence for a backarc or proto-forearc setting demand that it have formed on the upper plate, and thus require the re-evaluation of terrane accretion models in the northern Canadian Cordillera. The updated classification of lithostratigraphic units in the northern Cache Creek terrane into lower plate, upper plate and overlap assemblages challenges some accepted models of the evolution of the Cache Creek terrane. This new configuration requires the presence of suture(s) within the Cache Creek terrane that have not been recognised in past models of Cordilleran orogenesis. Identifying these terrane bounding faults, and within-terrane sutures, is paramount to a better understanding of accretionary tectonics in the northern Cordillera.

4.4 Suggestions for future study

Understanding the redox conditions in the mantle lithosphere at the time of melt depletion could potentially further constrain the tectonic setting of the Nahlin ophiolite. Analyses of coexisting spinel and olivine in the Nahlin ophiolite samples presented in this study were not calibrated appropriately to acquire high quality Fe^{3+} data, and the resulting calculated fO_2 are therefore only approximate. A more detailed investigation of oxygen fugacity recorded in harzburgites using appropriate calibrations and standards on the electron microprobe would be a valuable addition to the present work on the Nahlin ophiolite. Furthermore, as whole-rock and mineral chemistry in the harzburgites imply local melt-rock interaction, the redox conditions recorded in the replacive dunite channels should be investigated to elucidate the nature of the melts involved in this metasomatism.

Detailed geochemical study of pyroxene grains in the spinel harzburgite would be of use in further constraining the extent of metasomatic effects (e.g., identification of precipitated secondary pyroxene). This could potentially be accomplished by detailed chemical maps of individual clino- and orthopyroxene grains using the scanning electron microscope, for example. Or alternatively, by defining any zonation in trace elements in pyroxene grains by rim to rim grain transects on the LA-ICP-MS. As orthopyroxene displays porphyroclastic textures and generally large grain size it likely represents a “long-lived” phase in the mantle residue. Detailed study of orthopyroxene may therefore provide important clues to the thermal and magmatic history of the Nahlin peridotite. Studies in Hokkaido, Japan, for example, have applied a similar strategy in using chemical zonation in pyroxene porphyroclasts to infer differences in recorded lithospheric P-T conditions within the Horoman peridotite complex (Ozawa and Takahashi 1995; Ozawa 2004). These data were used to discern a local heating event during the ascent from the garnet to spinel stability fields, and to make large-scale interpretations on the role of an asthenospheric diaper in triggering uplift and deformation in the Horoman lithosphere (Ozawa 2004).

Also warranting further study are the effects of metasomatism on the peridotites of the Nahlin ophiolite, and the potential influence of melt-rock interaction on geothermometry. The impact of any trapped melt or additional metasomatic phases on the spinel harzburgite geochemistry could potentially be identified by mass balance calculations. Using the approach applied to major element data herein, one would follow the method of Albarede and Provost (1977) using trace element whole-rock and four phase mineral data. Significant residuals of this calculation may indicate the presence of trapped melt or additional secondary phases.

In the crustal section of the ophiolite it would be prudent to ensure that the negative Th-Nb-La anomaly observed in the volcanic and plutonic rocks of the Nahlin ophiolite reflects a subduction zone signature as interpreted herein. This anomaly in trace element profiles is also common in mantle-derived magmas that have assimilated continental crust (Davidson 1987). To investigate this, one could undertake isotopic studies of $^{143}Nd/^{144}Nd$ and/or $^{87}Sr/^{86}Sr$. Primitive magmas that have been contaminated by interaction with continental crust will tend to have high

^{87}Sr/^{86}Sr and low ^{143}Nd/^{144}Nd (Carter et al. 1978; Hawkesworth and Vollmer 1979; Davidson 1987). Such an isotopic signature in the Group A volcanic rocks of the Nahlin ophiolite would have strong implications for the tectonic settings proposed herein.

Finally, additional constraints on the timing of volcanism in the Nahlin ophiolite would be of great value in reconstructing the tectonic history of the northern Cache Creek terrane. Quantifying the timing between carbonate atoll formation through additional biostratigraphy, and initial eruption of the arc-marginal volcanic rocks, would help justify, or refute, the need for the Cache Creek terrane as presently drawn to be reconsidered as two separate terranes. However, finding samples of suitable lithology to date radiometrically, by U/Pb or K/Ar geochronology for example, is not trivial in the Menatatuline Range study area. Volcanic and volcaniclastic rocks in this area are almost exclusively mafic, and crosscutting dikes of promising composition (e.g., trondhjemite, or hornblende-bearing gabbro) typically lack appropriate mineralogy (i.e., no zircon) or sufficient concentrations of datable isotopes (i.e., low-K amphibole), to date. Further detailed mapping of the aerially-extensive volcanic rocks associated with the Nahlin ophiolite may yield datable samples, or intercalated sedimentary units with the potential to be dated using biostratigraphy or detrital zircon geochronology.

References

Aitken JD (1959) Atlin map-area, British Columbia (104 N). Geol Surv Canada Mem 307:1–89.

Alabaster T, Pearce JA, Malpas J (1982) The volcanic stratigraphy and petrogenesis of the Oman ophiolite complex. Contrib to Mineral Petrol 81:168–183. doi: 10.1007/BF00371294

Albarede F, Provost A (1977) Petrological and geochemical mass-balance equations: an algorithm for least-square fitting and general error analysis. Comput Geosci 3:309–326. doi: 10.1016/0098-3004(77)90007-3

Anonymous (1972) Penrose conference on ophiolites. In: Geotimes. pp 22–24

Arai S (1994) Characterization of spinel peridotites by olivine-spinel compositional relationships: Review and interpretation. Chem Geol 113:191–204. doi: 10.1016/0009-2541(94)90066-3

Ash CH (1994) Origin and tectonic setting of ophiolitic ultramafic rocks in the Atlin area, British Columbia (NTS 104N). British Columbia Geological Survey

Ash CH, Arksey RL (1990) The Atlin ultramafic allochthon: ophiolitic basement within the Cache Creek terrane; tectonic and metallogenic significance. Geol Fieldwork 1989 365–374.

Babechuk MG, Kamber BS, Greig A, et al (2010) The behaviour of tungsten during mantle melting revisited with implications for planetary differentiation time scales. Geochim Cosmochim Acta 74:1448–1470. doi: 10.1016/j.gca.2009.11.018

Baker MB, Beckett JR (1999) The origin of abyssal peridotites: A reinterpretation of constraints based on primary bulk compositions. Earth Planet Sci Lett 171:49–61. doi: 10.1016/S0012-821X(99)00130-2

Baker MB, Stolper EM (1994) Determining the composition of high-pressure mantle melts using diamond aggregates. Geochim Cosmochim Acta 58:2811–2827. doi: 10.1016/0016-7037(94)90116-3

Ballhaus C (1993) Redox states of lithospheric and asthenospheric upper mantle. Contrib to Mineral Petrol 114:331–348. doi: 10.1007/BF01046536

Ballhaus C, Berry RF, Green DH (1991) High pressure experimental calibration of the olivine-orthopyroxene-spinel oxygen geobarometer: implications for the oxidation state of the upper mantle. Contrib to Mineral Petrol 107:27–40. doi: 10.1007/BF00311183

Ballhaus C, Berry RF, Green DH (1990) Oxygen fugacity controls in the Earth’s upper mantle. Nature 348:437–440.

Barrett TJ, MacLean WH (1999) Volcanic sequences, lithogeochemistry, and hydrothermal alteration in some bimodal volcanic-associated massive sulfide systems. In: Reviews in Economic Geology. pp 101–131

Barrett TJ, Thompson JFH, Sherlock RL (1996) Stratigraphic, lithogeochemical and tectonic setting of the Kutcho Creek massive sulphide deposit, northern British Columbia. Explor Min Geol 5:309–338.

Barth MG, Mason PRD, Davies GR, et al (2003) Geochemistry of the Othris Ophiolite, Greece: Evidence for refertilization? J Petrol 44:1759–1785. doi: 10.1093/petrology/egg058

Batanova VG, Belousov IA, Savelieva GN, Sobolev AV (2011) Consequences of channelized and diffuse melt transport in supra-subduction zone mantle: Evidence from the Voykar Ophiolite (Polar Urals). J Petrol 52:2483–2521. doi: 10.1093/petrology/egr053

Batanova VG, Sobolev AV (2000) Compositional heterogeneity in subduction-related mantle peridotites, Troodos massif, Cyprus. Geology 28:55–58.

Beccaluva L, Coltorti M, Giunta G, Siena F (2004) Tethyan vs. Cordilleran ophiolites: A reappraisal of distinctive tectono-magmatic features of supra-subduction complexes in relation to the subduction mode. Tectonophysics 393:163–174. doi: 10.1016/j.tecto.2004.07.034

Bédard JH (1994) A procedure for calculating the equilibrium distribution of trace elements among the minerals of cumulate rocks, and the concentration of trace elements in the coexisting liquids. Chem Geol 118:143–153. doi: 10.1016/0009-2541(94)90173-2

Bezard R, Turner S, Davidson JP, et al (2015) Seeing through the effects of crustal assimilation to assess the source composition beneath the southern Lesser Antilles arc. J Petrol 56:815–844. doi: 10.1093/petrology/egv018

Bickerton L, Colpron M, Gibson D (2012) Cache Creek terrane, Stikinia, and overlap assemblages of eastern Whitehorse (NTS 105D) and western Teslin (NTS 105C) map areas. Yukon Geol Res 1–17.

Bizimis M, Salters VJM, Bonatti E (2000) Trace and REE content of clinopyroxenes from supra-subduction zone peridotites. Implications for melting and enrichment processes in island arcs. Chem Geol 165:67–85. doi: 10.1016/S0009-2541(99)00164-3

Bloodgood MA, Bellefontaine KA (1990) The geology of the Atlin area (Dixie Lake and Teresa Island) (104N/6 and parts of 104N/5 and 12). Geol Fieldwork 1989 205–215.

Brey GP, Köhler T (1990) Geothermobarometry in four-phase lherzolites II . New thermobarometers , and practical assessment of existing thermobarometers. J Petrol 31:1353–1378.

Canil D, Johnston ST, Mihalynuk MG (2006) Mantle redox in Cordilleran ophiolites as a record of oxygen fugacity during partial melting and the lifetime of mantle lithosphere. Earth Planet Sci Lett 248:91–102. doi: 10.1016/j.epsl.2006.04.038

Carter SR, Evensen NM, Hamilton PJ, O'Nions RK (1978) Neodymium and strontium isotope evidence for crustal contamination of continental volcanics. Science (80-) 202:743–747.

Cherniak DJ, Dimanov A (2010) Diffusion in pyroxene, mica and amphibole. Rev Mineral Geochemistry 72:641–690.

Childe F, Schiarizza P (1997) U-Pb geochronology, geochemistry and Nd isotopic systematics of the Sitlika assemblage, central British Columbia. Geol Fieldwork 1996 69–78.

Childe F, Thompson J (1997) Geological setting, U-Pb geochronology, and radiogenic isotopic characteristics of the Permo-Triassic Kutcho Assemblage, north-central British Columbia. Can J Earth Sci 34:1310–1324.

Choi SH, Mukasa SB, Shervais JW (2008a) Initiation of Franciscan subduction along a large-offset fracture zone: Evidence from mantle peridotites, Stonyford, California. Geology 36:595–598. doi: 10.1130/G24993A.1

Choi SH, Shervais JW, Mukasa SB (2008b) Supra-subduction and abyssal mantle peridotites of the Coast Range ophiolite, California. Contrib to Mineral Petrol 156:551–576. doi: 10.1007/s00410-008-0300-6

Cloos M (1993) Lithospheric buoyancy and collisional orogenesis: Subduction of oceanic plateaus, continental margins, island arcs, spreading ridges, and seamounts. Geol Assoc Am Bull 105:715–737.

Coleman RGR (1981) Tectonic setting for ophiolite obduction in Oman. J Geophys Res Solid Earth 86:2497–2508. doi: 10.1029/JB086iB04p02497

Cordey F, Gordey SP, Orchard MJ (1991) New biostratigraphic data for the northern Cache Creek terrane, Teslin map area, southern Yukon. In: Current Research, Part E. Geological Survey of Canada, pp 67–76

Cuffaro M, Miglio E (2012) Asymmetry of thermal structure at slow-spreading ridges: Geodynamics and numerical modeling. Comput Fluids 68:29–37. doi: 10.1016/j.compfluid.2012.07.028

Davidson JP (1987) Crustal contamination versus subduction zone enrichment: Examples from the Lesser Antilles and implications for mantle source compositions of island arc volcanic rocks. Geochim Cosmochim Acta 51:2185–2198. doi: 10.1016/0016-7037(87)90268-7

Devine FAM (2002) U–Pb geochronology, geochemistry, and tectonic implications of oceanic rocks in the northern Cache Creek Terrane, Nakina area, northwestern British Columbia. University of British Columbia, Vancouver, BC, Canada

Dewey JF (1976) Ophiolite obduction. Tectonophysics 31:93–120. doi: 10.1016/0040-1951(76)90169-4

Dick HJB, Fisher RL, Bryan WB (1984) Mineralogic variability of the uppermost mantle along mid-ocean ridges. Earth Planet Sci Lett 69:88–106. doi: 10.1016/0012-821X(84)90076-1

Dilek Y, Furnes H (2014) Ophiolites and their origins. Elements 10:93–100. doi: 10.2113/gselements.10.2.93

Dilek Y, Furnes H (2009) Structure and geochemistry of Tethyan ophiolites and their petrogenesis in subduction rollback systems. Lithos 113:1–20. doi: 10.1016/j.lithos.2009.04.022

Dilek Y, Furnes H, Shallo M (2008) Geochemistry of the Jurassic Mirdita Ophiolite (Albania) and the MORB to SSZ evolution of a marginal basin oceanic crust. Lithos 100:174–209. doi: 10.1016/j.lithos.2007.06.026

Dodson MH (1973) Closure temperature in cooling geochronological and petrological systems. Contrib to Mineral Petrol 40:259–274. doi: 10.1007/BF00373790

Droop GTR (1987) A general equation for estimating Fe3+ concentrations in ferromagnesian silicates and oxides from microprobe analyses, using stoichiometric criteria. Mineral Mag 51:431–435. doi: 10.1180/minmag.1987.051.361.10

Dygert N, Liang Y (2015) Temperatures and cooling rates recorded in REE in coexisting pyroxenes in ophiolitic and abyssal peridotites. Earth Planet Sci Lett 420:151–161. doi: 10.1016/j.epsl.2015.02.042

Dygert N, Liang Y, Kelemen PB (2016) Formation of plagioclase lherzolite and associated dunite – harzburgite – lherzolite sequences by multiple episodes of melt percolation and melt – rock reaction: an example from the Trinity ophiolite, California, USA. J Petrol 57:815–838. doi: 10.1093/petrology/egw018

English JM, Johnston ST (2005) Collisional orogenesis in the northern Canadian Cordillera: Implications for Cordilleran crustal structure, ophiolite emplacement, continental growth, and the terrane hypothesis. Earth Planet Sci Lett 232:333–344. doi: 10.1016/j.epsl.2005.01.025

English JM, Mihalynuk MG, Johnston ST (2010) Geochemistry of the northern Cache Creek terrane and implications for accretionary processes in the Canadian Cordillera. Can J Earth Sci 47:13–34. doi: 10.1139/E09-066

English JM, Mihalynuk MG, Johnston ST, Devine FAM (2002) Atlin TGI Part III : Geology and petrochemistry of mafic rocks within the northern Cache Creek terrane and tectonic implications. Geol Fieldwork 2001 19–30.

Fabries J (1979) Spinel-olivine geothermometry in peridotites from ultramafic complexes. Contrib to Mineral Petrol 69:329–336. doi: 10.1007/BF00372258

Forsyth DW (1977) The evolution of the upper mantle beneath mid-ocean ridges. Tectonophysics 38:89–118. doi: 10.1016/0040-1951(77)90202-5

Gabrielse H (1991) Late Paleozoic and Mesozoic terrane interactions in north-central British-Columbia. Can J Earth Sci 28:947–957. doi: 10.1139/e91-086

Gabrielse H (1998) Geology of Cry Lake and Dease Lake map areas, north-central British Columbia. Geological Survey of Canada Bulletin 504

Gabrielse H, Monger JWH, Wheeler JO, Yorath CJ (1991) Tectonic Framework, Part A: Morphogeological belts, tectonic assemblages and terranes. In: Gabrielse H, Yorath CJ (eds) Geology of the Cordilleran Orogen in Canada. Geological Survey of Canada, pp 15–28

Gaetani GA, Grove TL (1998) The influence of water on melting of mantle peridotite. Contrib to Mineral Petrol 131:323–346. doi: 10.1007/s004100050396

Gale A, Dalton CA, Langmuir CH, et al (2013) The mean composition of ocean ridge basalts. Geochemistry, Geophys Geosystems 14:489–518. doi: 10.1029/2012GC004334

Gordey SP, McNicoll VJ, Mortensen JK (1998) New U-Pb ages from the Teslin area, southern Yukon, and their bearing on terrane evolution in the northern Cordillera. In: Current Research 1998-F Radiogenic age and isotopic studies: Report 11. Geological Survey of

Canada, pp 129–148

Hanghøj K, Kelemen PB, Hassler D, Godard M (2010) Composition and genesis of depleted mantle peridotites from the Wadi Tayin massif, Oman ophiolite; Major and trace element geochemistry, and Os isotope and PGE systematics. J Petrol 51:201–227. doi: 10.1093/petrology/egp077

Hart SR, Zindler A (1986) In search of a bulk-Earth composition. Chem Geol 57:247–267. doi: 10.1016/0009-2541(86)90053-7

Hawkesworth CJ, Vollmer R (1979) Crustal contamination versus enriched mantle: 143Nd/144Nd and 87Sr/86Sr evidence from the Italian volcanics. Contrib to Mineral Petrol 69:151–165. doi: 10.1007/BF00371858

Hellebrand E, Snow JE, Dick HJ, Hofmann AW (2001) Coupled major and trace elements as indicators of the extent of melting in mid-ocean-ridge peridotites. Nature 410:677–681. doi: 10.1038/35070546

Ishikawa T, Nagaishi K, Umino S (2002) Boninitic volcanism in the Oman ophiolite: Implications for thermal condition during transition from spreading ridge to arc. Geology 30:899–902. doi: 10.1130/0091-7613(2002)030<0899:BVITOO>2.0.CO;2

Ishizuka O, Tani K, Reagan MK, et al (2011) The timescales of subduction initiation and subsequent evolution of an oceanic island arc. Earth Planet Sci Lett 306:229–240. doi: 10.1016/j.epsl.2011.04.006

Jenner GA (1996) Trace element geochemistry of igneous rocks: geochemical nomenclature and analytical geochemistry. In: Wyman DA (ed) Trace element geochemistry of volcanic rocks: Applications for massive sulphide exploration. Geological Association of Canada, Short Course Notes, pp 51–77

Jianping L, Kornprobst J, Vielzeuf D, Fabriès J (1995) An improved experimental calibration of the olivine-spinel geothermometer. Chinese J Geochemistry 14:68–77. doi: 10.1007/BF02840385

Jochum KP, Nohl U, Herwig K, et al (2005) GeoReM: a new geochemical database for reference materials and isotopic standards. Geostand Geoanalytical Res 29:333–338. doi: 10.1111/j.1751-908X.2005.tb00904.x

Johnson KTM, Dick HJB (1992) Open system melting and temporal and spatial variation of peridotite and basalt at the Atlantis II Fracture Zone. J Geophys Res 97:9219. doi:

10.1029/92JB00701

Johnson KTM, Dick HJB, Shimizu N (1990) Melting in the oceanic upper mantle: An ion microprobe study of diopsides in abyssal peridotites. J Geophys Res 95:2661. doi: 10.1029/JB095iB03p02661

Johnston ST, Borel GD (2007) The odyssey of the Cache Creek terrane, Canadian Cordillera: Implications for accretionary orogens, tectonic setting of Panthalassa, the Pacific superwell, and break-up of Pangea. Earth Planet Sci Lett 253:415–428. doi: 10.1016/j.epsl.2006.11.002

Kelemen PB, Dick HJB (1995) Focused melt flow and localized deformation in the upper mantle: Juxtaposition of replacive dunite and ductile shear zones in the Josephine peridotite, SW Oregon. J Geophys Res 100:423–438. doi: 10.1029/94JB02063

Kelemen PB, Dick HJB, Quick JE (1992) Formation of harzburgite by pervasive melt/rock reaction in the upper mantle. Nature 358:635–641. doi: 10.1038/358635a0

Kelemen PB, Hirth G, Shimizu N, et al (1997a) A review of melt migration processes in the adiabatically upwelling mantle beneath oceanic spreading ridges. Philos Trans R Soc London A355:283–318. doi: 10.1098/rsta.1997.0010

Kelemen PB, Koga K, Shimizu N (1997b) Geochemistry of gabbro sills in the crust-mantle transition zone of the Oman ophiolite: implications for the origin of the oceanic lower crust. Earth Planet Sci Lett 146:475–488. doi: 10.1016/S0012-821X(96)00235-X

Kelemen PB, Shimizu N, Salters VJM (1995) Extraction of mid-ocean-ridge basalt from the upwelling mantle by focused flow of melt in dunite channels. Nature 375:747–753.

Kimura G, Ludden J (1995) Peeling oceanic crust in subduction zones. Geology 23:217–220. doi: 10.1130/0091-7613(1995)023<0217

Kinzler RJ, Grove TL (1992a) Primary magmas of mid-ocean ridge basalts 1. Experiements and methods. J Geophys Res Earth 97:6885–6906. doi: 10.1029/91jb02841

Kinzler RJ, Grove TL (1992b) Primary magmas of mid-ocean ridge basalts 2. Applications. J Geophys Res 97:6907–6926. doi: 10.1029/91JB02841

Lagabrielle Y, Vitale Brovarone A, Ildefonse B (2015) Fossil oceanic core complexes recognized in the blueschist metaophiolites of Western Alps and Corsica. Earth-Science Rev 141:1–26. doi: 10.1016/j.earscirev.2014.11.004

Langmuir CH (1989) Geochemical consequences of in situ crystallization. Nature 340:199–205.

Langmuir CH, Klein EM, Plank T (1992) Petrological systematics of mid-ocean ridge basalts: Constraints on melt generation beneath ocean ridges. In: Blackman GK, Sinton JM (eds) Mantle Flow and Melt Generation at Mid-Ocean Ridges. American Geophysical Union, pp 183–280

Lapierre H, Bosch D, Tardy M, Struik LC (2003) Late Paleozoic and Triassic plume-derived magmas in the Canadian Cordillera played a key role in continental crust growth. Chem Geol 201:55–89. doi: 10.1016/S0009-2541(03)00224-9

Liang Y, Sun C, Yao L (2013) A REE-in-two-pyroxene thermometer for mafic and ultramafic rocks. Geochim Cosmochim Acta 102:246–260. doi: 10.1016/j.gca.2012.10.035

Liermann HP, Ganguly J (2003) Fe2+–Mg fractionation between orthopyroxene and spinel: experimental calibration in the system FeO–MgO–Al2O3–Cr2O3–SiO2, and applications. Contrib to Mineral Petrol 145:217–227. doi: 10.1007/s00410-007-0204-x

Liermann HP, Ganguly J (2007) Fe2+–Mg fractionation between orthopyroxene and spinel: experimental calibration in the system FeO–MgO–Al2O3–Cr2O3–SiO2, and applications. Contrib to Mineral Petrol 154:491–491. doi: 10.1007/s00410-007-0204-x

Lyubetskaya T, Korenaga J (2007) Chemical composition of Earth’s primitive mantle and its variance: 1. Method and results. J Geophys Res Solid Earth 112:1–21. doi: 10.1029/2005JB004223

MacLean WH (1990) Mass change calculations in altered rock series. Miner Depos 25:44–49. doi: 10.1007/BF03326382

Maffione M, Morris A, Anderson MW (2013) Recognizing detachment-mode seafloor spreading in the deep geological past. Sci Rep 3:2336. doi: 10.1038/srep02336

Maffione M, Thieulot C, Van Hinsbergen DJJ, et al (2015) Dynamics of intraoceanic subduction initiation: 1. Oceanic detachment fault inversion and the formation of supra-subduction zone ophiolites. Geochemistry Geophys Geosystems 16:1753–1770. doi: 10.1002/2015GC005745.Dynamics

Marchesi C, Garrido CJ, Proenza JA, et al (2016) Geochemical record of subduction initiation in the sub-arc mantle: Insights from the Loma Caribe peridotite (Dominican Republic). Lithos 252–253:1–15. doi: 10.1016/j.lithos.2016.02.009

McDonough WF, Sun S (1995) The Composition of the Earth. Chem Geol 120:223–253. doi: 10.1126/science.243.4889.367

McGoldrick S, Canil D, Zagorevski A (2017) Geochemistry of volcanic and plutonic rocks from the Nahlin ophiolite with implications for a Permo-Triassic arc in the Cache Creek composite terrane, northwestern British Columbia.

McGoldrick S, Zagorevski A, Canil D, et al (2016) Geology of the Cache Creek terrane in the Peridotite Peak – Menatatuline Range Area, northwestern British Columbia (Parts of NTS 104K/15 , /16). Geosci BC Summ Act 2015 149–162.

Mercier J-CC, Nicolas A (1975) Textures and fabrics of upper-mantle peridotites as illustrated by xenoliths from basalts. J Petrol 16:454–487.

Merran Y (2002) Mise en place et environnement de depot d'une plate-forme carbonatée intraoceanique: example du complexe d'Atlin, Canada. Université Claude Bernard, France

Mihalynuk MG (1999) Geology and mineral resources of the Tagish Lake area (NTS 104M/8,9,10E,15 and 104N/12W) northwestern British Columbia. British Columbia Geological Survey

Mihalynuk MG, Bellefontaine KA, Brown DA, et al (1996) Geological compilation, northwest British Columbia (NTS 94E, L, M; 104F, G, H, I, J, K, L, M, N, O, P; 114J, O, P).

Mihalynuk MG, Cordey F (1997) Potential for Kutcho Creek volcanogenic massive sulphide mineralization in the northern Cache Creek terrane: a progress report. Geol Fieldwork 1996 157–170.

Mihalynuk MG, Erdmer P, Ghent ED, et al (2004a) Coherent French Range blueschist: Subduction to exhumation in less than 2.5 m.y.? Geol Soc Am Bull 116:910–922. doi: 10.1130/B25393.1

Mihalynuk MG, Erdmer P, Ghent ED, et al (1998) Age constraints for emplacement of the northern cache creek terrane and implications of blueschist metamorphism. Geol Fieldwork 1997 127–141.

Mihalynuk MG, Fiererra L, Robertson S, et al (2004b) Geology and new mineralization in the Joss'alun belt, Atlin area. Geol Fieldwork 2003 61–82.

Mihalynuk MG, Johnston ST, English JM, et al (2003) Atlin TGI , Part II : Regional geology and mineralization of the Nakina area (NTS 104N / 2W and 3). Geol Fieldwork 2002 9–38.

Mihalynuk MG, Johnston ST, Lowe C, et al (2002) Atlin TGI Part II : Preliminary results from the Atlin Targeted Geoscience Initiative, Nakina area, northwest British Columbia. Geol Fieldwork 2001 5–18.

Mihalynuk MG, Nelson JA, Diakow LJ (1994) Cache Creek terrane entrapment: oroclinal paradox within the Canadian Cordillera. Tectonics 13:575–595. doi: 10.1029/93TC03492

Mihalynuk MG, Smith MT, Gabites JE, et al (1992) Age of emplacement and basement character of the Cache Creek terrane as constrained by new isotopic and geochemical data. Can J Earth Sci 29:2463–2477. doi: 10.1139/e92-193

Miyashiro A (1973) The Troodos ophiolitic complex was probably formed in an island arc. Earth Planet Sci Lett 19:218–224. doi: 10.1016/0012-821X(75)90198-3

Monger JWH (1977) Upper Paleozoic rocks of northwestern British Columbia. In: Report of Activities, Part A. Geological Survey of Canada, pp 255–262

Monger JWH (1975) Upper Paleozoic rocks of the Atlin terrane, northwestern British Columbia and south-central Yukon. Geological Survey of Canada Paper 74-47

Monger JWH, Ross CA (1971) Distribution of Fusulinaceans in the western Canadian Cordillera. Can J Earth Sci 8:259–278. doi: 10.1139/e71-026

Moores EM, Kellogg LH, Dilek Y (2000) Tethyan ophiolites, mantle convection, and tectonic “historical contingency”: A resolution of the “ophiolite conundrum.” In: Dilek Y, Moores EM, Elthon D, Nicolas A (eds) Ophiolites and Oceanic Crust: New Insights From Field Studies and Ocean Drilling Program. Geological Society of America Special Paper, pp 3–12

Morgan Z, Liang Y, Kelemen PB (2008) Significance of the concentration gradients associated with dunite bodies in the Josephine and Trinity ophiolites. Geochemistry, Geophys Geosystems. doi: 10.1029/2008GC001954

Morishita T, Tani K, Shukuno H, et al (2011) Diversity of melt conduits in the Izu-Bonin-Mariana forearc mantle : Implications for the earliest stage of arc magmatism. Geology 39:411–414. doi: 10.1130/G31706.1

Natural Resources Canada (1990a) Teditua Creek NTS 104K/16, 1:50 000 scale raster image.

Natural Resources Canada (1990b) Yeth Creek NTS 104K/15, 1:50 000 scale raster image.

Nelson JA, Colpron M (2011) A digital atlas of terranes for the northern Cordillera. In: BC Minist. Energy Mines, BCGS GeoFile 2011-11.

Nelson JA, Colpron M (2007) Tectonics and metallogeny of the British Columbia, Yukon and Alaskan Cordillera, 1.8 Ga to the present. In: Goodfellow WD (ed) Mineral Deposits of Canada: A synthesis of major deposit types, district metallogeny, the evolution of geological provinces, and exploration methods. Geological Association of Canada, Mineral Deposits Division, pp 755–791

Nicolas A (1989) Structures of ophiolites and dynamics of oceanic lithosphere, 1st edn. Springer Netherlands

Niu Y, Hékinian R (1997) Basaltic liquids and harzburgitic residues in the Garrett Transform: a case study at fast-spreading ridges. Earth Planet Sci Lett 146:243–258. doi: 10.1016/S0012-821X(96)00218-X

Niu YL (1997) Mantle melting and melt extraction processes beneath ocean ridges: Evidence from abyssal peridotites. J Petrol 38:1047–1074. doi: 10.1093/petrology/38.8.1047

Niu YL, Batiza R (1991) An empirical method for calculating melt compositions produced beneath ridges: Application for axis and off-axis (seamounts) melting. J Geophys Res 96:21753–21777.

Ohara Y, Fujioka K, Ishii T, Yurimoto H (2003) Peridotites and gabbros from the Parece Vela backarc basin: Unique tectonic window in an extinct backarc spreading ridge. Geochemistry, Geophys Geosystems 4:n/a-n/a. doi: 10.1029/2002GC000469

Ohara Y, Stern RJ, Ishii T, et al (2002) Peridotites from the Mariana Trough: first look at the mantle beneath an active back-arc basin. Contrib to Mineral Petrol 143:1–18. doi: 10.1007/s00410-001-0329-2

Orchard MJ, Cordey F, Rui L, et al (2001) Biostratigraphic and biogeographic constraints on the Carboniferous to Jurassic Cache Creek Terrane in central British Columbia. Can J Earth Sci 38:551–578. doi: 10.1139/e00-120

Ozawa K (1983) Evaluation of olivine-spinel geothermometry as an indicator of thermal history for peridotites. Contrib to Mineral Petrol 82:52–65. doi: 10.1007/BF00371175

Ozawa K (2004) Thermal history of the Horoman peridotite complex: A record of thermal perturbation in the lithospheric mantle. J Petrol 45:253–273. doi: 10.1093/petrology/egg110

Ozawa K, Takahashi N (1995) P-T history of a mantle diapir: the Horoman peridotite complex, Hokkaido, northern Japan. Contrib to Mineral Petrol 120:223–248. doi: 10.1007/BF00306505

Parkinson I, Pearce J (1998) Peridotites from the Izu-Bonin-Mariana Forearc (ODP Leg 125): Evidence for mantle melting and melt-mantle interaction in a supra-subduction zone setting. J Petrol 39:1577–1618. doi: 10.1093/petroj/39.9.1577

Pearce JA (1996) A user’s guide to basalt discrimination diagrams. In: Wyman DA (ed) Trace element geochemistry of volcanic rocks: Applications for massive sulphide exploration. Geological Association of Canada, Short Course Notes, pp 79–113

Pearce JA (1982) Trace element characteristics of lavas from destructive plate boundaries. In: Thorpe RS (ed) Orogenic andesites and related rocks. John Wiley and Sons, Chichester, UK, pp 525–548

Pearce JA, Alabaster T, Shelton AW, Searle MP (1981) The Oman ophiolite as a Cretaceous arc-basin complex: Evidence and implications. Philos Trans R Soc London A300:299–317.

Pearce JA, Lippard SJ, Roberts S (1984) Characteristics and tectonic significance of supra-suprasubduction zone ophiolites. Geol Soc Spec Publ 16:74–94.

Pearce JA, Norry MJ (1979) Petrogenetic implications of Ti, Zr, Y, and Nb variations in volcanic rocks. Contrib to Mineral Petrol 69:33–47. doi: 10.1007/BF00375192

Pearce JA, Peate DW (1995) Tectonic implications of the composition of volcanic arc magmas. Annu Rev Earth Planet Sci 23:251–285.

Pirard C, Hermann J, O’Neill HSC (2013) Petrology and geochemistry of the crust-mantle boundary in a nascent arc, Massif du Sud ophiolite, New Caledonia, SW Pacific. J Petrol 54:1759–1792. doi: 10.1093/petrology/egt030

Pomonis P, Tsikouras B, Hatzipanagiotou K (2006) Petrogenetic evolution of the Koziakas ophiolite complex (W. Thessaly, Greece). Mineral Petrol 89:77–111. doi: 10.1007/s00710-006-0138-4

Pouchou JL, Pichoir F (1985) “PAP” procedure for improved quantitative microanalysis. Microbeam Anal 20:104–106.

Rampone E, Romairone A, Hofmann AW (2004) Contrasting bulk and mineral chemistry in depleted mantle peridotites: Evidence for reactive porous flow. Earth Planet Sci Lett 218:491–506. doi: 10.1016/S0012-821X(03)00679-4

Reagan MK, Ishizuka O, Stern RJ, et al (2010) Fore-arc basalts and subduction initiation in the Izu-Bonin-Mariana system. Geochemistry, Geophys Geosystems 11:1–17. doi: 10.1029/2009GC002871

Reagan MK, McClelland WC, Girard G, et al (2013) The geology of the southern Mariana fore-arc crust: Implications for the scale of Eocene volcanism in the western Pacific. Earth Planet Sci Lett 380:41–51. doi: 10.1016/j.epsl.2013.08.013

Robinson JAC, Wood BJ, Blundy JD (1998) The beginning of melting of fertile and depleted peridotite at 1.5 GPa. Earth Planet Sci Lett 155:97–111. doi: 10.1016/S0012-821X(97)00162-3

Ross P-S, Bédard JH (2009) Magmatic affinity of modern and ancient subalkaline volcanic rocks determined from trace-element discriminant diagrams. Can J Earth Sci 46:823–839. doi: 10.1139/E09-054

Saccani E, Photiades A (2004) Mid-ocean ridge and supra-subduction affinities in the Pindos ophiolites (Greece): Implications for magma genesis in a forearc setting. Lithos 73:229–253. doi: 10.1016/j.lithos.2003.12.002

Salters VJM, Stracke A (2004) Composition of the depleted mantle. Geochemistry, Geophys Geosystems. doi: 10.1029/2003GC000597

Saunders AD, Norry M, Tarney J (1988) Origin of MORB and chemically-depleted mantle reservoirs: Trace element constraints. J Petrol 415–445.

Schiarizza P (2012) Geology of the Kutcho assemblage between the Kehlechoa and Tucho Rivers, northern British Columbia (NTS 104I / 01 , 02). Geol Fieldwork 2011 75–98.

Seyler M, Lorand J-P, Dick HJB, Drouin M (2007) Pervasive melt percolation reactions in ultra-depleted refractory harzburgites at the Mid-Atlantic Ridge, 15° 20′N: ODP Hole 1274A. Contrib to Mineral Petrol 153:303–319. doi: 10.1007/s00410-006-0148-6

Shervais JW, Kimbrough DL (1985) Geochemical evidence for the tectonic setting of the Coast Range ophiolite: a composite island arc-oceanic crust terrane in western California. Geology 13:35–38. doi: 10.1130/0091-7613(1985)13<35:GEFTTS>2.0.CO;2

Shervais JW, Kimbrough DL, Renne P, et al (2004) Multi-stage origin of the Coast Range ophiolite, California: Implications for the life cycle of supra-subduction zone ophiolites. Int Geol Rev 46:289–315. doi: 10.2747/0020-6814.46.4.289

Smith IEM, Price RC (2006) The Tonga-Kermadec arc and Havre-Lau back-arc system: Their role in the development of tectonic and magmatic models for the western Pacific. J Volcanol Geotherm Res 156:315–331. doi: 10.1016/j.jvolgeores.2006.03.006

Souther JG (1971) Geology and mineral deposits of Tulsequah map area, British Columbia (104K). Geol Surv Canada Mem 362:1–84. doi: 10.1017/CBO9781107415324.004

Stern RJ, Reagan MK, Ishizuka O, et al (2012) To understand subduction initiation, study forearc crust: To understand forearc crust, study ophiolites. Lithosphere 469–483. doi:

10.1130/L183.1

Stewart E, Lamb W, Newman J, Tikoff B (2016) The petrological and geochemical evolution of early forearc mantle lithosphere: an Example from the Red Hills ultramafic massif, New Zealand. J Petrol 57:751–776. doi: 10.1093/petrology/egw017

Struik LC, Schiarizza P, Orchard MJ, et al (2001) Imbricate architecture of the upper Paleozoic to Jurassic oceanic Cache Creek Terrane, central British Columbia. Can J Earth Sci 38:495–514. doi: 10.1139/cjes-38-4-495

Suhr G, Hellebrand E, Snow JE, et al (2003) Significance of large, refractory dunite bodies in the upper mantle of the Bay of Islands Ophiolite. Geochemistry, Geophys Geosystems. doi: 10.1029/2001GC000277

Sun C, Liang Y (2014) An assessment of subsolidus re-equilibration on REE distribution among mantle minerals olivine, orthopyroxene, clinopyroxene, and garnet in peridotites. Chem Geol 372:80–91. doi: 10.1016/j.chemgeo.2014.02.014

Sun S, McDonough WF (1989) Chemical and isotopic systematics of oceanic basalts: implications for mantle composition and processes. In: Saunders AD, Norry MJ (eds) Magmatism in the ocean basins. Geological Society of London, pp 313–345

Tamura Y, Tatsumi Y, Zhao D, et al (2002) Hot fingers in the mantle wedge: New insights into magma genesis in subduction zones. Earth Planet Sci Lett 197:105–116. doi: 10.1016/S0012-821X(02)00465-X

Tardy M, Lapierre H, Struik LC, et al (2001) The influence of mantle plume in the genesis of the Cache Creek oceanic igneous rocks: implications for the geodynamic evolution of the inner accreted terranes of the Canadian Cordillera. Can J Earth Sci 38:515–534.

Tempelman-Kluit DJ (1979) Transported cataclasite, ophiolite and granodiorite in Yukon: Evidence of arc-continent collision. Geological Survey of Canada Paper 79-14

Terry J (1977) Geology of the Nahlin ultramafic body, Atlin and Tulsequah map-areas, northwestern British Columbia. In: Report of Activities, Part A. Geological Survey of Canada, pp 263–269

Todd E, Gill JB, Wysoczanski RJ, et al (2011) Hf isotopic evidence for small-scale heterogeneity in the mode of mantle wedge enrichment: Southern Havre Trough and South Fiji Basin back arcs. Geochemistry, Geophys Geosystems. doi: 10.1029/2011GC003683

Uysal I, Ersoy EY, Dilek Y, et al (2016) Multiple episodes of partial melting, depletion, metasomatism and enrichment processes recorded in the heterogeneous upper mantle sequence of the Neotethyan Eldivan ophiolite, Turkey. Lithos 246–247:228–245. doi: 10.1016/j.lithos.2016.01.004

Uysal I, Ersoy EY, Karslĩ O, et al (2012) Coexistence of abyssal and ultra-depleted SSZ type mantle peridotites in a Neo-Tethyan Ophiolite in SW Turkey: Constraints from mineral composition, whole-rock geochemistry (major-trace-REE-PGE), and Re-Os isotope systematics. Lithos 132–133:50–69. doi: 10.1016/j.lithos.2011.11.009

Varga RJ, Moores EM (1985) Spreading structure of the Troodos ophiolite, Cyprus. Geology 13:846. doi: 10.1130/0091-7613(1985)13<846:SSOTTO>2.0.CO;2

Warren JM (2016) Global variations in abyssal peridotite compositions. Lithos 248–251:193–219. doi: 10.1016/j.lithos.2015.12.023

Warren JM, Shimizu N (2010) Cryptic variations in abyssal peridotite compositions: Evidence for shallow-level melt infiltration in the oceanic lithosphere. J Petrol 51:395–423. doi: 10.1093/petrology/egp096

Wasylenki LE, Baker MB, Kent AJR, Stolper EM (2003) Near-solidus melting of the shallow upper mantle: Partial melting experiments on depleted peridotite. J Petrol 44:1163–1191. doi: 10.1093/petrology/44.7.1163

Whattam SA, Stern RJ (2011) The “subduction initiation rule”: A key for linking ophiolites, intra-oceanic forearcs, and subduction initiation. Contrib to Mineral Petrol 162:1031–1045. doi: 10.1007/s00410-011-0638-z

Wills J, Hamester M, Nash M, et al (2007) PlasmaLab software.

Wilson SC, Murton BJ, Taylor RN (2013) Mantle composition controls the development of an Oceanic Core Complex. Geochemistry, Geophys Geosystems 14:979–995. doi: 10.1002/ggge.20046

Workman RK, Hart SR (2005) Major and trace element composition of the depleted MORB mantle (DMM). Earth Planet Sci Lett 231:53–72. doi: 10.1016/j.epsl.2004.12.005

Wysoczanski RJ, Todd E, Wright IC, et al (2010) Backarc rifting, constructional volcanism and nascent disorganised spreading in the southern Havre Trough backarc rifts (SW Pacific). J Volcanol Geotherm Res 190:39–57. doi: 10.1016/j.jvolgeores.2009.04.004

Zagorevski A (2016) Geochemical data of the northern Cache Creek and Stikine terranes and their overlap assemblages, British Columbia and Yukon. Geol Surv Canada Open File

8039:1–11. doi: 10.4095/299347

Zagorevski A, Corriveau A-S, McGoldrick S, et al (2015) Geological framework of ancient oceanic crust in northwestern British Columbia and southwestern Yukon GEM 2 Cordillera. Geol Surv Canada Open File 7957:1–10. doi: 10.4095/297273

Zagorevski A, Lissenberg CJ, van Staal CR (2009) Dynamics of accretion of arc and backarc crust to continental margins: Inferences from the Annieopsquotch accretionary tract, Newfoundland Appalachians. Tectonophysics 479:150–164. doi: 10.1016/j.tecto.2008.12.002

Zagorevski A, Mihalynuk MG, Joyce N, Anderson RG (2017) Late Cretaceous magmatism in the Atlin-Tagish area, northern British Columbia (104M , 104N). Geol Fieldwork 2016 133–152.

Zagorevski A, Mihalynuk MG, McGoldrick S, et al (2016a) Geological framework of ancient oceanic crust in northwestern British Columbia and southwestern Yukon GEM 2 Cordillera. Geol Surv Canada Open File 8140:1–13. doi: 10.4095/297273

Zagorevski A, Mihalynuk MG, Milidragovic D, et al (2016b) Characterization of volcanic and intrusive rocks across the British Columbia - Yukon border, GEM 2 Cordillera. Geol Surv Canada Open File 8141:1–13. doi: 10.4095/297272

Zagorevski A, van Staal CR (2011) The Record of Ordovician arc-arc and arc-continent collisions in the Canadian Appalachians during the closure of Iapetus. In: Brown D, Ryan PD (eds) Frontiers in Earth Sciences. Springer-Verlag Berlin Heidelberg, pp 341–371

A. Appendix

Figure A 1: Variations in core and/or rim closure temperatures with increasing grain size for several geothermometers.

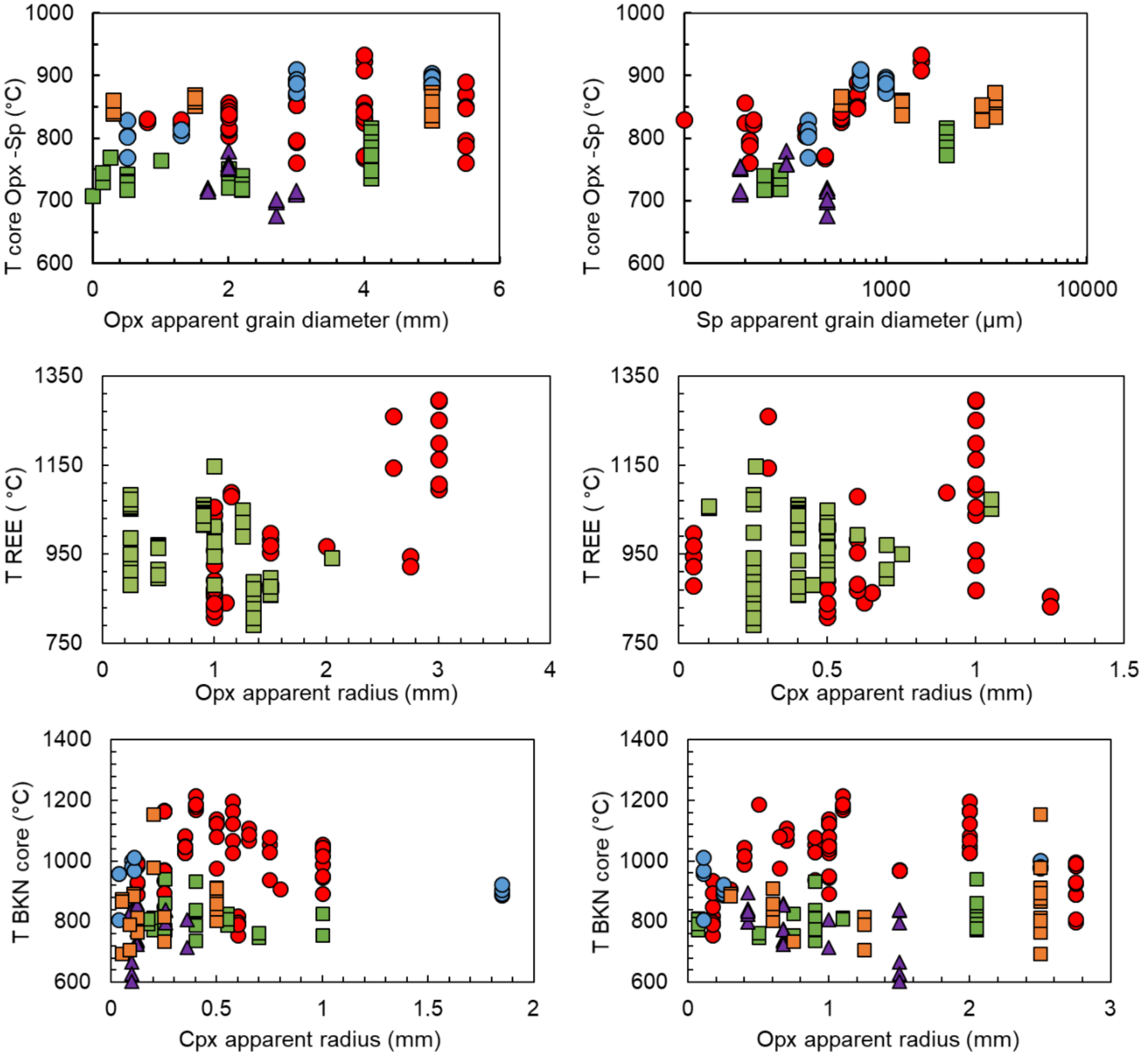

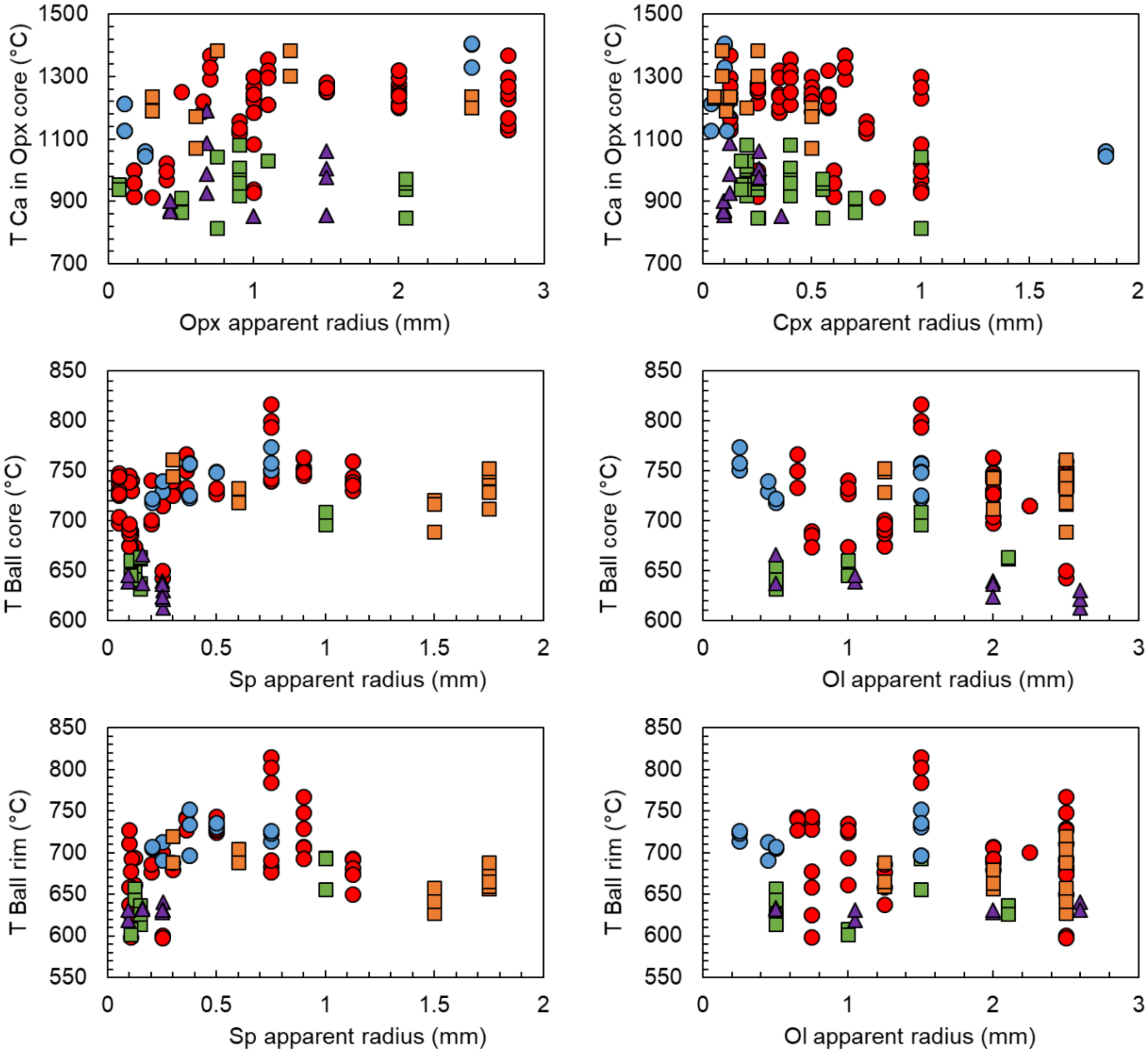
T Ca in Opx core (°C)
1500
1300
1100
900
700
0
1
2
3
Opx apparent radius (mm)
T Ca in Opx core (°C)
0
0.5
1
1.5
2
Cpx apparent radius (mm)
T Ball core (°C)
850
800
750
700
650
600
Sp apparent radius (mm)
T Ball core (°C)
Ol apparent radius (mm)
T Ball rim (°C)
550
Sp apparent radius (mm)
T Ball rim (°C)
Ol apparent radius (mm)

Figure A 2: Electron microprobe analysis locations.

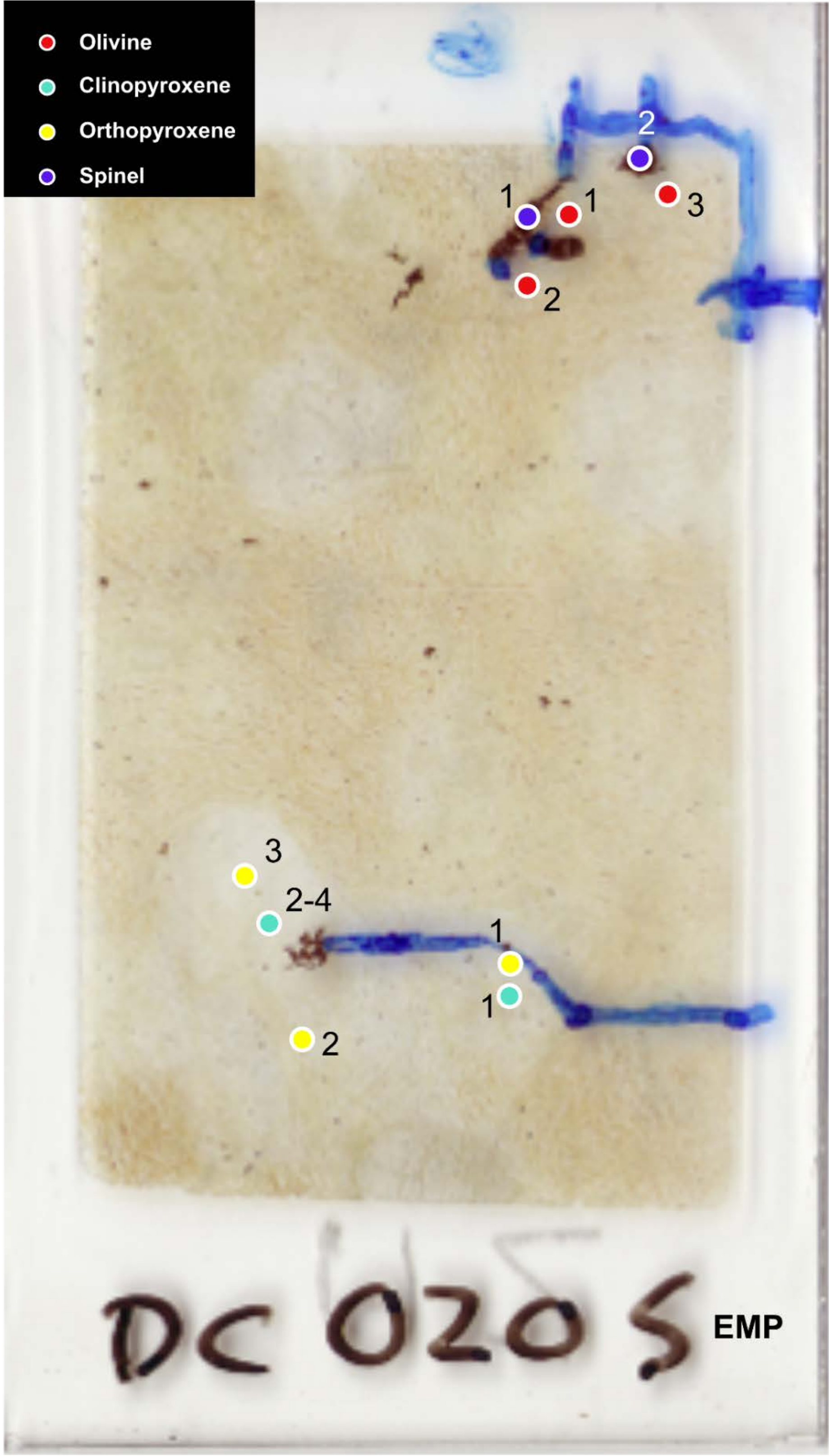

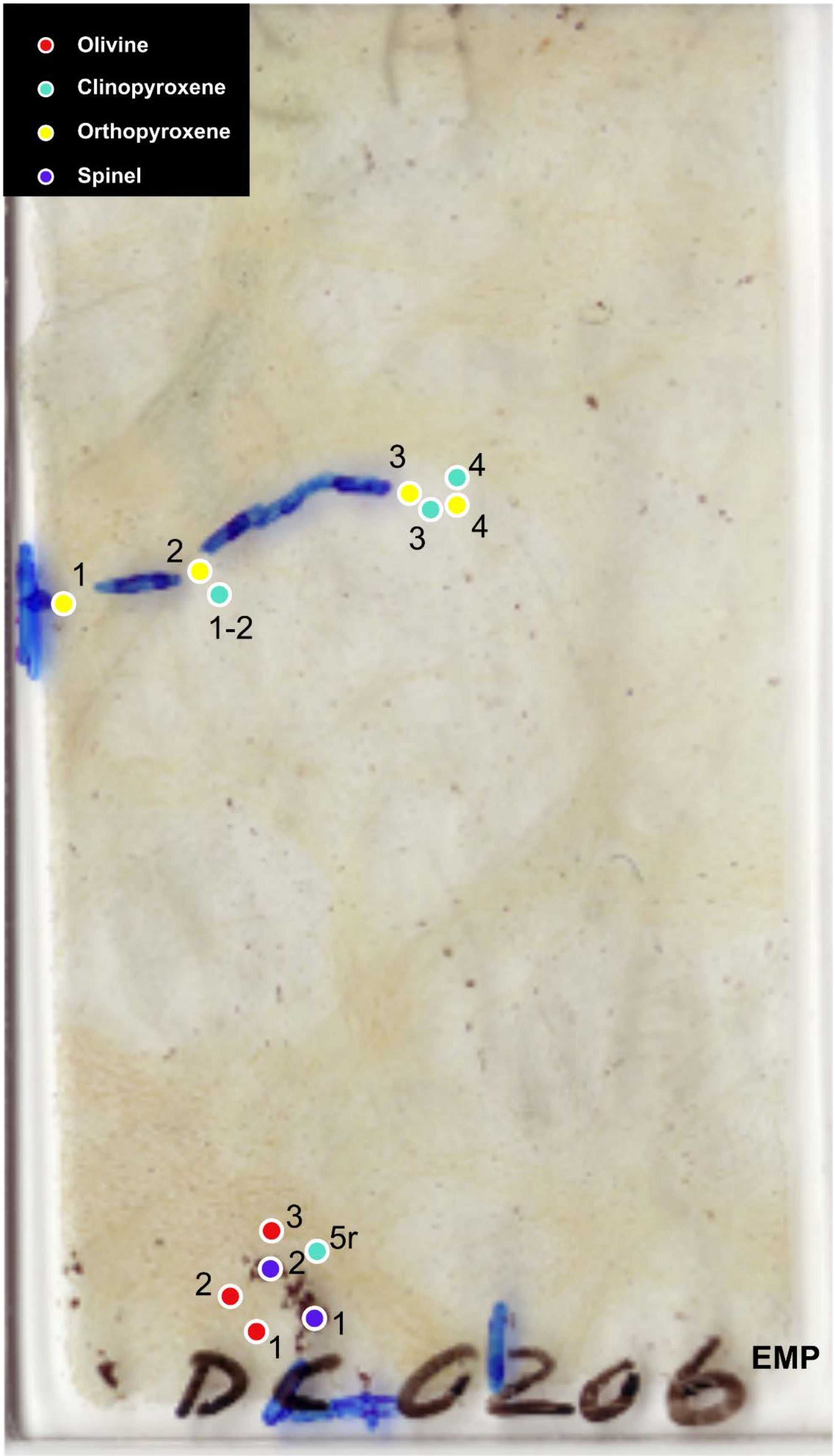
● Olivine
● Clinopyroxene
● Orthopyroxene
● Spinel
3
4
3
4
2
1
1-2
3
5r
2
2
1
1
DC-0206
EMP

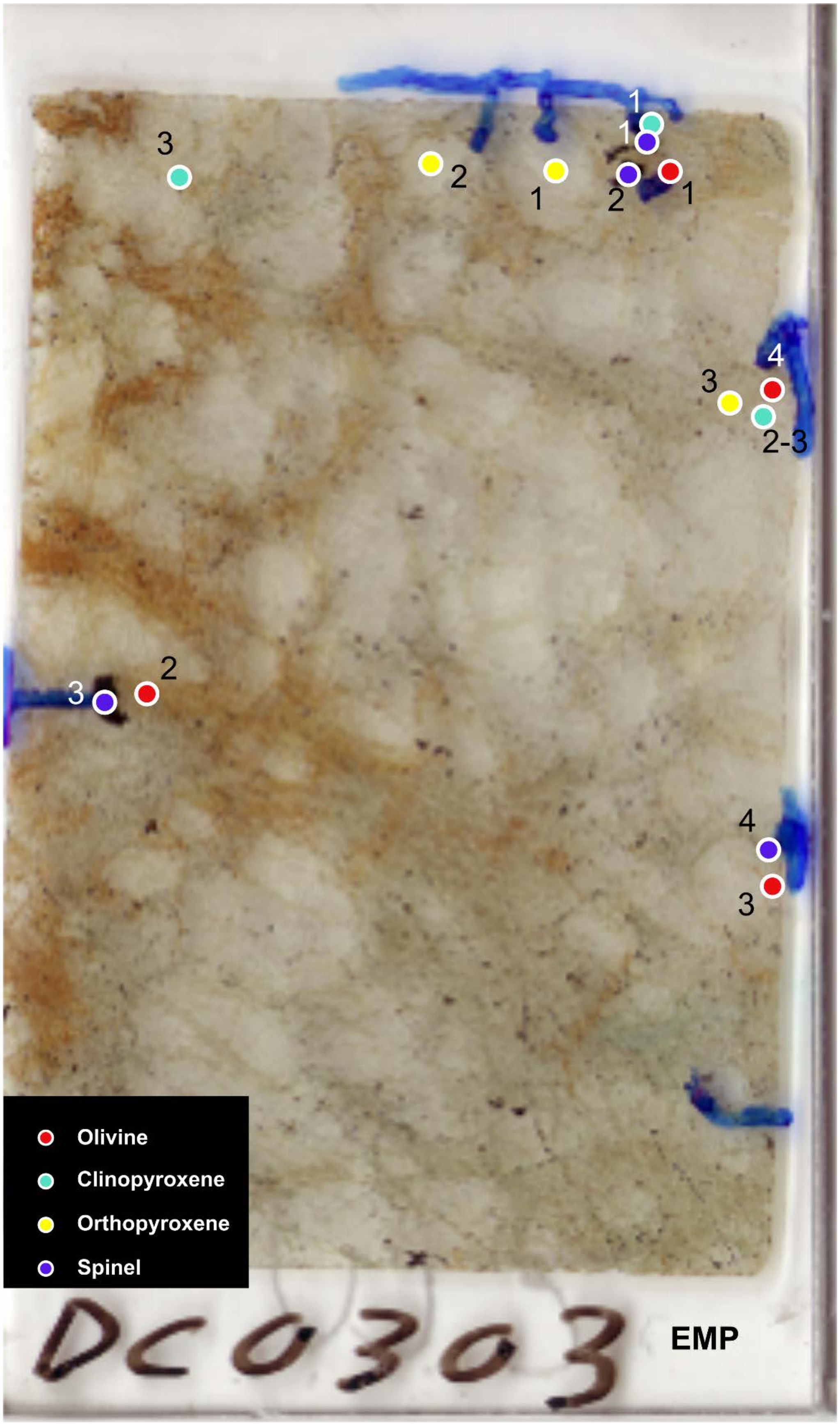
3
2
1
1
1
2
1
4
3
2-3
2
3
4
3
Olivine
Clinopyroxene
Orthopyroxene
Spinel
DC0303
EMP

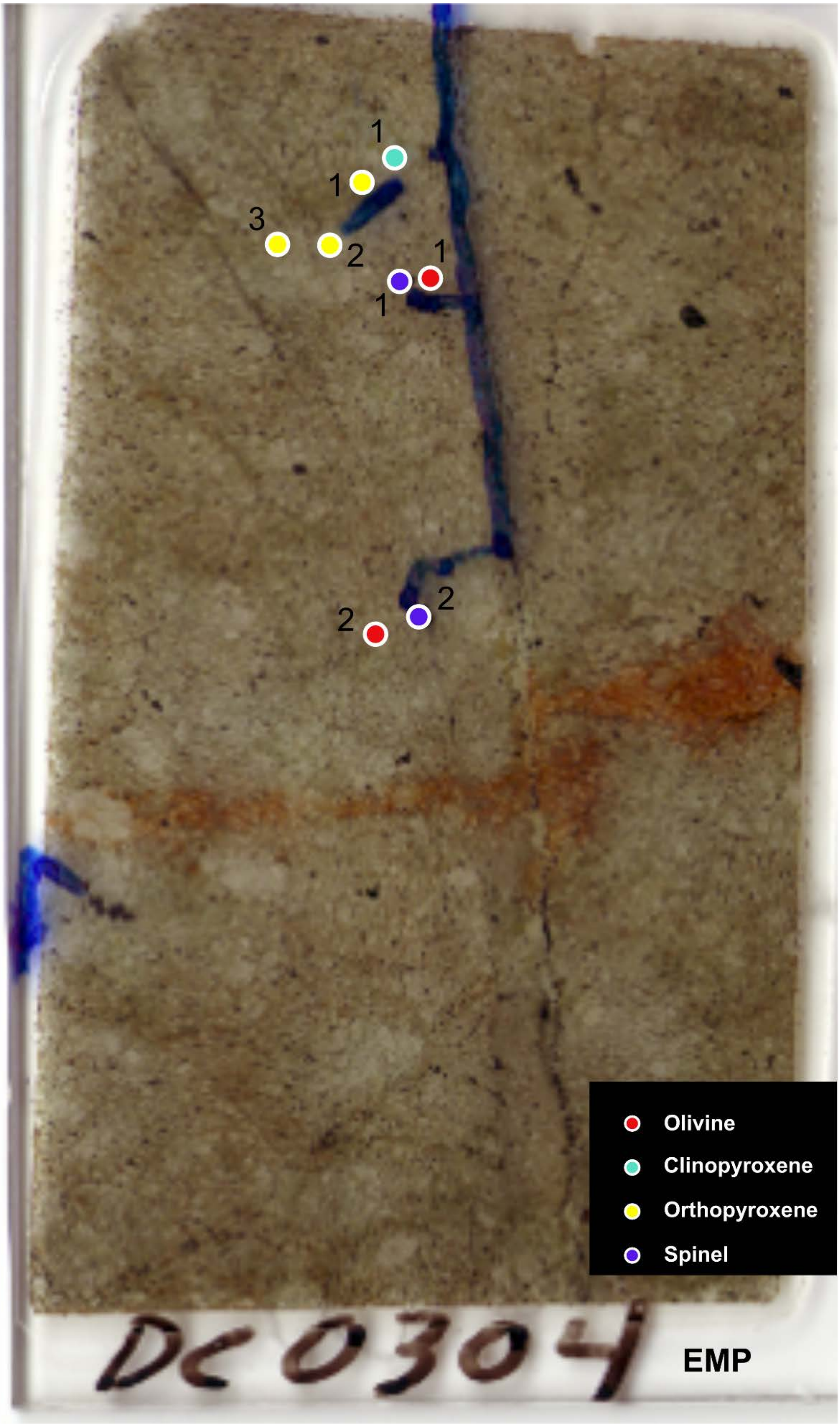
1
1
3
2
1
1
2
2
● Olivine
● Clinopyroxene
● Orthopyroxene
● Spinel
DC0304
EMP

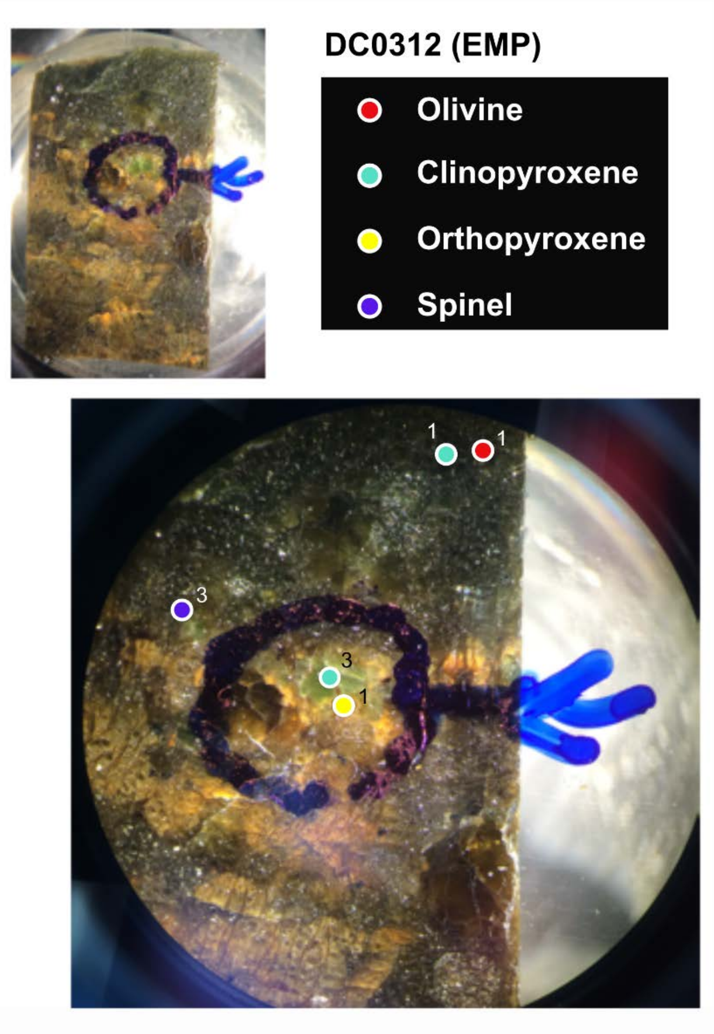
DC0312 (EMP)
Olivine
Clinopyroxene
Orthopyroxene
Spinel
1
1
3
3
1

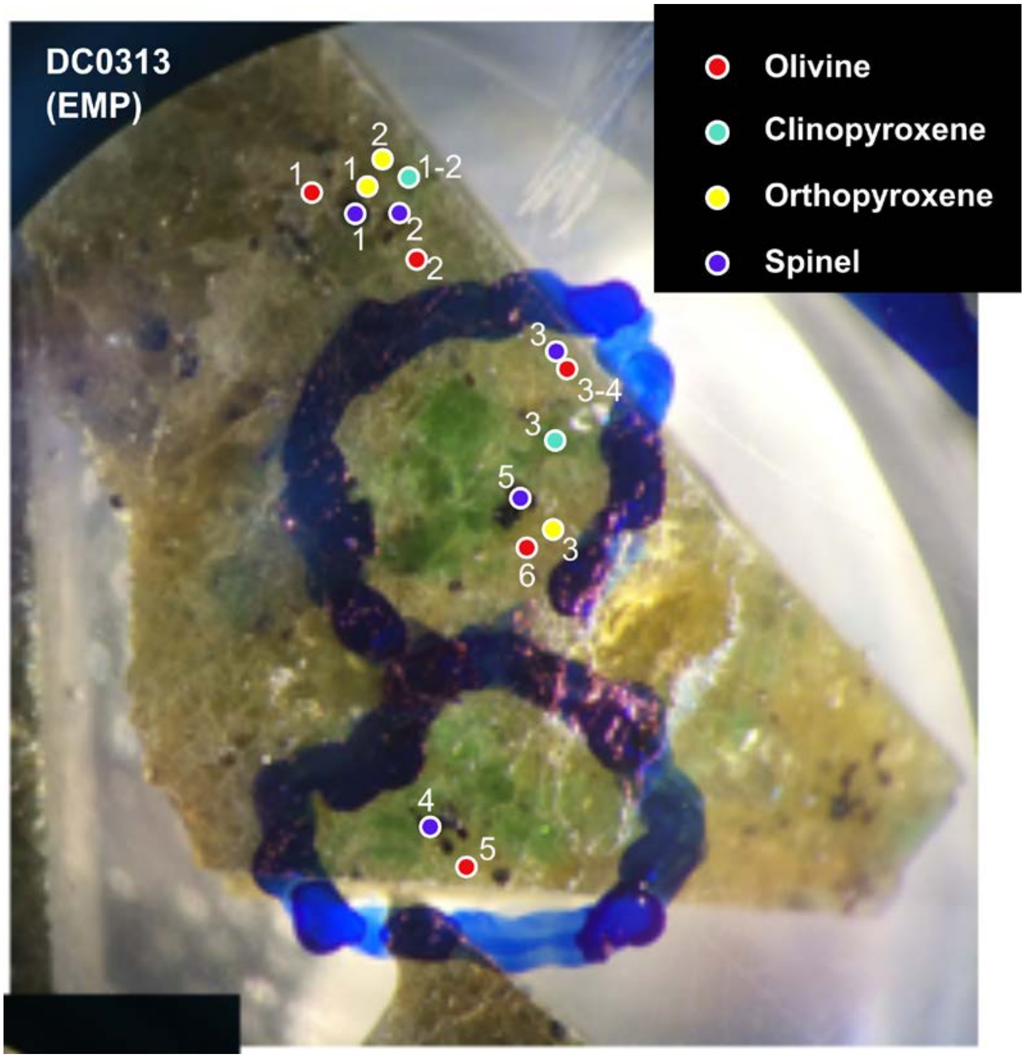
DC0313
(EMP)
● Olivine
● Clinopyroxene
● Orthopyroxene
● Spinel
2
1
1
1-2
1
2
2
3
3-4
3
5
3
6
4
5

DC0318 (EMP)

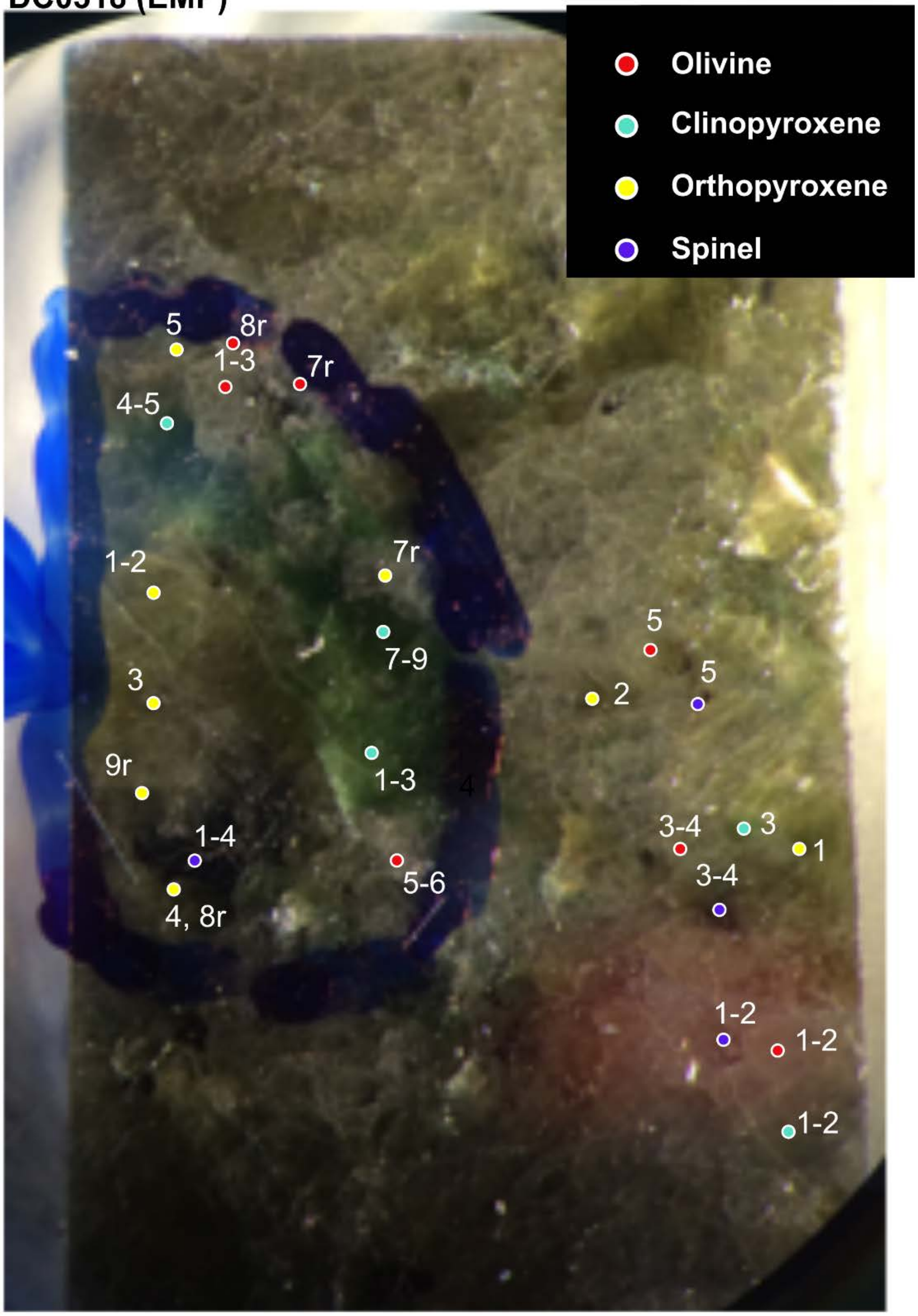
Olivine
Clinopyroxene
Orthopyroxene
Spinel
5
8r
1-3
7r
4-5
1-2
7r
7-9
3
9r
1-3
4
1-4
4, 8r
5-6
5
2
5
3-4
3
1
3-4
1-2
1-2
1-2

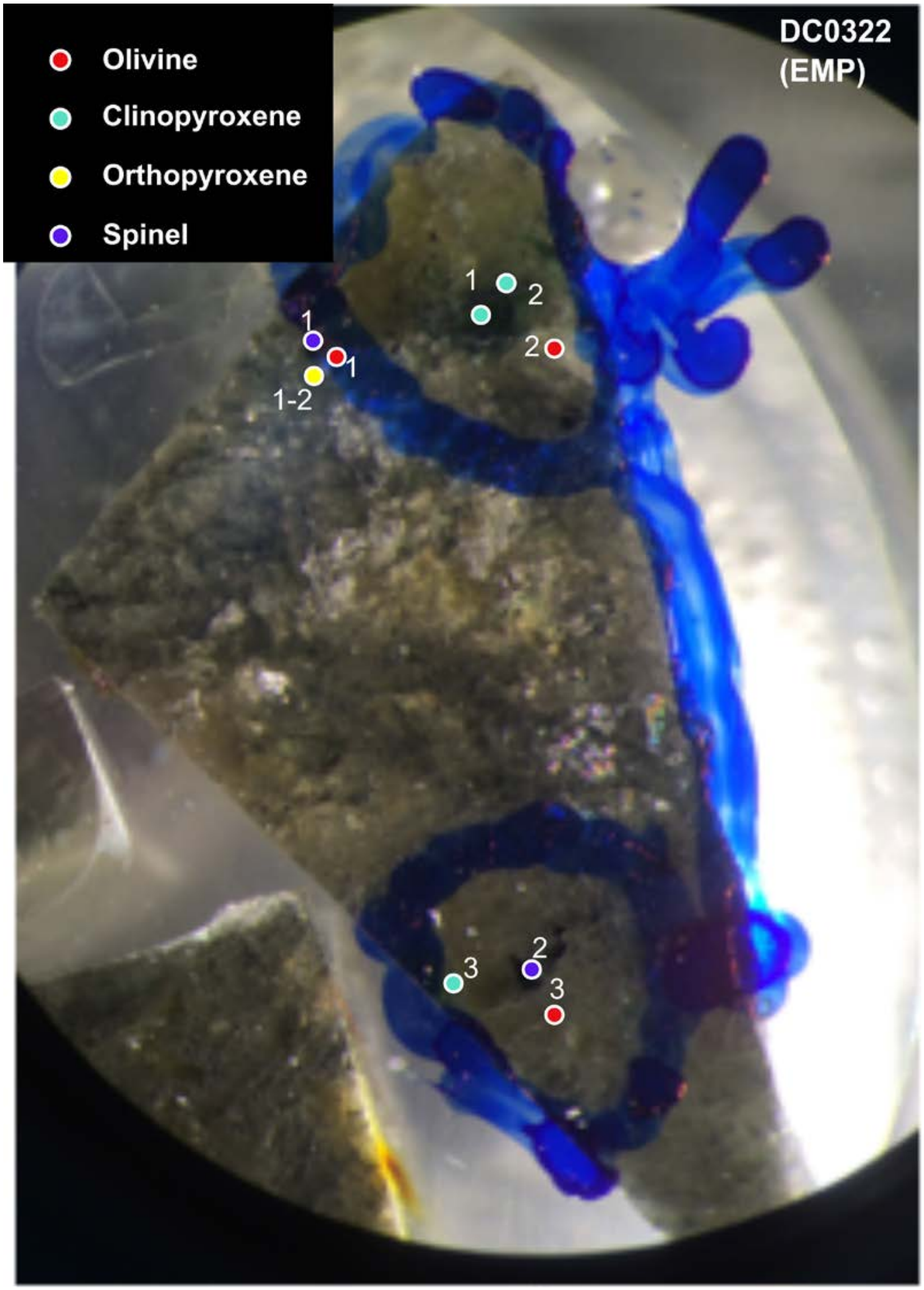
Olivine
Clinopyroxene
Orthopyroxene
Spinel
DC0322
(EMP)
1
1
1-2
1
2
2
2
3
2
3

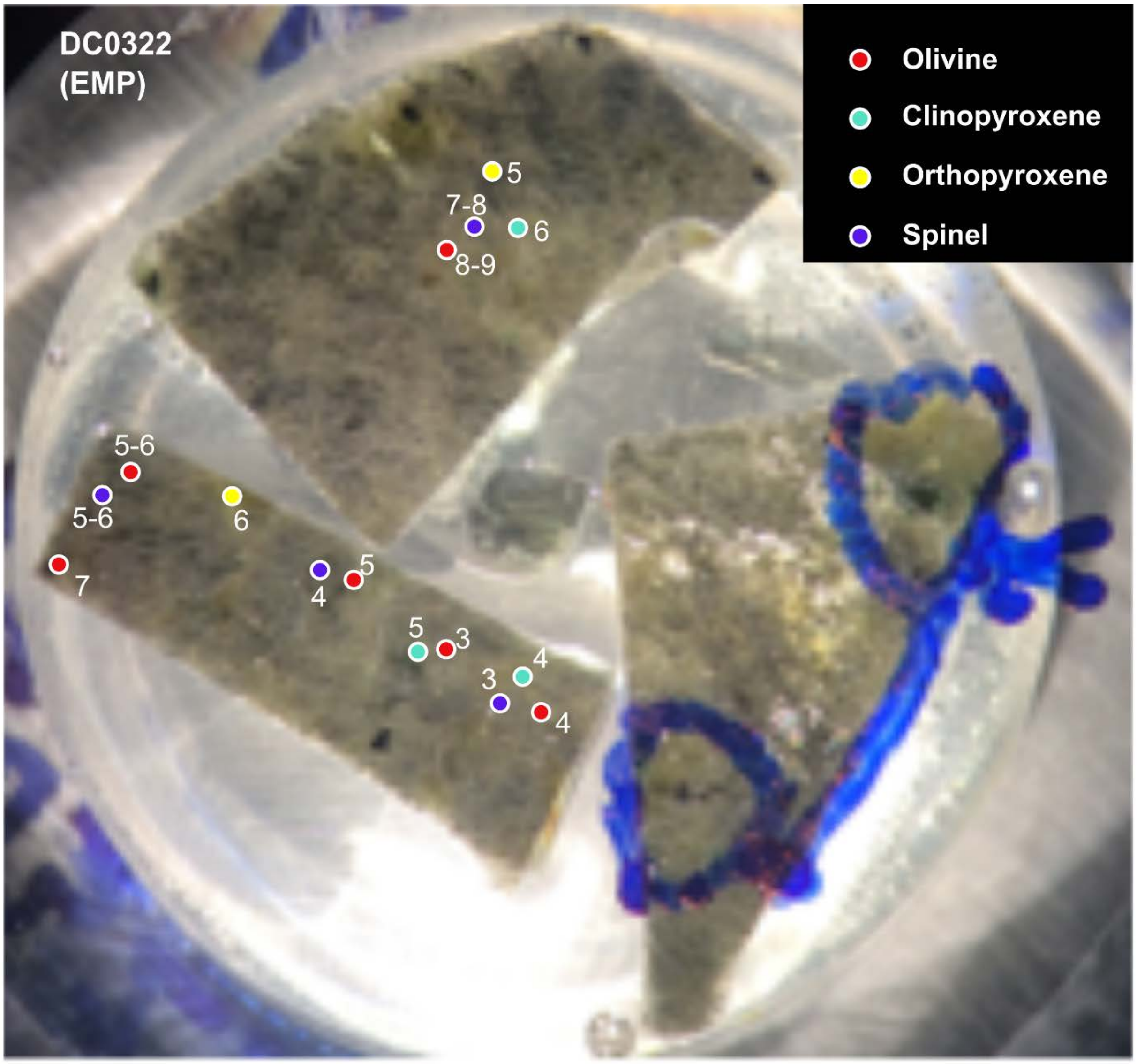
DC0322
(EMP)
● Olivine
● Clinopyroxene
● Orthopyroxene
● Spinel
5
7-8
6
8-9
5-6
5-6
6
7
5
4
5
3
4
3
4

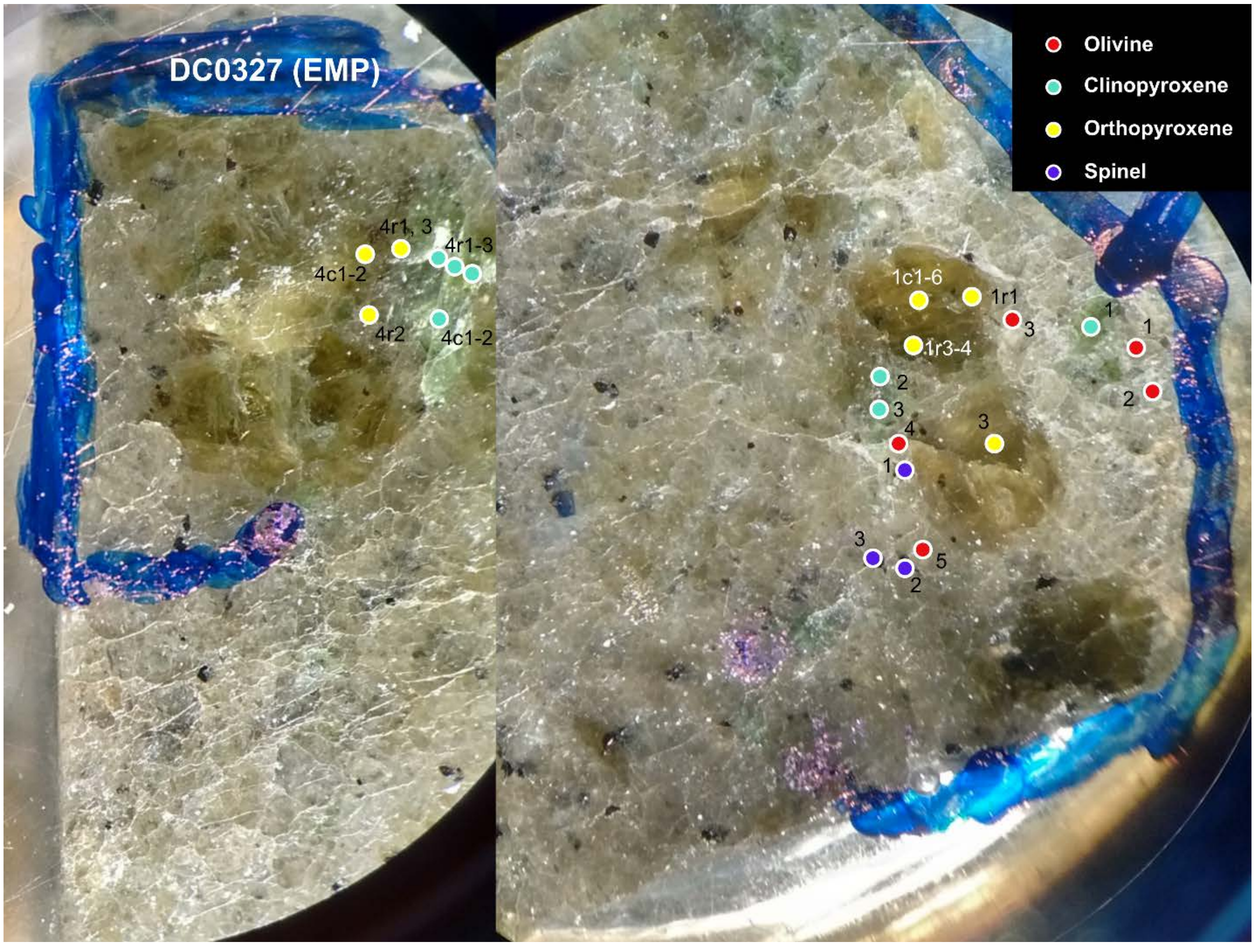
DC0327 (EMP)
● Olivine
● Clinopyroxene
● Orthopyroxene
● Spinel
4r1, 3
4r1-3
4c1-2
4r2
4c1-2
1c1-6
1r1
3
1
1
1r3-4
2
2
3
3
4
1
3
5
2

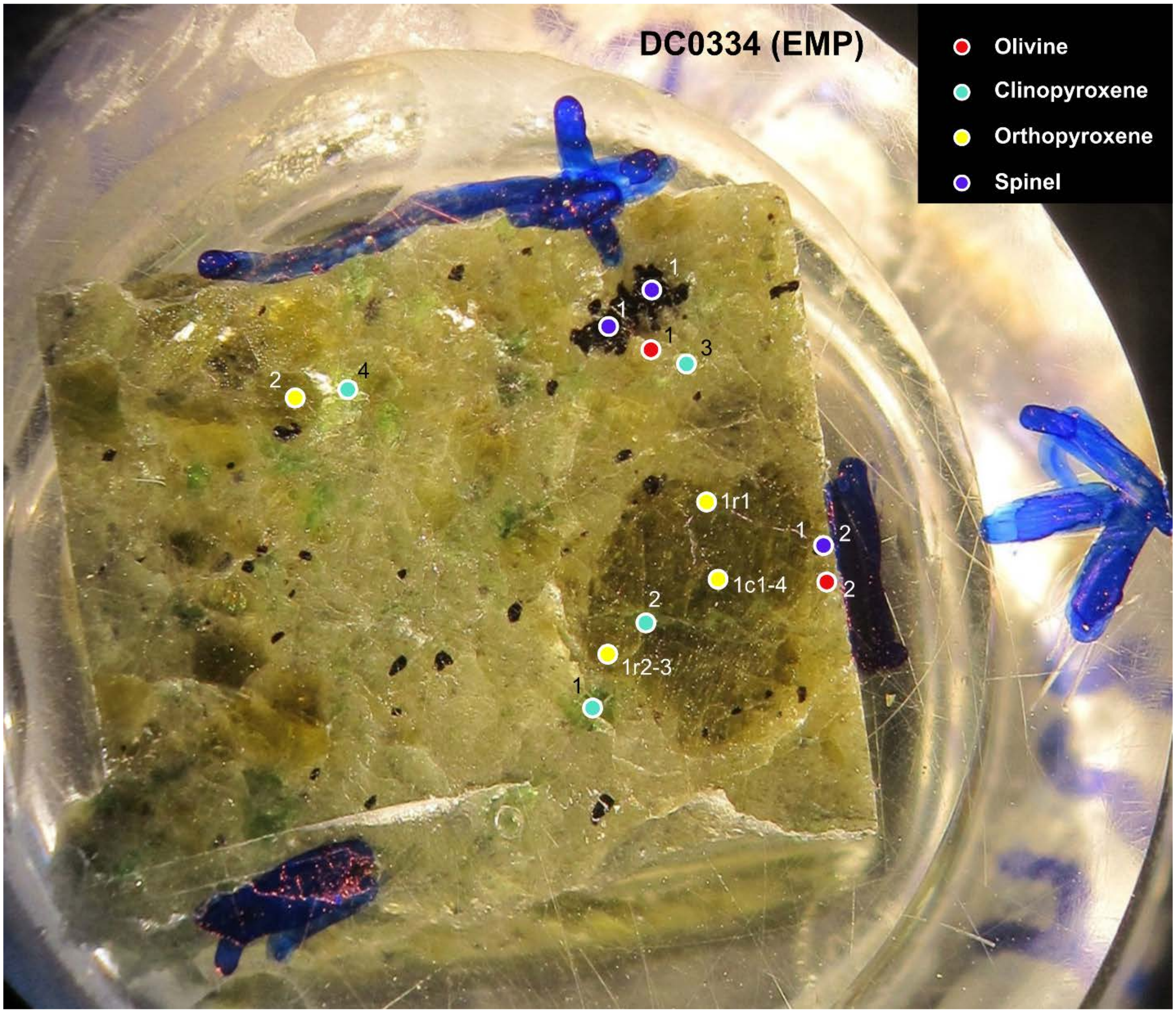
DC0334 (EMP)
● Olivine
● Clinopyroxene
● Orthopyroxene
● Spinel
1
1
1
3
2
4
1r1
1
2
1c1-4
2
2
1r2-3
1

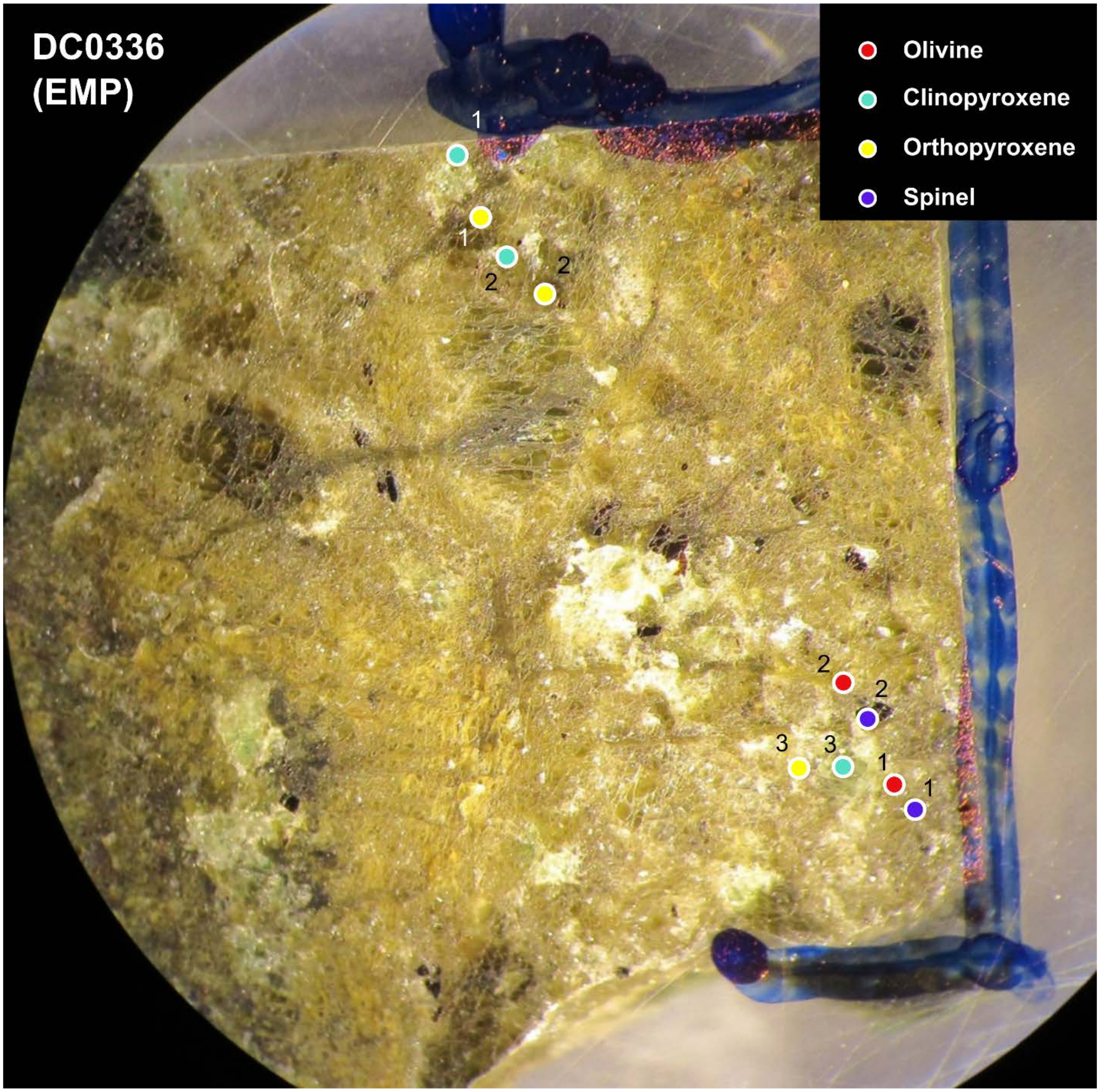
DC0336
(EMP)
● Olivine
● Clinopyroxene
● Orthopyroxene
● Spinel
1
1
2
2
2
2
3
3
1
1

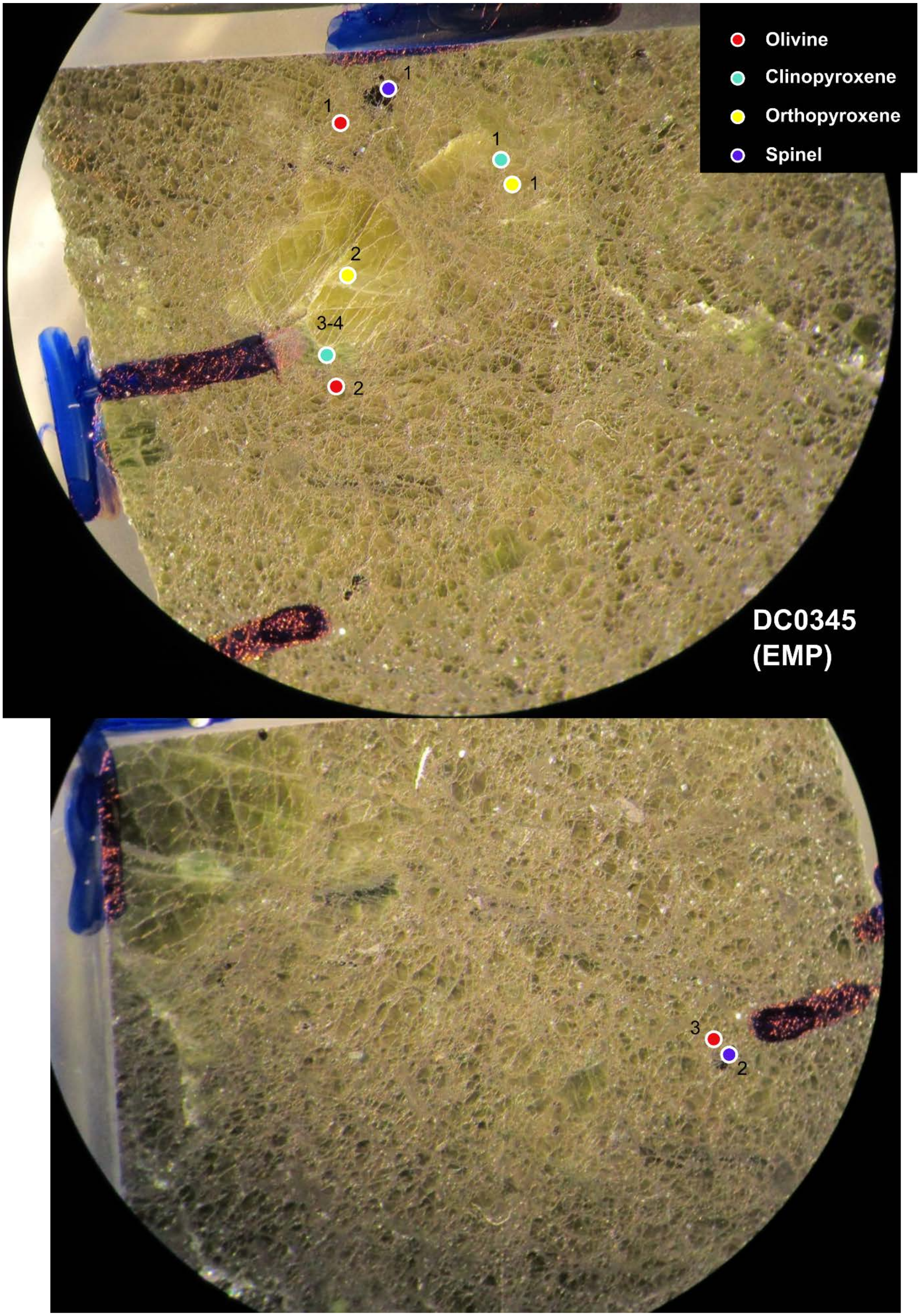
● Olivine
● Clinopyroxene
● Orthopyroxene
● Spinel
1
1
1
1
2
3-4
2
DC0345
(EMP)
3
2


● Olivine
● Clinopyroxene
● Orthopyroxene
● Spinel
1
2
1
2
4
2
3
1
1
2
EMP
15SM023

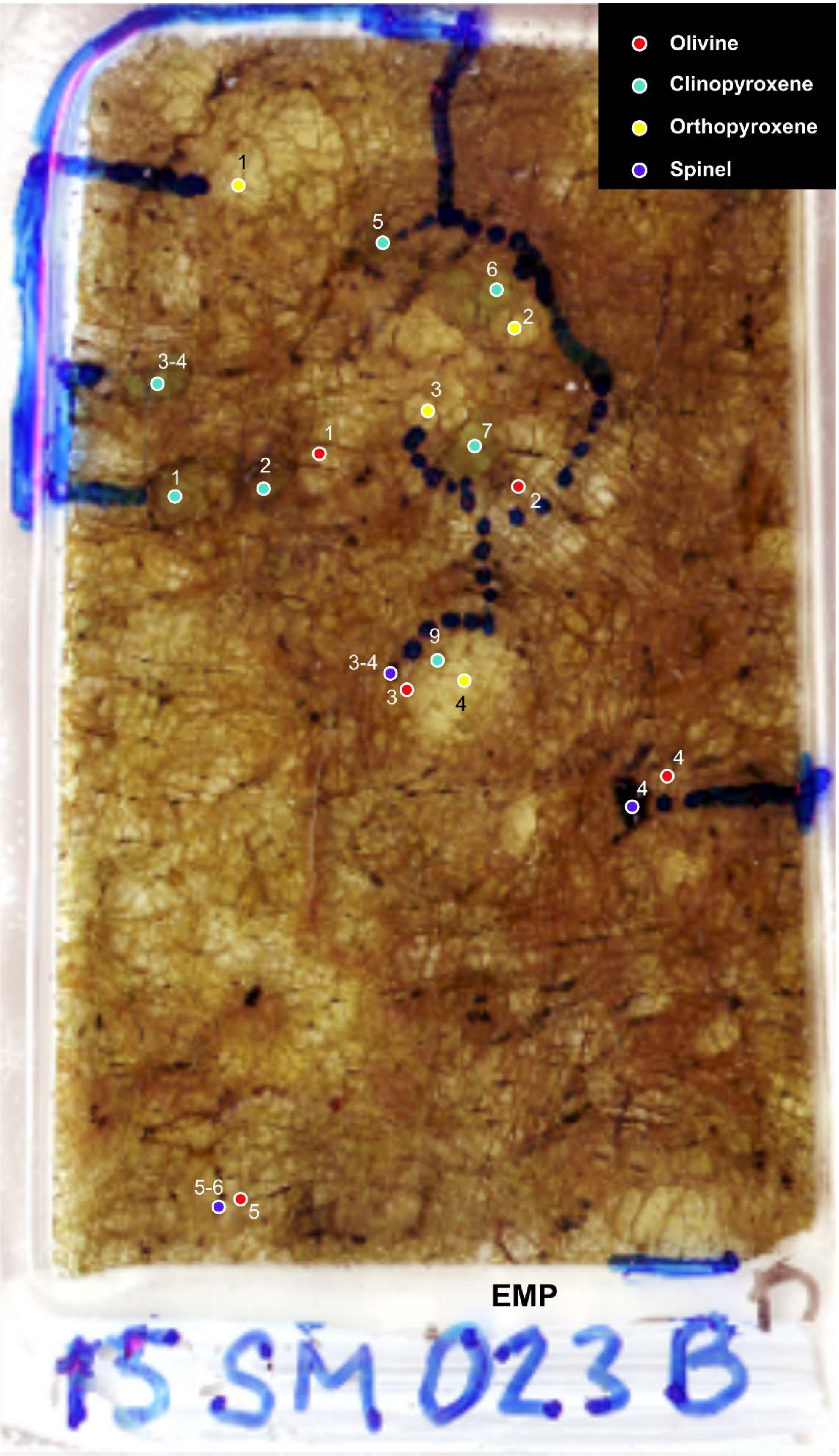
● Olivine
● Clinopyroxene
● Orthopyroxene
● Spinel
1
5
6
2
3-4
3
7
1
2
1
2
9
3-4
3
4
4
4
5-6
5
EMP
15SM023B

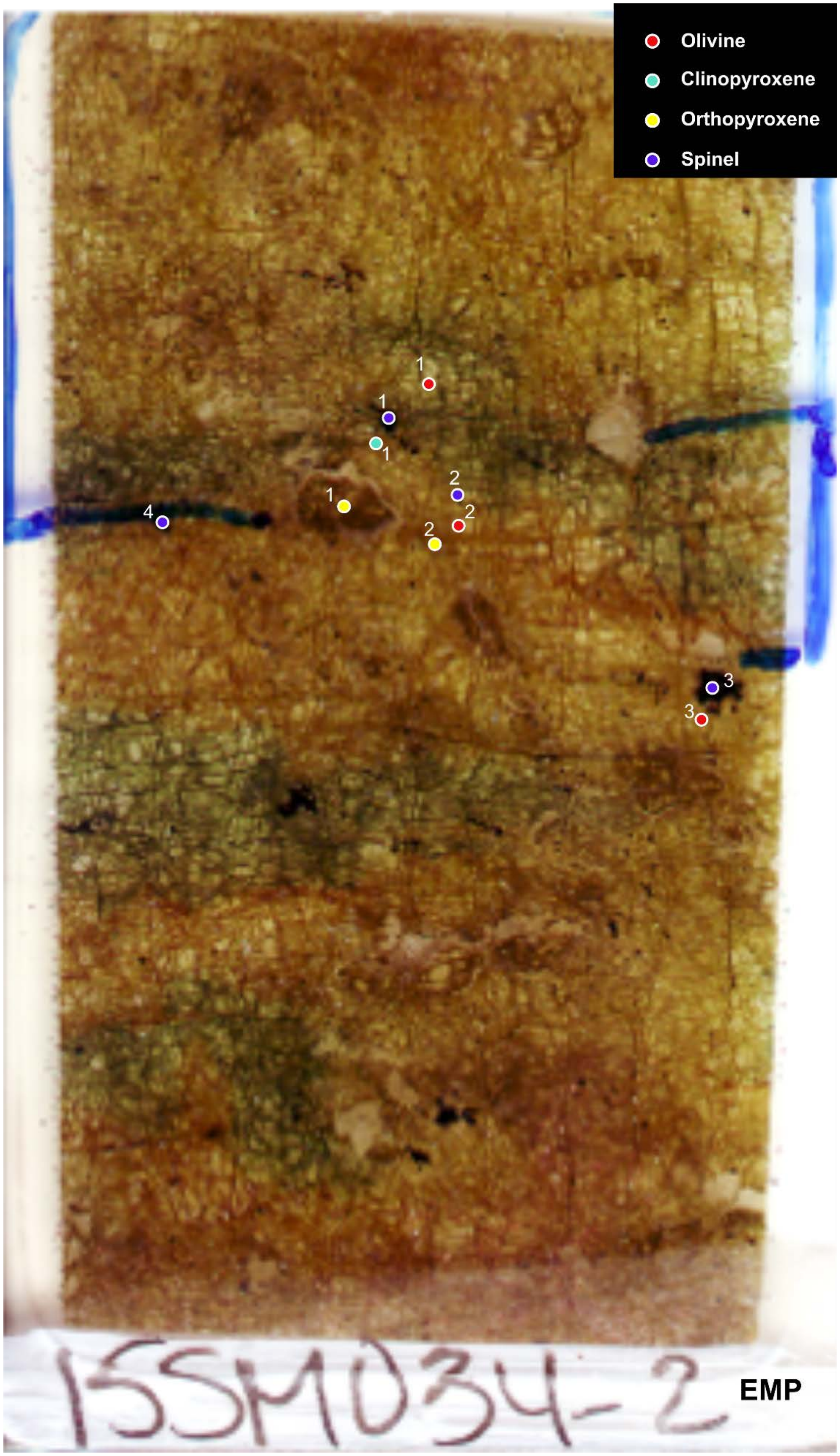
Olivine
Clinopyroxene
Orthopyroxene
Spinel
1
1
1
1
2
2
1
4
2
3
3
15SM034-2
EMP

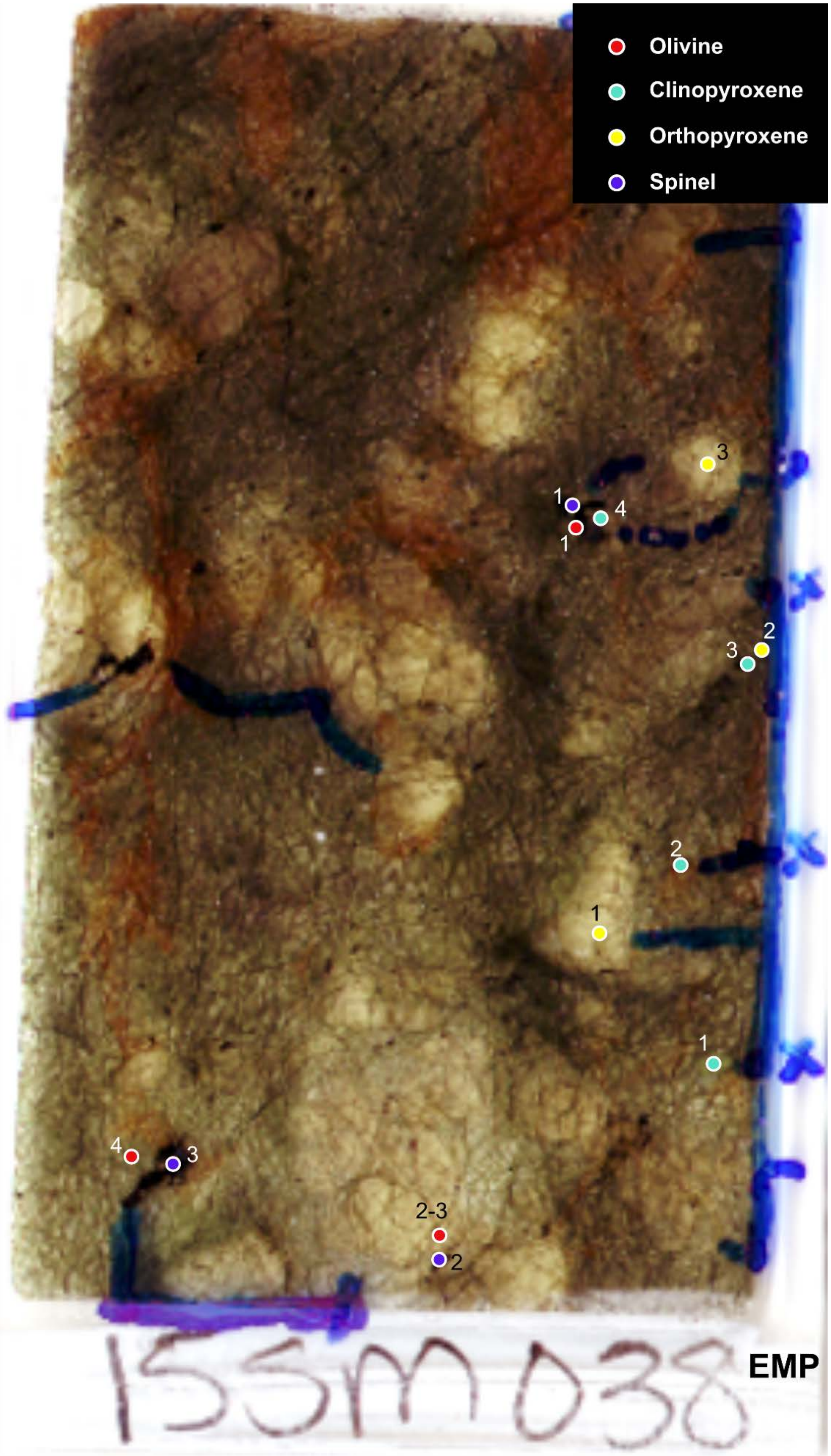
● Olivine
● Clinopyroxene
● Orthopyroxene
● Spinel
3
1
4
1
2
3
2
1
1
4
3
2-3
2
155m038
EMP

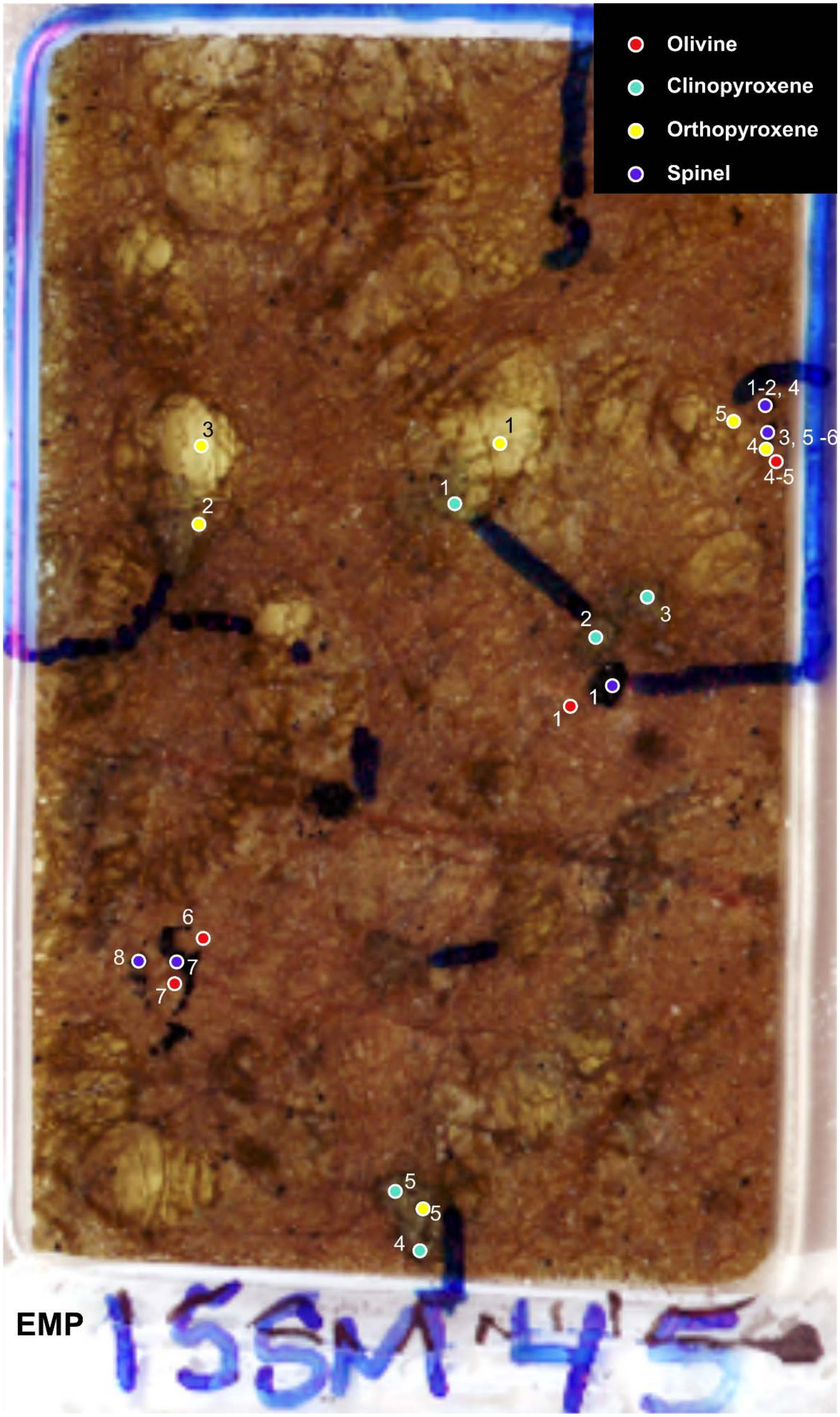
Olivine
Clinopyroxene
Orthopyroxene
Spinel
1-2, 4
5
3, 5 -6
4
4-5
3
1
1
2
3
2
1
1
6
8
7
7
5
5
4
EMP
15SM45

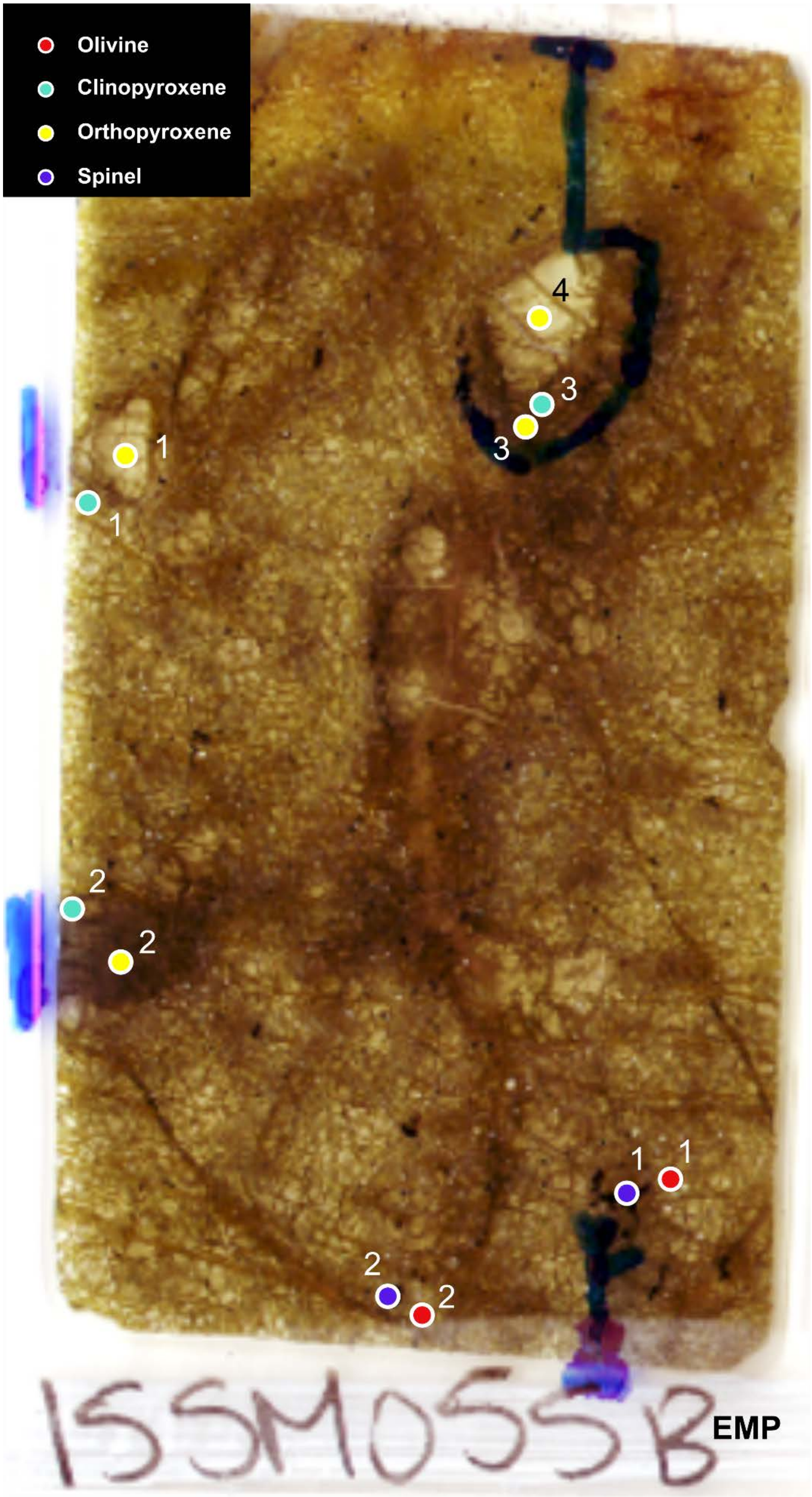
● Olivine
● Clinopyroxene
● Orthopyroxene
● Spinel
4
3
3
1
1
2
2
1
1
2
2
15SM055B
EMP

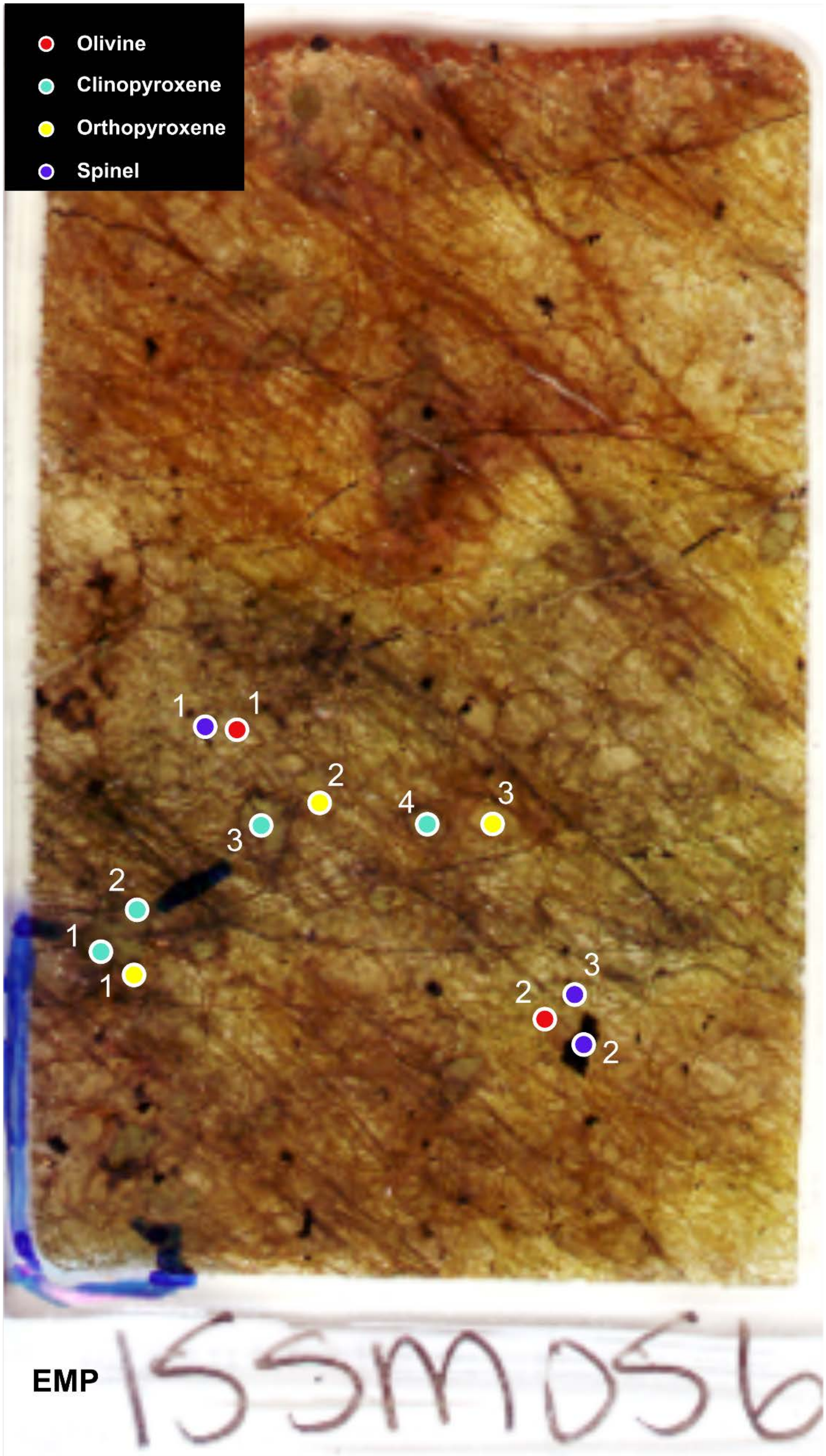
Olivine
Clinopyroxene
Orthopyroxene
Spinel
1
1
2
3
4
3
2
1
1
3
2
2
EMP
15SM056

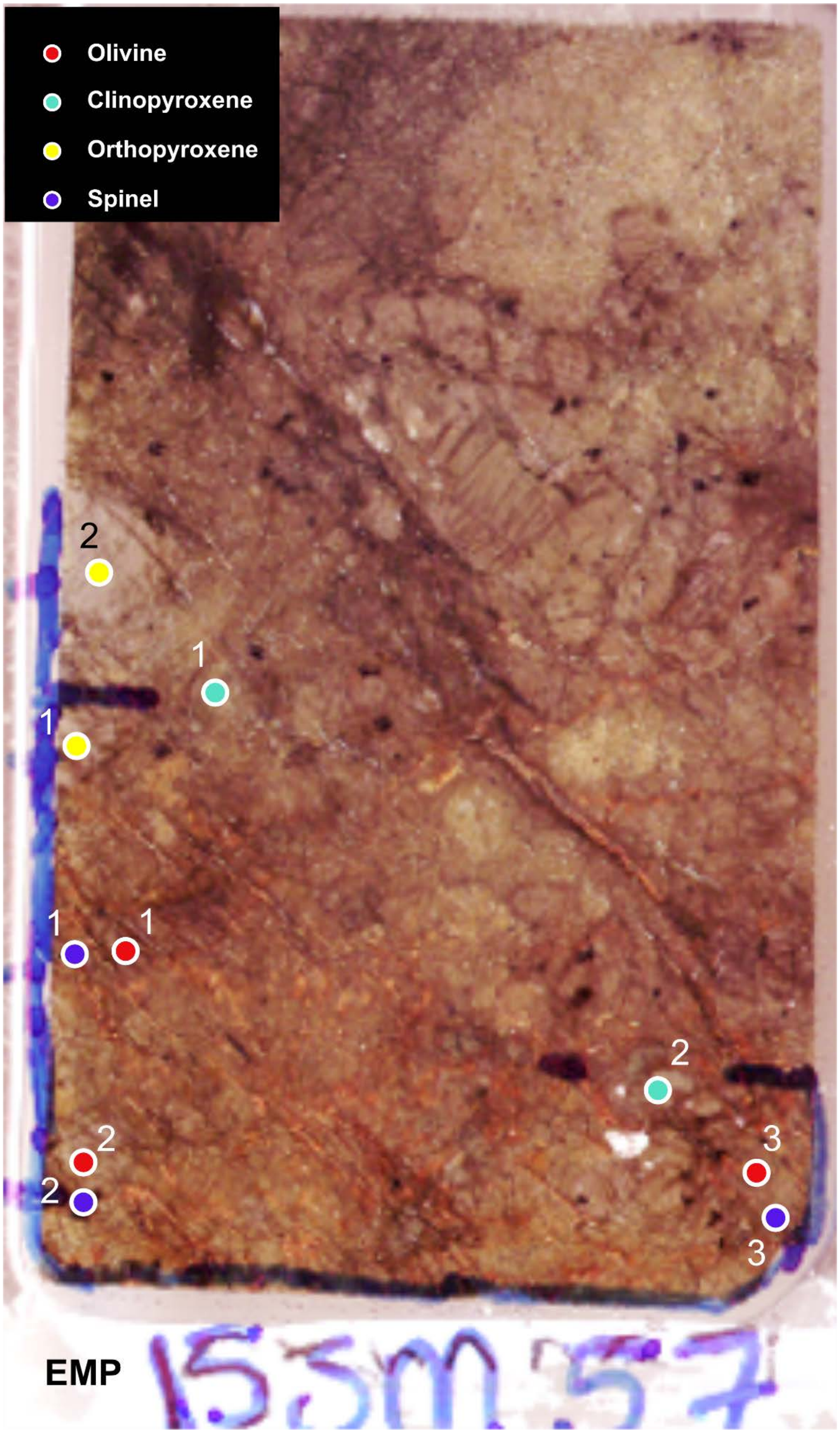
● Olivine
● Clinopyroxene
● Orthopyroxene
● Spinel
2
1
1
1
1
2
2
2
3
3
EMP
155m 57

Figure A 3: Laser ablation ICP-MS analysis locations.

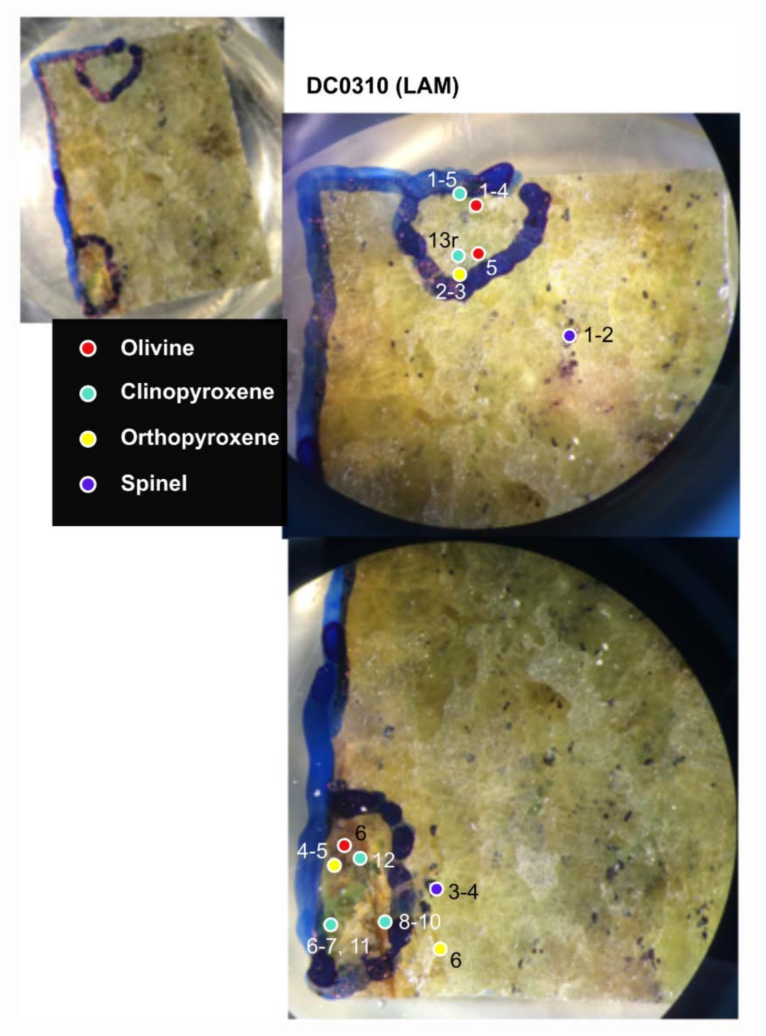

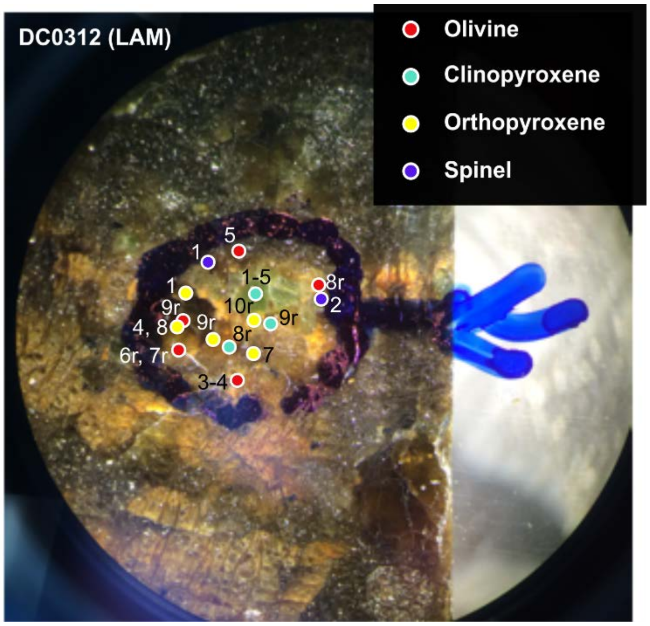
DC0312 (LAM)
● Olivine
● Clinopyroxene
● Orthopyroxene
● Spinel
5
1
1-5
8r
2
1
9r
10r
9r
4, 8
9r
8r
7
6r, 7r
3-4

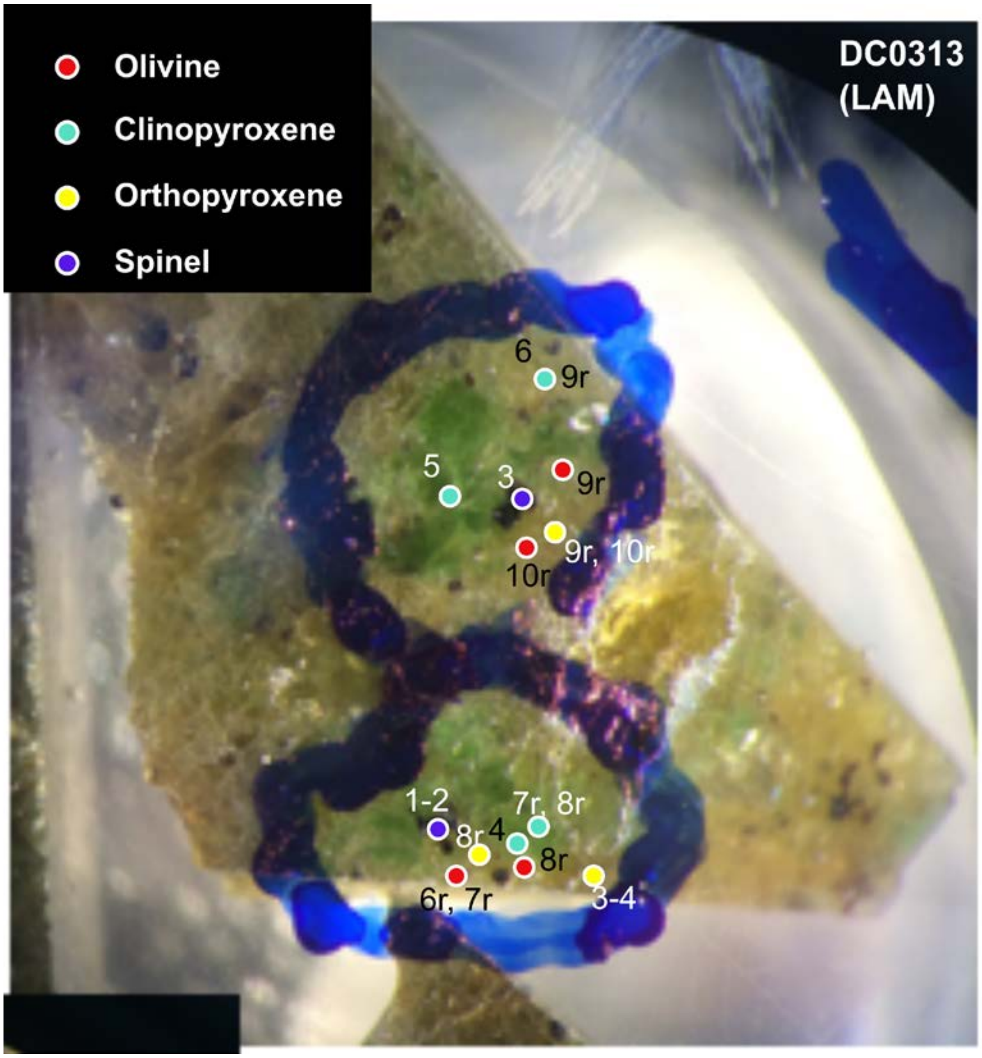
● Olivine
● Clinopyroxene
● Orthopyroxene
● Spinel
DC0313
(LAM)
6
9r
5
3
9r
9r, 10r
10r
1-2
7r, 8r
8r
4
8r
6r, 7r
3-4

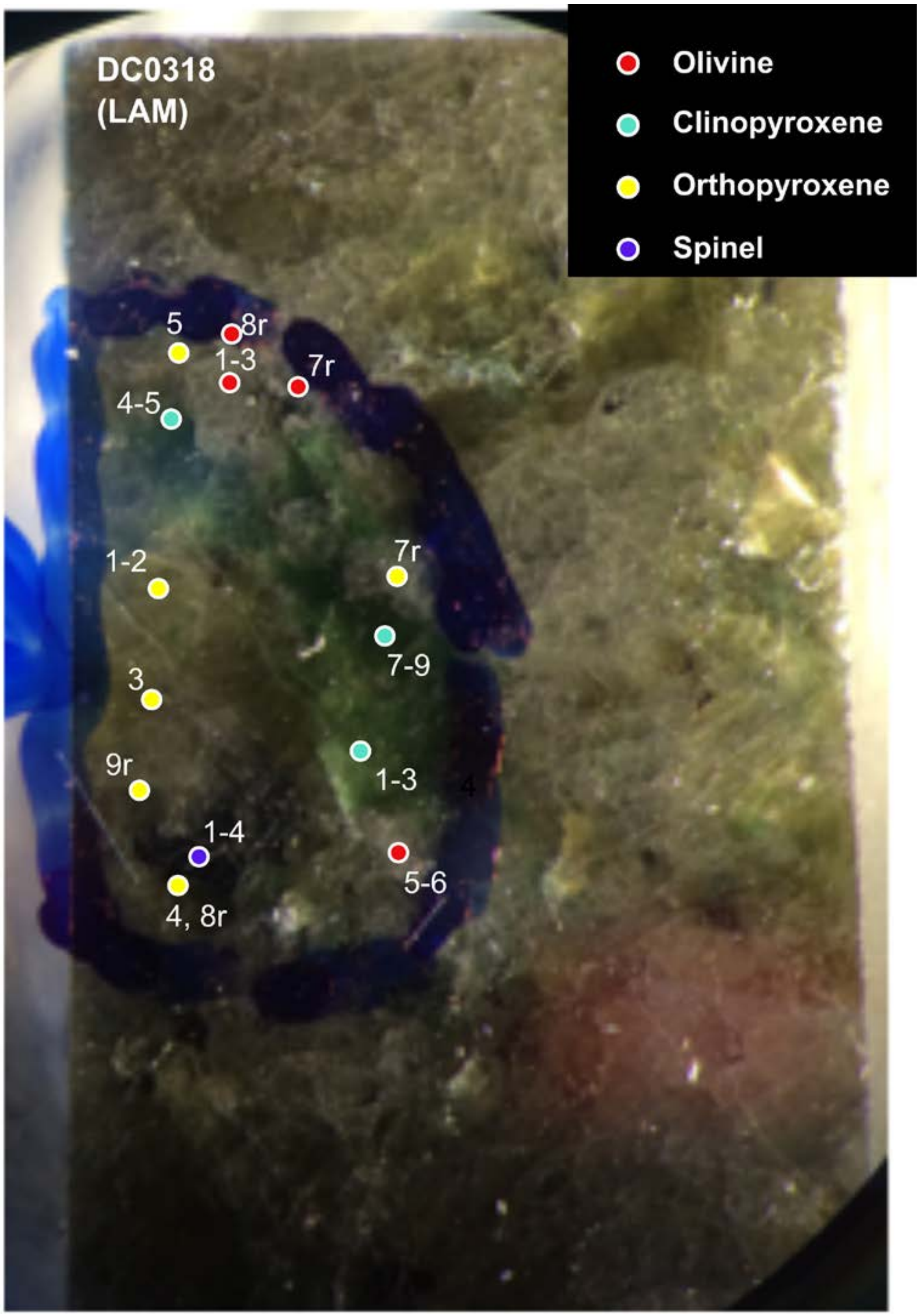
DC0318
(LAM)
● Olivine
● Clinopyroxene
● Orthopyroxene
● Spinel
5
8r
1-3
7r
4-5
1-2
7r
7-9
3
9r
1-3
4
1-4
5-6
4, 8r

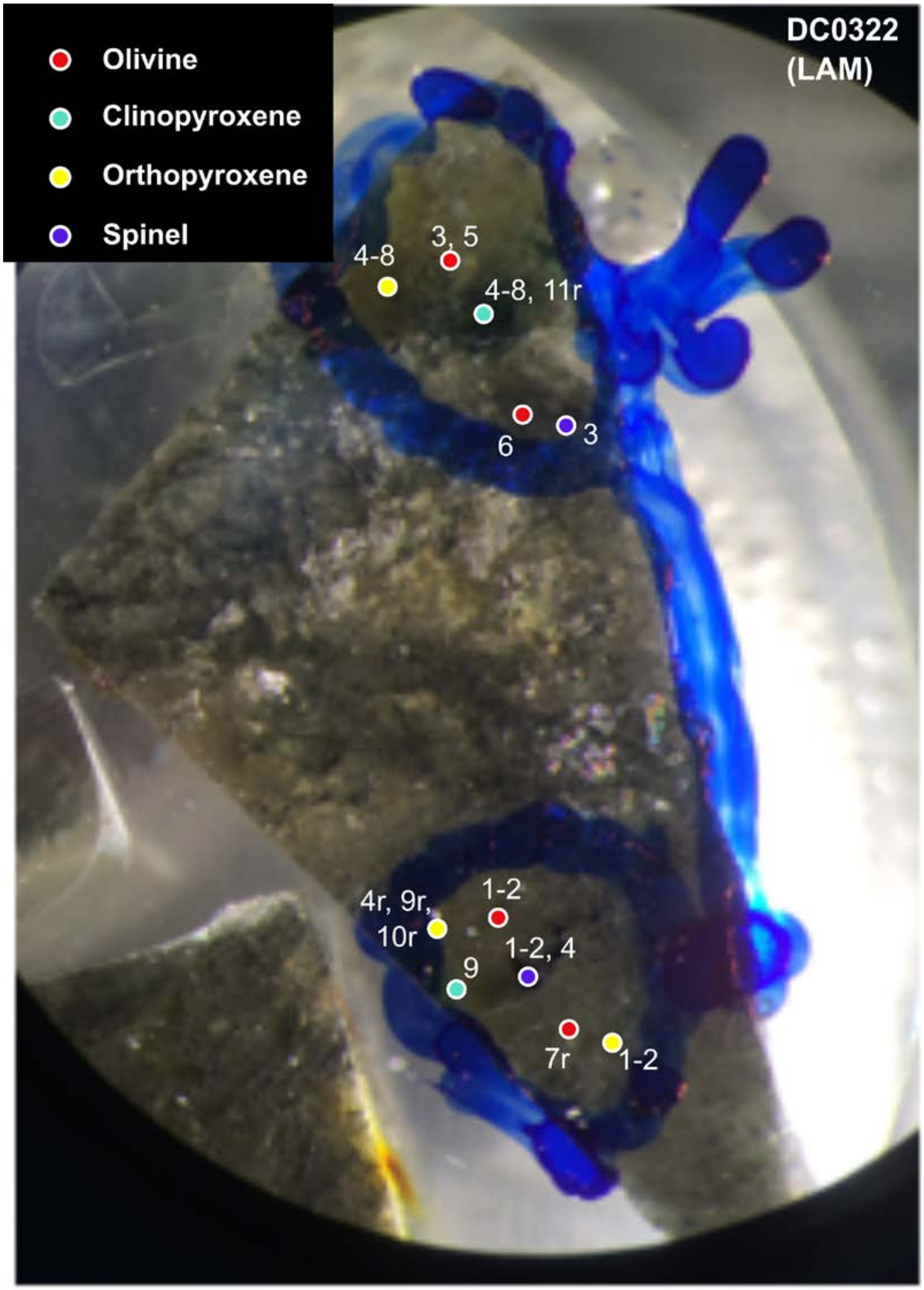
Olivine
Clinopyroxene
Orthopyroxene
Spinel
DC0322
(LAM)
4-8
3, 5
4-8, 11r
6
3
4r, 9r,
10r
1-2
1-2, 4
9
7r
1-2

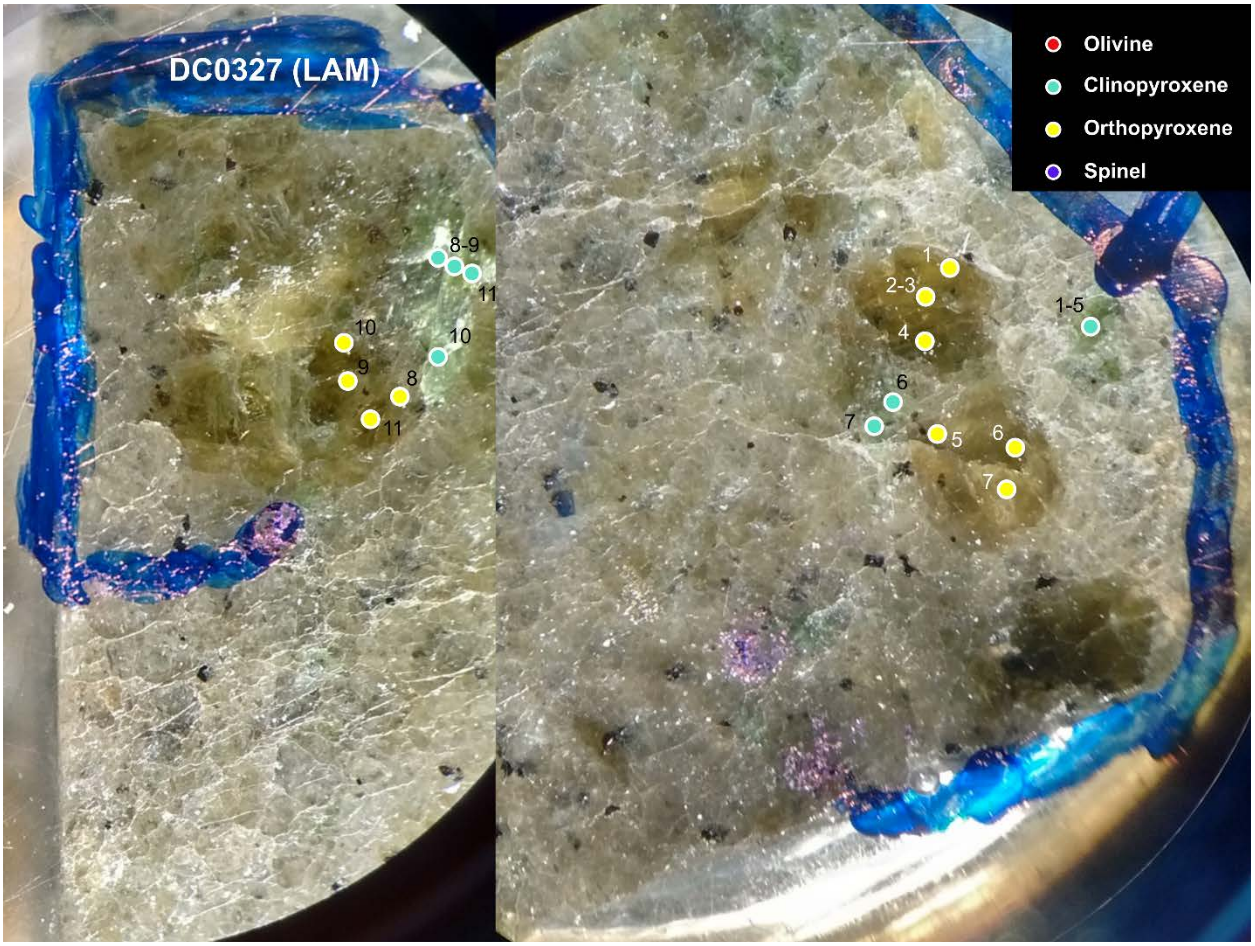
DC0327 (LAM)
Olivine
Clinopyroxene
Orthopyroxene
Spinel
8-9
11
10
10
9
8
11
1
2-3
4
1-5
6
7
5
6
7

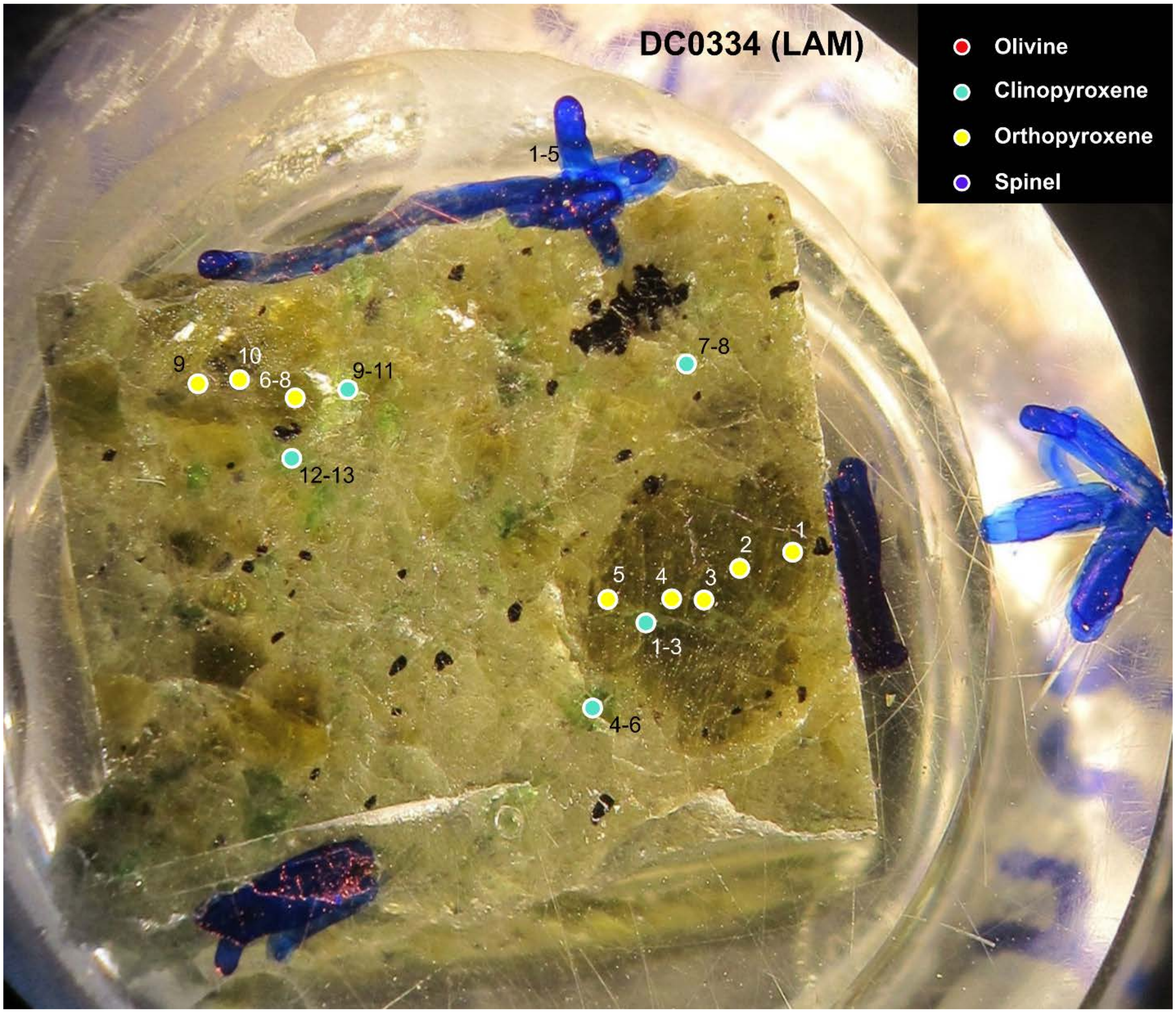
DC0334 (LAM)
Olivine
Clinopyroxene
Orthopyroxene
Spinel
1-5
9
10
6-8
9-11
7-8
12-13
1
2
5
4
3
1-3
4-6

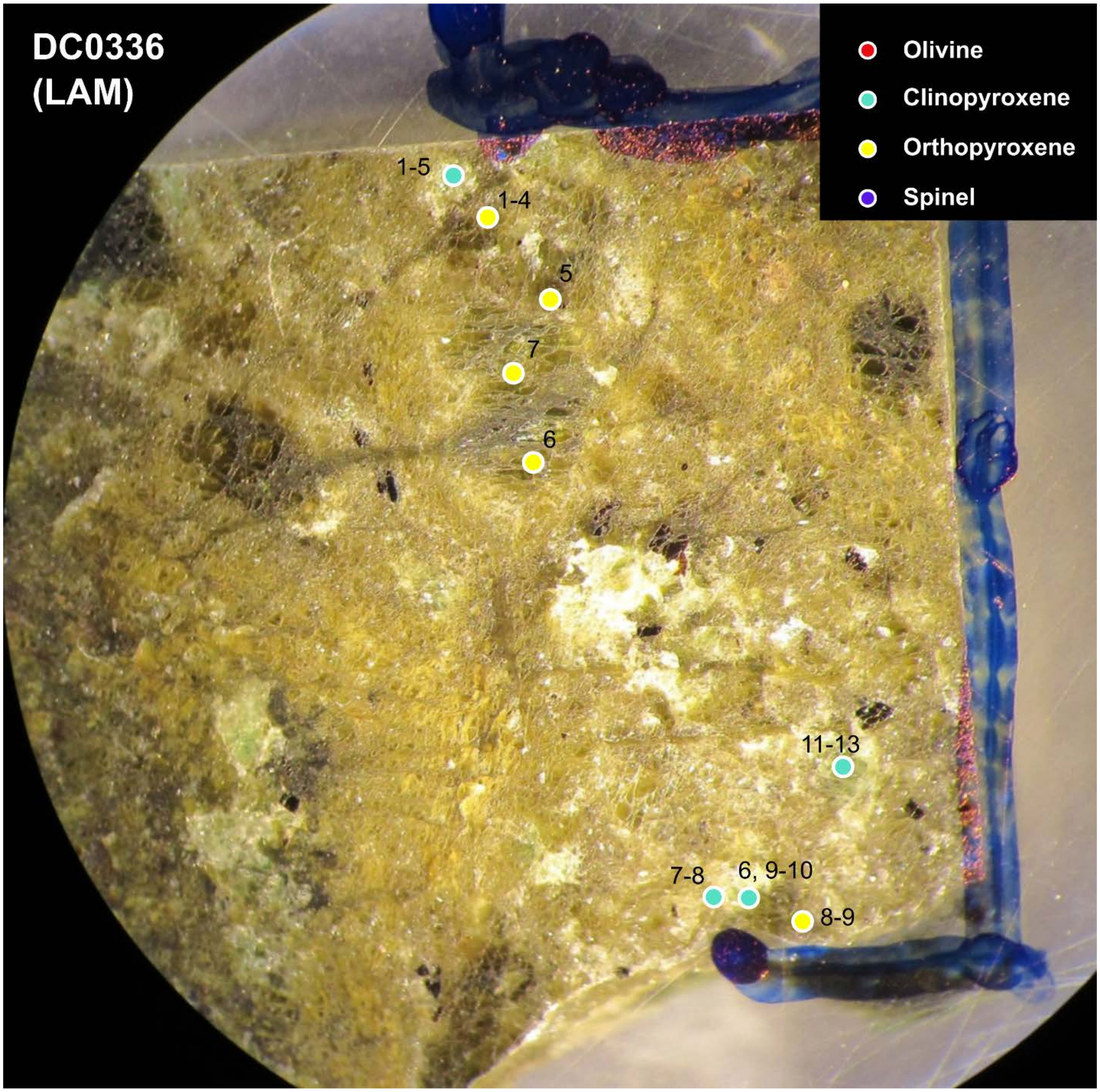
DC0336
(LAM)
● Olivine
● Clinopyroxene
● Orthopyroxene
● Spinel
1-5
1-4
5
7
6
11-13
7-8
6, 9-10
8-9

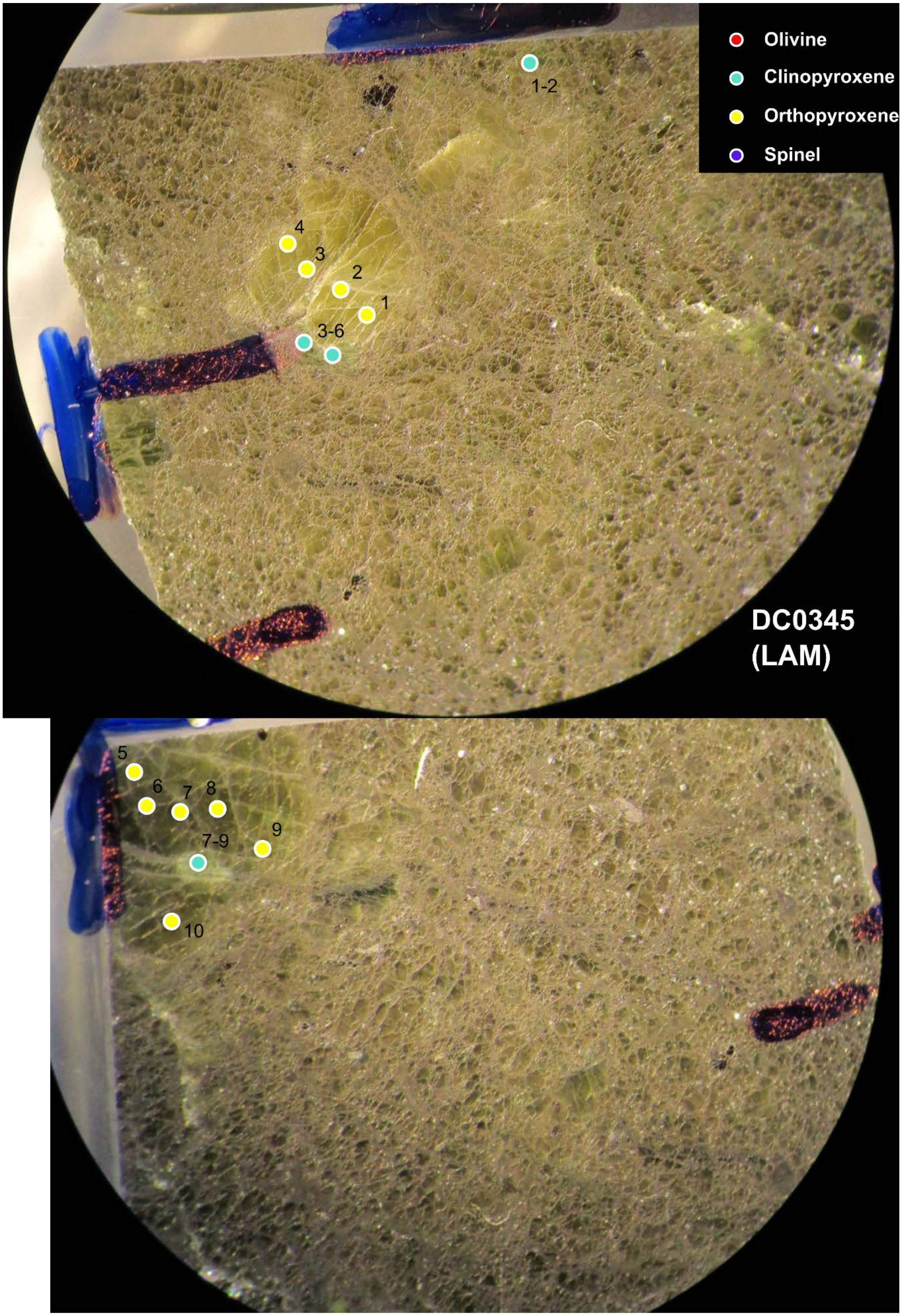
● Olivine
● Clinopyroxene
● Orthopyroxene
● Spinel
1-2
4
3
2
1
3-6
DC0345
(LAM)
5
6
7
8
7-9
9
10

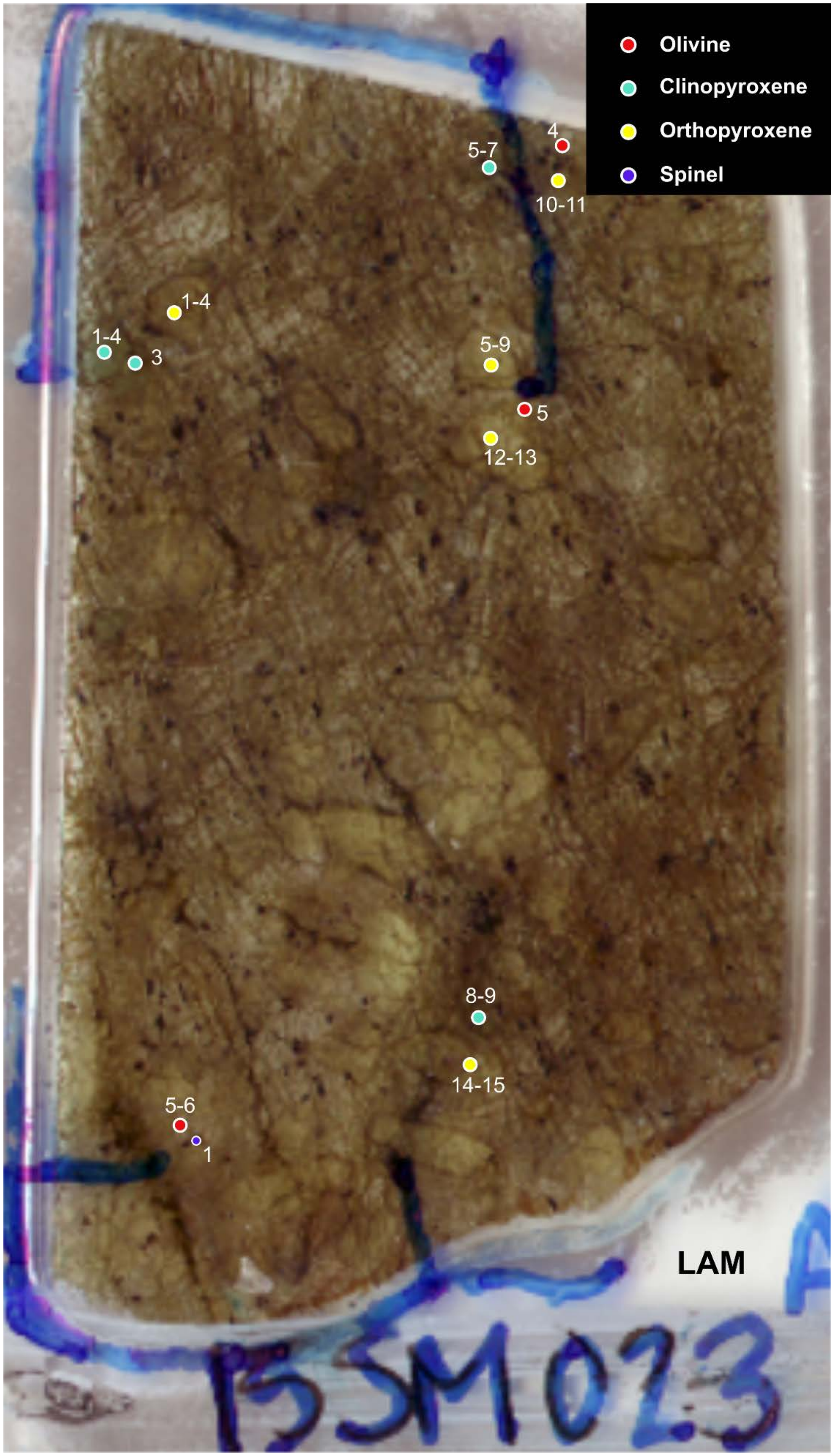
Olivine
Clinopyroxene
Orthopyroxene
Spinel
4
5-7
10-11
1-4
1-4
3
5-9
5
12-13
8-9
14-15
5-6
1
LAM
BSM023

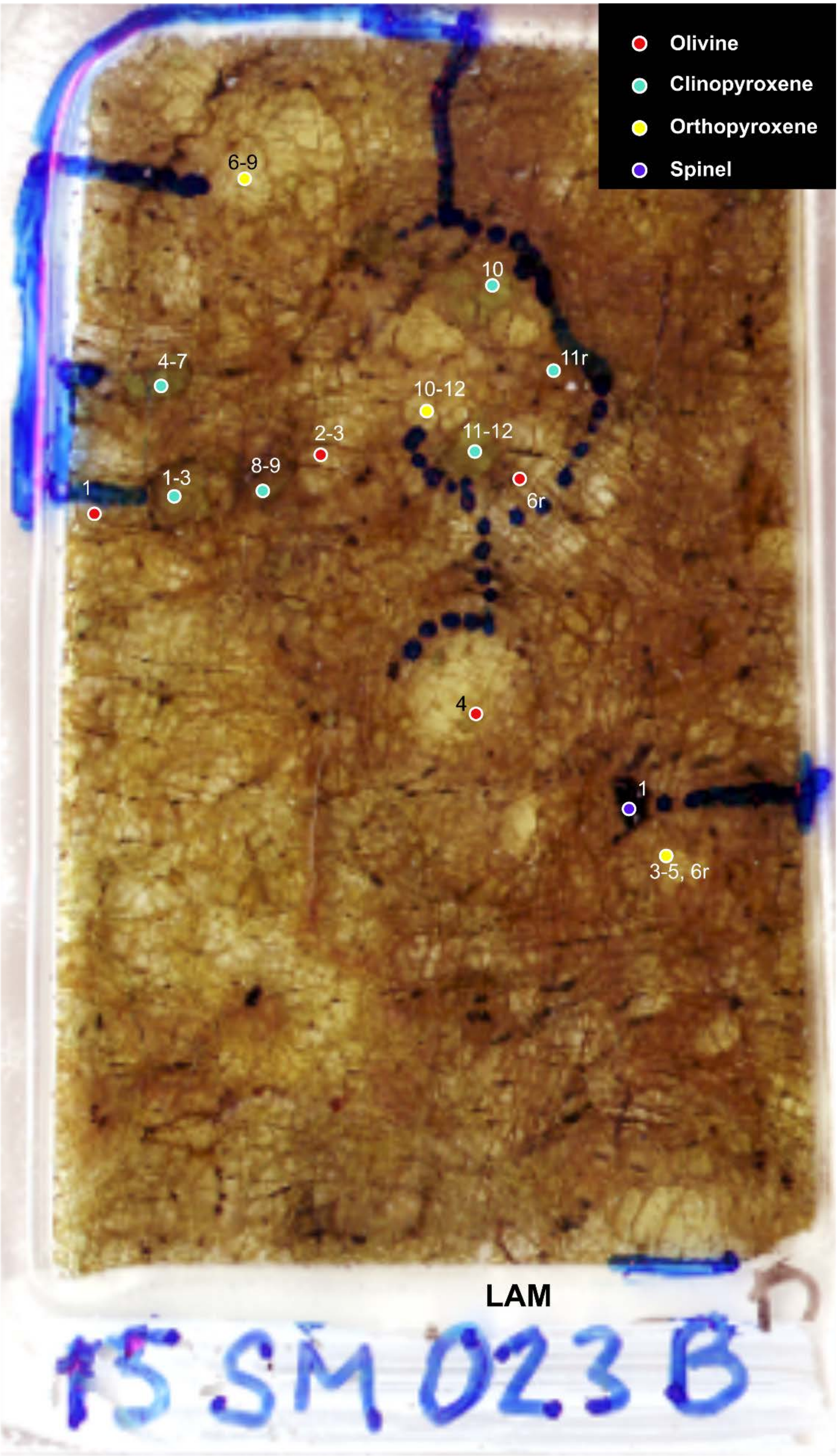
● Olivine
● Clinopyroxene
● Orthopyroxene
● Spinel
6-9
10
4-7
11r
10-12
2-3
11-12
1
1-3
8-9
6r
4
1
3-5, 6r
LAM
15SM023B


● Olivine
● Clinopyroxene
● Orthopyroxene
● Spinel
2-4
1-5
1
15SM034-2
LAM

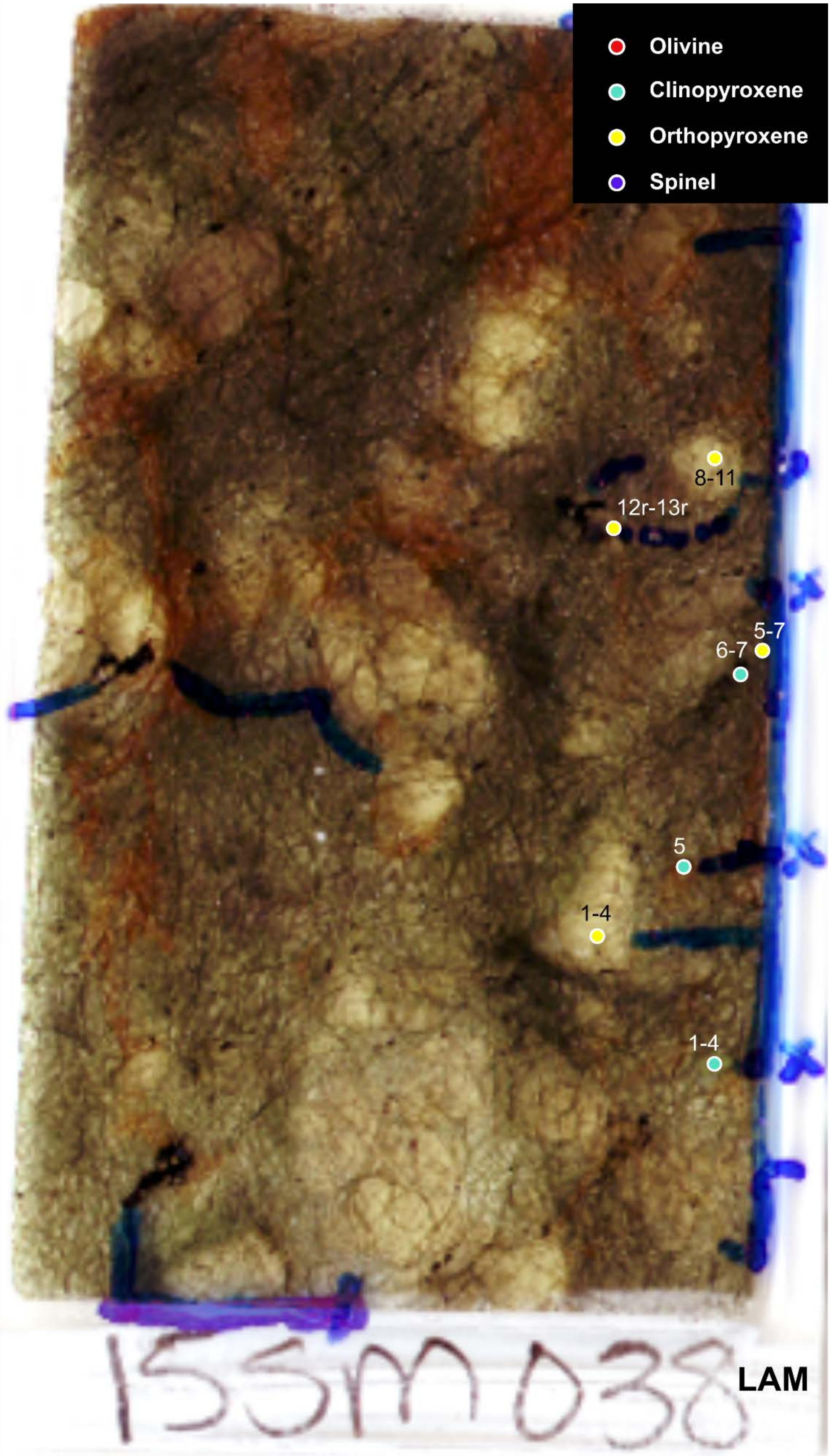
● Olivine
● Clinopyroxene
● Orthopyroxene
● Spinel
8-11
12r-13r
5-7
6-7
5
1-4
1-4
155M038
LAM

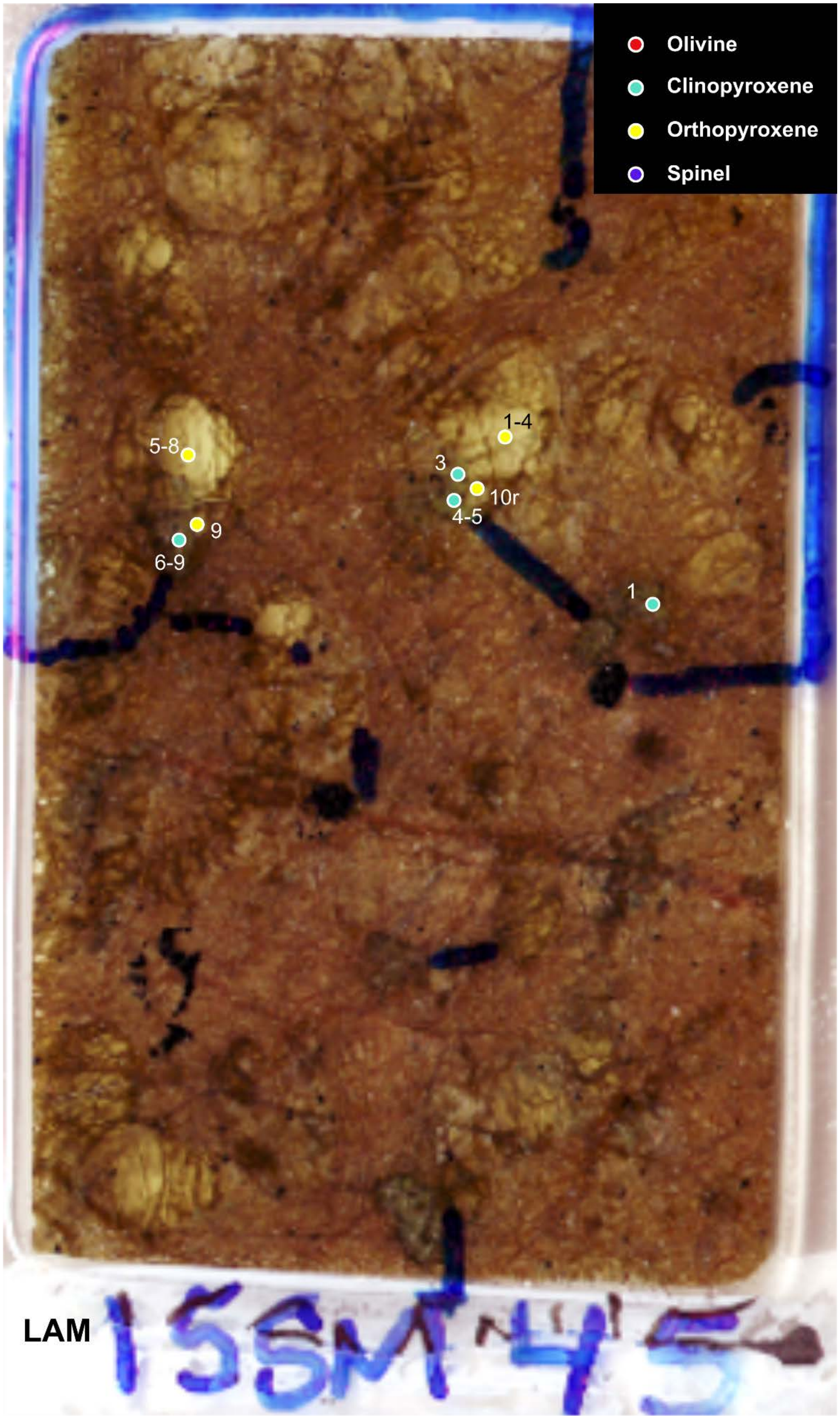
Olivine
Clinopyroxene
Orthopyroxene
Spinel
1-4
5-8
3
10r
4-5
9
6-9
1
LAM
15SM 45

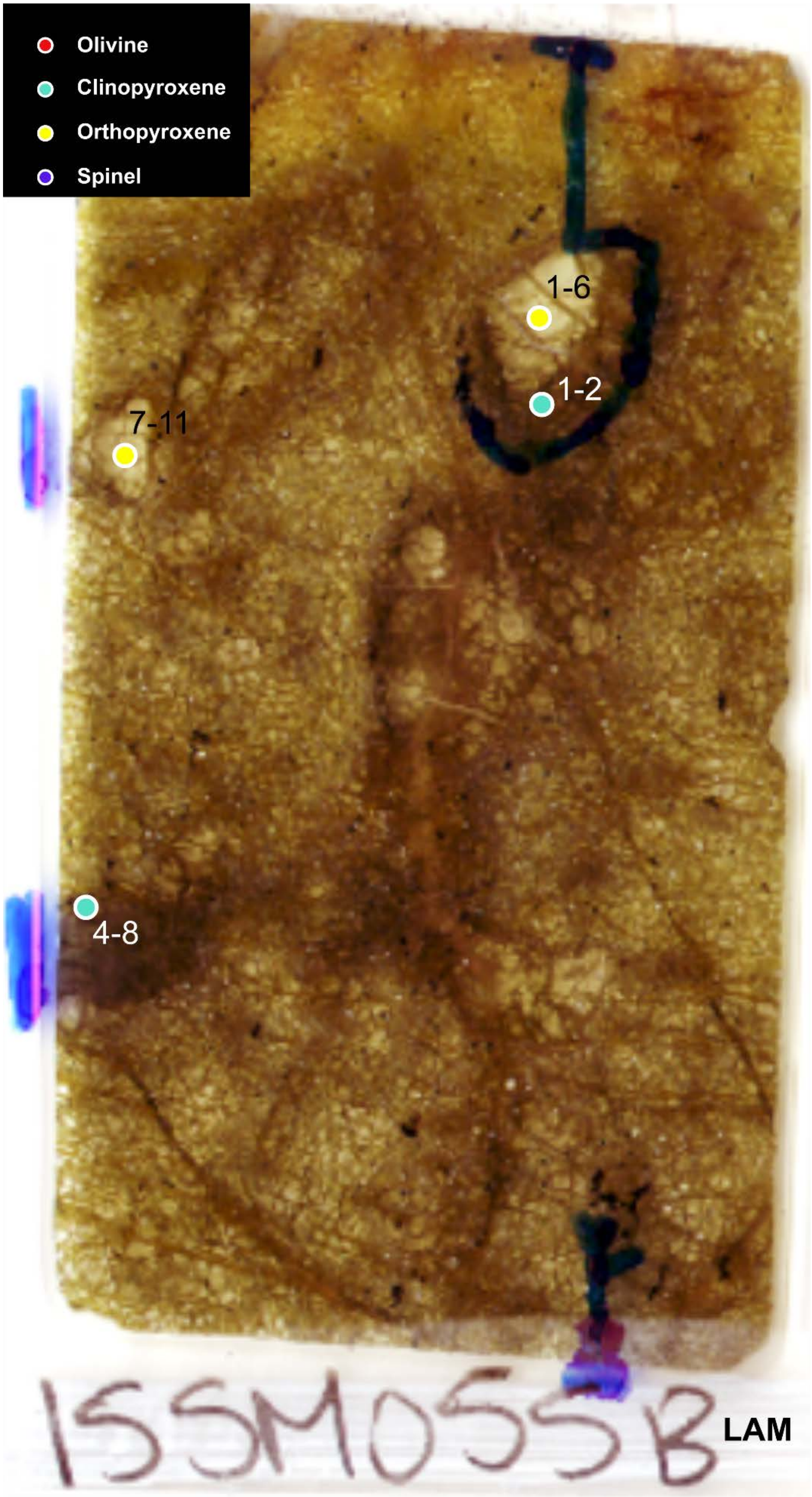
Olivine
Clinopyroxene
Orthopyroxene
Spinel
1-6
1-2
7-11
4-8
15SM055B
LAM

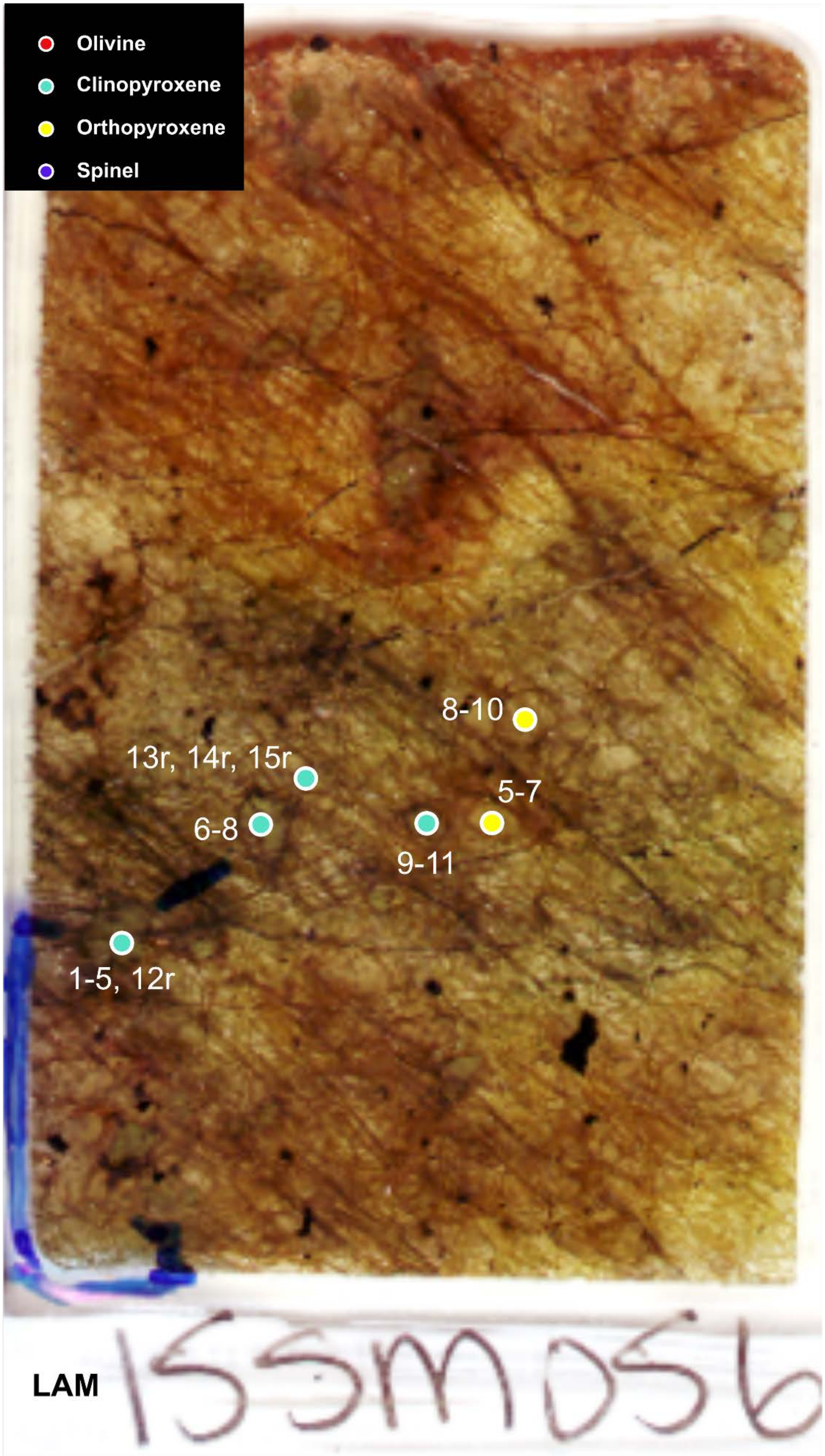
● Olivine
● Clinopyroxene
● Orthopyroxene
● Spinel
8-10
13r, 14r, 15r
5-7
6-8
9-11
1-5, 12r
LAM
155MD56

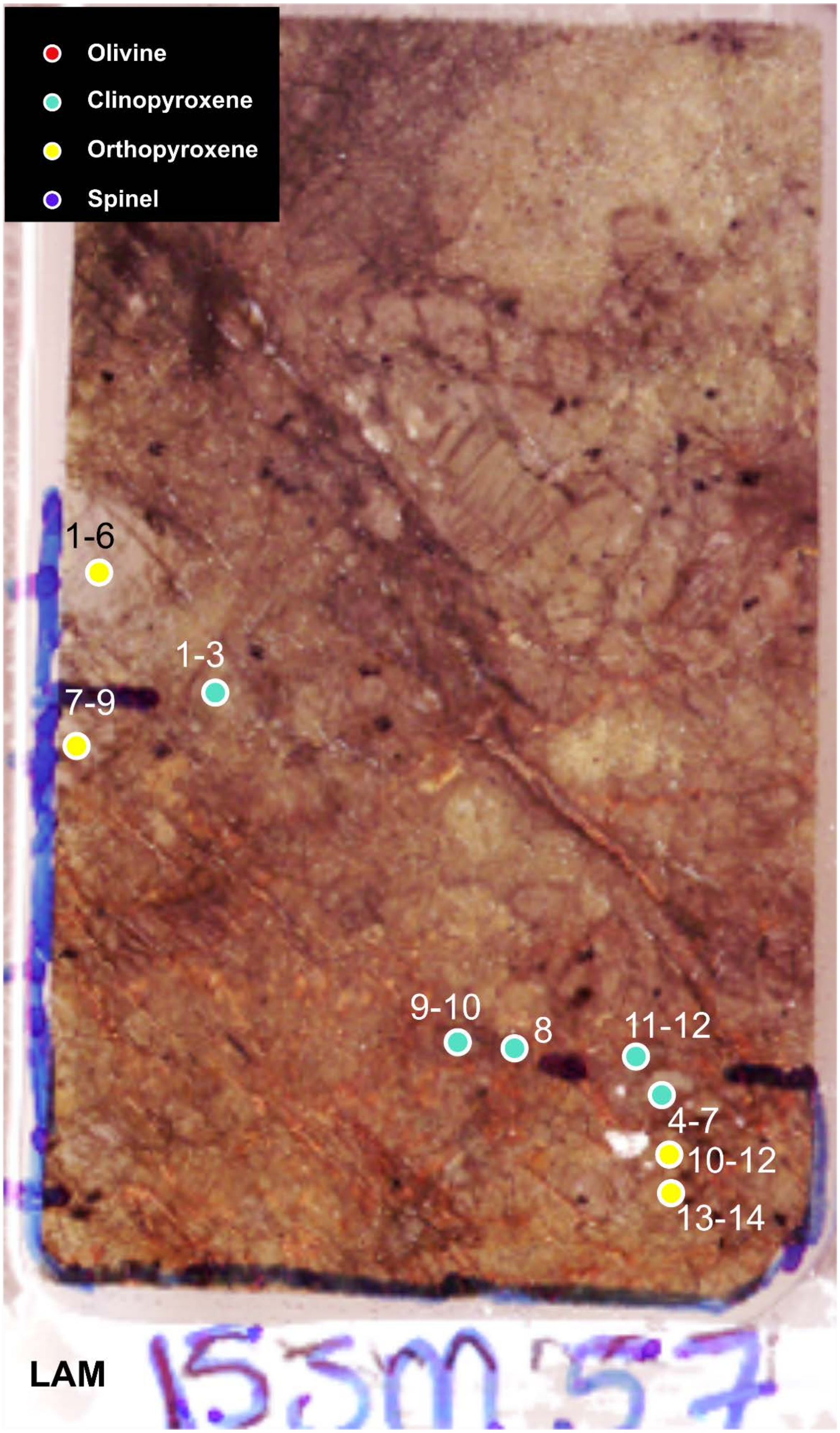
Olivine
Clinopyroxene
Orthopyroxene
Spinel
1-6
1-3
7-9
9-10
8
11-12
4-7
10-12
13-14
LAM
155m 57

Table A 1: Sample locations.

Sample	Location	Rock class	Lithology	Station code	Station	Latitude (°N)	Longitude (°W)
15SM014A	Menat	Intrusive	Gab	15SM	14	58.959	132.268
15SM014B	Menat	Ultramafic	Harz	15SM	14	58.959	132.268
15SM015	Menat	Intrusive	Db	15SM	15	58.958	132.268
15SM016	Menat	Ultramafic	Harz	15SM	16	58.955	132.267
15SM017	Menat	Ultramafic	Harz	15SM	17	58.954	132.268
15SM019	Menat	Ultramafic	List	15SM	19	58.952	132.266
15SM023A	Menat	Ultramafic	Harz	15SM	23	58.951	132.232
15SM023B	Menat	Ultramafic	Harz	15SM	23	58.951	132.232
15SM023C	Menat	Ultramafic	Harz	15SM	23	58.951	132.232
15SM025	Menat	Ultramafic	List	15SM	25	58.948	132.230
15SM027	Menat	Ultramafic	Harz	15SM	27	58.945	132.230
15SM030	Menat	Extrusive	MVx	15SM	30	58.935	132.260
15SM031A	Menat	Extrusive	MVx	15SM	31	58.932	132.257
15SM033	Menat	Intrusive	Db	15SM	33	58.936	132.246
15SM034-1	Menat	Ultramafic	Harz	15SM	34-1	58.934	132.241
15SM034-2	Menat	Ultramafic	Harz	15SM	34-2	58.934	132.239
15SM034-4	Menat	Ultramafic	Harz	15SM	34-4	58.935	132.237
15SM035	Menat	Ultramafic	Serp	15SM	35	58.946	132.222
15SM037	Menat	Ultramafic	Ophi	15SM	37	58.952	132.240
15SM038	Menat	Ultramafic	Harz	15SM	38	58.953	132.238
15SM039A	Menat	Extrusive	MV	15SM	39	58.962	132.214
15SM039B	Menat	Extrusive	MVx	15SM	39	58.962	132.214
15SM040	Menat	Extrusive	MVx	15SM	40	58.959	132.212
15SM042	Menat	Extrusive	MV	15SM	42	58.965	132.219
15SM043	Menat	Ultramafic	Harz	15SM	43	58.964	132.247
15SM045	Menat	Ultramafic	Harz	15SM	45	58.962	132.250
15SM048	Menat	Extrusive	MV	15SM	48	58.984	132.251
15SM050	Menat	Intrusive	Gab	15SM	50	58.971	132.239
15SM053	Menat	Extrusive	MV	15SM	53	58.974	132.237
15SM054A	Menat	Intrusive	Db	15SM	54	58.948	132.254
15SM054B	Menat	Intrusive	Db	15SM	54	58.948	132.254
15SM055A	Menat	Ultramafic	Harz	15SM	55	58.949	132.255
15SM055B	Menat	Ultramafic	Harz	15SM	55	58.949	132.255
15SM056	Menat	Ultramafic	Harz	15SM	56	58.966	132.250
15SM057	Menat	Ultramafic	Harz	15SM	57	58.966	132.248
15SM058	Menat	Intrusive	Db	15SM	58	58.968	132.246
15SM060	Menat	Extrusive	MV	15SM	60	58.973	132.234
15SM086A	Per Pk	Ultramafic	List	15SM	86	58.971	132.642
15SM090	Nahlin	Intrusive	AGab	15SM	90	58.973	132.679
15SM092	Per Pk	Intrusive	Gab	15SM	92	58.972	132.707
15SM093	Per Pk	Intrusive	Gab	15SM	93	58.972	132.708
15SM094	Per Pk	Intrusive	Dio	15SM	94	58.961	132.722
15SM098	Per Pk	Extrusive	MV	15SM	98	58.964	132.736
15SM099	Per Pk	Ultramafic	Serp	15SM	99	58.966	132.736
15SM105	Per Pk	Extrusive	MV	15SM	105	58.964	132.734
15SM108	Per Pk	Intrusive	Gab	15SM	108	58.968	132.721
15SM110	Per Pk	Extrusive	MV	15SM	110	58.979	132.699
15SM112A	Per Pk	Extrusive	MV	15SM	112	58.980	132.698
15ZE933	Tseta	Ultramafic	Harz	15ZE	933	58.912	132.367
15ZE943	Tseta	Extrusive	MV	15ZE	942	58.921	132.294
15ZE944	Tseta	Extrusive	MV	15ZE	944	58.915	132.291
15ZE945	Tseta	Extrusive	MV	15ZE	945	58.912	132.290
15ZE953	Tseta	Extrusive	MV	15ZE	953	58.878	132.371
15ZE955	Tseta	Extrusive	MV	15ZE	955	58.881	132.381
15ZE956A	Tseta	Intrusive	MCum	15ZE	956	58.886	132.373
15ZE959A	Tseta	Intrusive	MCum	15ZE	959	58.892	132.390
15ZE959B	Tseta	Ultramafic	Harz	15ZE	959	58.892	132.390
15ZE961A	Tseta	Ultramafic	Harz	15ZE	961	58.893	132.387
15ZE961B	Tseta	Ultramafic	Pxite	15ZE	961	58.893	132.387
15ZE965	Tseta	Intrusive	UMCum	15ZE	965	58.899	132.391
15ZE967A	Tseta	Ultramafic	Harz	15ZE	967	58.909	132.387
15ZE967C	Tseta	Ultramafic	Pxite	15ZE	967	58.909	132.387
15ZE971	Tseta	Extrusive	MV	15ZE	971	58.960	132.382
15ZE972	Tseta	Extrusive	MV	15ZE	972	58.962	132.374
15ZE985	Tseta	Extrusive	MV	15ZE	985	60.328	133.323
16SM160	Nahlin	Ultramafic	Harz	16SM	160	58.904	132.171
16SM161	Nahlin	Intrusive	Gab	16SM	161	58.902	132.169
16SM162	Nahlin	Ultramafic	Harz	16SM	162	58.901	132.169
16SM163	Nahlin	Intrusive	AGab	16SM	163	58.899	132.171
16SM166	Nahlin	Extrusive	MVx	16SM	166	58.888	132.177
16SM167	Nahlin	Extrusive	UMVx	16SM	167	58.885	132.188
16SM172	Nahlin	Extrusive	MVx	16SM	172	58.869	132.167
16SM178	Nahlin	Intrusive	AGab	16SM	178	58.863	132.114
16SM181	Nahlin	Ultramafic	Harz	16SM	181	58.860	132.106
16SM184	Nahlin	Ultramafic	Harz	16SM	184	58.857	132.086
16SM185	Nahlin	Extrusive	MVx	16SM	185	58.875	132.142
16SM186	Nahlin	Intrusive	Gab	16SM	186	58.878	132.143
16SM187	Nahlin	Ultramafic	Harz	16SM	187	58.883	132.131
16SM188	Nahlin	Ultramafic	Harz	16SM	188	58.889	132.125
16SM190	Menat	Ultramafic	Harz	16SM	190	58.962	132.272
16SM192	Menat	Ultramafic	Harz	16SM	192	58.961	132.273
16SM193	Menat	Ultramafic	Harz	16SM	193	58.960	132.269
16SM194	Menat	Ultramafic	Pxite	16SM	194	58.961	132.267
DC0205	Hardlk	Ultramafic	Harz	DC02	205	59.044	132.956
DC0206	Hardlk	Ultramafic	Harz	DC02	206	59.045	132.956
DC0303	Moho	Ultramafic	Harz	DC03	303	59.029	132.877
DC0304	Moho	Ultramafic	Harz	DC03	304	59.029	132.877
DC0310	Per Pk	Ultramafic	Lherz	DC03	310	58.979	132.752
DC0312	Per Pk	Ultramafic	Lherz	DC03	312	58.980	132.753
DC0313	Per Pk	Ultramafic	Lherz	DC03	313	58.980	132.753
DC0318	Per Pk	Ultramafic	Lherz	DC03	318	58.988	132.753
DC0322	Per Pk	Ultramafic	Harz	DC03	322	58.975	132.716
DC0327	Per Pk	Ultramafic	Lherz	DC03	327	58.984	132.744
DC0334	Per Pk	Ultramafic	Lherz	DC03	334	58.985	132.754
DC0336	Per Pk E	Ultramafic	Harz	DC03	336	58.953	132.619
DC0345	Per Pk E	Ultramafic	Harz	DC03	345	58.954	132.659

Hardlk, North of Hardluck Peaks; Menat, Menatatuline Range; Moho, "Moho Saddle"; Nahlin, Nahlin Mountain; Per Pk, Peridotite Peak; Per Pk E, Peridotite Peak East; Tseta, Tseta Creek area.

AGab, amphibole-bearing gabbro; Db, diabase; Dio, diorite; Gab, gabbro; Harz, harzburgite; Lherz, lherzolite; List, listwaenite; MCum, mafic cumulate; MV, mafic volcanic rock; MVx, mafic volcaniclastic rock; Ophi, ophicalcite; Pxite, pyroxenite; Serp, serpentinite; UMCum, ultramafic cumulate; UMVx, ultramafic volcaniclastic.

Station code refers to the senior mapping geologist and year (i.e., Zagorevski mapping in 2015 denoted as "ZE15", D. Canil mapping in 2003 denoted as "DC03").

Station number refers to mapping geologist and station (i.e., S. McGoldrick's second station denoted as "SM02").

Table A 2: Whole-rock major element (ICP-OES) and trace element (ICP-MS) data from ActLabs Ltd. from plutonic and volcanic rocks of the Menatatuline Range area (n.d. indicates no data).

Sample		15ZE-0943	15ZE-0944	15ZE953	15ZE955	15ZE-0985	ZE15SM030	ZE15SM031A	ZE15SM039B	ZE15SM040	ZE15SM105	16SM 167	16SM 172	ZE15SM033	ZE15SM054A	16SM 161	16SM 163	16SM 178	16SM 186	ZE15AC062	ZE15SM050	ZE15SM090	15ZE956A	15ZE959A	15ZE965	15ZE971	ZE15SM112A	15ZE-0945	15ZE-0972									
Latitude		58.921	58.915	58.878	58.881	60.328	58.935	58.932	58.962	58.959	58.964	58.885	58.869	58.936	58.948	58.902	58.899	58.863	58.878	58.961	58.971	58.973	58.886	58.892	58.899	58.960	58.980	58.912	58.962									
Longitude		-132.294	-132.291	-132.371	-132.381	-133.323	-132.260	-132.257	-132.214	-132.212	-132.734	-132.188	-132.167	-132.246	-132.254	-132.169	-132.171	-132.114	-132.143	-132.764	-132.239	-132.679	-132.373	-132.390	-132.391	-132.382	-132.698	-132.290	-132.374	Standards								
Rock type	Detection limit	Mafic volcanic	Mafic volcanic	Mafic volcanic	Mafic volcanic	Mafic volcanic	Mafic volcaniclastic	Mafic volcaniclastic	Mafic volcanic	Mafic volcaniclastic	Mafic volcanic	Ultramafic volcaniclastic	Mafic volcaniclastic	Diabasic dike	Diabasic dike	Gabbroic dike	Amph-bearing gabbroic dike	Amph-bearing gabbroic dike	Gabbroic dike	Gabbro	Gabbro	Amph-bearing gabbro	Gabbronorite cumulate	Gabbronorite cumulate	Plag-bearing olivine websterite cumulate	Mafic volcanic	Mafic volcanic	Mafic volcanic	Mafic volcanic	DNC-1			OREAS 101B			W-2a		
Affinity		IAT	IAT	IAT	IAT	IAT	IAT	IAT	IAT	IAT	IAT	IAT	IAT	IAT	IAT	IAT	IAT	IAT	IAT	IAT	IAT	IAT	IAT	IAT	IAT	OIB	OIB	EMORB	EMORB	Certified	Measured	% accuracy	Certified	Measured	% accuracy	Certified	Measured	% accuracy
SiO2 (wt %)	0.01	50.17	51.13	52.81	59.62	52.01	51.08	50.50	50.68	51.19	47.57	47.71	50.03	54.62	55.21	52.57	55.08	54.28	50.72	53.95	44.25	52.12	45.60	49.55	43.47	48.32	40.38	46.56	48.78	47.15	47.26	0.23				52.40	52.31	0.17
Al2O3	0.01	15.43	14.93	15.60	15.85	14.30	14.70	16.05	14.38	15.01	13.81	8.03	17.14	14.97	15.28	16.57	14.91	14.69	16.84	14.14	9.32	13.44	15.63	14.22	10.73	16.50	14.09	19.10	15.86	18.34	17.67	3.65				15.40	15.37	0.19
FeO	0.01	9.71	9.25	11.80	9.30	12.41	9.61	7.99	9.56	9.78	12.13	10.94	13.86	10.40	10.68	7.10	7.80	10.67	8.28	11.29	9.62	11.93	6.62	5.31	3.27	9.30	5.31	11.02	12.14	8.97	8.49	5.42				9.63	9.57	0.56
MnO	0.001	0.17	0.17	0.10	0.14	0.22	0.16	0.15	0.18	0.18	0.22	0.24	0.27	0.16	0.17	0.13	0.13	0.20	0.15	0.20	0.19	0.20	0.13	0.11	0.03	0.18	0.07	0.21	0.24	0.15	0.15	2.67				0.16	0.17	1.23
MgO	0.01	6.47	8.37	8.39	4.78	5.21	8.70	7.08	8.22	6.72	5.61	20.58	3.74	4.52	4.36	7.71	7.26	4.21	7.77	5.23	7.87	5.76	11.99	13.22	36.56	7.15	3.66	7.04	5.77	10.13	9.74	3.85				6.37	6.45	1.26
CaO	0.01	12.63	10.30	4.14	2.53	7.63	9.09	14.23	11.93	10.80	13.18	9.91	6.53	8.03	8.98	10.03	8.32	8.50	9.78	6.30	21.34	8.39	18.57	15.48	5.24	11.83	27.40	11.05	9.90	11.49	11.44	0.44				10.90	10.95	0.46
Na2O	0.01	2.62	3.00	2.50	5.99	4.07	3.79	1.85	2.04	3.39	3.87	0.30	4.34	4.78	2.87	4.04	4.13	4.76	3.19	5.55	4.74	4.47	0.42	1.28	0.18	3.16	3.58	1.58	3.02	1.89	1.93	2.12				2.14	2.17	1.40
K2O	0.01	0.12	0.55	1.77	0.07	0.54	0.27	0.20	0.21	0.33	0.25	0.02	0.68	0.15	0.14	0.41	0.52	0.10	1.33	0.21	0.13	0.45	0.04	0.06	0.01	0.19	2.12	0.45	0.49	0.23	0.22	5.98				0.63	0.60	4.15
TiO2	0.001	1.45	1.18	1.49	0.62	2.02	1.36	0.98	1.56	1.41	1.85	0.96	1.73	1.10	1.01	0.58	0.87	1.29	0.95	1.66	1.39	1.81	0.23	0.18	0.15	2.10	1.84	1.59	2.19	0.48	0.47	1.88				1.06	1.08	1.51
P2O5	0.01	0.13	0.11	0.10	0.06	0.19	0.14	0.06	0.16	0.10	0.19	0.09	0.15	0.10	0.10	0.05	0.10	0.13	0.06	0.15	0.13	0.09	-	0.01	-	0.25	0.95	0.18	0.27	0.07	0.07	0.00				0.13	0.13	0.00
Cr2O3	0.002	0.04	0.05	0.03	0.01	0.02	0.05	0.04	0.05	0.02	0.02	0.20	0.09	0.01	0.01	0.01	0.02		0.04	0.02	0.04	0.02	0.08	0.11	0.56	0.01	0.04	0.05	0.03	0.04	0.04	3.70				0.01	0.01	8.70
Total	0.01	100.00	100.01	100.00	99.99	99.99	99.98	99.99	99.99	100.01	100.03	100.00	100.00	100.00	100.00	99.98	100.00	100.02	100.00	99.95	100.03	99.99	99.98	100.02	100.01	100.02	99.98	100.00	100.01	99.90	98.38					99.89	99.86	
Cs (ppm)	0.1	n.d.	0.3	1.1	0.2	4.5	0.3	0.1	0.1	0.2	0.2	0.2	0.4	n.d.	n.d.	n.d.	0.1	n.d.	0.1	0.2	0.3	0.5	n.d.	n.d.	n.d.	0.6	2.7	0.2	0.6									
Rb	1	2	12	22	n.d.	14	5	3	4	3	2	n.d.	13	2	n.d.	7	7	n.d.	14	3	4	6	n.d.	n.d.	n.d.	7	35	10	11							21	20	4.8
Sr	2	49	38	194	25	97	81	53	151	94	424	18	90	137	162	223	218	171	365	142	27	118	257	323	4	136	159	620	114	144	139	3.5				190	192	1.1
Ba	3	14	34	301	17	781	20	9	9	49	149	9	124	19	27	40	51	27	30	24	n.d.	24	12	13	4	43	275	44	116	118	102	13.6				182	170	6.6
Y	0.5	31.4	25.3	22.5	11.5	45.9	27.2	20.7	31.6	28	37.9	22.7	26.3	19.3	20.2	12.6	20.8	26.7	24.2	35	27	28.5	6.2	4.3	2.1	21.7	18.5	28.5	34.4	18	17.7	1.7	178	180	1.1	24	21.7	9.6
Zr	1	79	66	92	43	108	97	54	114	81	123	53	88	68	69	43	65	78	57	99	78	77	5	9	7	138	107	101	139	38	37	2.6				94	95	1.1
Hf	0.1	2.1	1.8	2	0.9	2.7	2.1	1.2	2.4	1.8	2.8	1.4	2.4	1.6	1.6	1.1	1.8	2.2	1.7	2.3	1.7	1.8	0.2	0.2	n.d.	3	2.1	2.3	3.5							2.6	2.5	3.8
Nb	0.2	0.7	1.3	1.2	1	3.2	2.2	0.8	2.2	1.2	3.4	0.9	2.5	0.9	0.8	n.d.	1	0.9	0.8	1	1.3	0.9	n.d.	0.4	4.2	24.6	18.5	6.8	10.7							7.9	7.3	7.6
Ta	0.01	0.14	0.37	0.04	0.04	0.37	0.13	n.d.	0.11	0.04	0.19	0.07	0.19	0.02	n.d.	0.01	0.08	0.08	0.06	n.d.	0.05	n.d.	0.04	n.d.	0.05	2.12	1.27	0.6	0.92									
Sc	1	41	35	35	32	41	37	36	35	37	37	39	33	34	35	36	32	32	35	33	38	37	40	41	11	36	20	46	43	31	31	0.0				36	35	2.8
V	5	318	264	366	184	393	288	261	303	317	379	229	277	359	357	185	234	333	227	297	306	474	138	150	74	277	160	274	330	148	157	6.1				262	267	1.9
Ni	20	80	190	130	40	70	180	110	170	70	60	460	280	40	30	90	60	40	120	100	120	90	240	320	1110	60	80	140	130	247	270	9.3	9	< 20		70	70	0.0
Cu	10	70	60	50	n.d.	80	80	70	50	60	60	40	70	60	40	120	60	60	60	40	50	40	130	80	10	100	40	90	60	100	100	0.0	416	420	1.0	110	110	0.0
Zn	30	80	70	90	70	120	90	60	60	80	100	110	210	90	80	50	50	70	60	100	70	90	40	n.d.	n.d.	80	40	130	170							80	90	12.5
W	0.5	n.d.	1.8	0.6	0.6	1.8	0.7	0.6	n.d.	0.5	n.d.	n.d.	n.d.	n.d.	0.7	n.d.	n.d.	n.d.	n.d.	0.7	0.7	n.d.	n.d.	n.d.	0.6	1.8	1.1	n.d.	1.9							0.3	< 0.5	
As	5	n.d.	n.d.	n.d.	n.d.	n.d.	n.d.	n.d.	n.d.	n.d.	n.d.	n.d.	10	n.d.	n.d.	n.d.	n.d.	n.d.	n.d.	n.d.	n.d.	n.d.	n.d.	n.d.	n.d.	9	n.d.	n.d.	n.d.									
Tl	0.05	n.d.	0.08	n.d.	n.d.	0.14	n.d.	n.d.	n.d.	n.d.	n.d.	n.d.	n.d.	n.d.	n.d.	n.d.	n.d.	n.d.	n.d.	n.d.	n.d.	n.d.	n.d.	n.d.	n.d.	n.d.	0.07	0.07	0.1							0.2	0.06	70.0
Pb	5	n.d.	n.d.	n.d.	n.d.	n.d.	n.d.	n.d.	n.d.	n.d.	7	n.d.	n.d.	28	n.d.	n.d.	n.d.	n.d.	n.d.	33	n.d.	n.d.	n.d.	35	11	n.d.	n.d.	n.d.	n.d.									
Th	0.05	0.11	0.16	0.15	0.2	0.25	0.22	0.08	0.21	0.1	0.48	0.15	0.28	0.17	0.18	0.12	0.25	0.23	0.08	0.15	0.13	0.11	n.d.	0.06	0.5	1.7	1.47	0.63	0.84				37.1	39.8	6.8	2.4	2.5	4.2
U	0.01	0.18	0.11	0.09	0.15	0.14	0.14	0.12	0.12	0.05	0.2	0.18	0.32	0.11	0.11	0.07	0.15	0.16	0.04	0.1	0.05	0.07	n.d.	0.02	0.01	0.5	0.52	0.26	0.22				396	426	7.0	0.53	0.55	3.8
La	0.05	2.81	2.03	2.49	1.78	3.14	4.35	2.02	4.53	2.63	6.58	2.34	5.32	2.88	2.87	1.45	2.89	3.08	2.16	3.12	2.85	2.6	0.28	0.4	0.22	16.2	21.9	8.25	10.9				789	820	3.9			
Ce	0.05	9.2	6.91	8.17	4.53	10.8	12.4	6.34	13.7	8.69	17.9	6.48	11.6	8.51	8.36	4.51	7.95	9.1	6.86	10.6	9.08	8.51	0.74	1.04	0.62	35.7	40.9	19.1	25				1331	1430	7.4	23	24.8	7.8
Pr	0.01	1.57	1.29	1.4	0.69	1.99	1.94	1.09	2.13	1.51	2.75	1.02	1.94	1.37	1.35	0.77	1.19	1.5	1.14	1.87	1.48	1.44	0.15	0.15	0.11	4.45	4.67	2.61	3.64				127	129	1.6			
Nd	0.05	9.13	7.22	7.5	3.4	11.2	10.1	5.9	11.3	8.51	13.8	5.47	10.2	7.27	7.06	4.04	6.57	8.03	6.51	10.3	8.35	8.6	1.02	0.85	0.46	18.7	19.8	12.3	17.1				378	389	2.9	13	13.3	2.3
Sm	0.01	3.36	2.76	2.72	1.14	4.36	3.38	2.15	3.91	2.98	4.52	1.94	3.39	2.4	2.49	1.42	2.25	2.82	2.43	3.83	2.92	3.09	0.48	0.38	0.22	4.34	4.41	3.61	5.12				48	50	4.2	3.3	3.4	3.0
Eu	0.005	1.29	1.04	1.05	0.433	1.64	1.06	0.928	1.29	1.08	1.55	0.694	1.28	0.979	0.92	0.554	0.803	1	1.02	1.4	1.14	1.2	0.335	0.201	0.013	1.55	1.46	1.47	1.83	0.59	0.63	6.8	7.77	8.34	7.3			
Gd	0.01	4.68	3.8	3.49	1.68	6.37	4.34	3.17	4.94	4.2	6.16	2.85	4.5	3.23	3.16	1.83	2.86	3.7	3.32	5.32	4.16	4.17	0.82	0.6	0.22	4.47	4.27	4.53	5.73									
Tb	0.01	0.88	0.71	0.62	0.31	1.15	0.76	0.56	0.92	0.76	1.03	0.53	0.76	0.54	0.57	0.31	0.5	0.68	0.61	0.97	0.77	0.81	0.16	0.11	0.04	0.7	0.62	0.79	1				5.37	5.46	1.7	0.63	0.64	1.6
Dy	0.01	5.64	4.46	4.13	2.18	8.25	5.11	3.71	5.81	5.01	6.82	3.57	4.83	3.62	3.6	2.04	3.35	4.47	4.06	6.34	4.89	5.23	1.09	0.8	0.32	4.23	3.64	5.18	6.24				32.1	32.5	1.2			
Ho	0.01	1.16	0.95	0.83	0.46	1.69	1.04	0.8	1.21	1.06	1.43	0.78	0.96	0.77	0.78	0.43	0.71	0.94	0.87	1.33	1.02	1.09	0.25	0.18	0.07	0.79	0.66	1.06	1.27				6.34	6.44	1.6	0.76	0.81	6.6
Er	0.01	3.35	2.69	2.5	1.38	4.93	3.02	2.28	3.47	3.07	4.11	2.35	2.69	2.21	2.24	1.26	2.04	2.75	2.48	3.88	3.14	3.2	0.68	0.55	0.21	2.23	1.81	2.98	3.57				18.7	19.4	3.7	2.5	2.3	8.0
Tm	0.005	0.501	0.413	0.348	0.229	0.758	0.462	0.362	0.506	0.452	0.589	0.33	0.363	0.346	0.356	0.187	0.311	0.404	0.346	0.583	0.458	0.487	0.101	0.083	0.037	0.329	0.235	0.443	0.505				2.66	2.82	6.0			
Yb	0.01	3.26	2.64	2.22	1.56	4.95	2.87	2.34	3.36	2.97	3.96	2.14	2.34	2.34	2.25	1.16	2.02	2.65	2.33	3.93	2.89	3.18	0.62	0.52	0.28	1.9	1.47	2.95	3.21	2	2.1	5.0	17.6	18.2	3.4	2.1	2.1	0.0
Lu	0.002	0.52	0.404	0.336	0.213	0.739	0.447	0.346	0.507	0.471	0.621	0.339	0.375	0.338	0.335	0.185	0.329	0.427	0.373	0.584	0.457	0.498	0.091	0.075	0.046	0.279	0.21	0.438	0.468				2.58	2.63	1.9	0.33	0.32	3.0

Table A 3: Petrography notes. Mineral abbreviations: Plag, plagioclase; Cpx, clinopyroxene; Opx, orthopyroxene; Ol, olivine; Sp, spinel; Serp, serpentine; Ser, sericite; Chl, chlorite; Cal, calcite; Mag, magnetite.

Sample	Rock class	Lithology	Metamorphic facies	° of alt'n (/10)	Petrography notes
15ZE959	Intrusive	Porphyritic or varitextured gb	Greenschist	6	Coarse grained (varitextured) gabbro. Cpx varies from 0.5 mm to >12 mm. Could be a cumulate? Coarser subhedral to anhedral cpx +/- opx with post-cumulus (?) slightly finer grained (~1 mm) plag with nearly granoblastic plag-plag grain boundaries. Px often have emabayed grain boundaries and coarse exsolution lamellae, and many have sieve like textures. Some ser + chl aggregates after fspar.
15ZE965	Intrusive	Ultramafic cumulate	Greenschist	5	Coarse grained ultramafic cumulate. Aggregates of acicular to elongate prismatic tremolite +/- act after cpx +/- opx. Some primary cpx + opx left. Anhedral patches of very fine grained serp after olv (?). Radiating extinction in anhedral patches of chl (1st order greys). Some kinked trem after px (deformation in cumulate pile? later def? Not really pervasive, more evidence for cumulate pile?). Sparse subhedral oxides, generally clustered together, look like they were cube-like and therefore magmatic not holly-leaf texture as seen in some mantle tectonite harz. Rare plag. Some nice granoblastic grain boundaries.
15ZE965C	Intrusive	Gabbroic cumulate	Greenschist	5	Medium to coarse grained altered gabbroic cumulate; possibly silicified? Looks like almost entirely plag + cpx (very low birefringence) +/- anthophyllite or similar after opx? Maybe some relic opx but not quite high enough relief and slightly inclined extinction Gabbro or gabbronorite cumulate.
16SM161	Intrusive	Porphyritic gb	Greenschist	4	Fine grained gabbro with intergranular texture, euhedral to subhedral plag laths with anhedral to subhedral cpx (or opx? birefringence seems to low but one with cleavage seem to have inclined ext) between laths of plag. Rare ~1 mm anhdral ro subhedral opx (or anthophyllite after opx) phenocrysts. One cpx phenocryst ~1 mm, euhdral. Chl + ep + ser after plag, chl after px.
16SM163	Intrusive	Amph-bearing gb	Greenschist	7	Medium to fine grained amph-bearing gabbro. Plag pretty altered to ser + ep + chl, cpx +/- opx altered to chl. Amph alters to chl.
16SM178	Intrusive	Amph-bearing gb	Greenschist	6	Medium to fine grained amph-bearing gabbro. Plag pretty altered to ser + ep + chl, cpx +/- opx altered to chl. Amph alters to chl. Intergranular texture.
16SM186	Intrusive	Porphyritic gb	Greenschist	7	Medium to coarse grained amph-bearing gabbro. Subhedral to euhedral plag, intergranular cpx and opx. Plag alters to ser + chl + ep; cpx + opx alters to chl. Inequigranular plag - some up to 4 mm, with intergranular plag ~0.5-1 mm. Multiple generations?
15SM014A	Intrusive	Basaltic dyke	Greenschist	1	Plag 0.5-2 mm; ave ~1 mm; euhedral to subhedral; micro and large phenos and glomeroporphyric; some phenos zoned; some largest phenos look resorbed like they were melted by the host melt? Opx ~0.25 mm; microphenos; subhedral. Cpx <0.1 mm; in gmass; anhedral. Olivine 0.5-2 mm; ~1 mm ave; euhedral to subhedral; micro and large phenos. Some ol phenos zoned; some 100% replaced (serp pseudomorphs after ol phenos).Poorly defined grain boundaries in groundmass of px+oxides.
15SM033	Intrusive	Diabase dyke	Greenschist	4	Plag ~0.25-0.5 mm, subhedral to rare euhedral laths. Cpx 0.25-0.5 mm, anhedral, vaguely bladed; some 100% pseudomorph of ep after cpx; many have fuzzy, "feathered" appearance.
15SM054A	Intrusive	Diabase dyke	Greenschist	4	0.5 mm plag phenocrysts with synthetic twinning and interstitial plag without twinning and with weird, blebby symplectite texture. Some altered to ep +/- clinozoisite. Irreg grain boundaries between intergrowth symplectite plag. Opx: 0.5 mm; subhedral to euhedral. Cpx: 0.5 mm; subhedral to anhedral. Both pyroxenes being altered to ep +clinozoisite +/- chl. Intergranular?? Not really "ophitic" or subophitic overall texture. More like blades of px (replaced by ep??) and all intervening space filled by euhedral twinned plag laths and anhedral symplectite-like plag.
15SM50	Intrusive	Gabbro	Greenschist	9	Plag 1 mm, subhedral to euhedral, almost 100% replaced by sericite. Opx 1 mm, anhedral, rounded. Almost 100% replaced by chl. Cpx 1 mm, anhedral, rounded. Almost 100% replaced by chl. Oxides 0.5 mm subhedral to anhedral titanite after ilmenite?
15SM90	Intrusive	Gabbro or diorite	Greenschist	9	Fine to medium grained gabbro or diorite. Cut by trondjemitic veinlet. Contains primary euhedral to subhedral amph (pargasite?), Act + chl + another amph (?) + ep + ser metamorphic assemblage. Titanite after ilmenite.
15SM94	Intrusive	Tonalite	Greenschist	3	Fine to medium grained bt-titanite-bearing qtz diorite. Subhedral to anhedral bt and hbl. Subhedral accessory titanite. Looks like mostly qtz+plag (no kspar). Some nice growth zoning in plag. Plag partially altered to ser. Inequigranular - plag phenos with fg qtz.
15SM030	Extrusive	Mafic ash crystal tuff with sparse lithic lapilli	Greenschist	9	Very fine grained subrounded plag crystal fragments, rarely with twinning. Some fragments interpreted as quartz may actually be plag without twinning. Some rare cpx crystal fragments in same size range as plag+qtz fragments. Subrounded to subangular lithic clasts likely altered basalt (relict <0.1 mm plag laths +/- cpx altered to chl). Clast size average ~ 0.5 mm, range from 0.3 to 10 mm (*looks like clast of tuff in a tuff, might be a clast, or just altered differently than rest of slide). Very fine grained grey-green-brown matrix (devitrified glass?). Rare pseudo fiamme shapes, but largely does not look welded or that compacted.
15SM031B	Extrusive	Mafic ash to lapilli tuff	Greenschist	8	Subangular to subrounded mafic lithic clasts (lapilli) with relict ser-ep altered plag laths and chl altered cpx. Clasts have intergranular textures. Same very fine grained plag +/- qtz + sparse cpx subrounded crystal fragments as in SM030. Same matrix grain size (very fine grained) as SM030 but darker in colour (oxides? palagonite?).
15SM039B	Extrusive	Basalt	Greenschist	5	Intergranular texture of fine grained plag+cpx. Chl + act alteration (lower greenschist facies meta assemblage). Elongated blocky crystals of cpx pervasively altered to chl. Cut by qtz veins.
15SM040	Extrusive	Mafic lapilli tuff	Greenschist	7	Fine grained subrounded to subangular crystal fragments of plag+/-qtz + some rare cpx fragments. More cpx fragments (most now altered to chl) than in SM030 or SM031B. Disseminated anhedral oxides (opaques) throughout groundmass average 0.1 mm in size. Greater proportion of crystal fragments to very fine grained ash groundmass than in SM030 or SM031B. Pervasive chl alteration of primary px. Lithic lapilli contain plag+chl+/-ep pseudomorph after cpx. Grain size 0.5-1 mm, intergranular texture. ~30% lapilli clasts of basalt, 70% groundmass with crystal fragments.
15SM112A	Extrusive	Olivine - plag phyric basalt	Greenschist	9	Highly amygdaloidal plag + cpx + ol phyric basalt. Sparse coarse grained subhedral to euhedral plag phenocrysts almost entirely replaced by cal +/- other secondary minerals. Some have jagged broken faces, possibly crystal fragments? Sparse subhedral to euhedral medium to coarse grained phenocrysts of ol entirely replaced by secondary minerals. Mainly a yellow (in PPL) moderate relief mineral with low 1st order birefringence that can be anomalously dark (serp? chl?) and also fine grained aggregrates of oxides. Groundmass consists of fine grained plag laths (altered to ser +/- cal), chl alteration after px, and fine grained oxides + qtz + cal. Rounded amygdales average 1 mm diameter filled with cal. Thin section probably ~40% vesicles.
15SM105	Extrusive	Plag-phyric basalt (or fine grained gabbro)	Greenschist	7	Relict plag phenos ave 1 mm size, range 0.5 to 1.5 mm long one is 4 mm long, euhedral to subhedral. Some with growth zoning. Some darkened/blurry look from very fine grained aggregate of alteration in phenocrysts. Others almost entirely fresh. Rare opx phenos ~ 0.7 mm diameter. Groundmass consists of some relict plag + chl + qtz + ep + act. Some possible vesicles filled with qtz? Qtz has undulose extinction. Looks like a fine grained porphyritic gabbro or norite, or phenocryst-rich vx.
15ZE953	Extrusive	Plag-phyic basalt	Greenschist	8	Medium grained, 0.5 to 1 mm subhedral to euhedral plag-phyric basalt. Plag phenocrysts largely replaced by ser +/- chl +/- cal. Some plag phenocrysts have sieve texture. Groundmass consists of relict plag + chl + opaques. Chl filled amygdules 1 mm diameter.
15ZE955	Extrusive	Plag-phyic basalt	Greenschist	7	One single opx (?) phenocryst, long lath 1 mm long. Plag-phyric, with medium grained (~1 mm diameter) subhedral to anhedral plag phenocrysts - some with sieve texture. Groundmass consists of predominantly plag with minor cpx. Groundmass plag laths randomly oriented, max 0.5 mm long. Intergranular texture of fg plag+cpx in groundmass. Cpx almost entirely replaced by chl. Some plag replaced by cal +/- chl. Some cal amygdules (possibly - rare). Some cal-filled veins.
16SM166	Extrusive	Mafic lapilli crystal tuff	Greenschist	6	Mafic lithic lapilli tuff. One lapilli has variolitic texture with opx + plag phenocrysts 0.5 mm diameter. Another contains sparse 0.5-1 mm ol (?) phenocrysts in a cpx+plag (partially replaced by chl +/- ep) very fine grained groundmass. Ol are unusually fresh - potentially fractured cpx and not ol? Some plag microlites in the groundmass of that lapilli have pseudotrachytic textures. Fine grained to very fine grained subrounded to subangular crystal fragments of plag + opx + cpx (ol?) present between lithic lapilli in very fine grained groundmass.
16SM167	Extrusive	Ultramafic crystal tuff	Greenschist	8	Very fine grained microcrystalline groundmass with whispy texture to it (devitrified glass?), with floating fine grained rounded crystal fragments of opx + serp altered ol +/- plag. Many crystal fragments have undulose extinction. Size ranges from <0.2 mm to 1 mm. Serp after ol fragments are subrounded, max 0.4 mm diameter. Picritic tuff?
16SM172	Extrusive	Mafic lithic lapilli	Greenschist	7	Pervasively hematized lapilli tuff. Lapilli altered to chl + ser + cal +qtz. Igneous textures not preserved in lapilli. Very irregular, wavy shapes to lapilli borders. Not rounded like in other samples.
15SM014B	Mantle	Harzburgite	-	2	Harzburgite consisting of 2-5 mm ol, 2-6 mm opx, and fine grained (0.5 mm) sp. Ol is anhedral and fractured by serp veinlets. Opx is anhedral to subhedral, rounded. Coarsest opx grains have exsolution lamellae.
15SM023a	Mantle	Harzburgite	-	2	Harzburgite consisting of 4-5 mm ol, 2-4 mm opx, 0.5-2 mm cpx, and 0.5-2 mm sp. Ol is anhedral with highly irregular grain boundaries, almost looks amoeboid. Opx is anhedral, some elongated. Cpx is anhedral and rounded, with exsolution lamellae. Spinel is anhedral.
15SM023b	Mantle	Harzburgite	-	2	Harzburgite consisting of 4-5 mm ol, 4-5 mm opx, 2 mm cpx and 0.5-2 mm sp. Ol anhedral, however some ol-ol grain boundaries ~120 . Ol-px grain boundaries highly irregular. Opx anhedral to subhedral, with straight grain boundaries against cps, but highly irregular against ol. Cpx anhedral. Both px have exsolution lamellae. Sp anhedral, some holly leaf like.
15SM034-1	Mantle	Harzburgite	-	4	Harzburgite consisting of >2 mm ol (hard to estimate size - very fractured by serp veinlets), 3-5 mm opx, and 0.2-1 mm sp. Anhedral ol hihgly fractured. Subhedral to anhedral opx. Some ol-opx grain boundaries highly irregular. Opx displays exsolution lamellae. Some opx kink banded. Overall displays porphyroclastic texture.
15SM034-2	Mantle	Dunite	-	3	Dunite consisting of 2-5 mm anhedral ol (hard to judge size - highly fractured with serp veinlets), anhedral 1-2 mm opx, and anhedral to subhedral 0.2-1 mm sp. Rare holly leaf sp. "Fuzzy" creamy patches, some rimmed by sp. Irreg gbs, sometimes "halo" around px as in 034-1. Even some opx altered to serp. Green and brown "striped" appearance from areas with serp+oxides compared to areas with just serp.
15SM038	Mantle	Harzburgite	-	2	Harzburgite consisting of 2-5 mm ol (fractured by serp veinlets), anhderal 3-6 mm opx, anhedral (rounded) 1 mm cpx, and anhedral (some holly leaf like) 0.2 mm sp. Grain boundaries between opx and ol highly irregular. Both pyroxenes have exsolution lamellae. Protogranular texture, some areas look more porphyroclastic.
15SM045	Mantle	Harzburgite	-	4	Harzburgite consisting of anhedral 1-5 mm ol (highly fractured by serp veinlets), anhedral fractured 1-5 mm opx, anhedral 3-5 mm cpx, 0.5-2 mm sp. Finer grains of sp are euhedral to subhedral, larger grains are anhedral and have altered rims (to another opaque mineral). Even cpx looks cloudy with alteration. Lots of exsolution in both pyroxenes.
15SM055B	Mantle	Harzburgite	-	4	Harzburgite consisting of 2-4 mm anhedral ol (hard to judge size - highyl fractured by serp veinlets), 1-5 mm opx, anhedral 1 mm cpx, and very fine grained anhedral (<0.1 mm) sp. Opx anhedral and locally kink banded, some altered to serp. Contains only minor cpx. Overall displays porphyroclastic texture.
15SM056	Mantle	Harzburgite	-	3	Harzburgite consisting of 2-4 mm anhedral ol (hard to judge size - highyl fractured by serp veinlets), 2-5 mm anhedral opx, anhedral 1-2 mm cpx, and 0.5-1.5 mm anhedral sp. Both pyroxenes have exsolution lamellae.
15SM057	Mantle	Harzburgite	-	4	Harzburgite consisting of 0.5-5 mm anhedral opx with exsolution lamellae, 0.5 mm sp, and fine grained cpx and ol. Ol is anhedral and too fractured to serp veinlets to accurately estimate grain size. Magnetite present in wider serp veins. Pyroxenes also fractured.
DC0205	Mantle	Harzburgite	-	2	Protogranular, coarse grained harzburgite. Fine grained anhedral sp. Opx porphyroclasts and cpx with exsolution lamellae.
DC0206	Mantle	Harzburgite	-	2	Transitional between protogranular and porphyroclastic, coarse grained harzburgite. Fine grained anhedral sp - irregular/blebby shapes. Opx porphyroclasts and cpx with exsolution lamellae.
DC0303	Mantle	Harzburgite	-	2	Transitional between protogranular and porphyroclastic, coarse grained harzburgite. Fine grained anhedral sp. Opx porphyroclasts and cpx with exsolution lamellae.
DC0304	Mantle	Harzburgite	-	5	Transitional between protogranular and porphyroclastic, coarse grained harzburgite. Fine to medium grained anhedral sp - irregular/blebby shapes. Opx porphyroclasts and cpx with exsolution lamellae. Mag along serp veins. Hard to tell texture because so many serp veinlets.
DC0310	Mantle	Lherzolite	-	1	Protogranular II (secondary??), coarse grained harzburgite. Fine grained subhedral equant sp - often as inclusions in ol. Opx porphyroclasts and cpx with exsolution lamellae. Very fresh - almost zero serp.
DC0312	Mantle	Lherzolite	-	1	Protogranular, coarse grained harzburgite. Fine grained anhedral sp. Opx porphyroclasts and cpx with exsolution lamellae. Some serp but still very fresh.
DC0313	Mantle	Lherzolite	-	1	Porphyroclastic medium to coarse grained harzburgite. Fine grained subhedral to anhedral sp. Opx porphyroclasts and cpx with exsolution lamellae.
DC0318	Mantle	Lherzolite	-	1	Porphyroclastic medium to coarse grained harzburgite. Fine grained subhedral to anhedral sp. Opx porphyroclasts and cpx with exsolution lamellae.
DC0322	Mantle	Harzburgite	-	1	Protogranular coarse grained harzburgite. Fine grained anhedral to subhedral sp. Opx porphyroclasts and cpx with exsolution lamellae.
DC0336	Mantle	Harzburgite	-	3	Porphyroclastic medium to coarse grained harzburgite - hard to estimate grain size with so many serp veinlets. Fine grained anhedral rounded sp. Opx porphyroclasts and cpx with exsolution lamellae.
DC0345	Mantle	Harzburgite	-	2	Transitional between protogranular and porphyroclastic, coarse grained harzburgite. Fine grained anhedral sp - irregular/blebby shapes. Opx porphyroclasts and cpx with exsolution lamellae.

Table A 4: Whole-rock major element (ICP-OES) and trace element (ICP-MS) data from ActLabs Ltd. from peridotites of the Menatatuline massif (bdl indicates below detection limits; n.d. indicates no data).

Sample		**15SM14B**	**15SM23**	**15SM34-1**	**15SM34-2**	**15SM38**	**15SM45**	**15SM55A**	**15SM55B**	**15SM56**	**15SM57**	**16SM160**	**16SM162**	**16SM181**	**16SM184**	**16SM187**	**16SM188**	**16SM190**	**16SM192**	**16SM193**
Rock type		harz	harz	harz	harz	harz	harz	harz	harz	harz	harz	harz	harz	harz	harz	harz	harz	harz	harz	harz
Location		Menatatuline	Menatatuline	Menatatuline	Menatatuline	Menatatuline	Menatatuline	Menatatuline	Menatatuline	Menatatuline	Menatatuline	Nahlin Mountain	Nahlin Mountain	Nahlin Mountain	Nahlin Mountain	Nahlin Mountain	Nahlin Mountain	Menatatuline	Menatatuline	Menatatuline
Lat	Detection limit	58.959	58.951	58.934	58.934	58.953	58.962	58.949	58.949	58.966	58.966	58.904	58.901	58.860	58.857	58.883	58.889	58.962	58.961	58.960
Long		-132.27	-132.23	-132.24	-132.24	-132.24	-132.25	-132.26	-132.26	-132.25	-132.25	-132.17	-132.17	-132.11	-132.09	-132.13	-132.12	-132.27	-132.27	-132.27
SiO2 (wt %)	0.01	43.98	45.31	43.81	43.40	43.60	45.82	44.56	44.26	44.50	45.62	42.88	43.78	43.14	42.83	41.98	42.93	43.10	44.00	43.64
Al2O3	0.01	0.99	1.05	1.20	0.74	0.91	1.03	0.85	0.72	0.78	1.00	0.51	0.86	0.67	0.62	0.50	0.66	0.70	0.77	0.81
FeO	0.01	8.47	8.16	7.31	8.54	8.38	7.80	7.65	8.17	7.51	7.93	8.06	7.54	8.24	8.30	8.45	8.62	8.28	7.93	7.95
MnO	0.001	0.13	0.13	0.12	0.12	0.13	0.13	0.12	0.13	0.13	0.13	0.13	0.12	0.13	0.13	0.13	0.13	0.13	0.13	0.13
MgO	0.01	44.39	42.96	45.79	45.44	44.90	43.11	44.91	44.81	44.74	43.26	46.70	45.90	45.90	46.35	47.39	45.94	46.11	45.34	45.84
CaO	0.01	0.97	1.42	0.82	0.70	1.09	1.11	0.97	0.98	1.47	1.15	0.82	0.94	0.96	0.83	0.59	0.77	0.76	0.94	0.72
Na2O	0.01	0.07	0.03	0.10	0.08	0.03	0.09	0.05	0.03	0.02	0.02	0.01	0.01	0.03	0.02	0.01	0.01	<0.01	0.02	0.02
K2O	0.01	bdl	bdl	bdl	bdl	bdl	bdl	bdl	bdl	bdl	bdl	bdl	0.01	bdl	bdl	bdl	bdl	bdl	bdl	bdl
TiO2	0.001	0.03	0.02	0.03	0.02	0.01	0.03	0.02	0.01	0.01	0.01	0.00	0.01	0.00	0.00	0.00	0.00	0.00	0.00	0.01
P2O5	0.01	0.02	bdl	bdl	0.01	0.01	bdl	bdl	bdl	bdl	bdl	bdl	bdl	bdl	bdl	bdl	bdl	bdl	bdl	bdl
Total	0.01	100.00	99.99	99.99	100.01	99.99	99.99	99.98	100.02	99.98	99.99	100.01	100.01	100.01	100.01	99.99	100.03	100.01	100.02	99.99
Mg #		90.3	90.4	91.8	90.5	90.5	90.8	91.3	90.7	91.4	90.7	91.2	91.6	90.8	90.9	90.9	90.5	90.8	91.1	91.1
Sc (ppm)	1	10	12	8	8	11	10	10	10	11	11	9	9	9	10	8	9	9	11	9
V	5	42	52	41	32	46	43	43	41	44	50	34	36	36	39	31	37	39	45	36
Cr	20	2710	3230	2440	1900	2680	2530	2650	2540	2660	2510	2540	3320	3090	2780	2350	2310	2810	2710	2560
Co	1	111	108	100	110	108	105	107	103	110	104	121	115	119	122	118	118	122	121	112
Ni	20	2240	2230	2110	2230	2160	2160	2190	2140	2340	2160	2320	2250	2270	2320	2230	2260	2300	2260	2130
Cu	10	bdl	bdl	bdl	bdl	10	10	bdl	10	40	10	bdl	bdl	bdl	10	bdl	bdl	bdl	bdl	bdl
Zn	30	40	40	40	40	40	40	30	30	40	40	40	50	40	40	40	40	40	40	40
Ga	1	1	1	1	bdl	1	1	bdl	bdl	bdl	bdl	bdl	bdl	bdl	bdl	bdl	bdl	bdl	bdl	bdl
Rb	1	bdl	bdl	bdl	bdl	bdl	bdl	bdl	bdl	bdl	bdl	bdl	bdl	bdl	bdl	bdl	bdl	bdl	bdl	bdl
Sr	2	2	bdl	bdl	bdl	bdl	bdl	bdl	3	bdl	bdl	2	2	bdl	bdl	bdl	bdl	bdl	bdl	bdl
Y	0.5	0.6	bdl	0.5	bdl	bdl	0.7	bdl	bdl	bdl	bdl	bdl	bdl	bdl	bdl	bdl	bdl	bdl	bdl	bdl
Zr	1	3	bdl	2	2	2	3	2	3	2	1	2	2	bdl	1	1	1	3	2	1
Nb	0.2	0.3	bdl	bdl	bdl	bdl	0.2	bdl	bdl	bdl	bdl	bdl	bdl	bdl	bdl	bdl	bdl	bdl	bdl	bdl
Ba	3	bdl	bdl	bdl	bdl	bdl	bdl	bdl	bdl	bdl	bdl	9	7	4	6	5	4	9	3	3
La	0.05	0.09	bdl	0.12	0.05	0.07	0.15	0.13	bdl	0.06	0.07	bdl	0.77	bdl	bdl	bdl	bdl	bdl	bdl	bdl
Ce	0.05	0.27	0.10	0.28	0.15	0.14	0.31	0.26	0.06	0.11	0.12	0.07	1.10	bdl	bdl	0.09	bdl	bdl	bdl	bdl
Pr	0.01	0.04	0.02	0.03	0.02	0.01	0.04	0.03	bdl	bdl	bdl	0.02	0.06	0.01	bdl	0.02	bdl	0.01	bdl	bdl
Nd	0.05	0.23	0.14	0.16	0.1	0.08	0.26	0.15	bdl	bdl	0.06	0.06	0.2	0.06	bdl	bdl	bdl	bdl	bdl	bdl
Sm	0.01	0.07	0.05	0.06	0.08	0.03	0.06	0.03	bdl	bdl	0.02	0.03	0.04	0.02	bdl	0.05	bdl	bdl	0.01	0.01
Eu	0.005	0.019	0.007	0.012	0.006	bdl	0.013	0.006	bdl	bdl	bdl	bdl	bdl	bdl	bdl	bdl	bdl	bdl	bdl	bdl
Gd	0.01	0.06	0.04	0.07	0.06	0.03	0.1	0.07	0.01	bdl	0.01	0.02	0.02	bdl	bdl	0.01	bdl	bdl	0.01	bdl
Tb	0.01	0.01	bdl	0.01	bdl	bdl	0.01	0.01	bdl	bdl	bdl	bdl	bdl	bdl	bdl	bdl	bdl	bdl	bdl	bdl
Dy	0.01	0.1	0.07	0.07	0.03	0.01	0.09	0.09	0.03	0.02	0.03	0.02	0.02	bdl	bdl	bdl	bdl	0.01	bdl	0.01
Ho	0.01	0.02	0.01	0.02	bdl	bdl	0.02	0.02	bdl	bdl	bdl	bdl	bdl	bdl	bdl	bdl	bdl	bdl	bdl	bdl
Er	0.01	0.07	0.03	0.06	0.03	0.02	0.08	0.05	0.02	0.03	0.02	bdl	0.02	0.01	bdl	bdl	bdl	0.01	0.01	0.01
Tm	0.005	0.009	0.007	0.01	0.006	bdl	0.012	0.007	bdl	bdl	0.007	bdl	bdl	bdl	bdl	bdl	bdl	bdl	bdl	bdl
Yb	0.01	0.06	0.06	0.07	0.04	0.03	0.08	0.06	0.02	0.04	0.06	0.02	0.02	0.02	0.01	0.02	0.02	0.02	0.02	0.02
Lu	0.002	0.008	0.009	0.01	0.006	0.004	0.012	0.009	0.003	0.006	0.008	0.003	0.004	0.003	0.003	0.003	0.004	0.004	0.005	0.004
Hf	0.1	bdl	bdl	bdl	bdl	bdl	bdl	bdl	bdl	bdl	bdl	bdl	bdl	bdl	bdl	bdl	bdl	bdl	bdl	bdl
Ta	0.01	bdl	bdl	bdl	bdl	bdl	bdl	bdl	bdl	bdl	bdl	bdl	bdl	bdl	bdl	bdl	bdl	bdl	bdl	bdl
Pb	5	bdl	bdl	bdl	bdl	bdl	bdl	bdl	bdl	bdl	bdl	bdl	bdl	bdl	bdl	bdl	bdl	bdl	bdl	bdl
Th	0.05	bdl	bdl	bdl	bdl	bdl	bdl	bdl	bdl	bdl	bdl	bdl	bdl	bdl	bdl	bdl	bdl	bdl	bdl	bdl
U	0.01	bdl	bdl	bdl	bdl	bdl	bdl	bdl	bdl	bdl	bdl	bdl	0.01	bdl	bdl	bdl	bdl	0.03	bdl	bdl

Table A 5: Whole-rock major element (XRF) and trace element (ICP-MS) data from peridotites of the Hardluck massif (bdl indicates below detection limits; n.d. indicates no data). Major element data from McGill University or St. Mary’s University originally reported in Canil et al. (2006), and trace element data from Laurentian University originally reported in Babechuk et al. (2010).

Sample		DC0205	DC0206	DC0303	DC0304	DC0310	DC0313	DC0322	DC0327	DC0336	DC0312^b	DC0312^c		DC0345^b	DC0345^c				
Rock type		harz	harz	harz	harz	lherz	lherz	harz	lherz	lherz	lherz	lherz		lherz	lherz				
Location		N of Hardluck Peaks	N of Hardluck Peaks	Moho Saddle	Moho Saddle	Peridotite Peak	Peridotite Peak	Peridotite Peak	Peridotite Peak	Peridotite Peak East	Peridotite Peak	Peridotite Peak		Peridotite Peak East	Peridotite Peak East		ActLabs Standard		
Lat	Detection	59.044	59.045	59.029	59.029	58.979	58.980	58.975	58.984	58.953	58.980	58.980		58.954	58.954		W-2a	W-2a	
Long	Limit^a	-132.96	-132.96	-132.88	-132.88	-132.75	-132.75	-132.72	-132.74	-132.62	-132.75	-132.75	% accuracy	-132.66	-132.66	% accuracy	Certified	Measured	% accuracy
SiO2	0.01	43.41	45.48	45.81	43.10	44.19	45.07	42.18	44.01	45.14	44.62	44.94	0.7	43.35	43.80	1.0	52.4	52.3	0.2
Al2O3	0.01	0.52	0.78	0.91	0.45	1.39	1.88	0.93	1.57	1.40	1.85	1.96	6.2	1.15	1.21	5.5	15.4	15.37	0.2
FeO	0.01	7.97	7.32	7.68	8.41	7.95	7.92	8.69	7.95	8.39	7.95	8.14	2.4	7.89	8.00	1.4	9.6	9.57	0.6
MnO	0.001	0.13	0.12	0.16	0.13	0.12	0.12	0.13	0.12	0.13	0.12	0.13	10.9	0.12	0.13	7.3	0.163	0.165	1.2
MgO	0.01	46.30	44.23	43.01	46.13	43.25	42.43	46.31	43.47	41.49	42.90	41.83	2.5	44.89	44.57	0.7	6.37	6.45	1.3
CaO	0.01	0.71	1.09	1.27	0.59	2.08	1.69	1.12	1.78	1.54	1.97	2.02	2.4	1.31	1.34	2.3	10.9	10.95	0.5
Na2O	0.01	n.d.	n.d.	0.01	0.01	0.03	0.04	bdl	n.d.	0.03	bdl	0.04	-	0.01	0.04	322	2.14	2.17	1.4
K2O	0.01	n.d.	n.d.	0.02	0.02	0.01	0.01	0.01	n.d.	0.01	0.01	bdl	-	0.01	bdl	-	0.626	0.6	4.2
TiO2	0.001	0.01	0.01	0.01	0.03	0.02	0.03	0.02	0.02	0.02	0.02	0.02	10.2	0.02	0.01	52.5	1.06	1.076	1.5
P2O5	0.01	n.d.	n.d.	0.01	0.01	0.01	0.01	0.01	n.d.	0.01	0.01	bdl	-	0.01	bdl	-	0.13	0.13	0.0
Total	0.01	99.05	99.03	99.75	99.82	99.94	100.08	100.35	98.92	99.09	100.34	99.99	0.3	99.64	99.99	0.4	98.82	98.79	0.0
Mg #		91.2	91.5	90.9	90.7	90.6	90.5	90.5	90.7	89.8	90.6	90.2	0.5	91.0	90.8	0.2	54.1	54.6	0.8
Sc (ppm)	1	7.97	10.75	12.08	8.83	14.41	13.91	9.67	n.d.	11.37	13.66	13	4.8	9.67	9	6.9	36.0	35.0	2.8
V	5	31.69	43.88	44.85	31.11	57.31	59.10	33.89	n.d.	43.64	54.63	63	15.3	35.87	41	14.3	262	267	1.9
Cr	20.0	3044	4362	3242	2853	2890	2771	2418	4547	2492	2532	2910	14.9	2976	2990	0.5	92	100	8.7
Co	1	n.d.	n.d.	98.31	105.22	107.46	103.83	119.97	n.d.	99.91	102.93	110	6.9	104.26	120	15.1	43	44	2.3
Ni	20	2364	2332	1979	2104	2111	2006	2374	2299	1989	2037	2030	0.3	2056	2230	8.4	70	70	0.0
Cu	10	n.d.	n.d.	7.04	6.22	24.92	17.66	16.28	n.d.	12.97	18.41	20	8.6	5.12	bdl	-	110	110	0.0
Zn	30	n.d.	n.d.	38.70	40.79	38.48	36.75	41.31	n.d.	35.34	36.79	40	8.7	41.81	40	4.3	80	90	12.5
Ga	1	n.d.	n.d.	0.77	0.57	1.18	1.52	0.76	n.d.	0.94	1.28	2	56.5	0.92	1	8.3	17	18	5.9
Rb	1	n.d.	n.d.	0.24	0.10	0.02	0.04	0.01	n.d.	0.03	0.09	bdl	-	0.04	bdl	-	21	20	4.8
Sr	2	n.d.	n.d.	0.77	0.68	0.14	0.17	0.13	n.d.	0.13	0.23	bdl	-	0.12	bdl	-	190	192	1.1
Y	0.5	n.d.	n.d.	0.08	0.29	0.41	0.47	0.21	n.d.	0.29	0.64	0.70	9.5	0.26	bdl	-	24	21.7	9.6
Zr	1	n.d.	n.d.	0.07	0.44	0.03	0.05	0.21	n.d.	0.03	0.09	1	1022	0.04	1	2282	94	95	1.1
Nb	0.2	n.d.	n.d.	0.007	0.008	0.002	0.003	0.007	n.d.	0.001	0.003	bdl	-	0.002	bdl	-	7.9	7.3	7.6
Ba	3	n.d.	n.d.	5.45	0.74	0.79	0.76	0.09	n.d.	0.07	1.67	4	139	0.06	2	3150	182	170	6.6
La	0.05	n.d.	n.d.	0.009	0.017	0.001	0.002	0.002	n.d.	0.001	0.003	bdl	-	0.001	bdl	-	n.d.	n.d.	n.d.
Ce	0.05	0.063	0.083	0.012	0.042	0.002	0.004	0.005	n.d.	0.001	0.007	bdl	-	0.001	bdl	-	23	24.8	7.8
Pr	0.01	n.d.	n.d.	0.0018	0.0066	0.0003	0.0005	0.0006	n.d.	0.0001	0.0012	bdl	-	0.0002	bdl	-	n.d.	n.d.	n.d.
Nd	0.05	n.d.	n.d.	0.007	0.036	0.002	0.003	0.003	n.d.	0.001	0.008	bdl	-	0.002	bdl	-	13	13.3	2.3
Sm	0.01	n.d.	n.d.	0.001	0.015	0.004	0.004	0.002	n.d.	0.001	0.008	0.010	19.3	0.003	bdl	-	3.3	3.4	3.0
Eu	0.005	n.d.	n.d.	0.0005	0.0057	0.0021	0.0024	0.0010	n.d.	0.0007	0.0044	0.0070	57.6	0.0015	bdl	-	n.d.	n.d.	n.d.
Gd	0.01	n.d.	n.d.	0.002	0.025	0.019	0.021	0.008	n.d.	0.009	0.033	0.020	39.7	0.012	bdl	-	n.d.	n.d.	n.d.
Tb	0.01	n.d.	n.d.	0.001	0.005	0.006	0.006	0.003	n.d.	0.003	0.010	bdl	-	0.003	bdl	-	0.63	0.64	1.6
Dy	0.01	n.d.	n.d.	0.007	0.042	0.057	0.061	0.028	n.d.	0.034	0.088	0.090	2.4	0.033	0.04	21.4	n.d.	n.d.	n.d.
Ho	0.01	n.d.	n.d.	0.003	0.011	0.016	0.018	0.008	n.d.	0.011	0.025	0.020	20.3	0.010	bdl	-	0.76	0.81	6.6
Er	0.01	n.d.	n.d.	0.014	0.037	0.057	0.066	0.031	n.d.	0.043	0.086	0.080	6.8	0.036	0.04	9.7	2.5	2.3	8.0
Tm	0.005	n.d.	n.d.	0.003	0.007	0.011	0.012	0.006	n.d.	0.008	0.015	0.014	9.2	0.007	bdl	-	n.d.	n.d.	n.d.
Yb	0.01	0.001	0.018	0.031	0.055	0.078	0.092	0.047	n.d.	0.069	0.116	0.090	22.3	0.056	0.05	10.1	2.1	2.1	0.0
Lu	0.002	n.d.	n.d.	0.006	0.010	0.014	0.016	0.009	n.d.	0.012	0.020	0.017	13.9	0.010	0.009	10.6	0.33	0.32	3.0
Hf	0.1	n.d.	n.d.	0.0015	0.0120	0.0026	0.0030	0.0037	n.d.	0.0020	0.0037	bdl	-	0.0022	bdl	-	2.6	2.5	3.8
Ta	0.01	n.d.	n.d.	0.0005	0.0005	0.0002	0.0002	0.0002	n.d.	0.0001	0.0002	bdl	-	0.0002	bdl	-	n.d.	n.d.	n.d.
Pb	5	n.d.	n.d.	0.0603	0.0461	0.0212	0.0097	0.0238	n.d.	0.0080	0.0535	bdl	-	0.0069	bdl	-	n.d.	n.d.	n.d.
Th	0.05	n.d.	n.d.	0.0015	0.0026	0.0004	0.0006	0.0007	n.d.	0.0003	0.0004	bdl	-	0.0003	bdl	-	n.d.	n.d.	n.d.
U	0.01	n.d.	n.d.	0.0018	0.0022	0.0003	0.0003	0.0007	n.d.	0.0001	0.0005	bdl	-	0.0001	bdl	-	n.d.	n.d.	n.d.

Table A 6: Representative olivine major element chemistry measured by EMP (σ = one standard deviation).

Sample	DC0205				DC0206				DC0303				DC0304				DC0310			
Location	N of Hardluck Peaks				N of Hardluck Peaks				Moho Saddle				Moho Saddle				Peridotite Peak			
Mineral	ol				ol				ol				ol				ol			
n =	8		9		6		5		8		6		4		4		7		6	
	core	σ	rim	σ	core	σ	rim	σ	core	σ	rim	σ	core	σ	rim	σ	core	σ	rim	σ
MgO (wt %)	49.72	0.25	49.78	0.14	50.04	0.07	50.43	0.26	49.96	0.27	50.17	0.15	49.95	0.10	50.26	0.06	49.61	0.24	49.75	0.37
Al2O3	0.003	0.005	0.002	0.004	0.002	0.002	0.005	0.005	0.008	0.005	0.004	0.004	0.012	0.011	0.003	0.002	0.011	0.002	0.013	0.005
SiO2	41.45	0.15	41.38	0.17	41.45	0.12	41.61	0.08	41.07	0.14	41.20	0.24	41.37	0.09	41.40	0.10	41.42	0.22	41.71	0.20
CaO	0.045	0.011	0.026	0.008	0.031	0.006	0.016	0.005	0.043	0.011	0.044	0.011	0.034	0.006	0.038	0.004	0.012	0.004	0.007	0.004
TiO2	0.003	0.005	0.005	0.005	0.003	0.005	0.003	0.004	0.003	0.004	0.000	0.000	0.003	0.005	0.000	0.000	0.014	0.013	0.015	0.017
Cr2O3	0.002	0.003	0.012	0.011	0.006	0.003	0.072	0.045	0.013	0.009	0.019	0.012	0.013	0.005	0.012	0.009	0.003	0.004	0.124	0.101
MnO	0.13	0.01	0.12	0.01	0.14	0.01	0.12	0.02	0.14	0.01	0.13	0.01	0.12	0.01	0.12	0.01	0.15	0.02	0.13	0.02
FeO	8.86	0.19	8.72	0.17	8.66	0.11	8.02	0.33	8.70	0.22	8.44	0.15	8.71	0.05	8.62	0.05	9.04	0.10	8.65	0.26
NiO	0.37	0.02	0.40	0.02	0.42	0.02	0.43	0.02	0.44	0.03	0.45	0.02	0.42	0.02	0.41	0.03	0.39	0.04	0.42	0.02
Total	100.58	0.22	100.44	0.28	100.75	0.20	100.71	0.13	100.37	0.34	100.46	0.23	100.64	0.24	100.87	0.03	100.65	0.23	100.82	0.34
Fo (mol %)	90.91	0.19	91.05	0.17	91.15	0.11	91.81	0.34	91.10	0.24	91.37	0.16	91.09	0.04	91.22	0.04	90.72	0.12	91.11	0.27

Sample	DC0312				DC0313				DC0318				DC0322				DC0327			
Location	Peridotite Peak				Peridotite Peak				Peridotite Peak				Peridotite Peak				Peridotite Peak			
Mineral	ol				ol				ol				ol				ol			
n =	8		3		4		4		5		4		7		9		8		9	
	core	σ	rim	σ	core	σ	rim	σ	core	σ	rim	σ	core	σ	rim	σ	core	σ	rim	σ
MgO (wt %)	49.65	0.07	49.54	0.23	49.56	0.14	50.14	0.26	49.36	1.16	50.31	0.20	49.30	0.47	49.54	0.38	49.62	0.27	49.87	0.22
Al2O3	0.003	0.003	0.000	0.000	0.012	0.006	0.013	0.007	0.011	0.005	0.010	0.005	0.006	0.004	0.008	0.005	0.003	0.004	0.002	0.003
SiO2	41.66	0.26	41.73	0.04	41.42	0.06	41.51	0.07	41.53	0.14	41.46	0.20	41.91	0.40	42.01	0.28	40.96	0.36	41.20	0.28
CaO	0.012	0.008	0.016	0.008	0.015	0.006	0.009	0.005	0.014	0.007	0.014	0.008	0.007	0.004	0.008	0.006	0.012	0.003	0.011	0.007
TiO2	0.002	0.003	0.006	0.008	0.024	0.013	0.038	0.021	0.030	0.026	0.020	0.012	0.012	0.008	0.013	0.009	0.006	0.005	0.005	0.005
Cr2O3	0.009	0.013	0.016	0.007	0.011	0.009	0.117	0.023	0.031	0.021	0.147	0.101	0.026	0.015	0.082	0.054	0.004	0.004	0.062	0.068
MnO	0.13	0.01	0.13	0.01	0.13	0.01	0.12	0.02	0.13	0.02	0.13	0.01	0.13	0.02	0.13	0.02	0.14	0.02	0.13	0.01
FeO	8.98	0.16	8.94	0.09	9.18	0.07	8.49	0.16	8.77	0.18	8.36	0.15	8.85	0.15	8.59	0.28	9.11	0.10	8.79	0.24
NiO	0.39	0.02	0.40	0.02	0.40	0.01	0.46	0.03	0.42	0.03	0.43	0.02	0.38	0.03	0.40	0.04	0.40	0.02	0.41	0.02
Total	100.83	0.21	100.77	0.30	100.74	0.14	100.91	0.17	100.30	1.27	100.88	0.24	100.62	0.24	100.78	0.24	100.25	0.32	100.48	0.38
Fo (mol %)	90.79	0.15	90.81	0.09	90.59	0.09	91.32	0.19	90.93	0.19	91.47	0.17	90.85	0.16	91.13	0.29	90.66	0.12	91.00	0.25

Sample	DC0334				DC0336				DC0345				15SM23A				15SM23B			
Location	Peridotite Peak				Peridotite Peak East				Peridotite Peak East				Menatatuline Range				Menatatuline Range			
Mineral	ol				ol				ol				ol				ol			
n =	4		4		4		4		9		6		4		2		13		6	
	core	σ	rim	σ	core	σ	rim	σ	core	σ	rim	σ	core	σ	rim	σ	core	σ	rim	σ
MgO (wt %)	49.33	0.38	49.74	0.16	49.09	0.12	49.45	0.24	49.39	0.17	49.42	0.12	50.02	0.14	50.21	0.10	49.94	0.11	50.15	0.18
Al2O3	0.009	0.015	0.006	0.007	0.005	0.004	0.000	0.000	0.001	0.003	0.002	0.003	0.019	0.006	0.017	0.002	0.013	0.005	0.014	0.005
SiO2	41.41	0.26	41.31	0.12	41.56	0.26	41.65	0.20	41.53	0.16	41.56	0.14	41.70	0.13	41.71	0.06	42.20	0.18	42.25	0.12
CaO	0.006	0.005	0.008	0.005	0.009	0.001	0.013	0.008	0.011	0.005	0.007	0.004	0.096	0.011	0.046	0.008	0.067	0.015	0.047	0.008
TiO2	0.006	0.006	0.004	0.004	0.008	0.009	0.001	0.001	0.008	0.009	0.006	0.005	0.004	0.005	0.012	0.000	0.004	0.004	0.004	0.003
Cr2O3	0.007	0.007	0.053	0.054	0.002	0.004	0.089	0.077	0.003	0.004	0.007	0.010	0.019	0.013	0.020	0.008	0.006	0.006	0.035	0.015
MnO	0.14	0.01	0.12	0.02	0.13	0.01	0.12	0.02	0.13	0.02	0.12	0.02	0.12	0.01	0.15	0.01	0.13	0.02	0.13	0.02
FeO	8.67	0.14	8.52	0.33	8.88	0.05	8.49	0.23	8.61	0.12	8.64	0.19	8.89	0.15	8.77	0.07	8.98	0.09	8.71	0.22
NiO	0.41	0.04	0.39	0.03	0.39	0.03	0.43	0.04	0.40	0.02	0.42	0.01	0.39	0.01	0.36	0.01	0.40	0.03	0.41	0.02
Total	99.98	0.54	100.15	0.22	100.08	0.28	100.26	0.27	100.08	0.25	100.19	0.20	101.25	0.27	101.30	0.00	101.74	0.22	101.75	0.16
Fo (mol %)	91.03	0.15	91.23	0.33	90.79	0.06	91.21	0.25	91.09	0.13	91.06	0.19	90.93	0.15	91.08	0.08	90.84	0.08	91.12	0.23

Sample	15SM34-2				15SM38				15SM45				15SM55B				15SM56				15SM57			
Location	Menatatuline Range				Menatatuline Range				Menatatuline Range				Menatatuline Range				Menatatuline Range				Menatatuline Range			
Mineral	ol				ol				ol				ol				ol				ol			
n =	9		9		7		5		17		14		8		7		6		6		5		4	
	core	σ	rim	σ	core	σ	rim	σ	core	σ	rim	σ	core	σ	rim	σ	core	σ	rim	σ	core	σ	rim	σ
MgO (wt %)	50.36	0.12	50.21	0.31	50.05	0.45	50.15	0.43	50.10	0.31	50.82	0.22	49.63	0.07	49.64	0.07	50.49	0.08	51.05	0.24	49.80	0.16	49.63	0.45
Al2O3	0.004	0.003	0.003	0.003	0.002	0.003	0.008	0.003	0.009	0.016	0.002	0.004	0.006	0.014	0.003	0.004	0.005	0.006	0.004	0.003	0.003	0.003	0.005	0.006
SiO2	42.14	0.11	41.91	0.24	41.63	0.35	41.58	0.48	41.88	0.15	42.10	0.17	42.00	0.15	42.07	0.16	42.10	0.13	41.92	0.26	41.99	0.46	41.85	0.53
CaO	0.036	0.015	0.021	0.011	0.029	0.016	0.031	0.015	0.024	0.011	0.016	0.006	0.030	0.005	0.020	0.005	0.036	0.009	0.026	0.008	0.032	0.009	0.024	0.005
TiO2	0.009	0.007	0.006	0.010	0.003	0.005	0.004	0.005	0.005	0.006	0.005	0.007	0.006	0.008	0.002	0.004	0.006	0.008	0.007	0.006	0.002	0.005	0.005	0.005
Cr2O3	0.014	0.018	0.011	0.010	0.014	0.009	0.027	0.021	0.016	0.045	0.057	0.027	0.018	0.038	0.016	0.019	0.004	0.004	0.044	0.023	0.015	0.015	0.004	0.007
MnO	0.13	0.01	0.12	0.03	0.13	0.02	0.13	0.01	0.13	0.02	0.12	0.01	0.14	0.01	0.13	0.01	0.14	0.01	0.13	0.01	0.13	0.01	0.13	0.01
FeO	8.81	0.08	8.80	0.19	8.62	0.17	8.37	0.17	8.32	0.21	7.46	0.23	8.65	0.09	8.48	0.16	8.76	0.06	8.08	0.23	8.90	0.06	8.86	0.19
NiO	0.38	0.02	0.37	0.03	0.40	0.01	0.40	0.03	0.42	0.02	0.43	0.02	0.42	0.02	0.41	0.03	0.39	0.02	0.41	0.03	0.40	0.05	0.42	0.01
Total	101.88	0.19	101.45	0.35	100.88	0.58	100.71	0.73	100.90	0.28	101.01	0.32	100.91	0.15	100.77	0.21	101.93	0.11	101.67	0.33	101.27	0.62	100.93	0.90
Fo (mol %)	91.06	0.08	91.05	0.21	91.18	0.22	91.44	0.22	91.48	0.22	92.39	0.22	91.09	0.08	91.26	0.16	91.13	0.05	91.84	0.24	90.89	0.07	90.90	0.22

Table A 7: Representative spinel major element chemistry measured by EMP (σ = one standard deviation).

Sample	DC0205				DC0206				DC0303				DC0304				DC0310			
Location	N of Hardluck Peaks				N of Hardluck Peaks				Moho Saddle				Moho Saddle				Peridotite Peak			
Mineral	sp				sp				sp				sp				sp			
n =	5		5		5		5		10		9		4		4		4		4	
	core	σ	rim	σ	core	σ	rim	σ	core	σ	rim	σ	core	σ	rim	σ	core	σ	rim	σ
MgO (wt %)	12.68	0.14	12.18	0.36	12.43	0.23	12.23	0.34	12.97	0.17	12.85	0.23	11.00	0.20	10.76	0.06	14.95	0.61	15.04	0.62
Al2O3	22.80	0.09	24.30	0.45	22.70	0.19	23.58	0.50	22.65	0.30	22.86	0.55	17.52	0.66	17.90	0.38	37.78	0.49	39.04	0.94
SiO2	0.03	0.01	0.03	0.00	0.02	0.01	0.04	0.02	0.02	0.01	0.03	0.02	0.04	0.02	0.03	0.01	0.04	0.03	0.02	0.02
V2O3	0.02	0.01	0.02	0.01	0.03	0.01	0.03	0.01	0.03	0.01	0.04	0.02	0.12	0.01	0.11	0.01	0.06	0.02	0.05	0.01
TiO2	0.24	0.01	0.25	0.02	0.22	0.01	0.23	0.02	0.24	0.01	0.23	0.01	0.28	0.01	0.28	0.01	0.20	0.02	0.21	0.01
Cr2O3	45.12	0.13	43.39	0.24	45.78	0.21	44.65	0.43	46.49	0.46	46.11	0.64	49.38	0.84	48.38	0.13	28.04	0.58	25.97	1.90
MnO	0.19	0.01	0.24	0.02	0.23	0.01	0.22	0.03	0.22	0.03	0.22	0.02	0.29	0.03	0.27	0.02	0.17	0.01	0.16	0.03
FeO	18.00	0.18	18.80	0.52	17.93	0.29	18.41	0.56	17.10	0.32	17.48	0.61	21.02	0.44	21.83	0.22	16.64	1.44	17.03	1.43
NiO	0.10	0.01	0.09	0.02	0.10	0.02	0.09	0.01	0.09	0.02	0.09	0.02	0.07	0.04	0.10	0.01	0.16	0.01	0.21	0.02
Total	99.18	0.38	99.29	0.27	99.45	0.24	99.47	0.14	99.80	0.21	99.90	0.27	99.72	0.25	99.67	0.40	98.04	0.36	97.73	0.46
Mg #	59.9	0.6	57.4	1.5	58.7	1.0	57.6	1.4	60.9	0.8	60.2	1.1	53.6	0.6	52.5	0.1	65.2	2.4	65.4	2.4
Cr #	57.0	0.1	54.5	0.6	57.5	0.3	56.0	0.8	57.9	0.5	57.5	0.9	65.4	1.2	64.5	0.4	33.2	0.4	30.8	2.0
Y Fe3+	0.037	0.002	0.035	0.001	0.030	0.001	0.030	0.002	0.029	0.002	0.030	0.003	0.054	0.005	0.060	0.004	0.035	0.008	0.041	0.008

Sample	DC0312				DC0313				DC0318				DC0322				DC0327			
Location	Peridotite Peak				Peridotite Peak				Peridotite Peak				Peridotite Peak				Peridotite Peak			
Mineral	sp				sp				sp				sp				sp			
n =	6		3		5		5		5		5		8		10		6		7	
	core	σ	rim	σ	core	σ	rim	σ	core	σ	rim	σ	core	σ	rim	σ	core	σ	rim	σ
MgO (wt %)	17.14	0.33	17.53	0.41	17.08	0.23	17.26	0.50	16.11	0.20	15.91	0.59	15.12	0.19	15.14	0.56	16.61	0.20	16.72	0.26
Al2O3	46.50	0.53	48.36	1.70	45.82	0.82	46.61	1.23	41.86	1.36	41.49	2.33	37.80	1.00	38.75	1.60	44.06	0.55	44.50	0.65
SiO2	0.09	0.14	0.01	0.01	0.03	0.01	0.03	0.01	0.02	0.01	0.02	0.02	0.02	0.01	0.01	0.01	0.01	0.01	0.01	0.01
V2O3	0.02	0.01	0.02	0.01	0.05	0.01	0.05	0.02	0.04	0.02	0.04	0.03	0.04	0.01	0.04	0.01	0.02	0.01	0.03	0.02
TiO2	0.16	0.02	0.14	0.01	0.13	0.01	0.13	0.03	0.16	0.01	0.18	0.02	0.19	0.02	0.21	0.03	0.15	0.01	0.16	0.02
Cr2O3	18.91	0.47	17.50	1.98	20.85	0.82	20.28	1.02	24.36	1.45	24.34	2.14	28.12	1.32	26.84	1.53	24.33	0.59	24.09	0.68
MnO	0.15	0.02	0.13	0.02	0.13	0.02	0.14	0.01	0.15	0.02	0.16	0.03	0.17	0.02	0.17	0.02	0.15	0.02	0.13	0.02
FeO	14.84	0.73	13.99	0.19	13.89	0.40	13.62	0.76	15.43	0.30	15.76	0.83	16.35	0.67	16.48	1.39	14.73	0.30	14.50	0.60
NiO	0.25	0.02	0.27	0.03	0.25	0.02	0.23	0.03	0.22	0.01	0.18	0.04	0.17	0.02	0.17	0.02	0.20	0.03	0.20	0.02
Total	98.08	0.30	97.94	0.35	98.24	0.25	98.35	0.54	98.36	0.21	98.06	0.28	97.99	0.42	97.82	0.44	100.27	0.27	100.34	0.47
Mg #	71.3	1.0	72.5	1.0	71.3	0.7	71.7	1.6	68.6	0.5	68.0	1.7	66.0	0.7	66.0	2.0	69.6	0.6	69.8	0.8
Cr #	21.4	0.5	19.5	2.3	23.4	1.0	22.6	1.3	28.1	1.8	28.3	2.9	33.3	1.6	31.7	2.0	27.0	0.7	26.6	0.8
Y Fe3+	0.034	0.006	0.029	0.003	0.022	0.002	0.020	0.002	0.032	0.003	0.029	0.004	0.035	0.005	0.036	0.010	0.021	0.002	0.019	0.003

Sample	DC0334				DC0336				DC0345				15SM23B				15SM34-2			
Location	Peridotite Peak				Peridotite Peak East				Peridotite Peak East				Menatatuline Range				Menatatuline Range			
Mineral	sp				sp				sp				sp				sp			
n =	8		6		6		6		6		4		9		6		8		7	
	core	σ	rim	σ	core	σ	rim	σ	core	σ	rim	σ	core	σ	rim	σ	core	σ	rim	σ
MgO (wt %)	14.38	0.18	14.81	0.40	15.74	0.11	15.95	0.22	14.89	0.16	15.09	0.24	14.32	0.36	14.51	0.48	13.44	0.20	13.70	0.22
Al2O3	32.38	0.70	35.05	0.94	40.56	0.62	41.48	0.71	37.26	0.31	37.98	0.64	28.41	0.62	28.30	0.44	26.46	0.52	26.26	0.87
SiO2	0.03	0.05	0.02	0.02	0.02	0.01	0.01	0.01	0.03	0.01	0.02	0.01	0.01	0.01	0.02	0.01	0.03	0.02	0.03	0.01
V2O3	0.03	0.01	0.03	0.01	0.03	0.01	0.03	0.01	0.04	0.01	0.05	0.00	0.03	0.02	0.03	0.01	0.04	0.01	0.03	0.01
TiO2	0.21	0.02	0.22	0.01	0.17	0.01	0.18	0.02	0.15	0.01	0.17	0.02	0.23	0.02	0.24	0.01	0.23	0.02	0.22	0.01
Cr2O3	35.44	1.01	32.89	0.95	26.66	0.69	25.62	0.53	30.52	0.31	29.66	0.67	40.40	1.05	40.38	0.84	42.09	0.89	42.45	0.69
MnO	0.19	0.03	0.17	0.03	0.15	0.02	0.14	0.01	0.18	0.03	0.19	0.02	0.19	0.02	0.19	0.02	0.19	0.02	0.20	0.01
FeO	17.13	0.34	16.53	0.75	15.96	0.18	15.83	0.39	16.62	0.15	16.41	0.32	16.72	0.63	16.52	0.71	17.91	0.47	17.35	0.17
NiO	0.13	0.02	0.14	0.02	0.17	0.01	0.20	0.02	0.13	0.01	0.15	0.02	0.11	0.04	0.12	0.04	0.09	0.03	0.10	0.02
Total	99.92	0.31	99.85	0.42	99.46	0.12	99.43	0.40	99.81	0.22	99.71	0.27	100.43	0.24	100.32	0.31	100.48	0.25	100.34	0.53
Mg #	64.1	0.7	65.3	1.2	67.5	0.4	68.2	0.7	64.7	0.5	65.5	1.0	64.8	1.5	65.7	1.9	61.5	0.7	62.7	0.6
Cr #	42.3	1.2	38.6	1.2	30.6	0.9	29.3	0.8	35.5	0.4	34.4	0.9	48.8	1.2	48.9	0.9	51.6	1.0	52.0	1.2
Y Fe3+	0.034	0.001	0.030	0.005	0.029	0.003	0.030	0.003	0.026	0.001	0.027	0.001	0.035	0.003	0.037	0.002	0.036	0.003	0.035	0.002

Sample	15SM38				15SM45				15SM55B				15SM56				15SM57			
Location	Menatatuline Range				Menatatuline Range				Menatatuline Range				Menatatuline Range				Menatatuline Range			
Mineral	sp				sp				sp				sp				sp			
n =	8		8		21		16		7		8		8		6		6		3	
	core	σ	rim	σ	core	σ	rim	σ	core	σ	rim	σ	core	σ	rim	σ	core	σ	rim	σ
MgO (wt %)	13.24	0.57	13.01	1.23	12.85	0.27	12.88	0.52	12.92	0.40	12.51	0.84	13.75	0.06	13.60	0.22	14.31	0.14	14.45	0.15
Al2O3	26.96	0.61	27.12	1.25	23.85	0.70	24.88	0.89	24.38	0.63	24.80	1.19	26.54	0.68	27.13	0.58	29.83	0.39	30.69	0.52
SiO2	0.04	0.02	0.04	0.02	0.04	0.07	0.01	0.02	0.03	0.02	0.03	0.02	0.03	0.02	0.02	0.01	0.12	0.20	0.19	0.20
V2O3	0.03	0.01	0.03	0.01	0.03	0.01	0.03	0.01	0.02	0.01	0.02	0.01	0.03	0.01	0.03	0.01	0.02	0.01	0.03	0.02
TiO2	0.22	0.01	0.23	0.02	0.23	0.01	0.23	0.02	0.25	0.01	0.24	0.02	0.25	0.01	0.25	0.01	0.23	0.01	0.23	0.02
Cr2O3	41.70	0.69	41.31	1.14	43.73	0.75	42.46	0.98	44.38	1.04	43.07	1.92	41.96	0.88	41.26	0.78	38.42	0.60	37.14	0.30
MnO	0.22	0.03	0.20	0.04	0.22	0.02	0.22	0.03	0.22	0.04	0.23	0.03	0.21	0.03	0.22	0.02	0.17	0.03	0.17	0.02
FeO	17.77	0.80	18.26	1.78	19.14	0.61	19.18	1.08	17.64	0.70	18.80	2.01	17.75	0.13	18.06	0.42	16.55	0.16	16.67	0.41
NiO	0.10	0.02	0.10	0.03	0.11	0.02	0.10	0.03	0.09	0.02	0.08	0.02	0.09	0.01	0.10	0.03	0.13	0.03	0.16	0.03
Total	100.28	0.23	100.30	0.40	100.20	0.35	100.00	0.30	99.93	0.16	99.80	0.30	100.61	0.30	100.66	0.38	99.79	0.27	99.72	0.36
Mg #	60.7	2.4	59.6	4.8	59.8	1.2	59.8	2.1	60.2	1.8	58.4	3.7	62.8	0.4	62.0	0.8	64.5	0.3	64.8	0.2
Cr #	50.9	1.0	50.6	1.7	55.2	1.1	53.4	1.3	55.0	1.2	53.8	2.2	51.5	1.2	50.5	1.0	46.4	0.6	44.8	0.5
Y Fe3+	0.031	0.002	0.032	0.003	0.048	0.003	0.048	0.006	0.031	0.002	0.037	0.009	0.040	0.002	0.040	0.004	0.031	0.001	0.033	0.005

Table A 8: Representative orthopyroxene major element chemistry measured by EMP (σ = one standard deviation).

Sample	DC0205				DC0206				DC0303				DC0304				DC0310				DC0312				DC0313			
Location	N of Hardluck Peaks				N of Hardluck Peaks				Moho Saddle				Moho Saddle				Peridotite Peak				Peridotite Peak				Peridotite Peak			
Mineral	opx				opx				opx				opx				opx				opx				opx			
n =	7		4		8		3		8		8		6		6		3		3		2		2		3		2	
	core	σ	rim	σ	core	σ	rim	σ	core	σ	rim	σ	core	σ	rim	σ	core	σ	rim	σ	core	σ	rim	σ	core	σ	rim	σ
MgO (wt %)	33.51	0.55	34.12	0.46	33.51	0.84	34.61	0.35	33.31	0.32	33.94	0.40	34.53	0.75	35.18	0.23	34.14	0.22	34.84	0.31	33.71	0.09	34.29	0.54	33.85	0.12	34.44	0.15
Al2O3	1.95	0.05	1.86	0.17	1.82	0.11	1.69	0.15	1.90	0.04	1.91	0.06	1.12	0.07	1.10	0.05	2.64	0.19	1.92	0.43	3.40	0.10	2.93	0.61	3.61	0.07	2.58	0.10
SiO2	55.45	0.20	55.71	0.11	55.47	0.21	55.79	0.28	55.61	0.17	55.47	0.44	56.35	0.34	56.55	0.38	56.17	0.31	56.81	0.49	55.50	0.02	56.06	0.70	54.47	0.80	55.70	0.23
CaO	2.23	0.71	1.43	0.63	2.36	1.19	1.12	0.34	2.44	0.55	1.70	0.44	1.46	0.83	0.83	0.13	0.69	0.06	0.42	0.08	0.84	0.07	0.57	0.02	0.87	0.05	0.40	0.02
TiO2	0.01	0.01	0.00	0.00	0.01	0.01	0.00	0.00	0.01	0.01	0.01	0.01	0.03	0.01	0.03	0.01	0.02	0.00	0.03	0.01	0.03	0.00	0.03	0.00	0.07	0.00	0.05	0.01
Cr2O3	0.76	0.07	0.65	0.11	0.75	0.13	0.59	0.15	0.76	0.05	0.72	0.05	0.43	0.05	0.37	0.05	0.52	0.10	0.37	0.18	0.51	0.02	0.43	0.15	0.56	0.02	0.51	0.05
MnO	0.13	0.02	0.13	0.01	0.12	0.02	0.12	0.01	0.14	0.01	0.15	0.02	0.15	0.02	0.14	0.02	0.14	0.00	0.15	0.01	0.13	0.01	0.13	0.01	0.15	0.01	0.14	0.00
FeO	5.99	0.20	6.06	0.24	5.83	0.25	6.04	0.08	5.97	0.08	6.06	0.17	5.93	0.39	6.15	0.09	6.33	0.16	6.30	0.18	6.30	0.02	6.40	0.08	6.28	0.04	6.50	0.11
Na2O	0.05	0.01	0.06	0.02	0.06	0.01	0.06	0.01	0.08	0.02	0.07	0.02	0.11	0.05	0.09	0.02	0.01	0.01	0.00	0.00	0.01	0.01	0.01	0.00	0.01	0.01	0.02	0.02
NiO	0.10	0.02	0.09	0.01	0.10	0.02	0.10	0.01	0.11	0.02	0.10	0.01	0.09	0.01	0.10	0.02	0.07	0.02	0.07	0.01	0.08	0.01	0.07	0.02	0.10	0.01	0.05	0.02
Total	100.17	0.20	100.12	0.22	100.04	0.40	100.11	0.23	100.33	0.30	100.14	0.46	100.21	0.44	100.54	0.33	100.74	0.18	100.90	0.42	100.52	0.09	100.92	0.57	99.96	0.71	100.38	0.24
Mg #	90.9	0.1	90.9	0.3	91.1	0.2	91.1	0.1	90.9	0.1	90.9	0.2	91.2	0.4	91.1	0.1	90.6	0.3	90.8	0.2	90.5	0.0	90.5	0.0	90.6	0.1	90.4	0.2
X Ca	0.083	0.027	0.053	0.023	0.088	0.045	0.042	0.013	0.091	0.021	0.064	0.016	0.055	0.032	0.031	0.005	0.025	0.002	0.015	0.003	0.031	0.003	0.021	0.001	0.032	0.002	0.015	0.001

Sample	DC0318				DC0322				DC0327				DC0334				DC0336				DC0345				15SM23A			
Location	Peridotite Peak				Peridotite Peak				Peridotite Peak				Peridotite Peak				Peridotite Peak East				Peridotite Peak East				Menatatuline Range			
Mineral	opx				opx				opx				opx				opx				opx				opx			
n =	2		2		4		5		9		5		5		5		5		4		7		3		4		2	
	core	σ	rim	σ	core	σ	rim	σ	core	σ	rim	σ	core	σ	rim	σ	core	σ	rim	σ	core	σ	rim	σ	core	σ	rim	σ
MgO (wt %)	34.14	0.33	34.31	0.05	33.93	0.32	34.11	0.43	34.36	0.24	34.79	0.24	34.45	0.17	34.72	0.25	34.34	0.22	34.86	0.26	34.36	0.49	34.62	0.23	33.31	0.24	33.18	0.10
Al2O3	3.00	0.23	2.77	0.17	2.70	0.28	2.36	0.48	3.30	0.25	2.93	0.16	3.03	0.13	2.48	0.28	2.84	0.34	2.21	0.53	2.85	0.40	2.63	0.24	2.36	0.09	2.32	0.07
SiO2	55.63	0.46	55.86	0.08	56.12	0.58	56.69	0.50	54.93	0.36	55.33	0.26	55.29	0.22	55.80	0.20	55.64	0.29	56.36	0.47	55.73	0.35	55.85	0.25	55.99	0.20	55.77	0.14
CaO	0.69	0.14	0.58	0.04	0.69	0.13	0.67	0.22	0.86	0.19	0.55	0.15	0.66	0.11	0.60	0.16	0.75	0.27	0.41	0.04	0.87	0.44	0.51	0.05	2.35	0.36	2.59	0.14
TiO2	0.05	0.03	0.04	0.01	0.05	0.02	0.05	0.01	0.03	0.01	0.02	0.01	0.01	0.01	0.02	0.01	0.03	0.01	0.02	0.01	0.02	0.01	0.00	0.00	0.01	0.01	0.02	0.01
Cr2O3	0.54	0.02	0.52	0.06	0.55	0.10	0.42	0.13	0.62	0.10	0.50	0.07	0.79	0.08	0.61	0.02	0.54	0.14	0.32	0.18	0.66	0.18	0.58	0.15	0.84	0.03	0.83	0.05
MnO	0.16	0.01	0.11	0.01	0.15	0.04	0.15	0.01	0.14	0.02	0.15	0.02	0.14	0.02	0.15	0.01	0.15	0.02	0.15	0.02	0.13	0.01	0.14	0.02	0.14	0.02	0.15	0.01
FeO	6.12	0.06	6.37	0.02	6.26	0.05	6.30	0.08	6.20	0.10	6.36	0.11	6.13	0.05	6.25	0.10	6.26	0.20	6.42	0.05	5.93	0.18	6.02	0.05	5.85	0.08	5.95	0.03
Na2O	0.02	0.00	0.02	0.01	0.02	0.02	0.01	0.01	0.05	0.01	0.06	0.01	0.05	0.02	0.06	0.02	0.06	0.01	0.06	0.02	0.07	0.01	0.08	0.01	0.05	0.01	0.04	0.02
NiO	0.08	0.02	0.06	0.02	0.09	0.01	0.07	0.01	0.08	0.02	0.08	0.02	0.10	0.01	0.08	0.02	0.08	0.02	0.08	0.01	0.07	0.01	0.09	0.00	0.13	0.03	0.08	0.00
Total	100.42	0.33	100.64	0.30	100.56	0.36	100.82	0.32	100.56	0.34	100.75	0.19	100.65	0.13	100.77	0.27	100.70	0.31	100.89	0.16	100.68	0.04	100.54	0.14	101.01	0.23	100.93	0.05
Mg #	90.9	0.2	90.6	0.0	90.6	0.1	90.6	0.2	90.8	0.1	90.7	0.1	90.9	0.1	90.8	0.2	90.7	0.2	90.6	0.1	91.2	0.2	91.1	0.1	91.0	0.1	90.9	0.0
X Ca	0.026	0.005	0.021	0.001	0.025	0.005	0.025	0.008	0.032	0.007	0.020	0.005	0.024	0.004	0.022	0.006	0.028	0.010	0.015	0.002	0.032	0.016	0.019	0.002	0.087	0.014	0.096	0.005

Sample	15SM23B				15SM34-2				15SM38				15SM45				15SM55B				15SM56				15SM57			
Location	Menatatuline Range				Menatatuline Range				Menatatuline Range				Menatatuline Range				Menatatuline Range				Menatatuline Range				Menatatuline Range			
Mineral	opx				opx				opx				opx				opx				opx				opx			
n =	9		6		1		2		11		5		11		9		13		13		7		7		5		2	
	core	σ	rim	σ	core	σ	rim	σ	core	σ	rim	σ	core	σ	rim	σ	core	σ	rim	σ	core	σ	rim	σ	core	σ	rim	σ
MgO (wt %)	33.06	0.28	33.71	0.15	34.16		33.35	0.17	33.57	0.24	33.91	0.14	34.60	0.34	34.68	0.24	34.03	33.80	0.39	0.45	34.34	0.31	34.63	0.25	33.08	0.33	33.39	0.20
Al2O3	2.55	0.18	2.34	0.21	2.18		2.13	0.02	2.22	0.17	2.14	0.08	2.34	0.29	2.02	0.16	1.85	1.93	0.14	0.08	2.08	0.11	2.06	0.15	2.68	0.12	2.38	0.08
SiO2	56.27	0.21	56.57	0.13	56.50		55.66	0.14	56.07	0.56	56.47	0.10	56.34	0.78	56.51	0.70	56.53	56.50	0.31	0.18	56.57	0.15	56.60	0.35	55.85	0.19	56.22	0.37
CaO	2.26	0.29	1.61	0.12	1.68		2.52	0.29	1.86	0.42	1.43	0.21	0.83	0.21	0.88	0.15	1.88	2.04	0.45	0.45	1.42	0.38	1.00	0.18	2.20	0.34	1.61	0.26
TiO2	0.02	0.01	0.02	0.01	0.02		0.01	0.01	0.01	0.01	0.01	0.00	0.02	0.01	0.01	0.01	0.01	0.00	0.00	0.01	0.01	0.01	0.01	0.01	0.01	0.01	0.01	0.01
Cr2O3	0.85	0.09	0.74	0.07	0.68		0.73	0.00	0.75	0.09	0.68	0.06	0.79	0.17	0.66	0.04	0.66	0.75	0.08	0.06	0.65	0.04	0.59	0.10	0.90	0.10	0.66	0.04
MnO	0.13	0.02	0.15	0.02	0.11		0.15	0.00	0.14	0.03	0.14	0.02	0.13	0.02	0.14	0.02	0.14	0.14	0.02	0.02	0.14	0.02	0.16	0.01	0.14	0.01	0.17	0.00
FeO	5.89	0.06	6.02	0.09	5.97		5.87	0.05	6.04	0.23	6.10	0.07	5.88	0.14	5.86	0.18	5.73	5.75	0.11	0.12	5.93	0.10	5.98	0.10	5.97	0.07	6.12	0.02
Na2O	0.04	0.01	0.04	0.01	0.04		0.03	0.00	0.05	0.01	0.05	0.01	0.05	0.02	0.03	0.02	0.07	0.06	0.04	0.02	0.04	0.01	0.04	0.02	0.04	0.02	0.05	0.01
NiO	0.10	0.02	0.10	0.02	0.13		0.09	0.00	0.10	0.02	0.09	0.03	0.11	0.02	0.09	0.01	0.10	0.10	0.02	0.02	0.08	0.02	0.09	0.02	0.10	0.02	0.12	0.00
Total	101.18	0.14	101.30	0.21	101.46		100.56	0.07	100.80	0.53	101.01	0.17	101.07	0.41	100.87	0.44	101.00	101.07	0.28	0.23	101.28	0.19	101.16	0.27	100.98	0.17	100.72	0.22
Mg #	90.9	0.1	90.9	0.1	91.1	0.0	91.0	0.0	90.8	0.3	90.8	0.1	91.3	0.2	91.3	0.2	91.3	0.1	91.4	0.1	91.2	0.1	91.2	0.2	90.8	0.1	90.7	0.0
X Ca	0.083	0.011	0.059	0.004	0.062		0.093	0.011	0.069	0.016	0.053	0.008	0.030	0.008	0.032	0.006	0.075	0.017	0.069	0.017	0.052	0.014	0.037	0.007	0.081	0.013	0.059	0.010

Table A 9: Representative orthopyroxene trace element chemistry measured by LA-ICP-MS (σ = one standard deviation).

Sample		DC0310		DC0312		DC0313		DC0318		DC0322		DC0327		DC0334		DC0336		DC0345		15SM23A		15SM23B		15SM34-2		15SM38		15SM45		15SM55B		15SM56		15SM57	
Location		Peridotite Peak		Peridotite Peak		Peridotite Peak		Peridotite Peak		Peridotite Peak		Peridotite Peak		Peridotite Peak		Peridotite Peak East		Peridotite Peak East		Menatatuline Range		Menatatuline Range		Menatatuline Range		Menatatuline Range		Menatatuline Range		Menatatuline Range		Menatatuline Range		Menatatuline Range	
n =		5		6		3		6		9		8		5		6		6		15		11		5		12		6		11		6		13	
	Detection limit[1]	average	1 σ	average	1 σ	average	1 σ	average	1 σ	average	1 σ	average	1 σ	average	1 σ	average	1 σ	average	1 σ	average	1 σ	average	1 σ	average	1 σ	average	1 σ	average	1 σ	average	1 σ	average	1 σ	average	1 σ
Sc (ppm)	0.33	31.27	4.41	25.40	5.30	23.75	0.57	19.46	2.59	25.68	6.89	25.91	3.46	19.63	3.05	36.55	4.35	10.10	1.17	10.15	1.36	37.86	1.07	17.03	1.37	26.30	3.99	15.48	2.96	27.63	3.26	21.24	4.03	30.97	2.93
Ti (wt %)	0.001	0.012	0.001	0.014	0.002	0.018	0.000	0.008	0.001	0.009	0.002	0.012	0.001	0.006	0.001	0.014	0.001	0.002	0.000	0.002	0.000	0.009	0.000	0.009	0.001	0.005	0.001	0.003	0.001	0.004	0.000	0.004	0.001	0.007	0.001
V (ppm)	0.3	116	11	102	24	110	4	76	8	101	24	113	14	84	11	144	16	38	5	40	5	125	5	71	9	101	14	56	8	91	8	73	11	127	9
Cr	6	2792	431	3071	917	3168	261	2922	413	3021	600	3819	286	3145	541	4860	559	1600	163	1742	229	6058	220	3493	370	4509	675	2386	253	4597	396	3285	364	5737	509
Mn	0.32	bdl	bdl	bdl	bdl	bdl	bdl	bdl	bdl	bdl	bdl	248.19	40.42	181.79	25.63	326.19	38.58	85.39	11.91	95.95	18.04	320.01	15.28	180.21	26.63	264.93	56.22	126.67	20.85	235.96	26.98	177.61	31.59	276.60	21.47
Co	0.05	43.28	5.47	40.22	9.59	45.47	1.78	31.71	4.41	39.64	9.94	47.99	6.66	36.47	5.54	62.30	6.90	18.04	2.27	19.46	3.02	68.60	3.33	36.06	4.94	53.52	6.88	25.67	3.70	51.57	5.61	36.36	6.06	58.28	4.42
Ni	0.47	556	64	498	114	566	24	434	79	505	117	582	74	449	68	750	75	233	27	252	39	877	35	444	62	678	68	321	43	679	70	471	73	781	56
Cu	0.24	0.42	0.37	bdl	2.34	9.60	0.000	bdl	bdl	bdl	bdl	2.29	1.16	4.32	2.12	12.49	6.30	0.75	0.25	0.54	0.11	2.17	0.48	3.36	1.67	3.15	4.53	2.00	0.00	16.98	3.18	4.26	1.40	0.68	0.27
Zn	0.11	23.69	2.41	20.37	4.72	23.08	1.36	17.60	2.50	29.67	7.27	27.49	3.26	22.23	3.78	33.92	3.33	13.79	2.16	14.51	2.76	43.99	2.26	21.06	3.73	36.72	6.93	18.78	2.45	35.27	3.70	24.41	4.15	38.91	2.79
Ga	0.018	1.628	0.212	1.719	0.569	2.191	0.085	1.353	0.118	1.678	0.347	1.958	0.212	1.404	0.237	2.240	0.177	0.457	0.067	0.561	0.115	1.917	0.111	1.433	0.191	1.321	0.173	0.617	0.074	1.238	0.145	0.954	0.140	1.758	0.142
Sr	0.222	bdl	bdl	bdl	bdl	bdl	bdl	bdl	bdl	bdl	0.007	bdl	bdl	bdl	bdl	bdl	bdl	bdl	bdl	bdl	bdl	bdl	bdl	bdl	bdl	0.396	0.730	bdl	bdl	bdl	bdl	bdl	bdl	bdl	bdl
Y	0.018	0.347	0.033	0.412	0.091	0.383	0.062	0.226	0.034	0.276	0.048	0.451	0.039	0.212	0.027	0.475	0.040	0.079	0.008	0.082	0.012	0.239	0.016	0.280	0.026	0.163	0.028	0.115	0.016	0.113	0.009	0.194	0.027	0.274	0.024
Zr	0.092	bdl	bdl	bdl	bdl	bdl	bdl	bdl	bdl	bdl	0.005	bdl	bdl	bdl	bdl	0.194	0.000	bdl	bdl	bdl	bdl	bdl	bdl	bdl	bdl	bdl	bdl	bdl	bdl	bdl	bdl	bdl	bdl	bdl	bdl
Nb	0.005	bdl	bdl	0.008	0.017	bdl	bdl	bdl	bdl	bdl	bdl	bdl	bdl	bdl	bdl	0.048	0.000	bdl	bdl	bdl	bdl	bdl	bdl	bdl	bdl	0.004	0.006	0.006	0.001	bdl	bdl	bdl	bdl	bdl	bdl
Ba	0.167	bdl	bdl	bdl	bdl	bdl	bdl	bdl	bdl	bdl	bdl	bdl	bdl	bdl	bdl	0.721	0.000	bdl	bdl	bdl	bdl	bdl	bdl	bdl	bdl	bdl	bdl	bdl	bdl	bdl	bdl	bdl	bdl	bdl	bdl
La	0.009	bdl	bdl	0.014	0.000	bdl	bdl	bdl	bdl	bdl	bdl	bdl	bdl	bdl	bdl	bdl	bdl	bdl	bdl	bdl	bdl	bdl	bdl	bdl	bdl	bdl	bdl	bdl	bdl	bdl	bdl	bdl	bdl	bdl	bdl
Ce	0.023	bdl	bdl	bdl	bdl	bdl	bdl	bdl	bdl	bdl	bdl	bdl	bdl	bdl	bdl	bdl	bdl	bdl	bdl	bdl	bdl	bdl	bdl	bdl	bdl	bdl	bdl	bdl	bdl	bdl	bdl	bdl	bdl	bdl	bdl
Pr	0.003	bdl	bdl	bdl	bdl	bdl	bdl	bdl	bdl	bdl	bdl	bdl	bdl	bdl	bdl	bdl	bdl	bdl	bdl	bdl	bdl	bdl	bdl	bdl	bdl	bdl	bdl	bdl	bdl	bdl	bdl	bdl	bdl	bdl	bdl
Nd	0.013	bdl	bdl	bdl	bdl	bdl	bdl	bdl	bdl	bdl	bdl	bdl	bdl	bdl	bdl	bdl	bdl	bdl	bdl	bdl	bdl	bdl	bdl	bdl	bdl	bdl	bdl	bdl	bdl	bdl	bdl	bdl	bdl	bdl	bdl
Sm	0.006	bdl	bdl	0.052	0.000	bdl	bdl	bdl	bdl	bdl	bdl	bdl	bdl	bdl	bdl	bdl	bdl	bdl	bdl	bdl	bdl	bdl	bdl	bdl	bdl	bdl	bdl	bdl	bdl	bdl	bdl	bdl	bdl	bdl	bdl
Eu	0.001	bdl	bdl	bdl	bdl	bdl	bdl	bdl	bdl	bdl	bdl	bdl	bdl	bdl	bdl	bdl	bdl	bdl	bdl	bdl	bdl	bdl	bdl	bdl	bdl	0.007	0.000	bdl	bdl	bdl	bdl	bdl	bdl	bdl	bdl
Gd	0.006	0.015	0.000	bdl	bdl	bdl	bdl	bdl	bdl	0.012	0.000	0.013	0.000	bdl	bdl	0.012	0.000	bdl	bdl	bdl	bdl	bdl	bdl	0.014	0.000	bdl	bdl	bdl	bdl	bdl	bdl	bdl	bdl	bdl	bdl
Tb	0.001	0.004	0.000	bdl	bdl	bdl	bdl	bdl	bdl	0.004	0.000	0.003	0.001	0.002	0.000	0.003	0.001	bdl	bdl	bdl	bdl	0.001	0.001	0.002	0.000	bdl	bdl	bdl	bdl	bdl	bdl	0.001	0.000	0.002	0.003
Dy	0.006	0.029	0.021	0.051	0.024	0.094	0.000	bdl	bdl	0.029	0.008	0.042	0.009	0.019	0.004	0.041	0.010	0.007	0.002	bdl	bdl	0.014	0.006	0.027	0.007	0.013	0.006	0.007	0.001	0.014	0.000	0.018	0.004	0.019	0.006
Ho	0.001	0.010	0.005	0.012	0.011	0.017	0.001	0.012	0.001	0.011	0.008	0.014	0.002	0.008	0.001	0.016	0.005	0.003	0.001	0.003	0.001	0.007	0.001	0.011	0.001	0.006	0.002	0.004	0.001	0.004	0.001	0.006	0.001	0.009	0.002
Er	0.003	0.062	0.028	0.089	0.054	0.083	0.001	0.042	0.013	0.042	0.013	0.077	0.011	0.041	0.014	0.080	0.011	0.015	0.003	0.016	0.003	0.045	0.009	0.046	0.005	0.030	0.008	0.017	0.005	0.024	0.003	0.030	0.002	0.047	0.007
Tm	0.0005	0.009	0.005	0.021	0.006	0.019	0.010	0.011	0.001	0.014	0.003	0.017	0.004	0.009	0.002	0.020	0.004	0.004	0.001	0.004	0.001	0.011	0.002	0.011	0.002	0.008	0.002	0.005	0.002	0.006	0.001	0.007	0.002	0.011	0.002
Yb	0.004	0.083	0.021	0.176	0.085	0.156	0.021	0.084	0.018	0.109	0.026	0.159	0.033	0.089	0.019	0.196	0.023	0.036	0.006	0.043	0.009	0.119	0.012	0.091	0.011	0.072	0.016	0.040	0.013	0.061	0.011	0.063	0.017	0.106	0.011
Lu	0.001	0.024	0.006	0.029	0.018	0.026	0.019	0.019	0.004	0.018	0.006	0.030	0.005	0.017	0.003	0.042	0.005	0.008	0.001	0.009	0.001	0.025	0.002	0.021	0.002	0.015	0.005	0.008	0.003	0.014	0.002	0.013	0.002	0.021	0.004
Th	0.0003	0.0004	0.0008	0.0024	0.0034	bdl	bdl	bdl	bdl	bdl	bdl	bdl	bdl	bdl	bdl	bdl	bdl	bdl	bdl	bdl	bdl	bdl	bdl	bdl	bdl	0.0003	0.0009	0.0004	0.0002	bdl	bdl	bdl	bdl	0.0004	0.0018
U	0.0007	bdl	0.0007	0.0015	0.0033	bdl	bdl	bdl	bdl	bdl	bdl	bdl	bdl	bdl	bdl	bdl	bdl	0.0014	0.0018	bdl	bdl	bdl	bdl	bdl	bdl	0.0010	0.0020	bdl	bdl	bdl	bdl	bdl	bdl	bdl	bdl

[1] Median detection limit

Table A 10: Representative clinopyroxene major element chemistry measured by EMP (σ = one standard deviation).

Sample	DC0205		DC0206		DC0303		DC0304			
Location	N of Hardluck Peaks		N of Hardluck Peaks		Moho Saddle		Moho Saddle			
Mineral	cpx		cpx		cpx		cpx			
n =	7		10		8		4		4	
	core	σ	core	σ	core	σ	core	σ	rim	σ
MgO (wt %)	17.77	0.25	18.08	0.52	18.37	0.28	18.18	0.11	18.05	0.20
Al2O3	2.18	0.21	2.17	0.23	2.11	0.36	1.56	0.03	1.60	0.02
SiO2	52.13	0.41	52.04	0.24	52.25	0.58	53.02	0.42	52.94	0.12
CaO	23.74	0.32	23.40	0.93	22.82	0.51	22.69	0.21	23.03	0.29
TiO2	0.02	0.01	0.01	0.01	0.02	0.01	0.09	0.02	0.08	0.01
Cr2O3	1.07	0.24	1.11	0.18	0.96	0.18	0.91	0.01	0.94	0.04
MnO	0.08	0.02	0.07	0.01	0.08	0.02	0.09	0.01	0.06	0.02
FeO	2.31	0.15	2.18	0.21	2.56	0.17	2.50	0.04	2.35	0.08
Na2O	0.04	0.02	0.05	0.01	0.06	0.02	0.43	0.01	0.41	0.03
NiO	0.03	0.02	0.06	0.01	0.06	0.02	0.06	0.02	0.03	0.01
Total	99.39	0.23	99.16	0.21	99.31	0.53	99.53	0.54	99.48	0.17
Mg #	93.2	0.3	93.7	0.4	92.7	0.4	92.8	0.1	93.2	0.2
X Ca	0.937	0.014	0.925	0.040	0.901	0.017	0.917	0.004	0.930	0.013

Sample	DC0310				DC0312				DC0313				DC0318			
Location	Peridotite Peak				Peridotite Peak				Peridotite Peak				Peridotite Peak			
Mineral	cpx				cpx				cpx				cpx			
n =	3		3		3		3		2		3		3		3	
	core	σ	rim	σ	core	σ	rim	σ	core	σ	rim	σ	core	σ	rim	σ
MgO (wt %)	17.26	0.20	17.28	0.22	17.03	0.32	17.46	0.57	16.59	0.30	17.33	0.25	17.43	0.22	17.22	0.47
Al2O3	2.72	0.20	2.59	0.27	3.68	0.51	3.41	0.39	4.17	0.34	2.90	0.17	2.95	0.41	2.77	0.73
SiO2	52.86	0.41	53.03	0.36	52.31	0.43	52.52	0.20	51.76	0.28	52.62	0.37	52.42	0.24	52.40	0.68
CaO	23.79	0.19	23.98	0.27	23.51	0.33	23.04	1.30	23.50	0.11	23.63	0.50	23.63	0.32	23.98	0.21
TiO2	0.07	0.01	0.07	0.01	0.08	0.00	0.07	0.02	0.12	0.00	0.21	0.06	0.08	0.01	0.09	0.04
Cr2O3	0.78	0.15	0.76	0.14	0.82	0.15	0.70	0.13	0.97	0.14	0.58	0.07	0.80	0.20	0.79	0.29
MnO	0.06	0.01	0.07	0.01	0.08	0.01	0.06	0.01	0.07	0.00	0.07	0.01	0.06	0.02	0.05	0.01
FeO	2.13	0.08	2.13	0.18	2.29	0.14	2.34	0.21	2.32	0.19	2.18	0.19	2.18	0.16	2.10	0.11
Na2O	0.10	0.00	0.10	0.01	0.15	0.01	0.23	0.16	0.18	0.01	0.17	0.02	0.09	0.02	0.06	0.02
NiO	0.03	0.01	0.05	0.01	0.05	0.02	0.06	0.02	0.08	0.01	0.05	0.05	0.06	0.02	0.05	0.03
Total	99.81	0.26	100.07	0.25	100.01	0.17	99.89	0.34	99.75	0.17	99.73	0.46	99.70	0.26	99.52	0.22
Mg #	93.5	0.2	93.5	0.5	93.0	0.4	93.0	0.5	92.7	0.4	93.4	0.5	93.4	0.4	93.6	0.2
X Ca	0.935	0.008	0.940	0.011	0.926	0.015	0.912	0.041	0.931	0.006	0.934	0.019	0.930	0.015	0.944	0.006

Sample	DC0322				DC0327				DC0334				DC0336			
Location	Peridotite Peak				Peridotite Peak				Peridotite Peak				Peridotite Peak East			
Mineral	cpx				cpx				cpx				cpx			
n =	6		6		12		10		12		9		8		6	
	core	σ	rim	σ	core	σ	rim	σ	core	σ	rim	σ	core	σ	rim	σ
MgO (wt %)	17.22	0.27	17.45	0.30	17.03	0.22	17.40	0.30	17.41	0.24	17.57	0.19	17.47	0.24	17.65	0.26
Al2O3	3.27	0.18	2.31	0.37	3.97	0.24	3.08	0.52	3.00	0.23	2.31	0.15	2.42	0.34	2.18	0.46
SiO2	52.55	0.22	53.22	0.22	51.20	0.25	51.81	0.57	51.96	0.34	52.58	0.16	52.72	0.40	53.15	0.36
CaO	23.34	0.31	23.96	0.26	23.68	0.26	23.97	0.35	23.84	0.37	24.23	0.27	24.23	0.32	24.35	0.18
TiO2	0.07	0.02	0.07	0.01	0.06	0.01	0.07	0.01	0.04	0.01	0.04	0.01	0.06	0.01	0.06	0.02
Cr2O3	0.96	0.12	0.67	0.10	1.08	0.08	0.85	0.17	0.93	0.11	0.78	0.09	0.70	0.11	0.52	0.12
MnO	0.08	0.02	0.08	0.02	0.08	0.02	0.08	0.01	0.07	0.02	0.08	0.02	0.08	0.02	0.07	0.01
FeO	2.41	0.12	2.09	0.17	2.22	0.11	2.11	0.16	2.21	0.14	2.07	0.14	2.03	0.17	2.08	0.08
Na2O	0.08	0.00	0.07	0.02	0.13	0.02	0.10	0.02	0.05	0.01	0.03	0.01	0.07	0.01	0.07	0.02
NiO	0.06	0.02	0.05	0.02	0.05	0.02	0.04	0.02	0.05	0.02	0.05	0.02	0.05	0.02	0.05	0.01
Total	100.02	0.31	99.97	0.33	99.49	0.15	99.52	0.44	99.56	0.38	99.74	0.12	99.83	0.31	100.18	0.19
Mg #	92.7	0.3	93.7	0.5	93.2	0.3	93.6	0.5	93.4	0.3	93.8	0.4	93.9	0.5	93.8	0.3
X Ca	0.914	0.015	0.938	0.010	0.939	0.012	0.948	0.013	0.938	0.013	0.950	0.011	0.952	0.015	0.953	0.005

Sample	DC0345				15SM23A				15SM23B				15SM38			
Location	Peridotite Peak East				Menatatuline Range				Menatatuline Range				Menatatuline Range			
Mineral	cpx				cpx				cpx				cpx			
n =	12		10		3		5		15		10		4		5	
	core	σ	rim	σ	core	σ	rim	σ	core	σ	rim	σ	core	σ	rim	σ
MgO (wt %)	17.35	0.21	17.40	0.32	19.41	0.30	19.54	1.40	18.64	0.82	18.25	0.24	18.90	0.74	18.32	0.27
Al2O3	2.75	0.36	2.49	0.19	3.36	0.09	3.16	0.10	3.38	0.17	3.14	0.11	3.15	0.06	2.58	0.24
SiO2	52.70	0.36	52.87	0.43	52.47	0.36	52.67	0.25	52.63	0.20	52.81	0.16	52.49	0.13	52.86	0.21
CaO	23.42	0.28	23.62	0.52	20.07	0.37	20.12	1.93	21.15	1.08	22.03	0.34	21.21	1.09	22.81	0.28
TiO2	0.07	0.02	0.07	0.02	0.02	0.00	0.02	0.01	0.02	0.01	0.03	0.01	0.01	0.00	0.01	0.01
Cr2O3	0.95	0.18	0.82	0.14	1.39	0.02	1.28	0.09	1.38	0.09	1.18	0.08	1.34	0.06	0.94	0.08
MnO	0.07	0.02	0.07	0.02	0.09	0.01	0.09	0.02	0.10	0.02	0.09	0.02	0.10	0.03	0.08	0.01
FeO	2.05	0.11	2.10	0.29	3.23	0.07	3.11	0.38	3.04	0.24	2.88	0.08	2.94	0.18	2.70	0.10
Na2O	0.36	0.03	0.33	0.02	0.04	0.03	0.04	0.01	0.04	0.01	0.04	0.01	0.03	0.02	0.04	0.01
NiO	0.05	0.02	0.04	0.02	0.09	0.02	0.06	0.01	0.06	0.03	0.08	0.01	0.06	0.02	0.06	0.03
Total	99.78	0.34	99.80	0.34	100.16	0.19	100.11	0.17	100.43	0.21	100.52	0.20	100.23	0.21	100.40	0.22
Mg #	93.8	0.3	93.7	0.7	91.5	0.1	91.8	0.4	91.6	0.3	91.9	0.1	92.0	0.2	92.4	0.3
X Ca	0.939	0.011	0.944	0.020	0.780	0.017	0.782	0.079	0.821	0.044	0.856	0.015	0.825	0.044	0.888	0.011

Sample	15SM45				15SM55B				15SM56				15SM57			
Location	Menatatuline Range				Menatatuline Range				Menatatuline Range				Menatatuline Range			
Mineral	cpx				cpx				cpx				cpx			
n =	11		11		5		4		9		7		6		4	
	core	σ	rim	σ	core	σ	rim	σ	core	σ	rim	σ	core	σ	rim	σ
MgO (wt %)	17.52	0.28	17.71	0.27	18.10	0.22	18.49	0.15	18.23	0.46	17.95	0.33	17.97	0.42	17.90	0.34
Al2O3	2.56	0.12	2.27	0.22	2.26	0.19	2.06	0.09	3.03	0.08	2.70	0.12	3.37	0.05	3.07	0.21
SiO2	52.68	0.26	53.04	0.37	53.18	0.28	53.21	0.18	52.49	0.37	52.86	0.17	52.56	0.41	52.87	0.59
CaO	23.29	0.39	23.49	0.33	23.38	0.50	22.89	0.33	22.12	0.64	23.06	0.39	22.00	0.64	22.42	0.39
TiO2	0.02	0.01	0.02	0.01	0.02	0.01	0.01	0.01	0.02	0.01	0.03	0.01	0.02	0.01	0.02	0.00
Cr2O3	1.11	0.10	0.94	0.16	1.01	0.14	0.83	0.06	1.35	0.05	1.12	0.08	1.33	0.03	1.15	0.16
MnO	0.07	0.02	0.08	0.02	0.08	0.02	0.09	0.02	0.10	0.01	0.09	0.01	0.09	0.01	0.07	0.01
FeO	2.34	0.11	2.29	0.12	2.33	0.18	2.48	0.08	2.70	0.10	2.46	0.09	2.82	0.19	2.68	0.08
Na2O	0.24	0.02	0.22	0.03	0.05	0.01	0.04	0.01	0.05	0.01	0.06	0.01	0.05	0.01	0.04	0.01
NiO	0.05	0.02	0.04	0.02	0.06	0.03	0.05	0.01	0.06	0.02	0.06	0.02	0.06	0.02	0.06	0.02
Total	99.86	0.34	100.10	0.33	100.47	0.12	100.15	0.21	100.14	0.40	100.39	0.24	100.26	0.41	100.29	0.11
Mg #	93.0	0.2	93.2	0.3	93.3	0.4	93.0	0.2	92.3	0.1	92.9	0.2	91.9	0.4	92.3	0.1
X Ca	0.925	0.015	0.929	0.012	0.910	0.020	0.892	0.014	0.864	0.027	0.899	0.016	0.857	0.024	0.873	0.018

Table A 11: Representative clinopyroxene trace element chemistry measured by LA-ICP-MS (σ = one standard deviation).

Sample		DC0310		DC0312		DC0313		DC0318		DC0322		DC0327		DC0334		DC0336		DC0345		15SM23A		15SM23B		15SM38		15SM45		15SM55B	15SM56		15SM57	
Location		Peridotite Peak		Peridotite Peak		Peridotite Peak		Peridotite Peak		Peridotite Peak		Peridotite Peak		Peridotite Peak		Peridotite Peak East		Peridotite Peak East		Menatatuline Range		Menatatuline Range		Menatatuline Range		Menatatuline Range		Menat.	Menatatuline Range		Menatatuline Range	
n =		13		7		6		5		7		8		12		7		7		9		13		5		8		1	15		12	
	Detection limit[1]	average	1 σ	average	1 σ	average	1 σ	average	1 σ	average	1 σ	average	1 σ	average	1 σ	average	1 σ	average	1 σ	average	1 σ	average	1 σ	average	1 σ	average	1 σ	average	average	1 σ	average	1 σ
Sc (ppm)	0.33	67.69	3.60	67.54	1.88	55.00	1.93	58.95	2.49	58.68	3.28	54.97	3.48	57.37	3.35	60.65	4.00	62.60	8.91	57.07	3.57	55.25	4.30	55.07	0.44	62.74	6.27	88.70	58.27	4.17	55.27	3.36
Ti (wt %)	0.001	0.034	0.003	0.053	0.002	0.061	0.003	0.032	0.002	0.028	0.001	0.037	0.002	0.023	0.002	0.035	0.002	0.039	0.004	0.013	0.001	0.014	0.001	0.012	0.001	0.011	0.001	0.015	0.013	0.001	0.013	0.001
V (ppm)	0.3	236	7	243	11	227	9	230	6	227	4	249	9	228	6	215	12	201	8	246	20	251	11	229	12	199	7	285	224	8	242	18
Cr	6	5241	537	6667	1142	6422	735	8387	511	6627	771	7826	1085	6279	506	5126	896	7848	601	9910	1470	9937	755	9292	1115	6357	747	11496	9129	698	9408	1173
Mn	0.32	bdl	bdl	bdl	bdl	bdl	bdl	bdl	bdl	bdl	bdl	183.78	11.59	160.20	12.02	172.34	12.37	186.14	29.15	240.41	22.13	249.00	15.38	220.78	7.70	164.44	24.04	259.54	200.77	18.18	217.49	28.54
Co	0.05	19.41	1.87	20.44	2.18	22.08	3.27	19.98	2.50	20.34	3.33	25.08	2.65	20.58	2.13	25.16	3.16	19.79	0.98	35.65	4.53	35.23	3.10	32.32	1.56	21.57	4.42	54.23	27.31	3.36	30.71	5.84
Ni	0.47	363.28	38.74	335.42	20.12	377.45	71.74	345.50	31.86	358.24	35.46	426.13	62.85	349.27	31.06	403.71	89.74	323.22	12.55	509.89	72.15	514.25	42.33	499.94	24.81	375.58	145.06	712.76	433.07	46.34	466.83	67.11
Cu	0.24	17.36	49.16	1.12	1.19	bdl	bdl	bdl	bdl	0.71	0.45	4.37	4.13	5.33	1.76	70.00	85.18	10.67	3.04	9.28	2.80	6.45	2.20	4.10	3.10	bdl	bdl	35.48	13.36	6.79	2.08	1.38
Zn	0.11	7.38	0.99	6.71	1.15	7.49	1.31	8.78	2.03	9.25	3.25	10.78	2.18	8.18	1.32	11.35	3.57	8.92	1.71	20.64	2.28	19.95	1.99	16.33	1.16	9.49	2.00	49.97	13.50	2.33	15.82	4.30
Ga	0.018	1.658	0.231	2.181	0.352	2.521	0.344	2.283	0.196	1.920	0.187	2.362	0.411	1.757	0.210	1.478	0.239	1.706	0.134	2.050	0.175	2.034	0.288	1.941	0.214	1.123	0.114	2.012	1.898	0.162	2.216	0.245
Sr	0.222	bdl	bdl	bdl	bdl	bdl	bdl	bdl	bdl	bdl	bdl	bdl	bdl	bdl	bdl	bdl	bdl	0.607	0.033	bdl	bdl	bdl	bdl	0.234	0.270	2.099	0.101	4.435	bdl	bdl	0.274	0.730
Y	0.018	3.983	0.275	6.376	0.539	5.117	0.124	3.986	0.263	3.477	0.218	4.707	0.170	2.832	0.177	3.802	0.322	5.076	0.668	1.522	0.110	1.553	0.189	1.160	0.034	1.540	0.151	1.100	1.792	0.199	1.584	0.118
Zr	0.092	bdl	bdl	bdl	bdl	bdl	bdl	bdl	bdl	bdl	bdl	bdl	bdl	bdl	bdl	bdl	bdl	0.333	0.060	bdl	bdl	bdl	bdl	bdl	bdl	bdl	bdl	bdl	bdl	bdl	bdl	bdl
Nb	0.005	bdl	bdl	bdl	bdl	bdl	bdl	bdl	bdl	bdl	bdl	bdl	bdl	bdl	bdl	bdl	bdl	bdl	bdl	bdl	bdl	0.015	0.004	bdl	bdl	0.010	0.004	bdl	bdl	bdl	bdl	bdl
Ba	0.167	0.464	0.862	0.549	0.391	bdl	bdl	bdl	bdl	bdl	bdl	0.961	0.000	bdl	bdl	0.920	0.000	bdl	bdl	0.211	0.310	bdl	bdl	bdl	bdl	bdl	bdl	bdl	bdl	bdl	bdl	bdl
La	0.009	0.011	0.000	0.017	0.006	bdl	bdl	bdl	bdl	bdl	bdl	bdl	bdl	bdl	bdl	bdl	bdl	bdl	bdl	bdl	bdl	bdl	bdl	bdl	bdl	0.035	0.004	bdl	bdl	bdl	bdl	bdl
Ce	0.023	bdl	bdl	bdl	bdl	bdl	bdl	bdl	bdl	bdl	bdl	bdl	bdl	bdl	bdl	bdl	bdl	bdl	bdl	bdl	bdl	bdl	bdl	bdl	bdl	0.091	0.005	bdl	bdl	bdl	bdl	bdl
Pr	0.003	bdl	bdl	0.008	0.000	bdl	bdl	bdl	bdl	bdl	bdl	bdl	bdl	bdl	bdl	bdl	bdl	bdl	bdl	bdl	bdl	bdl	bdl	bdl	bdl	0.012	0.002	bdl	bdl	bdl	bdl	bdl
Nd	0.013	bdl	bdl	bdl	bdl	bdl	bdl	bdl	bdl	bdl	bdl	bdl	bdl	bdl	bdl	bdl	bdl	0.038	0.000	bdl	bdl	bdl	bdl	bdl	bdl	0.049	0.008	bdl	bdl	bdl	bdl	bdl
Sm	0.006	0.054	0.038	0.113	0.037	0.080	0.005	bdl	bdl	0.039	0.020	0.025	0.006	0.014	0.001	0.016	0.004	0.065	0.014	bdl	bdl	bdl	bdl	bdl	bdl	0.014	0.006	bdl	0.010	0.007	bdl	bdl
Eu	0.001	0.024	0.007	0.046	0.024	0.048	0.016	0.022	0.006	0.025	0.011	0.017	0.004	0.007	0.001	0.014	0.003	0.039	0.004	0.002	0.001	0.002	0.001	0.001	0.000	0.008	0.002	bdl	0.005	0.002	0.002	0.001
Gd	0.006	0.189	0.055	0.389	0.141	0.311	0.067	0.206	0.045	0.177	0.030	0.207	0.028	0.090	0.010	0.124	0.022	0.271	0.032	0.031	0.009	0.028	0.009	0.012	0.003	0.026	0.007	bdl	0.073	0.022	0.024	0.012
Tb	0.001	0.044	0.009	0.077	0.022	0.076	0.020	0.053	0.012	0.043	0.010	0.067	0.006	0.033	0.003	0.047	0.005	0.080	0.012	0.014	0.002	0.013	0.003	0.009	0.002	0.012	0.003	0.003	0.023	0.004	0.011	0.002
Dy	0.006	0.624	0.072	0.905	0.156	0.750	0.088	0.558	0.092	0.554	0.056	0.669	0.051	0.368	0.021	0.519	0.032	0.730	0.108	0.176	0.018	0.182	0.013	0.125	0.024	0.157	0.024	0.096	0.238	0.032	0.174	0.026
Ho	0.001	0.134	0.016	0.177	0.029	0.192	0.019	0.143	0.019	0.126	0.016	0.175	0.011	0.112	0.010	0.137	0.012	0.196	0.026	0.058	0.006	0.059	0.007	0.041	0.001	0.055	0.005	0.037	0.068	0.010	0.059	0.007
Er	0.003	0.454	0.103	0.683	0.127	0.631	0.079	0.508	0.065	0.484	0.050	0.591	0.038	0.394	0.032	0.488	0.050	0.658	0.108	0.233	0.021	0.232	0.024	0.170	0.011	0.225	0.013	0.171	0.246	0.027	0.234	0.024
Tm	0.000	0.069	0.007	0.111	0.021	0.083	0.015	0.075	0.009	0.075	0.011	0.099	0.007	0.064	0.007	0.082	0.007	0.107	0.018	0.043	0.005	0.046	0.006	0.032	0.009	0.043	0.004	0.039	0.039	0.003	0.045	0.004
Yb	0.004	0.370	0.053	0.817	0.173	0.679	0.125	0.543	0.051	0.423	0.053	0.671	0.030	0.488	0.040	0.544	0.040	0.715	0.094	0.357	0.019	0.349	0.027	0.273	0.028	0.281	0.035	0.323	0.306	0.037	0.319	0.034
Lu	0.001	0.049	0.007	0.079	0.025	0.102	0.013	0.090	0.015	0.063	0.006	0.102	0.007	0.075	0.006	0.083	0.005	0.108	0.018	0.059	0.005	0.063	0.006	0.045	0.004	0.050	0.006	0.056	0.049	0.007	0.053	0.005
Th	0.000	0.0021	0.0038	bdl	bdl	bdl	bdl	bdl	bdl	0.0011	0.0015	bdl	bdl	bdl	bdl	bdl	bdl	bdl	bdl	0.0003	0.0000	bdl	bdl	bdl	bdl	bdl	bdl	bdl	bdl	bdl	bdl	bdl
U	0.0007	0.0010	0.0020	0.0014	0.0035	bdl	bdl	bdl	bdl	bdl	bdl	bdl	bdl	bdl	bdl	bdl	bdl	bdl	bdl	bdl	bdl	0.0037	0.0021	bdl	bdl	0.0011	0.0000	bdl	bdl	bdl	bdl	bdl

[1] Median detection limit

Table A 12: Accuracy of La-ICP-MS on USGS glass standard BCR-2 (Jochum et al. 2005) over period of study.

Standard	**BCR-2**							**% accuracy**
	Cert.	Meas.	Meas.	Meas.	Meas.	Meas.	Meas.	
Date		Nov-16	Jan-16	Feb-16	Jun-16	Oct-16	Average	
Mg	**2.16**	2.16	1.85	1.91	2.21	2.21	2.07	4.5
Al	**7.14**	6.72	7.17	6.88	6.90	7.29	6.99	2.1
Si	**25.29**	25.09	24.96	24.04	25.41	24.39	24.78	2.0
Ca	**5.09**	5.09	5.09	5.09	5.09	5.09	5.09	0.0
Sc (ppm)	**33**	35.67	33.30	33.28	32.38	31.74	33.27	0.8
Ti	**1.35**	1.35	1.43	1.38	1.38	1.39	1.38	2.2
V	**416**	399.59	417.79	411.54	420.90	422.27	414.42	0.4
Cr	**18**	6.82	8.02	8.36	9.34	8.44	8.20	54.5
Mn	**1520**	0.15	338.38	375.24	400.74	392.15	301.33	80.2
Co	**37**	32.45	32.07	33.96	36.19	35.40	34.01	8.1
Ni	**18**	105.20	123.97	126.57	138.43	142.15	127.26	607.0
Cu	**21**	14.21	13.64	14.08	14.32	14.26	14.10	32.9
Zn	**127**	123.27	127.99	128.19	133.73	123.68	127.37	0.3
Ga	**23**	27.42	28.71	25.07	25.08	24.41	26.14	13.6
Sr	**340**	331.16	341.19	341.44	344.28	343.87	340.39	0.1
Y	**37**	34.04	36.09	34.98	33.91	33.66	34.54	6.7
Zr	**184**	183.03	188.31	181.70	175.89	173.58	180.50	1.9
Nb	**12.6**	11.97	13.28	12.80	12.77	12.56	12.68	0.6
Ba	**677**	662.57	678.38	647.36	679.40	680.27	669.60	1.1
La	**24.9**	24.62	26.06	24.87	24.58	24.74	24.97	0.3
Ce	**52.9**	51.34	54.36	51.98	53.68	53.92	53.06	0.3
Pr	**6.7**	6.89	6.85	6.65	6.87	6.74	6.80	1.5
Nd	**28.7**	27.15	29.56	28.01	28.58	28.53	28.37	1.2
Sm	**6.58**	6.91	6.74	6.56	6.61	6.42	6.65	1.0
Eu	**1.96**	1.80	1.97	1.97	2.00	1.96	1.94	0.9
Gd	**6.75**	6.05	6.82	6.62	6.53	6.39	6.48	4.0
Tb	**1.07**	0.85	1.07	1.02	1.02	1.03	1.00	6.7
Dy	**6.41**	6.80	6.66	6.29	6.28	6.25	6.46	0.7
Ho	**1.28**	1.09	1.33	1.24	1.26	1.26	1.23	3.7
Er	**3.66**	3.42	3.77	3.58	3.59	3.58	3.59	2.0
Tm	**0.54**	0.49	0.56	0.53	0.52	0.52	0.52	2.9
Yb	**3.38**	2.78	3.41	3.31	3.34	3.41	3.25	3.9
Lu	**0.503**	0.34	0.51	0.49	0.50	0.49	0.47	7.0
Th	**5.7**	6.19	5.99	5.42	5.67	5.96	5.85	2.6
U	**1.69**	1.78	1.66	1.54	1.69	1.83	1.70	0.6

Cert., certified concentrations in USGS standard BCR-2 (Jochum et al. 2005).

Meas., measured concentrations on LA-ICP-MS at the University of Victoria.

Table A 13: Detection limits of LA-ICP-MS over period of study.

Table A 13: Detection limits of LA-ICP-MS over period of study.

Date	11/26/2015	1/29/2016	2/15/2016	6/29/2016	10/3/2016				
Detection limit						Minimum	Maximum	Median	Average
Mg (%)	0.2142	0.0767	0.0030	0.0007	0.0113	0.0007	0.0767	0.0071	0.0229
Al	0.0514	0.0297	0.0009	0.0004	0.0090	0.0004	0.0297	0.0050	0.0100
Si	0.2913	5.4535	0.2822	0.0444	0.0475	0.0444	5.4535	0.1648	1.4569
Ca	0.1985	0.0317	0.0205	0.0024	0.0113	0.0024	0.0317	0.0159	0.0165
Sc (ppm)	0.4826	1.0919	0.3446	0.0161	0.3138	0.0161	1.0919	0.3292	0.4416
Ti	0.0065	0.0019	0.0002	0.0001	0.0016	0.0001	0.0019	0.0009	0.0009
V	2.2082	1.3207	0.1397	0.0333	0.4613	0.0333	1.3207	0.3005	0.4888
Cr	205.9603	14.8503	8.7466	0.5972	2.9543	0.5972	14.8503	5.8505	6.7871
Mn	0.0010	1.8945	0.2083	0.0537	0.4229	0.0537	1.8945	0.3156	0.6449
Co	0.9016	0.5332	0.0141	0.0092	0.0896	0.0092	0.5332	0.0519	0.1615
Ni	18.1636	6.6230	0.1429	0.1890	0.7535	0.1429	6.6230	0.4713	1.9271
Cu	1.3088	1.1048	0.0374	0.0596	0.4282	0.0374	1.1048	0.2439	0.4075
Zn	1.7938	0.5172	0.0611	0.0269	0.1654	0.0269	0.5172	0.1132	0.1926
Ga	0.1619	0.0453	0.0047	0.0040	0.0309	0.0040	0.0453	0.0178	0.0212
Sr	1.7320	0.4310	0.0309	0.0157	0.4122	0.0157	0.4310	0.2216	0.2225
Y	0.1378	0.0822	0.0026	0.0013	0.0325	0.0013	0.0822	0.0175	0.0296
Zr	0.7590	0.1618	0.0222	0.0070	0.1907	0.0070	0.1907	0.0920	0.0954
Nb	0.0619	0.0096	0.0013	0.0012	0.0139	0.0012	0.0139	0.0055	0.0065
Ba	2.0125	0.2640	0.0696	0.0059	0.7148	0.0059	0.7148	0.1668	0.2636
La	0.0810	0.0149	0.0025	0.0010	0.0272	0.0010	0.0272	0.0087	0.0114
Ce	0.2146	0.0420	0.0050	0.0025	0.0579	0.0025	0.0579	0.0235	0.0269
Pr	0.0207	0.0054	0.0008	0.0004	0.0077	0.0004	0.0077	0.0031	0.0036
Nd	0.1187	0.0237	0.0030	0.0018	0.0369	0.0018	0.0369	0.0134	0.0164
Sm	0.0466	0.0119	0.0013	0.0019	0.0107	0.0013	0.0119	0.0063	0.0064
Eu	0.0138	0.0021	0.0004	0.0006	0.0039	0.0004	0.0039	0.0014	0.0018
Gd	0.0535	0.0158	0.0015	0.0015	0.0114	0.0015	0.0158	0.0064	0.0075
Tb	0.0055	0.0016	0.0002	0.0003	0.0012	0.0002	0.0016	0.0008	0.0008
Dy	0.0495	0.0116	0.0013	0.0011	0.0114	0.0011	0.0116	0.0064	0.0063
Ho	0.0088	0.0030	0.0002	0.0003	0.0019	0.0002	0.0030	0.0011	0.0013
Er	0.0202	0.0080	0.0006	0.0009	0.0044	0.0006	0.0080	0.0026	0.0035
Tm	0.0055	0.0012	0.0001	0.0002	0.0008	0.0001	0.0012	0.0005	0.0006
Yb	0.0203	0.0089	0.0010	0.0010	0.0061	0.0010	0.0089	0.0036	0.0043
Lu	0.0039	0.0014	0.0001	0.0002	0.0009	0.0001	0.0014	0.0005	0.0006
Th	0.0146	0.0002	0.0003	0.0002	0.0064	0.0002	0.0064	0.0003	0.0018
U	0.0083	0.0013	0.0000	0.0000	0.0026	0.0000	0.0026	0.0007	0.0010